

PMFSEL REPORT NO. 86-7  
JUNE 1986

GROUTED PILE-TO-SLEEVE CONNECTION TESTS

by

William B. Lamport  
James O. Jirsa  
Joseph A. Yura

Report on a Research Project

Sponsored by

Brown and Root International, Inc.  
Chevron USA, Inc.  
Exxon Production Research Co.  
Pennzoil Exploration and Production Co.  
Phillips Petroleum  
Shell Development Co.  
Standard Oil Production Co.  
Texaco, USA  
Union Oil of California

PHIL M. FERGUSON STRUCTURAL ENGINEERING LABORATORY  
Department of Civil Engineering  
Bureau of Engineering Research  
The University of Texas at Austin  
Austin, Texas 78712

June 1986

To my wife Rochelle, and my parents for  
their love, patience and support

## ACKNOWLEDGMENTS

The experimental portion of this research program was conducted at the Phil M. Ferguson Structural Engineering Laboratory, Department of Civil Engineering, The University of Texas at Austin. The help of the laboratory staff is greatly appreciated.

The author would like to thank Drs. Ramon Carrasquillo and Stelios Kyriakides for their help and suggestions throughout his dissertation program. Special appreciation is extended to Dr. John L. Tassoulas for his infinite patience in helping the author understand and implement the classical plasticity models used in the analytical portion of this dissertation.

This project was under the supervision of Drs. James O. Jirsa and Joseph A. Yura. The author would like to thank Drs. Jirsa and Yura for their tireless patience and invaluable suggestions which greatly improved the continuity and clarity of the text. Special appreciation is extended to Dr. Jirsa for his steady influence and his ability to simplify the complex. The author would like to also thank Dr. Yura for sharing his great insight, not only in the field of engineering but of life in general.

The author would also like to thank his fellow graduate students for their help and friendship. A special appreciation is extended to Wayne Stocks and Moyeenul Haque for their support and friendship.

Finally, and most of all I would like to thank my wife Rochelle who sacrificed so much on my behalf and without whose support and love I could have never achieved this goal.

## ABSTRACT

The ultimate axial strength of grouted pile-to-sleeve connections was investigated to determine the influence of moment, relative shear key location between pile and sleeve, eccentric pile and sleeve position and grout strength. A total of eighteen tests were conducted. These tests were divided into six series containing three replicates each.

The results showed that moment had no detrimental effect on the ultimate strength of a grouted pile-to-sleeve connection. The ultimate strength was not affected by extremes in the shear-key arrangements or by the variations in the thickness of the grout annulus. The strength of the connections varied with the square root of the grout strength.

The measured strengths were compared with empirical equations for the ultimate axial strength of a grouted pile-to-sleeve connection, recommended by the American Petroleum Institute (API) and the United Kingdom Department of Energy. The API equation was found to be more conservative in all cases. The United Kingdom Department of Energy formulation yielded strengths that were in better agreement with the measured values, although the solutions were not always conservative.

The behavior of the grouted pile-to-sleeve connection was examined in order to develop a simple analytical solution for ultimate strength. The empirical design equations yield reasonable

estimates of ultimate strength but do not provide insight into the load-resisting mechanism of the connection. An examination of tested specimens revealed that one of the major load-resisting mechanisms of a grouted connection is the grout compression struts which develop throughout the length of the connection. Another significant component of load transfer was found to be the friction that develops at the steel-grout interface.

A model based on classical plasticity was developed using the assumption that the tubes were infinitely stiff. By examining solutions based on different constitutive relations it was shown that the constitutive relations should include triaxial effects. Existing constitutive relations developed for normal strength grouts (3000 - 5000 psi) may not be applicable to grout strengths exceeding 6000 psi.

## Table of Contents

### Chapter

1	Introduction .....	1
1.1	Background .....	1
1.2	Parameters Affecting the Strength of Grouted Pile-to-Sleeve Connections .....	7
1.3	Empirical Design Equations .....	9
1.3.1	United Kingdom Department of Energy Formulation .....	9
1.3.2	American Petroleum Institute Formulation ..	12
1.3.3	Comparison of Empirical Formulations .....	16
1.4	Analytical Methods .....	20
1.4.1	Paslay Analytical Model .....	20
1.4.2	Chilvers Analytical Model .....	25
1.4.2.1	Application of Chilvers Equation to Loadings Other than Tension- Compression .....	30
1.4.3	Van Lee Thesis .....	35
1.4.4	Brown and Root Report .....	37
1.4.5	Summary of Empirical and Analytical Methods .....	38
1.5	Scope of Work .....	39
2	Test Program .....	41
2.1	Selection of Specimens .....	41
2.1.1	Test Series .....	42
2.1.2	Specimen Fabrication .....	45
2.2	Grouting Material and Methods .....	48
2.2.1	Grout Mix Design .....	48
2.2.2	Specimen Preparation .....	50
2.2.3	Grouting Process .....	56
2.2.4	Grout Columns .....	60
2.2.5	Grout and Specimen Curing .....	61
2.2.6	Determination of Grouted Length and Grout Annulus .....	64
2.3	Experimental Test Procedures .....	66
2.3.1	Test Frame .....	66
2.3.2	Specimen Positioning .....	66
2.3.3	Loading System .....	69
2.3.4	Instrumentation .....	72
2.3.5	General Loading .....	74
2.3.6	Determination of Grout Properties .....	76
2.3.7	Steel Coupon Test .....	81

3	Test results .....	84
3.1	General .....	84
3.2	Series 1: Reference Tests .....	88
3.2.1	Test UTA1 .....	89
3.2.2	Test UTA2 .....	90
3.2.3	Test UTA3 .....	90
3.3	Series 2: Combined Loading .....	93
3.3.1	Test UTM1 .....	94
3.3.2	Test UTM2 .....	94
3.3.3	Test UTM3 .....	97
3.4	Series 3: Relative Shear-key Location .....	97
3.4.1	Test UTA4 .....	97
3.4.2	Test UTA5 .....	98
3.4.3	Test UTA6 .....	100
3.5	Series 4: Length Effect on Combined Loading .....	100
3.5.1	Test UTA13 .....	100
3.5.2	Test UTM5 .....	102
3.5.3	Test UTM6 .....	104
3.6	Series 5: Eccentric Pile and Sleeve .....	104
3.6.1	Test UTA7 .....	106
3.6.2	Test UTA8 .....	106
3.6.3	Test UTA9 .....	108
3.7	Series 6: High Strength Grout .....	108
3.7.1	Test UTA10 .....	108
3.7.2	Test UTA11 .....	110
3.7.3	Test UTA12 .....	110
3.8	Measurement of Compressive Strength .....	111
3.9	Grout Column Cube Results .....	114
4	Evaluation of Test Results .....	118
4.1	General .....	118
4.2	Repeatability Between Tests .....	121
4.3	Comparison with Calculated Values .....	125
4.4	Grout Cube Size Effects .....	129
4.5	Comparison of Injected Grout Column Cubes with ASTM C109 Cubes .....	132
4.6	Orientation of Crack Patterns in Tested Specimens .....	134
5	Predicting Ultimate Axial Strength of Grouted Connections .....	139
5.1	General .....	139
5.2	The Failure Mechanism .....	140
5.3	Qualitative Effects of Parameters Affecting Grouted Connection Strength .....	144



5.3.1	Radial Connection Stiffness .....	144
5.3.2	Grout Strength .....	147
5.3.3	Shear Key Height .....	150
5.3.4	Shear Key Spacing .....	152
5.3.5	Summary of the Effect of Basic Parameters Affecting the Ultimate Strength of Grouted Connections .....	153
5.4	Modeling the Grouted Connection .....	155
5.4.1	Shear Key Force Component of Overall Strut Strength .....	159
5.4.2	Coulomb Friction Component of Overall Strut Strength .....	163
5.5	Constitutive Relations for Grout .....	165
5.6	Development of Chen's Constitutive Relations for Concrete .....	166
5.7	Development of Fardis' Monotonic Constitutive Law for Concrete .....	178
5.7.1	Modification of Constants for Grout .....	190
5.8	Application of Constitutive Relations to Axial Specimens with Normal Strength Grout .....	193
5.8.1	General .....	193
5.8.2	Predicted Strength of Series 1 Axial Specimens Using Chen's Constitutive Relations .....	194
5.8.3	Predicted Strength of Series 1 Axial Specimens Using Fardis' Constitutive Relations .....	198
5.8.4	Discussion of Predicted Series 1 Strengths Using Chen's and Fardis' Constitutive Relations .....	198
5.9	Effect of Load Step, Material and Geometric Parameters Using Fardis' Constitutive Relations ..	200
5.9.1	Effect of Load Step Size .....	200
5.9.2	Effect of Radial Stiffness .....	202
5.9.3	Effect of Cube Strength Variation .....	206
5.9.4	Effect of Poisson's Ratio .....	208
5.9.5	Effect of Grout Modulus .....	210
5.9.6	Effect of Shear Key Height .....	213
5.9.7	Effect of Shear Key Spacing .....	213
5.9.8	Optimal Shear Key Height and Spacing .....	218
5.9.9	Application of Fardis' Constitutive Relations to Axial Specimens with High Strength Grout .....	218
5.9.10	Summary of Computed Grouted Connection Strength .....	230

6	Summary and Conclusions .....	233
6.1	General .....	233
6.2	Summary of Experimental Results .....	234
6.2.1	Pile-to-Sleeve Connection Tests .....	234
6.2.2	Effect of Cube Size on Grout Strength .....	235
6.2.3	Injected Grout Column Cubes vs ASTM C109 Cubes .....	235
6.3	Summary of Analytical Study .....	236
6.4	Recommendations for Future Work .....	238
Appendix A: Tabulated Shear Key Specimen Data .....		241
Appendix B: Equations in SI Units .....		245
Appendix C: Offshore Grouting Methods, Materials and Mix Design.....		248
C.1	General .....	249
C.2	Offshore Oil Industry Applications .....	249
C.3	Offshore Grouting Methods .....	250
C.4	Grout Materials .....	252
C.4.1	Cement Classes and Type .....	254
C.4.2	Admixtures .....	256
C.4.3	Fine Aggregate and Solids .....	257
Appendix D: Grout Properties .....		259
Appendix E: Bond Stress vs Displacement .....		287
Appendix F: Sample Calculations .....		306
Appendix G: Program Listings .....		310
References .....		335

## LIST OF TABLES

Table		Page
1.1	UK Recommended Limits for Equations 1-6 .....	10
1.2	API Recommended Limits for Equations 7 and 8 .....	16
1.3	Geometric Properties of Selected Series P and A Specimens .....	33
1.4	Measured and Computed Ultimate Bond Stress for Selected Series P and A Specimens .....	33
2.1	Data Base for Specimens with Shear Keys .....	42
2.2	Recommended Limits for Grouted Pile-to-Sleeve Connections .....	48
2.3	Mix I Proportions by Weight .....	50
2.4	Mix J Proportions by Weight .....	50
2.5	Specimen Shear Key Geometry .....	53
2.6	Out-of-Roundness of Steel Tubulars .....	54
2.7	Average Surface Roughness of Steel Tubulars .....	56
2.8	Grout Densities .....	58
2.9	Average Grouted Length and Annulus Properties .....	65
2.10	Size and Quantity of Grout Cubes used to Determine $f_{cu}$ .....	77
2.11	Summary of Tension Coupon Tests .....	83
3.1	Test Program Results .....	85
3.2	Constant Grouted Lengths used for Calculation of $f_{bu}^2$ .....	88
3.3	Results of Series 1: Reference Tests .....	89
3.4	Results of Series 2: Combined Loading .....	93
3.5	Results of Series 3: Relative Shear-Key Location .....	98

3.6	Results of Series 4: Length Effect on Combined Loading.	102
3.7	Results of Series 5: Eccentric Pile and Sleeve .....	106
3.8	Results of Series 6: High Strength Grout .....	110
3.9	Compressive Strength for Mix I: Multiplication Factors with Respect to 2-in. Cubes .....	115
3.10	Compressive Strength for Mix J: Multiplication Factors with Respect to 2-in. Cubes .....	116
3.11	Compressive Strength: Multiplication Factors on Day of Testing with Respect to 2-in. Cubes .....	116
4.1	Comparison of Measured and Calculated $f_{bu}$ Using Mean Eqs. 5 and 9 .....	126
4.2	Comparison of Measured and Allowable Bond Stresses Using UK Eq. 8 and API Eq. 10 .....	127
4.3	Summary of Cube Unconfined Compressive Strength Scatter .....	131
4.4	Summary of 7-day Column Cube Results Using Mix I .....	133
4.5	Summary of 28-day Column Cube Results using Mix I .....	133
5.1	Predicted Axial Strengths for Series 1 Using Chen's Constitutive Relations .....	197
5.2	Predicted Axial Strengths for Series 1 Using Fardis' Constitutive Relations .....	197
5.3	Effect of Load Step Size on Calculated Strength of Axial Specimen UTAl .....	201
5.4	Optimal Shear Key Heights for Different Shear Key Spacings .....	220
5.5	Calculated Loads for Specimens with High Strength Grout and $L/D_p=1$ .....	220
5.6	Effect of Increasing Grout Strength on the Ultimate Strength of UTAl .....	223
C.1	Typical Offshore Grout Formulations Ref. 59 .....	255

## LIST OF FIGURES

Figure		
1.1	Typical template platform .....	3
1.2a	Cluster piles .....	5
1.2b	Skirt piles .....	5
1.3	Typical grouted pile-to-sleeve connection .....	6
1.4	Least square fit of Eq. 4 to experimental data .....	13
1.5	API Eqs. 9 and 10 plotted with respect to experimental data base .....	15
1.6	Comparison between Eqs. 5 and 9 with previous test results having constant stiffness coefficient, K, and varying grout strengths .....	17
1.7	Comparison between Eqs. 5 and 9 with previous test results for constant $f_{cu}$ and variable stiffness coefficient, K .....	19
1.8	Generic element of Paslay model including all prescribed forces and displacements .....	22
1.9	Punch used to represent back-to-back shear keys separated by frictionless wall .....	23
1.10	Van Lee's local bond stress vs slip relationship .....	36
2.1a	Standard shear key arrangement .....	44
2.1b	Series 3 shear key arrangement .....	44
2.2a	Standard concentric tube arrangement .....	44
2.2b	Series 5 eccentric tube arrangement .....	44
2.3	Specimen geometry .....	46
2.4	Grout entry port .....	51
2.5	Application of Press-O-Film to determine tubular surface roughness .....	55

2.6	Spring micrometer used to determine surface roughness from Press-O-Film .....	55
2.7	Positioning of Series 1 specimens for grouting .....	57
2.8	Mud balance used to determine grout density .....	57
2.9	Specimen showing grout flow over pile during grouting process .....	59
2.10	Casting of cube molds, 4-in. x 8-in. cylinders and shrinkage specimens .....	59
2.11	Injection of grout into 2-in. x 2-in. grout columns ...	62
2.12	Typical specimen storage during curing .....	63
2.13	Test frame schematic .....	67
2.14	Leveling bolt .....	68
2.15	Specimen in the test frame .....	68
2.16	Schematic of axial load system .....	70
2.17	Electric pump, load maintainer and HP system .....	71
2.18	Schematic of combined loading system .....	73
2.19	Instrumentation used to obtain relative displacements with LVDT's .....	75
2.20	Shrinkage specimen in digital length comparator .....	78
2.21	Typical location of grout cubes for 3-ft column .....	80
2.22	Typical location of grout cubes for 6-ft column .....	80
2.23	Typical stress-strain plot for tension coupons .....	82
3.1	Typical average bond stress versus displacement curve ..	86
3.2	Grout surface on sleeve side for Specimen UTA2 .....	91
3.3	Grout surface on pile side for Specimen UTA2 .....	91
3.4	Grout profile of Specimen UTA2, showing crack pattern .	92

3.5	Grout surface on sleeve side for Specimen UTM2 .....	95
3.6	Grout surface on pile side for Specimen UTM2 .....	95
3.7	Grout profile of Specimen UTM2, showing crack pattern .	96
3.8	Grout surface on sleeve side for Specimen UTA5 .....	99
3.9	Grout surface on pile side for Specimen UTA5 .....	99
3.10	Grout profile of Specimen UTA5, showing crack pattern .	101
3.11	Grout surface on sleeve side for Specimen UTM5 .....	103
3.12	Grout surface on pile for Specimen UTM5 .....	103
3.13	Grout profile of Specimen UTM5, showing crack pattern .	105
3.14	Typical annulus for eccentrically placed pile and sleeve specimens .....	105
3.15	Grout surface on sleeve side for Specimen UTA8 .....	107
3.16	Grout surface on pile side for Specimen UTA8 .....	107
3.17	Grout profile of Specimen UTA8 showing crack pattern for side with 1/2-in. annulus .....	109
3.18	Grout profile of Specimen UTA8 showing crack pattern for side with 1-1/2 in. annulus .....	109
3.19	Grout surface on sleeve side for Specimen UTA12 .....	112
3.20	Grout surface on pile side for Specimen UTA12 .....	112
3.21	Grout profile of Specimen UTA12 showing crack pattern..	113
3.22	Histogram of pumped grout column cubes vs ASTM C109 cubes for mix design I .....	117
4.1	Ultimate measured bond stress vs unconfined compressive strength times (h/s) for 92 shear-key specimens .....	119
4.2	Ultimate measured bond stress vs unconfined compressive strength times (h/s) for 18 University of Texas shear- key specimens .....	120
4.3	Schematic showing crack orientation for Specimen UTA2..	135

4.4	Schematic showing crack orientation for Specimen UTA5 .	135
4.5	Schematic showing crack orientation for 1/2" annulus side of Specimen UTA8 .....	135
4.6	Schematic showing crack orientation for 1-1/2" annulus side of Specimen UTA8 .....	135
4.7	Schematic showing crack orientation for Specimen UTA12.	135
5.1a	Idealized stage 1 development of failure mechanism ....	142
5.1b	Idealized stage 2 development of failure mechanism ....	142
5.1c	Idealized stage 3 development of failure mechanism ....	142
5.2	Effect of radial connection stiffness on ultimate bond strength for Wimpey Labs series P and R .....	146
5.3	Effect of grout strength on ultimate bond strength for seven University of Texas axial specimens .....	148
5.4	Parabolic relationship between ultimate bond strength and cube strength .....	149
5.5	Effect of shear key height on ultimate bond strength for Wimpey Labs series R .....	151
5.6	Effect of shear key spacing on ultimate bond strength for Wimpey Labs series Q .....	154
5.7	Idealized grout compression strut .....	157
5.8	Forces acting on idealized grout compression strut.....	158
5.9	Elemental block showing stress-state in grout wedge region of grout compression strut .....	160
5.10	Chen's initial yield and failure surfaces in principal-stress space ref. [36] .....	170
5.11	Chen's subsequent loading surfaces in $I_1, J_2$ space Ref. [36] .....	171
5.12	Flow chart for Chen's constitutive relations .....	179
5.13	Flow chart of subroutines for Chen's constitutive relations .....	180



5.14	Definition of Fardis' parameters, $d$ and $d_{max}$ for generalized shear modulus .....	184
5.15	Flow chart for Fardis' constitutive relations .....	191
5.16	Flow chart of subroutines for Fardis' constitutive relations .....	192
5.17	Uniaxial stress-strain curve for grout mix I3 .....	195
5.18	Ratio of the calculated lateral confining stress to bearing stress vs bearing stress as predicted by the Fardis constitutive relations .....	203
5.19	Variation of radial stiffness of steel tube as a function of $D/t$ .....	205
5.20	Effect of cube strength variation on predicted ultimate strength .....	207
5.21	Effect of Poisson's ratio on predicted ultimate strength .....	209
5.22	Effect of grout modulus on predicted ultimate strength.	211
5.23	Variation of moduli with grout strength .....	212
5.24	Effect of shear key height on predicted ultimate strength .....	214
5.25	Effect of shear key spacing on predicted ultimate strength .....	215
5.26	Effect of assumed strut orientation in establishing effective shear key spacing .....	217
5.27	Optimal shear key height for given shear key spacing ..	219
5.28	Effect of increasing grout strength on predicted ultimate strength .....	222
5.29	Comparison of Carrasquillo's experimentally obtained uniaxial compression test strains with those predicted using Fardis' constitutive relations, for high strength gravel concrete .....	225

5.30	Comparison of Carrasquillo's experimentally obtained uniaxial compression test strains with those predicted using Fardis' modified constitutive relations, for high strength gravel concrete .....	228
C.1	Conventional two-stage method .....	253
C.2	Packer method .....	253
C.3	Balanced pressure method .....	253

CHAPTER 1  
INTRODUCTION

1.1 Background

The offshore oil industry began off the coast of California in the 1890s. In 1937 the Superior Oil Company and the Pure Oil Company leased 33,000 acres offshore in the Gulf of Mexico and commissioned Brown and Root, Inc. to design a platform to be placed in 14 ft. of water about a mile from the coastline. This timber platform was the first to be constructed in the Gulf in an area remote from shore [1].

In 1947 The Superior Oil Company designed two platforms that became the design standard for many years to come. The new design called for six steel templates or jackets to be fabricated on shore and carried to the site by barge. The jackets were then lowered by a crane and fixed to sea floor using steel piles driven through the jacket legs [2]. The term "template" derives from the fact that the jacket legs serve as guides for the tubular piles. This construction method allowed the actual placement of the structure in the water to be completed in about two weeks as opposed to about two months required by the common method of on-site construction used in timber platforms. This new method of construction allowed platforms to be

placed in much deeper water than had previously been possible. Figure 1.1 shows a typical template platform.

In shallow water (less than 150 ft.) it is normal for a single pile to be placed through each jacket leg of the structure. The pile usually extends to the top of the structure so the deck structure can be welded directly to it. The annulus between the pile and the jacket leg is then filled with cement grout. The jacket resists the effects of environmental loading and is stabilized by the piles. The grout transmits the lateral forces between the jacket-legs and the foundation piles and protects against corrosion, but is not normally relied upon to transmit vertical loads from the deck superstructure to the piles. Bond stresses along the steel-grout interface are low and debonding is unlikely to cause any problems. The typical pile size in the mid-1950s, was 30 inches (76 cm) in outside diameter [2]. By 1969, the average pile had reached its current size of 48 inches (122 cm), with a range of 16 to 96 inches in the Gulf of Mexico. In the North Sea slightly larger average pile diameters of 60 inches (152 cm) are common. Pile wall thicknesses normally range from 0.625 inches (16 mm) to 1.25 inches (32 mm) with the heaviest wall being at the mudline [3]. The sleeve wall thicknesses are usually thinner since they are not required to carry the loads which develop in the piles during installation.

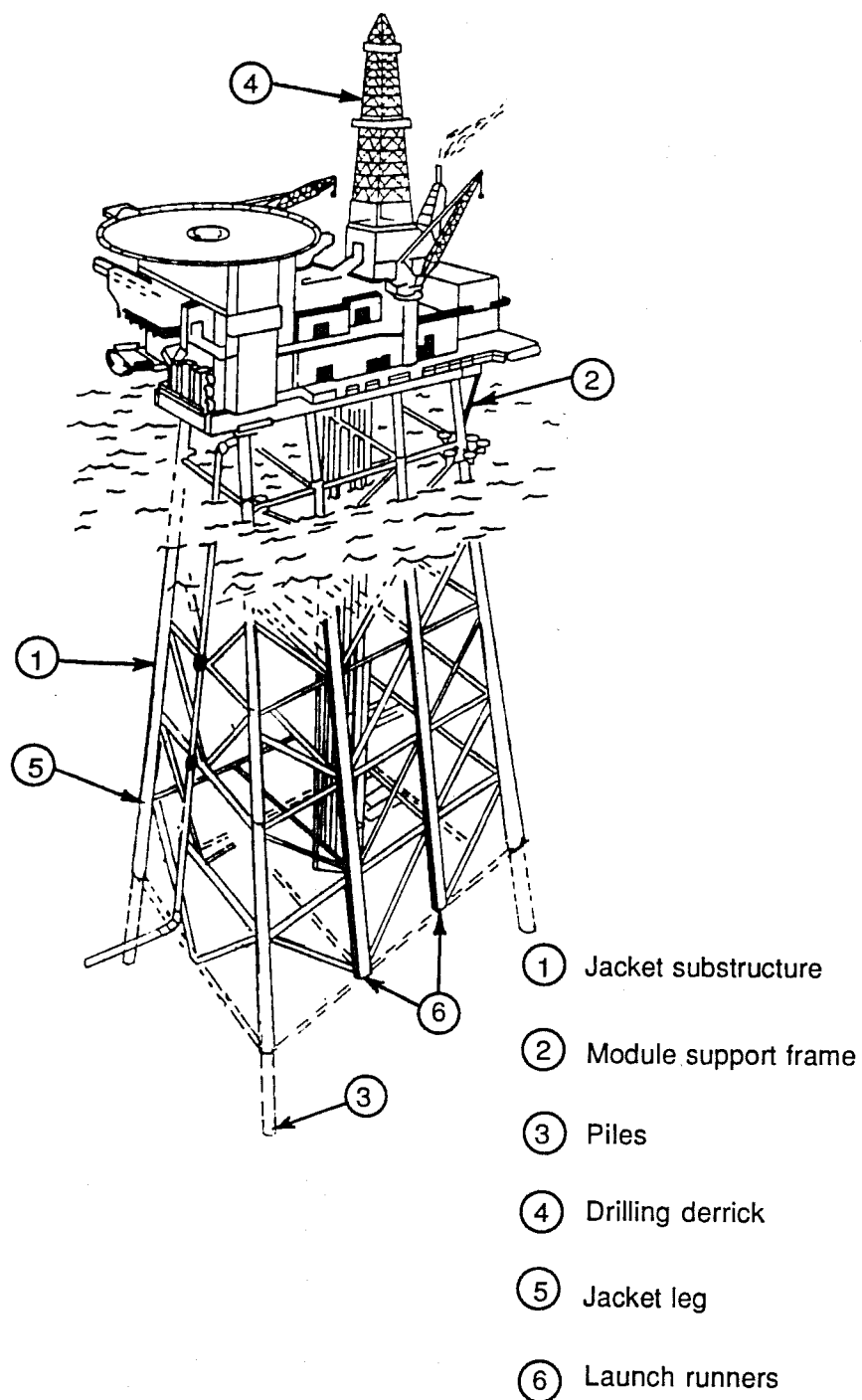


Fig. 1.1 Typical template platform

For fixed platforms in deeper water the cost of extending the piles the full length of the jacket leg becomes prohibitive. Thus, in deeper waters the piles are normally installed through sleeves which are attached to the lower section of the structure. The two basic types of arrangements are: cluster piles where the sleeves are attached in clusters around the legs of the jacket via shear plates or skirt piles where the sleeves are spaced around the perimeter of the jacket to form an integral part of the lower structural bracing system, see Fig. 1.2a and 1.2b.

The annulus formed between the tubular steel sleeve and pile is usually filled with a cementitious grout, which unlike the jacket platform, forms the only structural connection between the jacket and the foundation. The connection is known as a grouted pile-to-sleeve connection, commonly shortened to a grouted connection. A typical section of a grouted connection is shown in Fig. 1.3. The grout must transmit all the forces arising from the dead weight of the structure, and environmental loadings.

As the capacity of offshore construction plants for handling and driving piles increases, a trend towards foundations consisting of smaller numbers of larger diameter, less radially stiff grouted connections makes it necessary to investigate the factors affecting the strength of grouted connections. The results of tests on large diameter plain pipe connections show that excessive lengths are

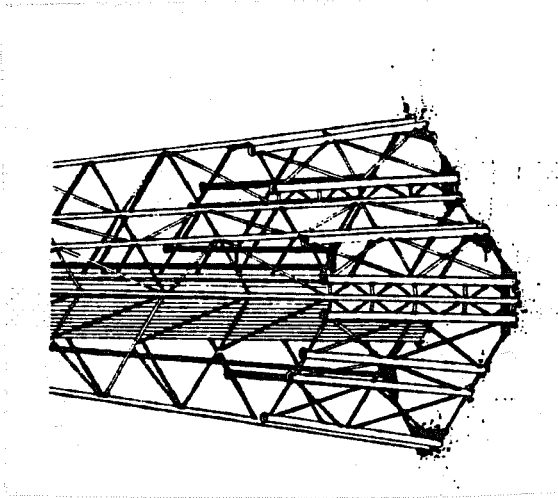


Fig. 1.2b Skirt piles

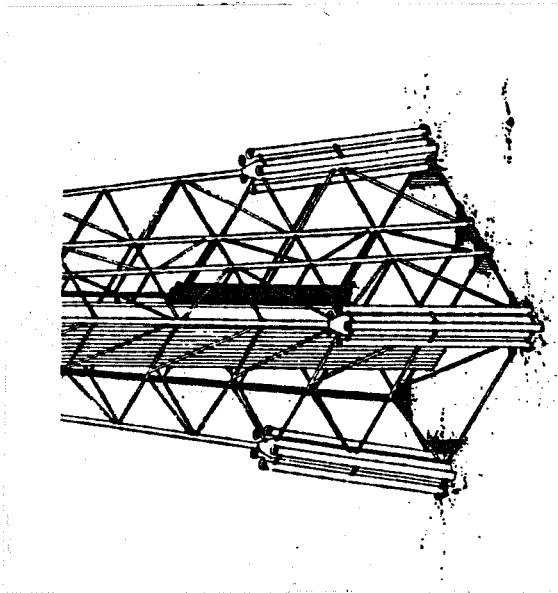


Fig. 1.2a Cluster piles

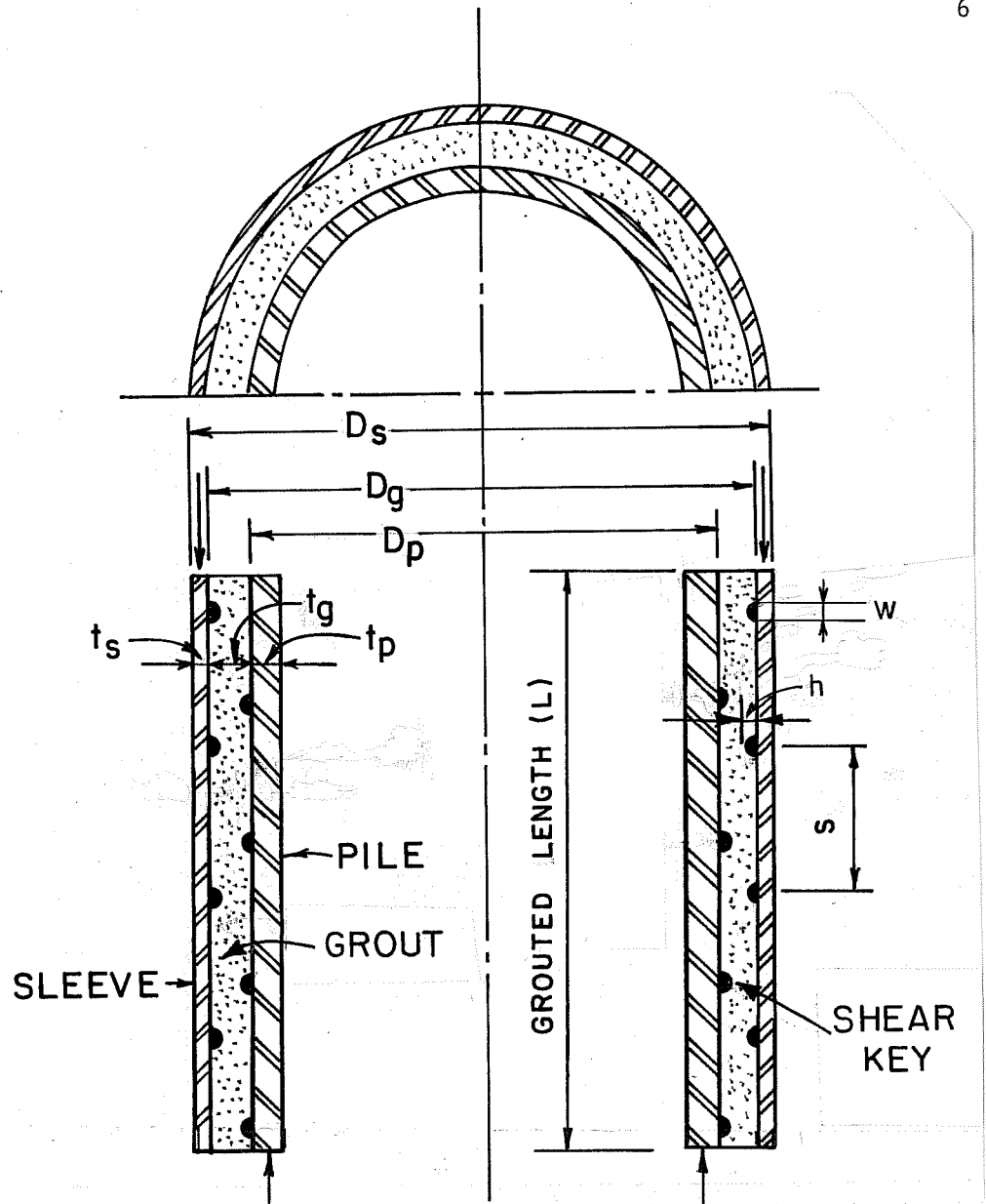


Fig. 1.3 Typical grouted pile-to-sleeve connection



required to develop needed strengths in deep water platforms and as a result the mechanical shear keys shown in Fig. 1.3 were introduced. These keys consist of weld beads or welded bars, forming rings around the circumference of the inner surface of the sleeve and the outer surface of the pile, which key into the grout and greatly enhance the bond strength. Normally the spacing of the keys is kept constant for both the sleeve and pile.

#### 1.2 Parameters Affecting the Strength of Grouted Pile-to-Sleeve Connections

The behavior of grouted connections has been investigated by several researchers [4,5,6,7] since the early 1970's. The majority of the early research was for specific projects of individual oil companies. The results of these early tests were useful in establishing the parameters that affected the strength (axial load capacity) of the grouted connection and also provided a great deal of experimental data on the static axial capacity. They did not, however, cover all aspects of the problem.

As late as 1977 the only design guidance available for grouted connections was given in Section 2.3 of the American Petroleum Institute (API) Specification RP 2A [8]. Section 2.3 limited the design bond strength for plain pipe connections to 20.0 psi (0.138 N/mm<sup>2</sup>). Although the factor of safety was not specifically stated, it was assumed to be six [9]. At this time, the specification did not

include any guidance on the design of grouted connections with shear keys.

The ultimate strength of plain pipe grouted connections was investigated at Wimpey Laboratories for British Petroleum beginning in 1973. The results of these tests showed that the factor of safety may be considerably lower than six as assumed [9]. Rather than increasing the length of the piles to ensure the minimum safety factor of six, the use of mechanical shear keys was investigated. Subsequent tests performed from 1973 to 1978 by Wimpey Labs showed that very large increases in bond strength could be achieved by employing mechanical shear keys.

Ultimate strength equations available as of 1987 were derived from experimental data usually using some form of regression analysis. Design equations differ as to the values of the exponents and coefficients which are combined with each parameter, and as a result, ultimate strength equations vary between investigators. Based on Wimpey's investigations the following parameters were identified as important in determining the ultimate capacity of grouted connections:

- Tube and grout geometries;
- Geometry and spacing of mechanical shear keys;
- Grouted length to pile diameter ratio;
- Surface condition of steel tubulars;
- Long term grout shrinkage or expansion.

The last two parameters are of major significance only for plain pipe connections.

### 1.3 Empirical Design Equations

Investigators have developed empirical equations describing the ultimate strength of grouted connections using the available data base [9, 10, 11, 12, 13, 14, 15, 16, 17, 18, 19, 20]. A complete listing of shear-keyed specimens is given in Appendix A.

1.3.1 United Kingdom Department of Energy Formulation. In 1978 the United Kingdom (UK) Department of Energy commissioned Wimpey Laboratories to formulate a research program to study the behavior of grouted connections [10]. The experimental program consisted of 62 static tests on plain pipe and shear-key grouted connections.

Based on empirical data from 108 tests consisting of the 62 tests from the UK study, 34 tests carried out for individual oil companies, and an additional 12 tests carried out at the conclusion of the UK program [21], engineers at Wimpey Laboratories proposed a bond strength formula for grouted connections, applicable within the geometric limits given in Table 1.1.

Billington and Lewis [22] found that bond strength is a function of grout cube compression strength, which is independent of grout mix.

$$f_{bu} \propto f_{cu} \tag{1}$$

The bond strength was normalized with respect to a grout cube strength. Thus a dimensionless bond strength parameter,  $F_{bu}$

TABLE 1.1 UK Recommended Limits for Equations 1-6 [21]

Parameter	Limits
Sleeve Geometry	$40 \leq (D/t)_s \leq 140$
Pile Geometry	$20 \leq (D/t)_p \leq 32$
Grout Annulus	$10 \leq (D/t)_g \leq 45$
Shear Key Spacing	$0 \leq D_p/s \leq 8$
Shear Key Ratio	$0 \leq h/s \leq 0.04$

was developed and is defined by

$$F_{bu} = \frac{f_{bu}}{160} \left( \frac{7260}{f_{cu}} \right)^{0.5} \quad (2)$$

where  $f_{bu}$  = the ultimate bond strength in psi  
 $f_{cu}$  = the mean unconfined grout compressive strength in psi, determined from 3 in. (76 mm) grout cubes  
 160 = implied API ultimate bond strength for plain pipe connections taken as six times the API RP 2A [8] allowable bond stress.

Therefore,  $F_{bu}$  is the multiple of the API plain pipe ultimate bond strength, at a grout strength of 7260 psi (50 N/mm<sup>2</sup>). In other words, if  $F_{bu}$  is unity the connection has a safety factor of six

against the design stress permitted by API RP 2A [8] for plain pipe connections at a grout strength of 7260 psi (50 N/mm<sup>2</sup>).

Billington and Tebbet proposed that the generalized grout bond formula be of the form;

$$F_{bu} = KC_L(AC_s + B h/s) \quad (3)$$

The constants A and B were determined from a least-squares analysis of the data. A value of 76 was found for the intercept A and 9468 for the slope B when  $C_s$  was taken as unity for the shot-blasted surface condition of the test specimens. The mean formula established for the bond strength parameter is

$$F_{bu} = KC_L(76C_s + 9468 h/s) \quad (4)$$

where K = stiffness coefficient defined as:

$$= 1/m (D/t)_g^{-1} + [(D/t)_s + (D/t)_p]^{-1}$$

m = modular ratio ( $E_s/E_g$ )

D/t = out-to-out diameter-to-thickness ratio of grout (g), sleeve (s), or pile (p) respectively

$C_L$  = length coefficient as defined in UK Department of Energy Guidance Notes, [23]

$C_s$  = surface coefficient as defined in UK Department of Energy Guidance Notes [23]

h = height of shear key

s = spacing of shear key

Figure 1.4 indicates the fit of Eq. 4 to the data. Substituting for  $F_{bu}$  from Eq. 2 gives the ultimate bond strength

$$f_{bu} = 16KC_L(9C_s + 1100 \text{ h/s})f_{cu}^{0.5} \quad (5)$$

Equation 5 is a mean fit to the data. A lower bound ultimate bond strength formula was taken as the characteristic strength defined as that value below which not more than 5% of the test results fall [21]. For a grouted connection the characteristic strength,  $f_{bd}$ , which is 0.75 times the mean strength [4] given by Eq. 5, is the bond strength given by Eq. 6 and is currently included in the UK Department of Energy Guidance Notes as Amendment No. 4 [23].

$$f_{bd} = 12KC_L(9C_s + 1100 \text{ h/s})f_{cu}^{0.5} \quad (6)$$

Equation 6 can be written in terms of the nondimensional bond strength parameter as

$$F_{bd} = KC_L(57C_s + 7100 \text{ h/s}) \quad (7)$$

A factor of safety is not given with UK Guidance Notes, but if a factor of six is used, the allowable bond strength,  $f_{ba}$ , is

$$f_{ba} = 2KC_L(9C_s + 1100 \text{ h/s})f_{cu}^{0.5} \quad (8)$$

1.3.2 American Petroleum Institute Formulation. The formulation currently recommended by API is based on work by Karsan and Krahl [5,24]. Karsan and Krahl presented two equations, one for estimating the ultimate strength of grouted connections, and a second modified form for design strength. The equations were derived from a

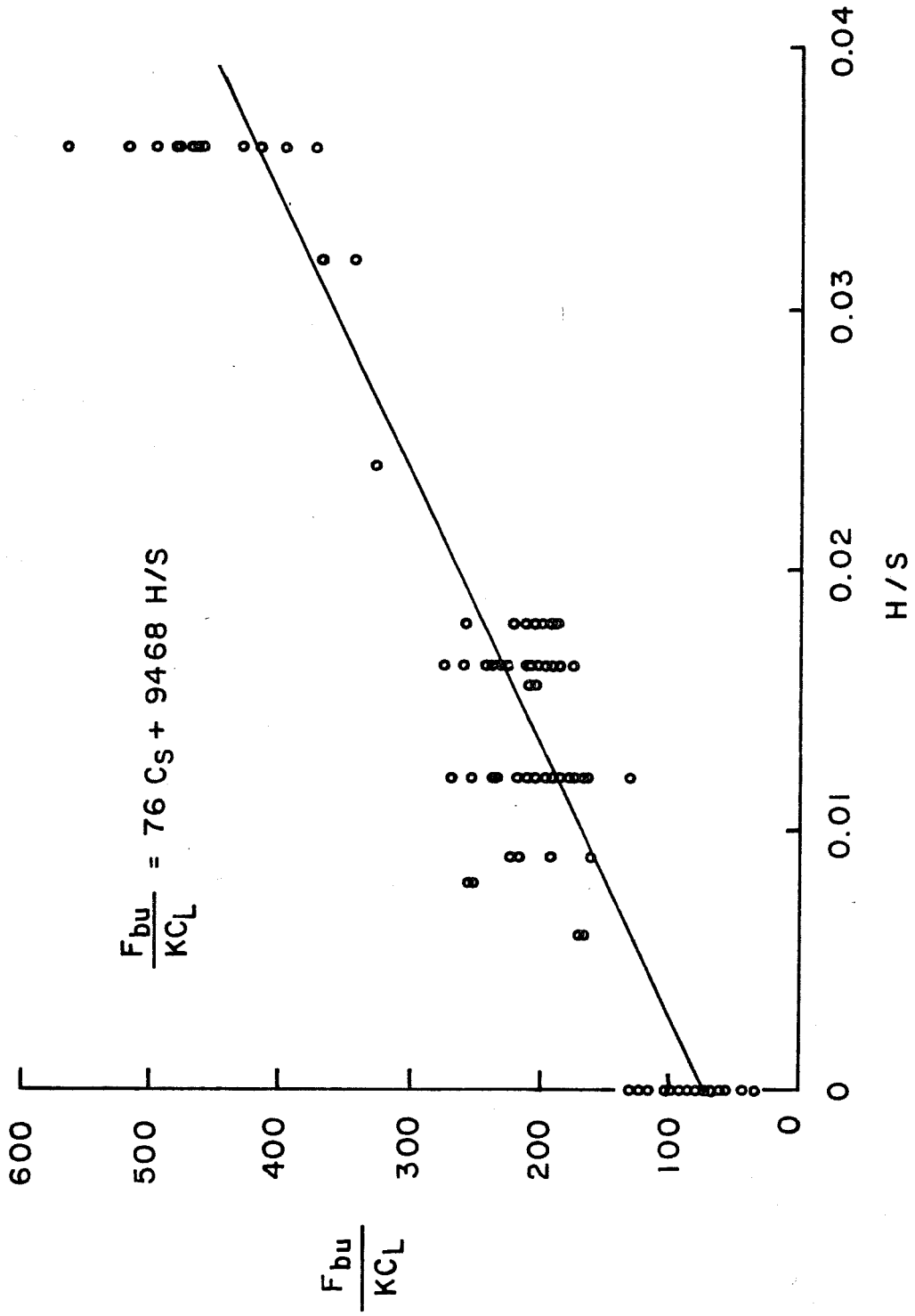


Fig. 1.4 Least square fit of Eq. 4 to experimental data

data base of 147 specimens in which 85 had mechanical shear keys and 62 were plain pipe grouted connections. The data represented a collection of experimental test results and included specimens with  $f_{cu}$  determined from 3 in. (76 mm) cubes and also specimens with  $f_{cu}$  determined from 2 in. (50.8 mm) cubes. Yet, there was no distinction made between the experimental data based on cube size. The ultimate strength of the connection (mean fit to data) is

$$f_{bu} = 167 + 1.72f_{cu}h/s \quad (9)$$

The equation suggested by Karsan and Krahl for design using API provisions is

$$f_{ba} = 20 + 0.5f_{cu}h/s \quad (10)$$

Equation 10 was adopted in the 14th Edition of API RP 2A [25]. These equations are applicable within the limits given in Table 1.2. For those grouted connections with no shear keys,  $h/s$  becomes zero and Eq. 10 gives an allowable stress of 20 psi (0.138 MPa), the same allowable value included in API RP 2A for years.

In Fig. 1.5, Eqs. 9 and 10 are compared with the 147 tests results. The ultimate bond stress  $f_{bu}$  (obtained by dividing the ultimate load by the area of the grout in contact with the pile,  $\pi D_p L$ ) is plotted against the unconfined grout compressive  $f_{cu}$  times  $h/s$ . Equations 1 through 10 are in U.S. units. All equations are listed in SI units in Appendix B.



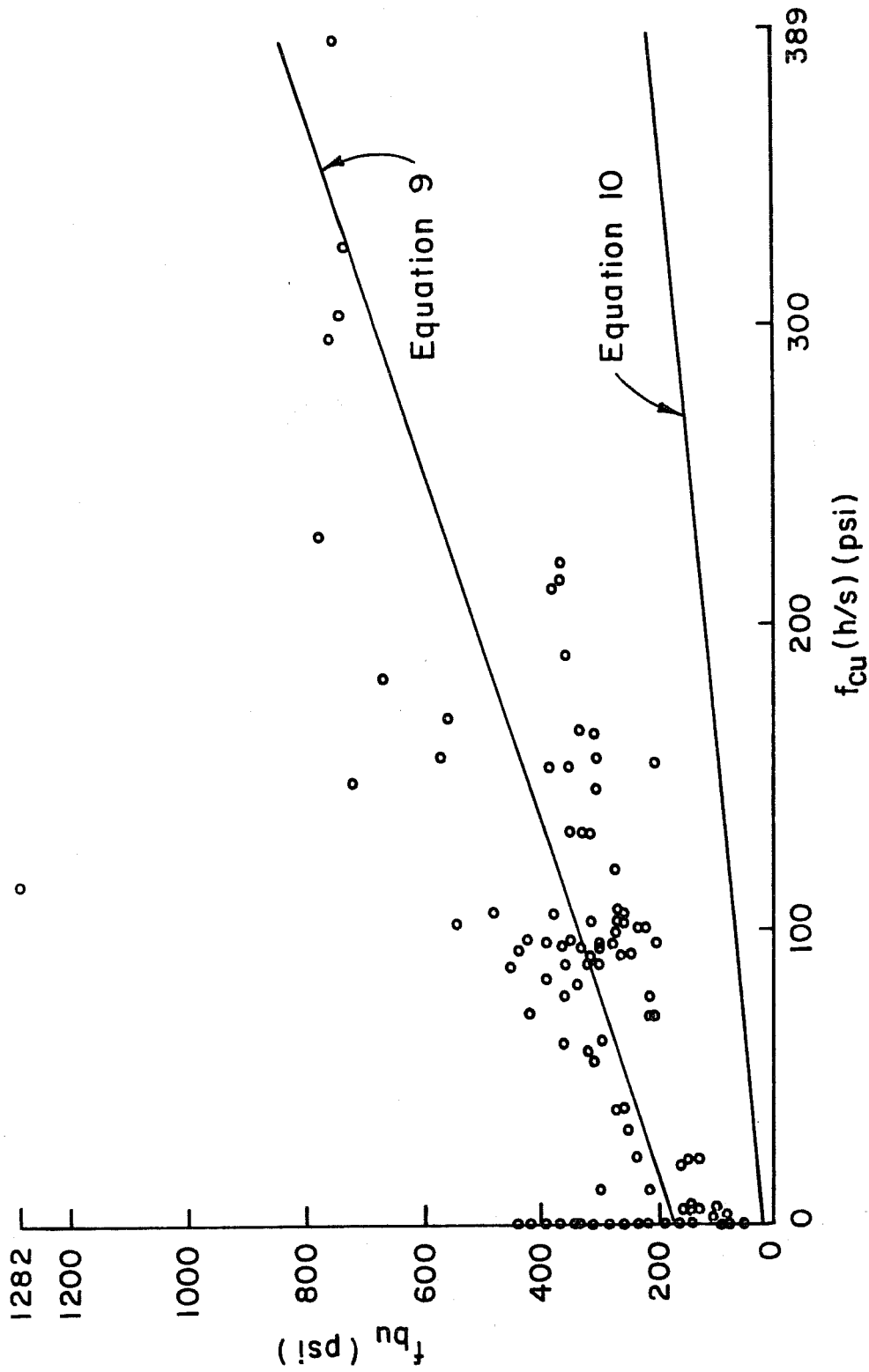


Fig. 1.5 API Eqs. 9 and 10 plotted with respect to experimental data base

TABLE 1.2 API Recommended Limits for Equations 7 and 8 [24]

Parameter	Limits
Sleeve Geometry	$(D/t)_s \leq 80$
Pile Geometry	$(D/t)_p \leq 40$
Grout Annulus	$7 \leq (D/t)_g \leq 45$
Shear Key Spacing	$2.5 \leq D_p/s \leq 8$
Shear Key Ratio	$h/s \leq 0.10$

1.3.3 Comparison of Empirical Formulations. The UK Department of Energy formulation given in Eq. 5 and the API formulation given in Eq. 9 are not directly comparable since Eq. 5 includes a confinement factor,  $K$ , and is a function of  $\sqrt{f_{cu}}$  instead of  $f_{cu}$  as in Eq. 9. However, Fig. 1.6 illustrates the effect of varying grout strength for Eq. 5 and 9. A typical value for the stiffness coefficient for specimens with shear keys is  $K=0.010$ . Values of  $f_{cu}$  from 4000 psi (28 MPa) to 9000 psi (62 MPa) represent a practical range for most grouts used in offshore applications. About 70% of the keyed specimens had grout strengths in this range. The data points shown are for shear-keyed specimens [7,11] with  $K$  values between 0.0095 and 0.0105 psi. Figure 1.6 shows that for typical connection stiffnesses and grout strengths, both Eq. 5 and 9 give similar ultimate strength and bound the experimental data.

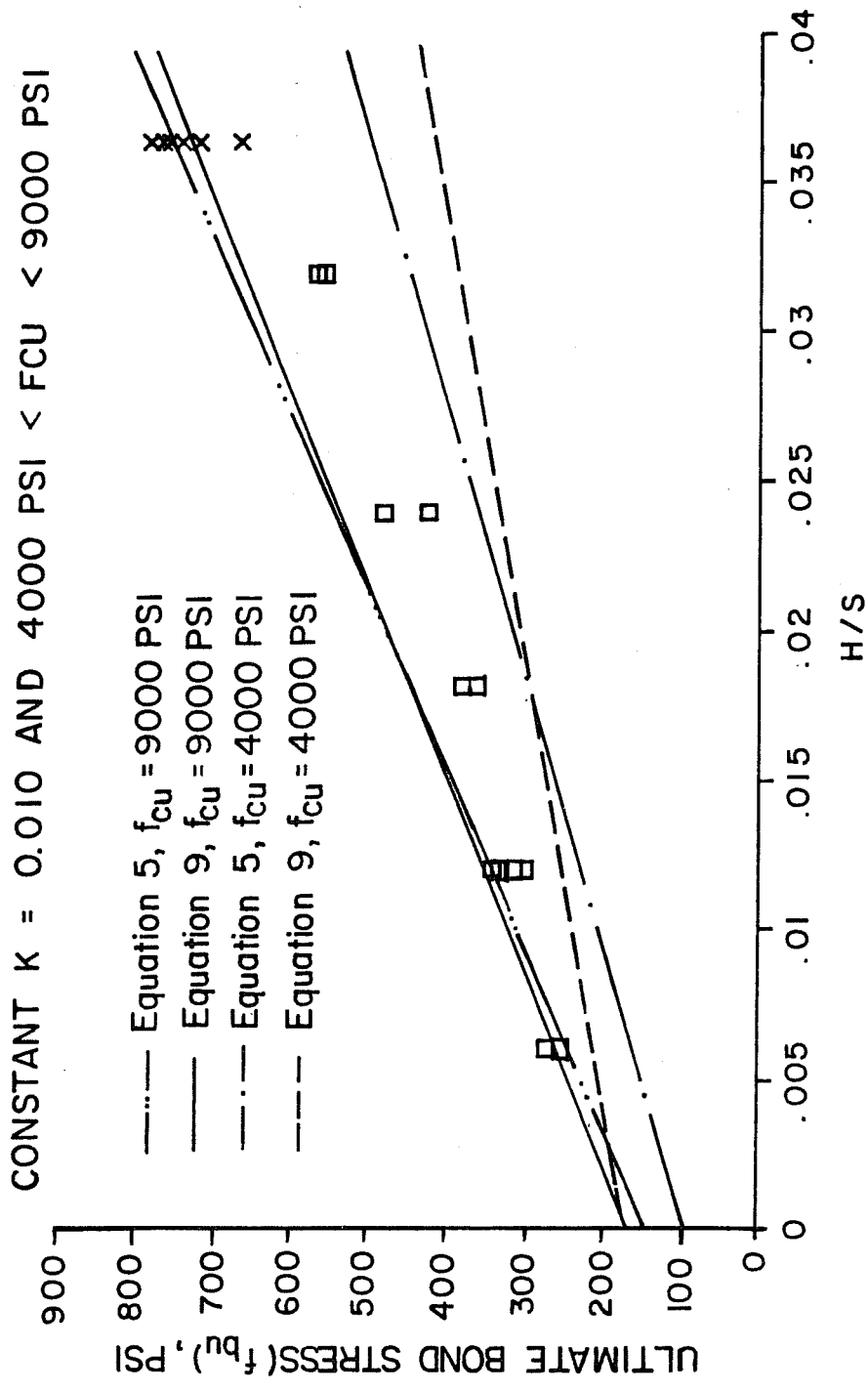


Fig. 1.6 Comparison between Eqs. 5 and 9 with previous test results having constant stiffness coefficient,  $K$ , and varying grout strengths

Figure 1.7 shows the effect of different values of  $K$  on the ultimate bond strength of grouted connections. The selected values of  $K$  represent the upper and lower limits of shear-keyed specimens. The data points shown are for shear-keyed specimens with  $f_{cu}$  values between 6000 psi (41 MPa) and 8000 psi (55 MPa). Figure 1.7 shows that for a constant unconfined grout strength  $f_{cu}$ , and varying stiffness  $K$ , Eq. 5 bounds the experimental data, whereas Eq. 9 cannot account for varying radial tube stiffnesses. Thus Eq. 5 and 9 may give significantly different values for ultimate bond stress. Although both empirical formulations are applicable only within specified limits neither formulation places an upper bound on the connection strength.

In both Fig. 1.6 and 1.7 the ordinate represents the ultimate bond stress, defined previously, and the abscissas are corresponding values of  $h/s$ .

A comparison of the API Eq. 9 with that of the UK Eq. 5 indicates the following differences.

- For the API Eq. 9 the plain pipe bond component is a constant.
- In the API Eq. 9 bond strength varies linearly with grout strength  $f_{cu}$ , instead of with the  $\sqrt{f_{cu}}$  as in the UK Eq. 5.

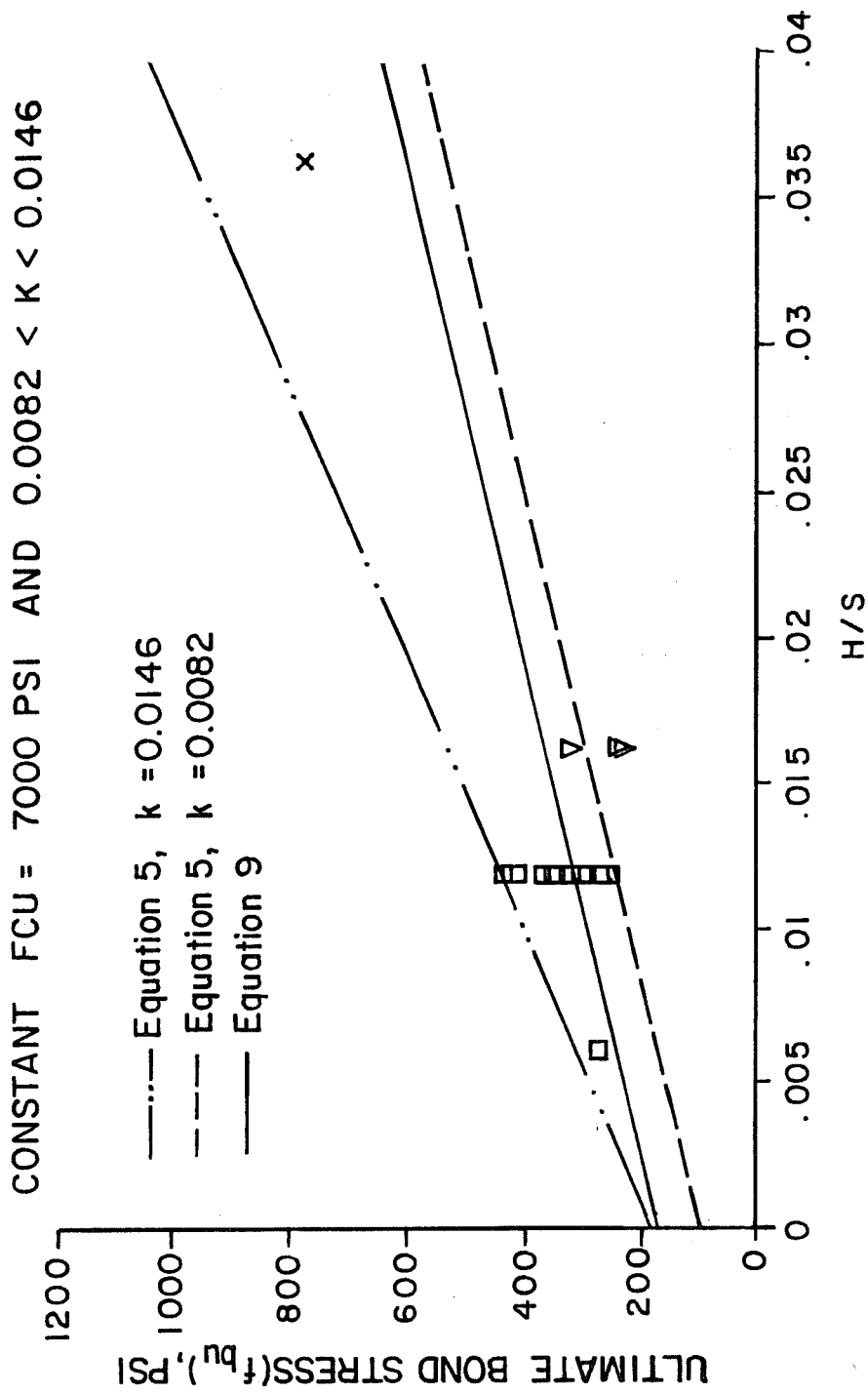


Fig. 1.7 Comparison between Eqs. 5 and 9 with previous test results for constant  $f_{cu}$  and variable stiffness coefficient, K

- In the UK equation the effects of radial tube stiffness,  $K$  is included whereas in the API equation connection stiffnesses are not considered.
- In the API equation, the connection length effect  $C_L$  is not included.

#### 1.4 Analytical Methods

Analytical solutions defining grouted connection ultimate strength are difficult to develop because of the nonlinear material behavior of the grout near ultimate strength. Furthermore, the exact state of triaxial stress in the grout is difficult to access, due to the fact that the stress state is affected by so many parameters, such as connection stiffness, shear-key geometry and grout strength. Analytical solutions however, have been attempted in recent years but as yet they are not widely accepted.

1.4.1 Paslay Analytical Model. Paslay Incorporated developed an analytical model [26] to predict the ultimate axial capacity of a grouted connection. As reported by Chilvers [27], the model is designed to simulate a grouted connection loaded in axial compression, transferring the load from the sleeve at one end to the pile at the other end. The model assumes three mechanisms are available to transfer the load across the steel-grout interface. These are;

- Adhesion of the grout to the sleeve or pile
- Coulomb friction along the interface
- Concentrated loads at the shear keys.

The behavior of the grout is assumed to be elastic-perfectly plastic in the analysis and is governed by a Von-Mises yield criterion.

The grouted connection is idealized as a series of axial elements. Each element has a shear key on one end of the pile and on the other end of the sleeve. Figure 1.8 shows an exploded view of an element, including all assumed forces and displacements essential to the analysis. All forces in the grout are assumed to be compressive. This was established from experimental observation of the cracking patterns in the grout, where cracks ran from the sleeve to the pile at the shear key locations. The analysis also assumes that the bond stress is constant over the length of each element.

Twenty-four simultaneous equations are written for each element. Since many of the equations are nonlinear, an incremental approach is used to obtain a solution. A linear solution is obtained for each small increment of load and the incremental equations are modified as the bond states change.

To establish the load-slip relationship for the shear keys Paslay performed some simple punch indentation tests on confined grout specimens. The punch was assumed to resemble back-to-back shear keys which were separated by a frictionless wall as shown in Fig. 1.9.

- CG: Axial compressive force on grout, left end
- CI: Axial compressive force on pile, left end
- CO: Axial compressive force on sleeve, left end
- PI: Average pressure between grout and pile
- PO: Average pressure between grout and sleeve
- SI: Axial component of force on pile shear key, left end
- SO: Axial component of force on sleeve shear key, right end
- SSI: Shear stress between grout and pile
- SSO: Shear stress between grout and sleeve
- XG: Axial displacement of grout, left end
- XI: Axial displacement of pile, left end
- XICR: Axial crush at pile shear key, left end
- XO: Axial displacement of sleeve, left end
- XOCR: Axial crush at sleeve shear key, right end
- $\xi^A$ : Value of  $\xi$  at right end

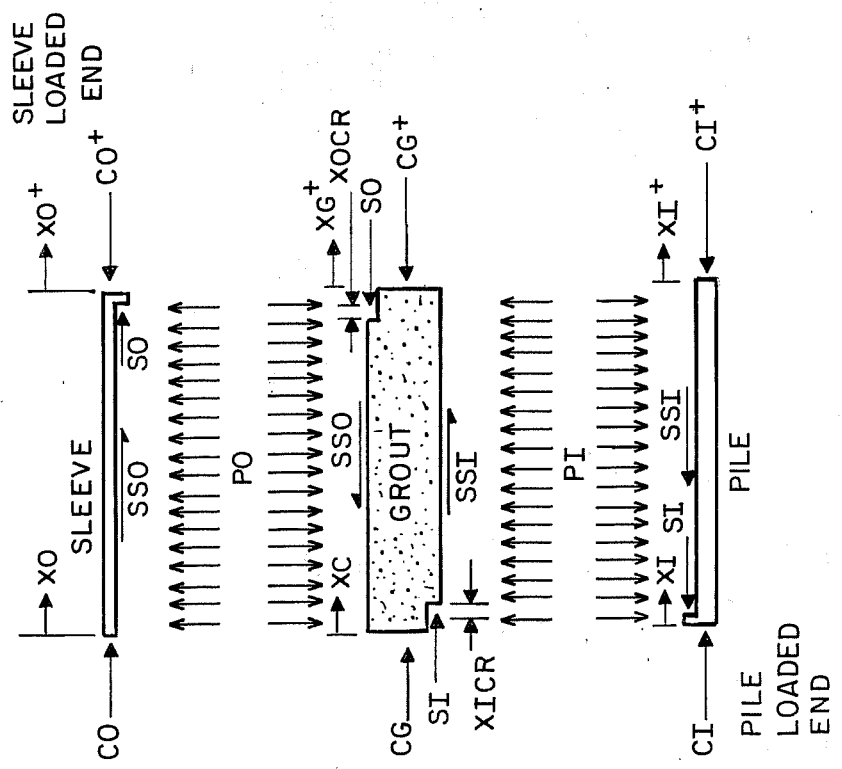


Fig. 1.8 Generic element of Paslay Model including all prescribed forces and displacements



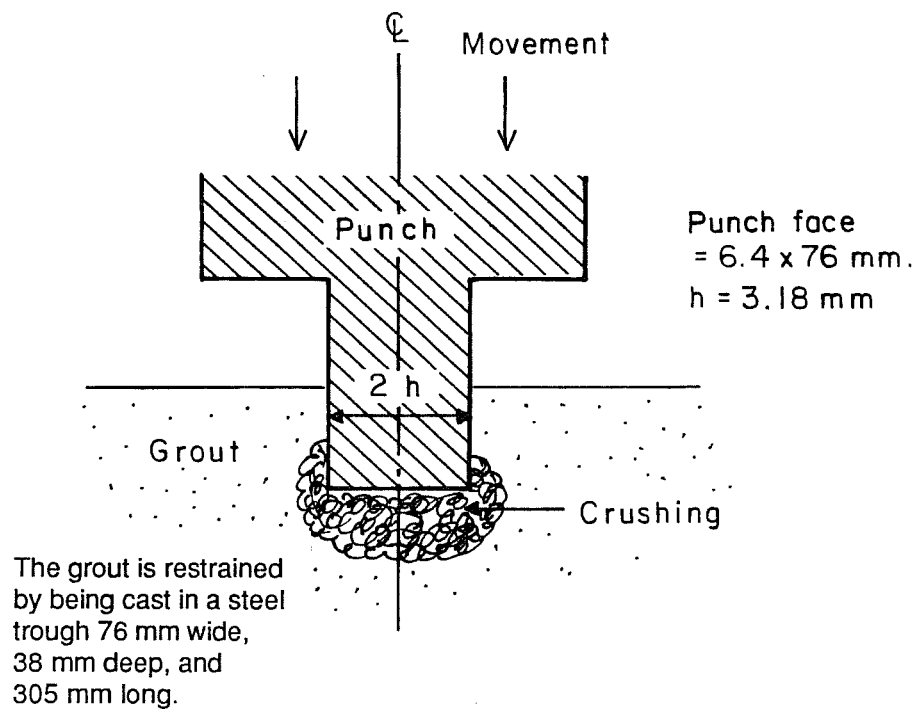


Fig. 1.9 Punch used to represent back-to-back shear keys separated by frictionless wall

Results from these experiments indicated the maximum pressure to be about five to six times the grout cube strength. Therefore, Paslay assumed a maximum shear key stress of

$$\sigma_k = 5.5f_{cu} \quad (11)$$

to reflect increased grout capacity due to confinement by the steel tubes.

A program is included in Paslay's report for the previously described analysis. Computer analyses were conducted for connection geometries which were experimentally examined by Chicago Bridge and Iron Company and Wimpey Laboratories. In implementing Paslay model the experimental connection geometry has to be modified so that the pile and sleeve shear keys are directly across from one another instead of staggered as in the actual test specimens. In general Chilvers states that the Paslay model was found to over estimate the capacity of the grouted connection.

The error in ultimate capacities from the Paslay model can be attributed to the idealization of the grout behavior with a Von Mises plasticity model. A Von Mises model works well for a ductile material such as steel where there is no appreciable effect of hydrostatic pressure on yielding, and the material exhibits equal yield stresses in tension and compression. However, the application of a Von Mises criteria to a fracturing, pressure sensitive material such as grout is

too drastic an idealization to accurately model the behavior and strength.

1.4.2 Chilvers Analytical Model. Chilvers' bond strength formula [27] develops connection capacity from friction at the grout pile-sleeve interface. Chilvers' analysis assumes that the connection strength is a function of the same three basic mechanisms described by Paslay. Thus the basic bond formula is expressed as:

$$f_{bu} = c + \mu\sigma_n + \sigma_m h/s \quad (12)$$

The mechanisms are:

- Adhesion of the grout to the sleeve or pile,  $c$ , taken as a constant. When the connection is grouted an adhesion of the grout to the steel occurs which has a capacity to transfer shear and tensile stresses across the steel-grout interface. So long as this bond is intact the strains at the interface are equal for the grout and the steel. Once the stresses exceed the adhesive bond strength, this mechanism is no longer active nor can it be regained upon unloading. Thus Chilvers assumes this value is small in comparison to the other values and may be neglected.
- Coulomb friction that develops due to the normal compressive stresses  $\sigma_n$  across the boundary. Where  $\mu$  is an experimentally determined coefficient of friction.

Relative slip at the steel-grout interface occurs whenever  $\tau > \mu\sigma_n$  where  $\tau$  is the shear stress at the interface.

- Load transfer through shear keys. Chilvers states that the concentrated loads at the shear keys can be determined from experimental results. The loads are defined as a function of slip and effective shear key height (actual height less radial separation). Thus  $\sigma_m$  represents an experimentally determined constant for shear key strength.

The mean value for the normal bond stress  $\bar{\sigma}_n$ , over the whole length of the grouted connection at ultimate is

$$\bar{\sigma}_n = k_n(u_m - \Delta') > 0 \quad (13)$$

where  $k_n$  = normal bond stiffness

$u_m$  = maximum surface roughness

$\Delta'$  = mean radial bond opening

$\bar{\sigma}_n$ , is a general term, not accounting for the difference in  $\sigma_n$  on the sleeve and pile bonds. Taking the hoop stress for a thin ring as

$$\sigma_o = \bar{\sigma}_n r / t \quad (14)$$

where  $r$  = centerline radius of ring

$t$  = wall thickness of ring

Substituting Eq. 13 into 14 yields the hoop stiffness

$$\sigma_o = k_n r (u_m - \Delta') / t \quad (15)$$

From the theory of elasticity the mean hoop strain neglecting the effect of radial confinement can be expressed as

$$\epsilon_o = \Delta / r = (\sigma_o - \nu \sigma_z) / E_s \quad (16)$$

where  $\Delta$  = mean radial displacement

$\sigma_z$  = mean axial stress

$\nu$  = Poisson's ratio

$E_s$  = modulus of elasticity of steel

The mean average axial stress for a stiffened sleeve can be expressed in terms of the ultimate bond stress,  $f_{bu}$  as

$$\sigma_z = f_{bu} \pi r_p L / (2\pi r_s t_s + A_s) \quad (17)$$

where  $r_p$  = radius of pile

$r_s$  = radius of sleeve

$t_s$  = wall thickness of sleeve

$L$  = grouted length of connection

$A_s$  = area of stiffeners

Thus the mean radial expansion due to axial stress can be expressed using Equations 15-17

$$\Delta'_s = r_s [k_n r_s (u_m - \Delta') + \nu f_{bu} \pi r_p / (2\pi r_s t_s + A_s)] / t_s E_s \quad (18)$$

$$\Delta'_p = r_p [k_n r_p (u_m - \Delta') + \nu f_{bu} L / 2] / t_p E_s \quad (19)$$

The mean expansion is then

$$\Delta' = \Delta'_s + \Delta'_p/2 \quad (20)$$

The signs of Eq. 20 are based on the pile being in tension and the sleeve in compression since this type of loading was used in the Wimpey Lab tests. Substituting Eq. 18 and 19 into 20 and solving for  $\Delta'$

$$\Delta' = (k_n u_m \gamma + \nu f_{bu} L r_p \theta / 2) / (2E_s + k_n \gamma) \quad (21a)$$

where 
$$\gamma = \frac{r_s^2}{t_s} + \frac{r_p^2}{t_p} \quad (21b)$$

$$\theta = \frac{\pi r_s}{(\pi r_s t_s + A_s / 2)} + \frac{1}{t_p} \quad (21c)$$

To arrive at Chilvers' Equation for the ultimate bond stress capacity of a grouted connection, substitute Eq. 13 and 21 into Eq. 12 with  $c=0$ :

$$f_{bu} = \frac{2E_s [\mu k_n u_m + \sigma_m h / s] + \sigma_m k_n \gamma h / s}{2E_s + k_n \gamma + \mu k_n \nu (L/D) r_p^2 \theta} \quad (22)$$

Chilvers determined the coefficient of friction,  $\mu$  from a series of pushout tests [27]. The results of these tests indicated that for grout cast against a shot-blasted surface  $\mu = 3.0$ . The surface roughness,  $u_m$  for shot-blasted tubes was determined to be 2 mils. The exact value of the normal bond stiffness factor,  $k_n$ , to use in the ultimate bond stress formula is not explicitly stated by Chilvers. However, Chilvers states that as the stiffness of the sleeve and pile increases the rate of increase in  $\sigma_n$  gradually reduces

and for stiffness above  $184\text{k/in}^3$  ( $50\text{ N/mm}^3$ ) there is very little strength increase in a grouted connection. This he reasoned was due to the limited sleeve and pile stiffnesses which can not resist very large  $\sigma_n$  stresses. Thus, there is no advantage in using values of  $k_n$  larger than  $184\text{k/in}^3$  ( $50\text{ N/mm}^3$ ). The upper limit on  $\sigma_n$  is given by  $\sigma_n < u_m k_n = 0.363\text{ k/in}^2$  ( $2.5\text{N/mm}^2$ ). For use in the ultimate strength equation Chilvers uses a mean value of  $k_n = 92\text{ k/in}^3$  ( $25\text{ N/mm}^3$ ), for a grout strength of  $f_{cu} = 7260\text{ psi}$  ( $50\text{ N/mm}^2$ ). For the constant defining shear key strength,  $\sigma_m$  Chilvers assumes a value of  $\sigma_m = 14.5\text{ k/in}^2$  ( $100\text{ N/mm}^2$ ) for  $f_{cu} = 7260\text{ psi}$  ( $50\text{ N/mm}^2$ ). Substituting these values along with  $E_s = 29 \times 10^6\text{ psi}$  ( $2 \times 10^5\text{ N/mm}^2$ ) and  $\nu = 0.3$  into Eq. 22 yields

$$f_{bu} = \left[ \frac{58000[552 + 14500h/s] + 1.334 \times 10^6 \gamma h/s}{58000 + 92\gamma + 82.8(L/D_p)r_p^2\theta} \right] \quad (23)$$

For grouted connections with grout strength other than  $f_{cu} = 7260\text{ psi}$  ( $50\text{ N/mm}^2$ ) the ultimate bond stress formula should be modified by  $(f_{cu}/7260)^{0.5}$ . Multiplying through and reducing gives

$$f_{bu} = \left[ \frac{681[552 + 14500\text{ h/s}] + 15667\gamma h/s}{58000 + 92\gamma + 82.8(L/D)r_p^2\theta} \right] f_{cu}^{0.5} \quad (24)$$

When using Eq. 24 Chilvers suggests that for  $h/s > 0.06$  use  $h/s = 0.06$  and for  $L/D_p < 2$ , use  $L/D_p = 2$  and multiply the result by

0.8. This is an approximate allowance for the length effect that has been shown to occur in specimens with  $L/D_p < 2$ .

One of the major differences in Chilvers' formulation, from the previously discussed formulations is the presence of the geometric parameter  $\gamma$ . Chilvers' equation suggests a degree of weakening with increasing scale; whereas the current empirical equations are independent of connection size. Equation 24 also indicates a reduction in bond strength with increasing  $L/D_p$ . The rate of reduction is a function of the radial stiffness of the connection, with stiffer connections exhibiting a smaller rate of bond strength reduction with  $L/D_p$ . These trends are consistent with experimental results [9,10]. Chilvers' equation cannot show the reduction of strength for  $L/D_p < 2$ , since these reductions are believed to be due to end effects which were not considered in the development of the equation.

1.4.2.1 Application of Chilvers Equation to Loadings Other than Tension-Compression. The normal dead and environmental loadings to which an offshore platform is subjected cause the pile and sleeve to be in compression. In the case of an uplift or overturning moment, both pile and sleeve could be subjected to tensile loadings. Wimpey Labs experimental loading case of the pile in tension and the sleeve



in compression was done solely for the purpose of finding a lower bound and was not intended to represent actual loading conditions.

As mentioned previously, Chilvers' bond strength Eq. 24 was developed assuming the pile to be in loaded in tension and the sleeve in compression. The equation should however, be able to be modified to account for the different loadings by simply putting the appropriate sign on the  $\Delta'_s$  and  $\Delta'_p$  terms in Eq. 20 and  $\sigma_z$  of Eq. 16. These expressions represent the radial contraction or expansion of a thin ring due to axial loading and a hoop stress. To modify Eq. 16 and 20 for tension-tension loading the sign of  $\sigma_z$  should be positive and  $\Delta'_s$  is now negative. Thus the modified bond stress equations for tension - tension loading are as follows:

$$f_{bu} = \left[ \frac{681[552 + 14500 h/s] + 15670 \gamma h/s}{58000 + 92\gamma + 82.8(L/D_p)r_p^2\theta} \right] f_{cu}^{0.5} \quad (25a)$$

$$\text{where } \gamma = \frac{r_p^2}{t_p} - \frac{r_s^2}{t_s} \quad (25b)$$

$$\theta = \frac{1}{t_p} - \frac{\pi r_s}{\pi r_s t_s + A_s/2} \quad (25c)$$

Chilvers performed three tests (A1, A2, A3) at City University [27] in which all geometric parameters were the same as specimens in Series P of Wimpey Laboratories [10,11]. The purpose of these tests was to examine the effect of loading application (Poisson's effect) on

the ultimate strength of grouted connections. Table 1.3 gives the geometric details of the similar specimens. All specimens had  $L/D_p=2$ .

In Table 1.4, the measured ultimate bond stresses are listed for this series of tests, along with the calculated values using Eq. 25a-25c.

The experimental results indicate that connection capacity is independent of loading application. When the measured results are normalized with respect to  $\sqrt{f_{cu}}$  the tension-tension specimens show a slight decrease of about 10% in capacity, from the compression-tension connections. This indicates that Poisson's effect can be considered minimal in determining the ultimate strength of a grouted connection.

When Chilvers' Eq. 25 is applied to compression-tension loading specimens, computed and measured results compare well with Chilvers' theoretical solution yielding conservative results in all cases.

When applied to the tension-tension cases, however, Chilvers' Eq. 25 significantly overestimates the capacity of the grouted connection. The extent of this overestimation depends on whether the longitudinal stiffeners which were welded to the sleeves are considered effective in resisting the applied axial load. In most of the Wimpey specimens longitudinal stiffeners, usually consisting of flat plates, were welded to the sleeve to prevent local yielding and

Table 1.3 Geometric Properties of Selected Series P and A Specimens

Spec. No.	Loading	Pile		Sleeve		Grout		Shear Conn.		
		D	t	D	t	D	t	h	s	h/s
		(in.)	(in.)	(in.)	(in.)	(in.)	(in.)	(in.)	(in.)	(in.)
A1	Ten-Ten	20.0	1.0	22.4	0.20	22.0	1.0	0.08	6.65	0.012
P3	Ten-Comp	20.0	1.0	22.4	0.20	22.0	1.0	0.08	6.65	0.012
P4	Ten-Comp	20.0	1.0	22.4	0.20	22.0	1.0	0.08	6.65	0.012
A2	Ten-Ten	20.0	0.63	22.4	0.20	22.0	1.0	0.08	6.65	0.012
P9	Ten-Comp	20.0	0.63	22.4	0.20	22.0	1.0	0.08	6.65	0.012
P10	Ten-Comp	20.0	0.63	22.4	0.20	22.0	1.0	0.08	6.65	0.012
A3	Ten-Ten	20.0	0.50	22.4	0.20	22.0	1.0	0.08	6.65	0.012
P15	Ten-Comp	20.0	0.50	22.4	0.20	22.0	1.0	0.08	6.65	0.012
P16	Ten-Comp	20.0	0.50	22.4	0.20	22.0	1.0	0.08	6.65	0.012

Table 1.4 Measured and Computed Ultimate Bond Stress for Selected Series P and A Specimens

Spec. No.	$f_{cu}$	Meas. $f_{bu}$	Eq. 25 $f_{bu}$	$f_{bu}/f_{cu}$
A1	10300	343	529	3.38
P3	7756	331	302	3.76
P4	7314	321	292	3.76
A2	9572	314	556	3.22
P9	7778	301	284	3.41
P10	7759	311	283	3.53
A3	10300	317	615	3.12
P15	8345	311	283	3.40
P16	7649	298	271	3.41

buckling of the sleeve before a connection failure in the grout. The exact size and location of the longitudinal stiffeners is not specified by Chilvers [27], thus it is assumed that the arrangement is the same as that used in Wimpey series P specimens.

Generally an unstiffened tube will exhibit more of a Poisson's effect than a longitudinally stiffened tube. Yet, in a grouted connection stiffeners decrease the local bending at the shear key locations, which would tend to offset the reduced Poisson's effect, implying that for a grouted connection loaded in tension the capacity of the connection will be greater for the unstiffened sleeve than a stiffened sleeve if all other parameters are kept constant. If the area of the stiffeners is neglected in Eq. 17 the connection capacities are as given in Table 1.4, for specimens A1, A2, A3. By more accurately including the assumed area of the stiffeners in calculating the capacity of the grouted connections the following ultimate bond strengths are obtained for specimens A1, A2 and A3 respectively 1120 psi, 1260 psi, and 1474 psi. These results indicate behavior which is contrary to the expected results. Chilvers' Eq. 25 gives good results when compared with the tension-compression tests results from which the constants  $k_n$ ,  $\gamma$ ,  $u_m$  and  $\sigma_m$  were determined. But when applied to the actual loading cases such as compression-compression or tension-tension the results are very poor. One reason for this behavior is the large dependence of the method on Poisson's

effect, which test results tend to indicate is unimportant. Also, the constants used by Chilvers are somewhat suspect since there is no explanation of how they were obtained or if they should be varied for different loadings, grout strength and tube stiffnesses.

1.4.3 Van Lee Thesis. Another analysis of grouted connections, limited to plain pipes without shear keys was carried out by Van Lee at the Massachusetts Institute of Technology [28].

Three models were examined. The first model considered only longitudinal, normal and shear stresses and displacements. The behavior was assumed to be linear elastic. The method employed a simple elastic analysis. By using geometric compatibility equations in the three material layers, based on a linear bond stress-slip relationship derived from experimental results and shown in Fig. 1.10 a fourth order differential equation was produced. By using appropriate boundary conditions on the normal stresses in the pile and sleeve a solution was obtained.

The second model was analogous to the one-dimensional model described previously with the inclusion of radial and circumferential normal stresses. Once again the governing equation becomes a fourth order differential equation which is solved using appropriate boundary conditions.

The third model employed an Automatic Dynamic Incremental Non-linear Analysis program (ADINA), to develop an axisymmetric model.

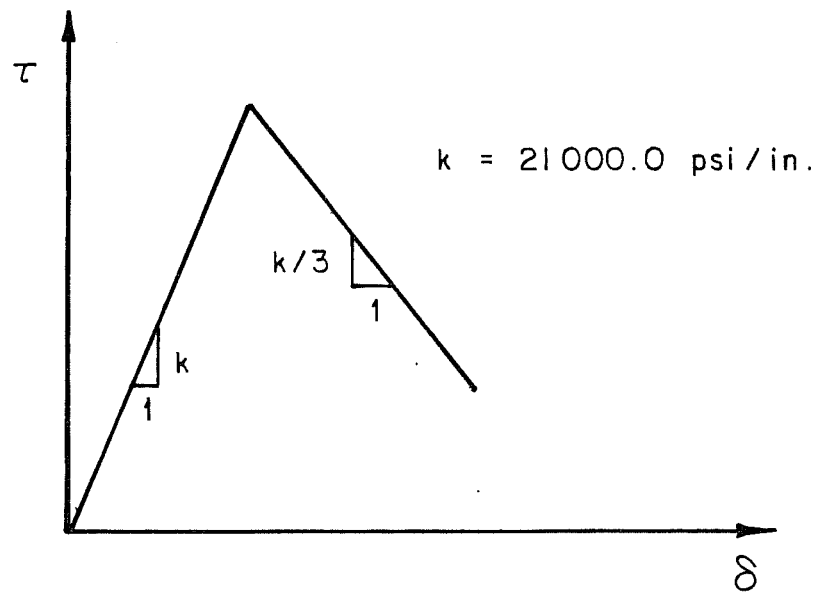


Fig. 1.10 Van Lee's local bond stress versus slip relationship

The steel and the grout are considered elastic but the model accounts for the non-linear relationship between bond shear stresses and deformation (slip) at the steel-grout interface. The effects of bending were also included in the analysis.

The results of these models were all in reasonable agreement with the experimental results from which the bond stress-slip relationship was derived. As a result of these models Van Lee made the following two main conclusions with regard to plain pipe connections. Poisson's effect can be significant for grouted connections without shear keys due to the fact that the three dimensional stress state can be an important parameter in determining the amount of friction bond since the latter is dependent upon the normal stresses at the interface. Normal stresses and displacements do not change appreciably when the behavior of the steel-grout interface becomes plastic.

1.4.4 Brown and Root Report. In the Brown and Root Report [29], an attempt is made, using shell theory, to find the key nondimensional parameters affecting the strength of grouted connections. Many assumptions and simplifications are made with regard to the interaction of the steel-grout bond for plain-pipe connections thus, the resulting parameters are only a rough guide. Six nondimensional parameters were produced for each ring of material.

For plain-pipe connections these parameters are;  $P/EtR$ ,  $\Delta/L$ ,  $R/t$ ,  $L/R$ ,  $\nu$ ,  $\mu$ . Two additional groupings,  $h/s$  and  $h/R$  are used to describe shear key geometry where;

$P$  = Axial load

$R$  = Radius of ring

$L$  = Grouted length

$\Delta$  = Slip

$t$  = ring wall thickness

$\mu$  = coefficient of friction

$E$  = modulus of elasticity

$\nu$  = Poisson's ratio

$h$  = height of shear key

$s$  = spacing of shear key

1.4.5 Summary of Empirical and Analytical Methods. The above discussion briefly summarizes the present empirical and analytical approaches which have been attempted in modeling the behavior of grouted connections.

In Chapter 4 the experimental results given in Chapter 3 will be compared with both the API and United Kingdom Department of Energy empirical formulation given in this chapter.

As of yet the analytical models have been unable to accurately model the behavior of the grouted connection. Paslay's



model requires the use of a computer program which is not available to the author and yields unconservative results due the constitutive equations used to model the nonlinear behavior of the grout, therefore no comparisons will be made with this model.

Chilvers' model, Section 1.4.2.2, yielded good results only for the tension-compression loading case from which the constants  $k_n$  and  $\sigma_m$  were determined. The application of Chilvers' method to the compression-compression loadings used in this investigation would not be expected to be anymore accurate than for the tension-tension loading case discussed previously thus no comparisons will be made with the model.

#### 1.5 Scope of Work

Despite the large number of tests conducted on grouted connections no systematic study was ever conducted on load interaction, effects of position of pile shear keys with respect to the sleeve keys and the effects of pile-sleeve eccentricity. An experimental research program was undertaken at The University of Texas to study these effects. The program consisted of 18 scale model tests divided into six test series of three specimens each. Based on the typical geometries, for grouted connections used in the North Sea and the Gulf of Mexico the specimens represent approximately 1/3 to 1/2 size scale models diametrically. The specimens were also selected

to correlate with the sizes used by previous investigators. Series 1 were axial tests used as reference tests for the other five series. Series 2 to 6 investigated the effect of combined loading (axial and bending), relative shear key location between pile and sleeve, length of grouted connection under combined loading, eccentricity of tubulars; and grout strength, respectively. Chapter 2 describes the tests series and experimental test procedures. Chapter 3 contains the test results for each test along with an explanation of the determination of grout compressive strength and grout column cube results. The data are analyzed in Chapter 4. Chapter 5 develops a simplified analytical model, and discusses the main parameters which affect the ultimate strength of a grouted connection. Finally a summary and suggestions for further study are given in Chapter 6.

CHAPTER 2  
TEST PROGRAM

2.1     Selection of Specimens

The determination for the size of the grouted connection specimen was based on two main criteria:

- Limitation of available loading frame capacity;
- Size should be similar to other tests so that correlations could be drawn between results.

At the start of the research program in the fall of 1984, the author obtained data from approximately 200 test results for both plain pipe and shear-key specimens. Of these 200 sets of test results only 147 meet the requirements given by API RP 2A [25] and the UK Department of Energy [23]. The remaining set of 147 tests consisted of 85 specimens with shear keys and 62 plain pipe connections. Only 80 grouted connections with shear keys and 44 plain pipe grouted connections listed sufficient information to allow for comparisons between prediction's from existing empirical methods. A summary of the shear-key specimens is given in Table 2.1.

Based on the data distribution in Table 2.1 and loading frame capacity the pile selected had an 18 in. (457 mm) outer diameter with a 5/8 in. (15.9 mm) wall thickness while the sleeve had a 21 in. (533 mm) outer diameter with a 1/2 in. (12.7 mm) wall thickness. Thus the grout annulus between the two concentric tubulars was 1 in. (25.4 mm) nominal. The length of the tubulars was 39 in. (991 mm); this

allowed for a 3 in. (76 mm) offset between the pile and sleeve and yielded a nominal length to diameter ratio  $L/D_p$  of two. This  $L/D_p$  ratio was the most prevalent ratio used by previous researchers [4,5,6] and was the maximum that would meet the loading limitations of the test frame.

TABLE 2.1 Data Base for Specimens with Shear Keys

Quantity	Reference No. (in.)	Grout Thickness (in.)	Pile Size (in.)	Sleeve Size
1	22	0.469	8.625	10.75
2	11	0.500	20.00	21.39
12	7	0.543	12.38	13.78
10	11	0.637	12.75	14.41
22	11	0.738	18.00	19.76
1	22	0.746	18.00	19.78
2	11	0.764	18.00	20.00
1	22	0.768	18.00	20.00
6	11	1.000	20.00	22.32
18	11	1.000	20.00	22.39
6	11	1.000	20.00	22.63
1	22	1.140	21.25	24.00
2	11	2.000	20.00	24.39
1	22	2.500	54.00	60.00
Total 85				

2.1.1 Test Series. The 18 specimens were divided into six series each containing three replicates.

Test Series 1. Series 1 consisted of three specimens under pure axial loading with a  $(L/D_p)$  of two. These tests were used as

reference tests for the other five series and as a means of establishing correlation with tests conducted elsewhere.

Test Series 2. Series 2 was designed to determine the effect of combined loads on the grouted connection. The specimens were subjected to a proportionally applied bending moment and axial load. Eccentricity of load to pile diameter ratios ( $e/D_p$ ) of between 0.1 and 0.5 were established as realistic bounds for combined loading. In this series an  $e/D_p$  ratio of approximately 0.3 was used which gave a triangular stress distribution across the section. This case was considered the most severe that could be applied with the testing frame.

Test Series 3. In previous investigations shear keys on the sleeve were always located halfway between those of the pile as shown in Fig. 2.1a. However, there is little or no control over the final relative shear key location between pile and sleeve in the field. In Series 3, the consequences of the relative shear key location on the pile and sleeve were examined. In all three specimens of Series 3 the shear keys were placed directly across from each other, see Fig. 2.1b. Again, an  $L/D_p$  ratio of two was maintained.

Test Series 4. In Series 4 the effect of specimen length on a connection under combined loading was studied. The same geometry and loading as used in Series 2 was maintained for two specimens but the  $L/D_p$  ratio was shortened to one. The third specimen was tested under pure axial loading to establish an axial test reference point.

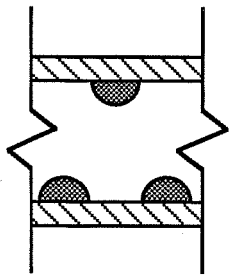


Fig. 2.1a Standard shear key arrangement

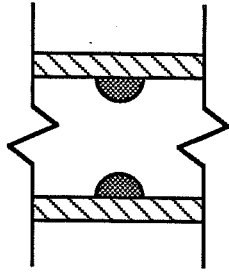


Fig. 2.1b Series 3 shear key arrangement

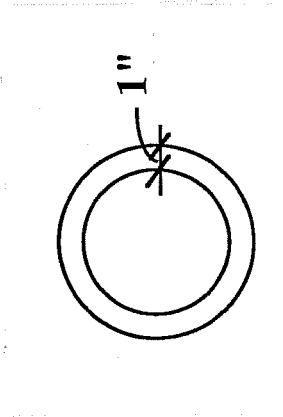


Fig. 2.2a Standard concentric tube arrangement

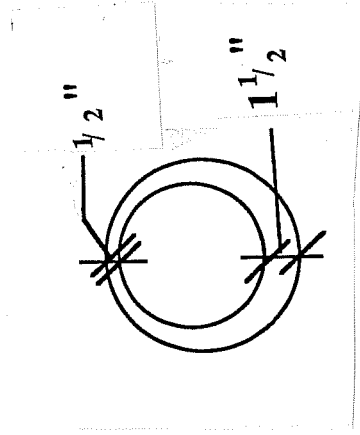


Fig. 2.2b Series 5 eccentric tube arrangement

Test Series 5. In field installation the driven pile would rarely be concentric with the sleeves. Consequently, in Series 5, the effect of having eccentrically placed piles and sleeves was examined. The eccentricity in the test specimens resulted in the grout annulus varying from a minimum of a 1/2 in. (12.7 mm) to a maximum of 1-1/2 in. (38 mm), as shown in Fig. 2.2a and 2.2b. Again, a  $L/D_p$  ratio of two was used.

Test Series 6. In Series 6 the effect of grout strength on the connection capacity was investigated. In the previous five series, unconfined compressive strengths of 4000 - 6000 psi (27.5 - 41.3 MPa) were used. For Series 6, a high strength grout of approximately 11000 psi (75.8 MPa) at 28 days was used. Since previous investigators [4,5,6] have indicated that connection strength is a function of grout strength, a  $L/D_p$  ratio of one was used to ensure that the connection strength did not exceed the loading frame capacity. These specimens were subjected to axial load only.

2.1.2 Specimen Fabrication. Figure 2.3 shows the specimen geometry used in The University of Texas test program. All test specimens were fabricated by Superior Fabricators Inc. of Baldwin, Louisiana. The tubulars were formed from flat sheets, with the piles being fabricated from A572 Grade 50 ( $F_y = 50$  ksi) and the sleeves from A588 Grade 50 ( $F_y = 50$  ksi) steel. After forming, a full penetration groove weld was run the entire length (39 in.) to join the section. The full penetration groove welding process followed the





American Welding Society (AWS) Specification A5.2. A semi-manual mig-wire process was used with a class E71T1 electrode (0.045 diameter alloy rod 7100 wire) in a dual shielded gas flux of 75% argon and 25% carbon dioxide. The end of the pile or sleeve that would bear against the loading platens during testing was milled to ensure a uniform bearing surface. Shear keys were then placed on the inside of the sleeves and on the outside of the piles. The shear keys were formed by running weld beads at 4-1/4 in. (108 mm) centers around the circumference of the tubulars. The height (outstand) of the shear keys was a nominal 1/16 in. (1.6 mm) and the width a nominal 1/8 in. (3.2 mm). The nominal h/s ratio was 0.015. In most previous research h/s ratios between 0.01 to 0.02 were used with only a few specimens at h/s ratios over 0.03. The weld beads were deposited in accordance with AWS Specification SFA5.18 using a short arc mig-wire process with a 0.035 diameter alloy 65 wire that was shielded in carbon dioxide.

Table 2.2 shows a comparison between API RP 2A [25], the UK Department of Energy Guidance Notes limitations [21] given previously and The University of Texas specimens.

Table 2.2 indicates that for the sleeve geometry parameter  $(D/t)_s$  The University of Texas specimens are at the lower end of the UK recommendations. In the Wimpey Laboratory research program used to establish the UK limitations, most specimens had  $(D/t)_s$  ratios

TABLE 2.2 Recommended Limits for Grouted Pile-to-Sleeve Connections

Parameter	API	UK	U.T.
Sleeve Geometry	$(D/t)_s \leq 80$	$40 \leq (D/t)_s \leq 140$	$(D/t)_s = 42$
Pile Geometry	$(D/t)_p \leq 40$	$20 \leq (D/t)_p \leq 32$	$(D/t)_p = 28.8$
Grout Annulus	$7 \leq (D/t)_g \leq 45$	$10 \leq (D/t)_g \leq 45$	$(D/t)_p = 20$
Shear Key Spacing	$2.5 \leq D_p/s \leq 8$	$0 \leq D_p/s \leq 8$	$D_p/d = 4.3$
Shear Key Ratio	$h/s \leq 0.10$	$0 \leq h/s \leq 0.04$	$h/s = 0.0147$

from 75 to 140. The high  $(D/t)_s$  ratio required the sleeves to be to establish the UK limitations, most specimens had  $(D/t)_s$  ratios stiffened with longitudinal stiffeners so that buckling would not occur. By using a lower  $(D/t)_s$  ratio the longitudinal stiffeners were not required and a grout failure was ensured.

## 2.2 Grouting Materials and Methods

### 2.2.1 Grout Mix Design.

Pile-to-sleeve connection grouts are normally formulated with some type of inorganic hydraulic cement which yields a high early strength to ensure the stability of the structure. Since the platform load is transferred from the sleeve to the pile via the grout, specific grout properties vary for a given platform design and installation process. The grout slurries are usually simple mixes, that provide the required strength and pumpability. A commonly used grout is a portland cement with a low water/cement ratio and one or more admixtures used to impart specific

grout properties. Appendix C gives a brief summary of offshore grouting methods, materials and mix designs. Section 2.8.4c of API RP 2A [25] specifies that  $2500 \text{ psi (17.25 MPa)} \leq f_{cu} \leq 16000 \text{ psi (110 MPa)}$  in grouted connections.

In this test program the following criteria for grout were established:

- 28-day cube strength of 4000 psi (27.5 Mpa) to 6000 psi (41.3 MPa) to ensure a grout failure at a  $L/D_p$  ratio of 2.
- Grout material properties determined in accordance with ASTM Specifications.
- Connection specimens and test cubes cured in an environment representing the offshore curing conditions.
- Neutral shrinkage/swell characteristic.

Many preliminary mix designs were tried in order to obtain the required strength, consistency, pumpability and segregation properties. The results of these preliminary mix designs indicated that an inert filler such as sand reduced the strength and yet maintained grout consistency. Sand also reduced the shrinkage/swell characteristics of the mix and helped reduce segregation. The two final mix designs are given in Tables 2.3 and 2.4. Mix Design I was used for test Series 1 through 5 and Mix Design J for high strength grout was used for test Series 6.

2.2.2 Specimen Preparation. The test specimen surfaces were prepared by shot-blasting the outside surface of the piles and the inside surface of the sleeves with a No. 3 blasting sand (fine) to a white metal condition. All sandblasting was done at one time. This removed all mill scale and imparted a uniform surface roughness to the specimens. Next, all excess weld splatter not removed by shot-blasting was removed. A 3/4-in. nipple was then welded over the 3/4-in. hole that had been cut in the bottom part of the sleeve. This nipple shown in Fig. 2.4 provided the grout entry port during the grouting operation.

TABLE 2.3 Mix I Proportions by Weight

Material	Percent by Weight
* Class A cement	34.7
Water	19.7
** Sand	45.6
w/c ratio	0.57

TABLE 2.4 Mix J Proportions by Weight

Material	Percent by Weight
* Class A cement	44.9
Water	14.8
** Sand	40.3
w/c ratio	0.33

\* API specification, ASTM specification Type 1

\*\* 100% sand passed #8 sieve

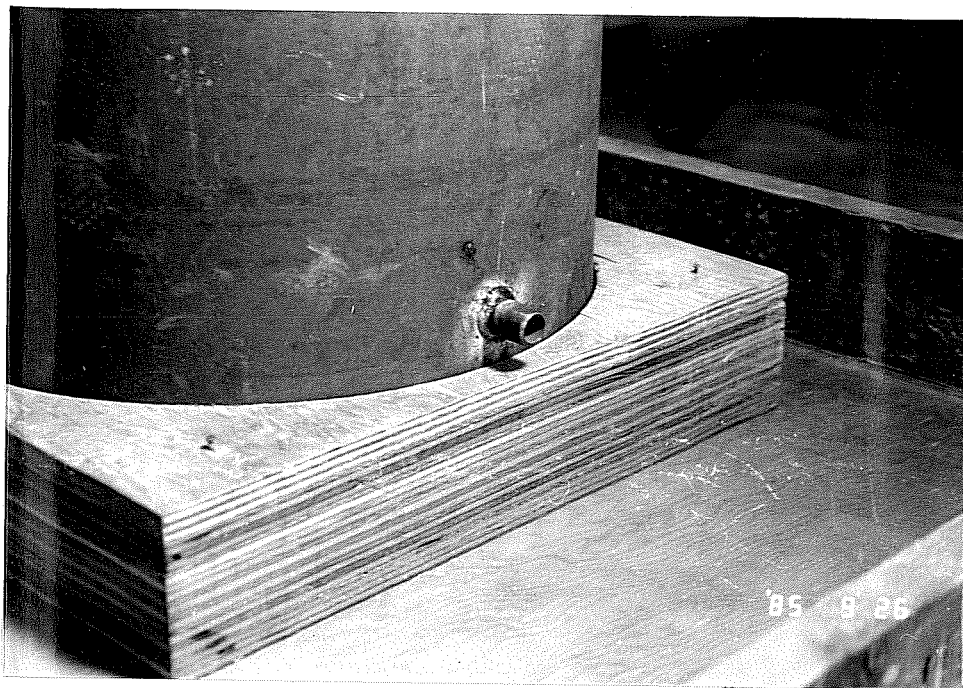


Fig. 2.4 Grout entry port

Shear key spacing, width, and height were recorded for each pile and sleeve set. Measurements were taken at two diametrically opposite locations for each shear key and then an average value was calculated for all shear keys on a given sleeve or pile. The results are given in Table 2.5.

The out-of-roundness of the fabricated tubulars was also determined, with the results given in Table 2.6. The API limits for fabricated structural steel pipe [30] is given as 1% of the nominal diameter (0.18 in. for pile and 0.21 in. for sleeve).

Just before grouting, the tubulars were cleaned using acetone and a high pressure air hose was used to remove any residual particles. An average surface roughness of both the sleeve and pile were then determined using KTA-Tator Press-O-Film tape as shown in Fig. 2.5. Three Press-O-Film tapes were used to determine an average surface roughness of the sleeve or pile. The tapes were spaced at the upper and lower ends and at midheight, with approximately a 120° spacing between the tapes. The film tape was rubbed on to the shot-blasted surface in accordance with KTA-Tator specifications and the replica image measured using a spring micrometer as shown in Fig. 2.6. Table 2.7 contains the average surface roughness of each tube.

The piles were set into formwork designed to yield the required sleeve-pile offset and grout annulus. After the piles were leveled and plumbed, the sleeves were lowered into position and also

TABLE 2.5 Specimen Shear Key Geometry

Series No.	Spec. No.	Sleeve			Spacing (in.)	Pile		*h/s	*w/h
		Spacing (in.)	Width (in.)	Height (in.)		Width (in.)	Height (in.)		
1	UTA1	4.26	0.221	0.073	4.28	0.193	0.061	0.016	3.11
1	UTA2	4.25	0.184	0.081	4.25	0.182	0.059	0.016	2.63
1	UTA3	4.25	0.188	0.077	4.26	0.203	0.063	0.016	2.81
2	UTM1	4.25	0.227	0.076	4.24	0.182	0.064	0.016	2.93
2	UTM2	4.25	0.203	0.076	4.25	0.211	0.065	0.017	2.92
2	UTM3	4.25	0.189	0.076	4.25	0.180	0.076	0.018	2.44
3	UTA4	4.24	0.168	0.079	4.25	0.248	0.059	0.016	3.17
3	UTA5	4.25	0.172	0.078	4.25	0.242	0.064	0.017	2.98
3	UTA6	4.25	0.150	0.077	4.25	0.193	0.065	0.017	2.47
4	UTA13**	4.24	0.184	0.073	4.26	0.223	0.060	0.016	3.06
4	UTM5**	4.25	0.195	0.075	4.29	0.195	0.063	0.016	2.83
4	UTM6**	4.23	0.211	0.069	4.26	0.223	0.062	0.015	3.31
5	UTA7	4.26	0.184	0.075	4.24	0.188	0.069	0.017	2.57
5	UTA8	4.26	0.203	0.070	4.27	0.221	0.059	0.015	3.32
5	UTA9	4.25	0.209	0.077	4.28	0.191	0.066	0.017	2.80
6	UTA10**	4.22	0.203	0.073	4.25	0.172	0.061	0.016	2.80
6	UTA11**	4.23	0.199	0.075	4.28	0.172	0.073	0.017	2.50
6	UTA12**	4.23	0.188	0.076	4.27	0.203	0.067	0.017	2.72

\* Average value of pile and sleeve

\*\* Values calculated using only those shear keys within the grouted length

TABLE 2.6 Out-of-Roundness of Steel Tubulars

Specimen No.	Sleeve		Out-of- Roundness (%)	Pipe		Out-of- Roundness (%)
	Major Dia. (in.)	Minor Dia. (in.)		Major Dia. (in.)	Minor Dia. (in.)	
UTA1	21.09	21.00	0.4	18.12	18.00	0.7
UTA2	21.22	20.84	1.8	18.06	18.00	0.3
UTA3	21.22	20.91	1.5	18.06	17.94	0.7
UTM1	21.31	20.88	2.0	18.22	17.88	1.9
UTM2	21.22	20.84	1.8	18.22	17.81	2.3
UTM3	21.22	20.84	1.8	18.09	17.94	0.8
UTA4	21.06	21.00	0.3	18.06	17.91	0.8
UTA5	21.22	20.91	1.5	18.22	17.88	1.9
UTA6	21.19	21.00	0.9	18.12	17.91	1.2
UTA13	21.19	21.00	0.9	18.19	17.94	1.4
UTM5	21.19	21.00	0.9	18.06	17.94	0.7
UTM6	21.12	21.00	0.6	18.12	17.88	1.3
UTA7	21.12	21.06	0.3	18.12	17.88	1.3
UTA8	21.31	20.81	2.4	18.16	18.00	0.9
UTA9	21.31	20.91	1.9	18.16	18.00	0.9
UTA10	21.09	21.06	0.1	18.12	17.84	1.6
UTA11	21.22	20.97	1.2	18.00	17.94	0.3
UTA12	21.47	20.91	2.7	18.12	17.78	1.9



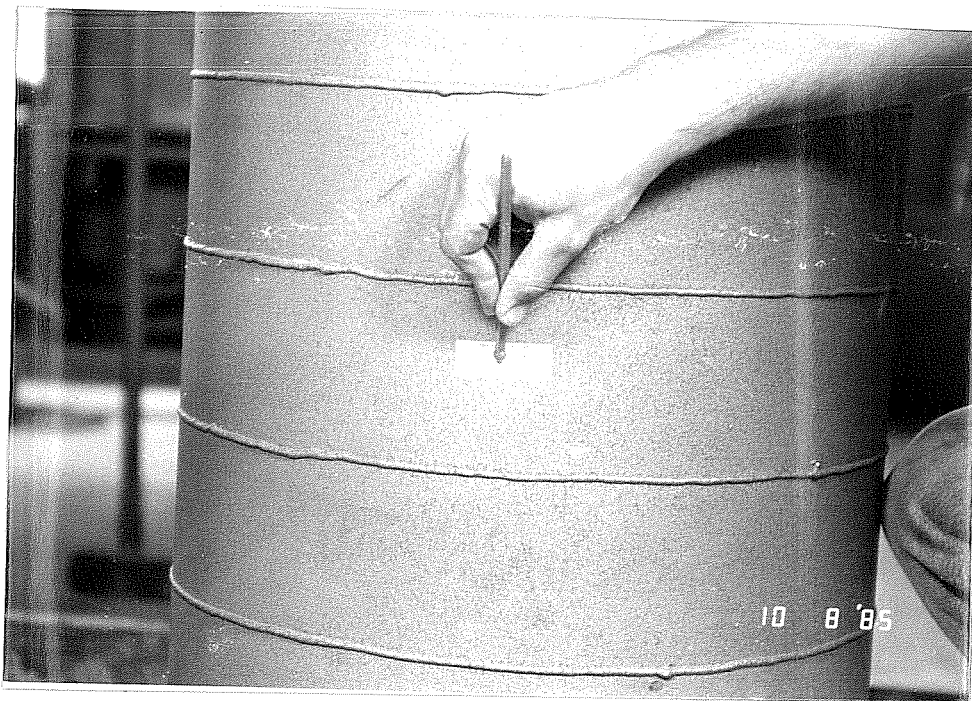


Fig. 2.5 Application of Press-O-Film to determine tubular surface roughness

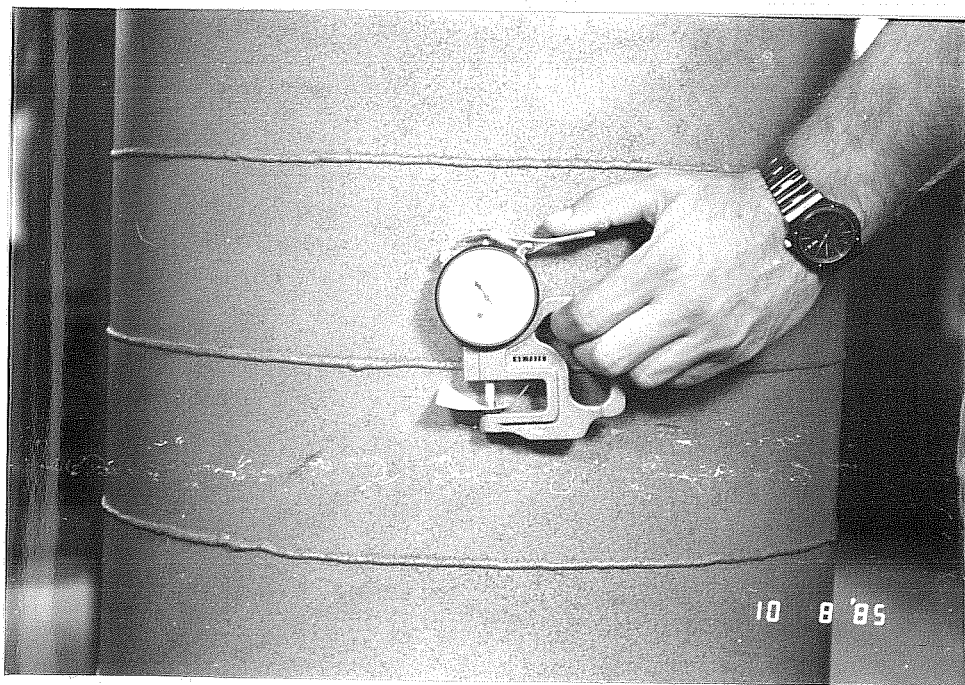


Fig. 2.6 Spring micrometer used to determine surface roughness from Press-O-Film

TABLE 2.7 Average Surface Roughness of Steel Tubulars

Specimen No.	Sleeve (mils)	Pile (mils)	Specimen No.	Sleeve (mils)	Pile (mils)
UTA1	1.9	2.1	UTA13	2.4	2.4
UTA2	2.3	2.1	UTM5	1.9	2.2
UTA3	2.0	2.2	UTM6	2.1	2.1
UTM1	2.2	2.4	UTA7	1.9	2.0
UTM2	2.0	2.1	UTA8	2.0	2.2
UTM3	2.3	2.1	UTA9	2.0	2.1
UTA4	2.2	2.1	UTA10	1.9	2.1
UTA5	2.2	2.1	UTA11	2.2	2.2
UTA6	2.3	2.3	UTA12	2.0	2.2

1 mil = 0.001 in.

leveled and plumbed. Three specimens were prepared at one time for a single grouting operation as shown in Fig. 2.7. The width of the grout annulus was controlled using steel wedges, making sure that both pile and sleeve were kept plumb and level. All specimens were arranged so that the longitudinal full penetration groove weld on the sleeve was always 180° from the weld on the pile.

2.2.3 Grouting Process. The grout was batch mixed to the desired weight specifications in an 8-cu. ft. mortar mixer. Some of the grout slurry was then transferred to an electric screw-driven grout pump. The balance of the slurry was continually mixed to avoid segregation. The grout density was determined using a mud balance shown in Fig. 2.8. The density results are given for each batch in Table 2.8.

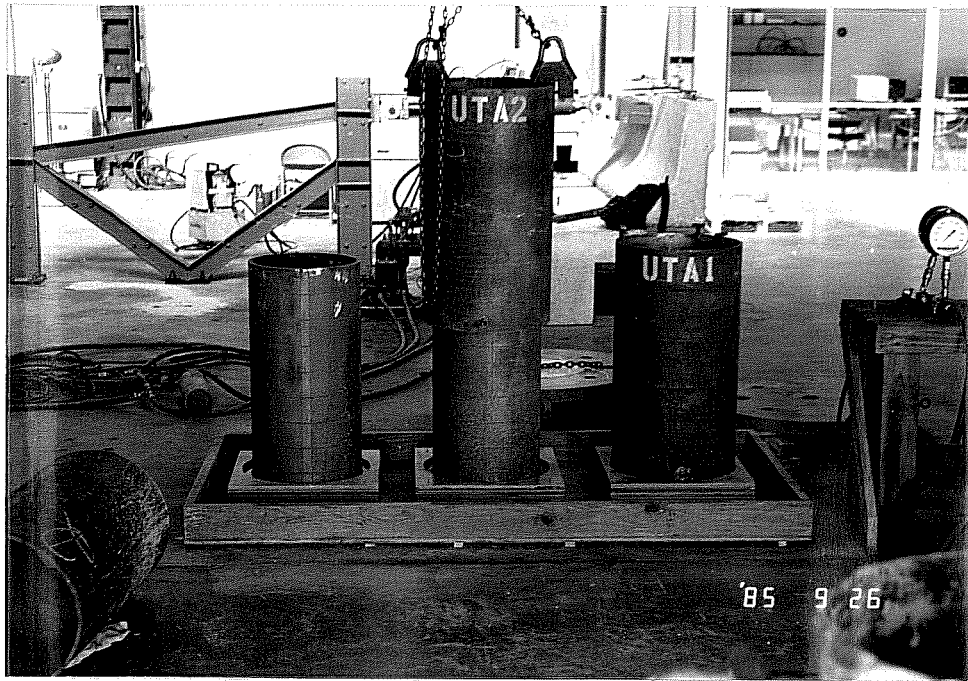


Fig. 2.7 Positioning of Series 1 specimens for grouting

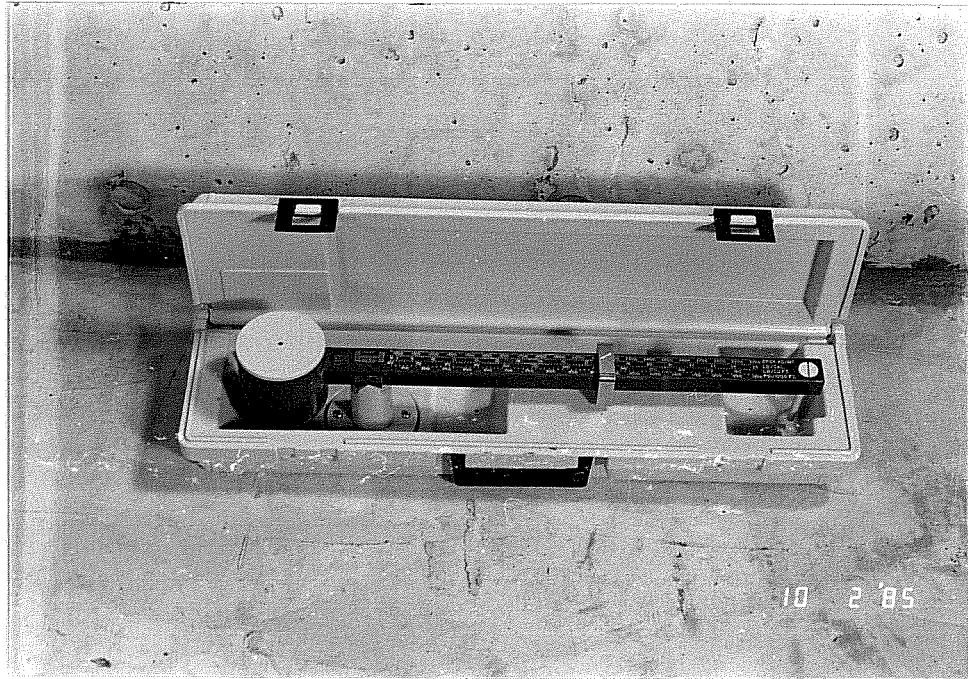


Fig. 2.8 Mud balance used to determine grout density

TABLE 2.8 Grout Densities

Specimen No.	Mix Type	Pour No.	Density lb/gal
UTA1, UTA2, UTM1	I	3	17.6
UTA3, UTM2, UTM3	I	4	17.7
UTA4, UTA5, UTA6	I	5	17.6
UTA13, UTM5, UTM6	I	6	17.5
UTA7, UTA8, UTA9	I	7	17.6
UTA10, UTA11, UTA12	J	2	19.0

A manual shut-off valve was installed on the 3/4-in. nipple welded to the bottom of the sleeve and the grout line from the pump was attached. Next, the annulus between the pile and sleeve was filled with water to simulate the displacement method of offshore grouting described in Appendix C.

The grout slurry was injected into the bottom of the annulus by opening the shut-off valve. After all the water had been displaced, the grout slurry was allowed to flow out over the pile, as shown in Fig. 2.9, until there was a change in the color of the grout. Initially the slurry was diluted by the water in the annulus causing it to become lighter in color. When all of the diluted slurry was displaced from the annulus, its color darkened to that in the grout pump. This process was repeated for all specimens in each group. The rate of pumping was approximately four to five gallons per

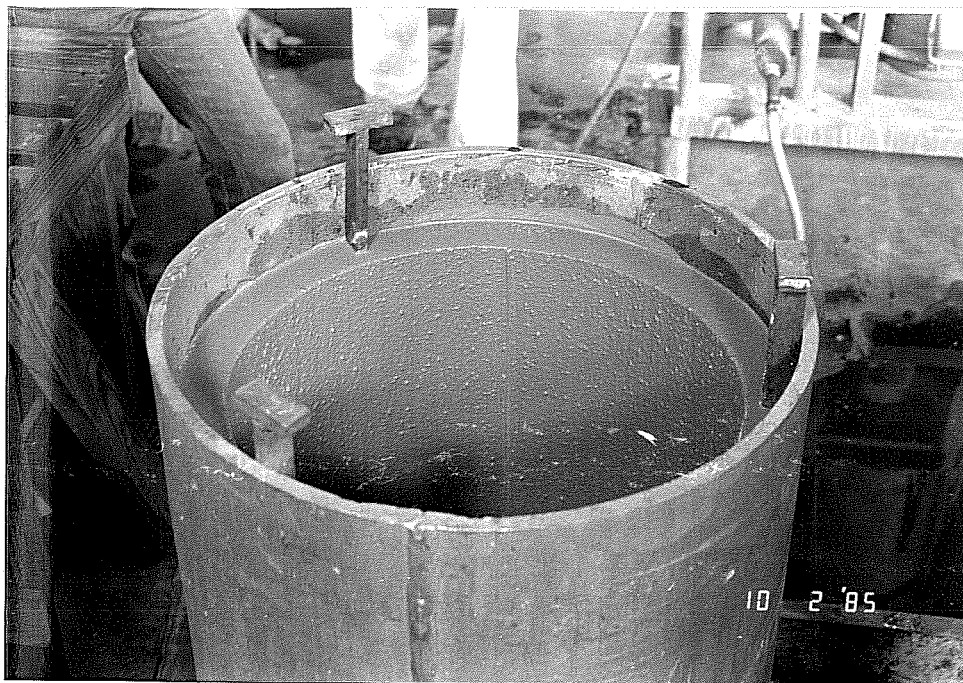


Fig. 2.9 Specimen showing grout flow over pile during grouting process



Fig. 2.10 Casting of cube molds, 4-in. x 8-in. cylinders and shrinkage specimens

minute. After grouting, all specimens were covered with plastic vapor barriers.

Grout was taken from the mortar mixer to mold 2-in. (50.8 mm) cube specimens in accordance with ASTM C109-80 for determination of  $f_{cu}$ . Also, 4 x 8 in. (101.5 x 203 mm) grout cylinders were poured for the determination of the modulus of elasticity and Poisson's ratio in accordance with ASTM C469-75. For test Series 3 to 6, 3 in. (76 mm) cubes and six shrinkage/swell specimens were cast. Figure 2.10 shows the many molds and specimens required to determine the grout properties.

The molds for the shrinkage specimens were constructed of 1-in. (25.4 mm) I. D. schedule 40 PVC pipe and were a nominal 11-5/8 in. (295.3 mm) long. The specimens had gage points cast into each end for measurement purposes. The 1-in. (25.4 mm) diameter was selected to correlate with the specimen grout annulus.

2.2.4 Grout Columns. Model grout columns were constructed to simulate specific aspects of offshore platform grouting. These included the effects of pumping on grout strength, strength variation with respect to grout column height and the correlation between ASTM C109-80 cubes and grout cubes removed from the pumped grout columns.

Nominal 3 ft (914.4 mm) and 6 ft (1828.8 mm) grout columns were fabricated out of transparent acrylic so that the grout slurry could be viewed during pumping. The two-piece acrylic forms also offered the added benefit of being nonporous thus yielding an

accurate representation of the sleeve-pile annulus. The inside dimensions of the columns were 2-in. x 2-in. Thus after form removal the columns could be cut into cubes which would correlate with the ASTM C109-80 cubes.

The grout columns shown in Fig. 2.11 were injected with grout at the same time as grouted sleeve-pile connection specimens. A manual shut-off valve was installed on a 3/4-in. nipple located at the lower end of the grout column. The column was then filled with water to simulate the displacement method of offshore grouting. The grout slurry was injected into the bottom of the column form by opening the shut-off valve. The slurry was allowed to flow over the form until all the water had been displaced and there was a change in the color of the grout flowing over the form as described previously.

2.2.5 Grout and Specimen Curing. Immediately after grouting all grouted connection specimens were covered with plastic vapor barriers. After three days (one day for Series 6), the specimens were removed from the forms and placed into 10-in. deep rubber tubs. The tubs were then filled with water to contact the bottom end of the grout ring. Next, the inside of each specimen was saturated with water and a plastic vapor barrier was placed over the specimen as shown in Fig. 2.12. Prior to testing each specimen was checked daily and water added as required.

All cube molds were placed in vapor barriers for the first 24 hours, after which the molds were stripped and the cubes labeled. In

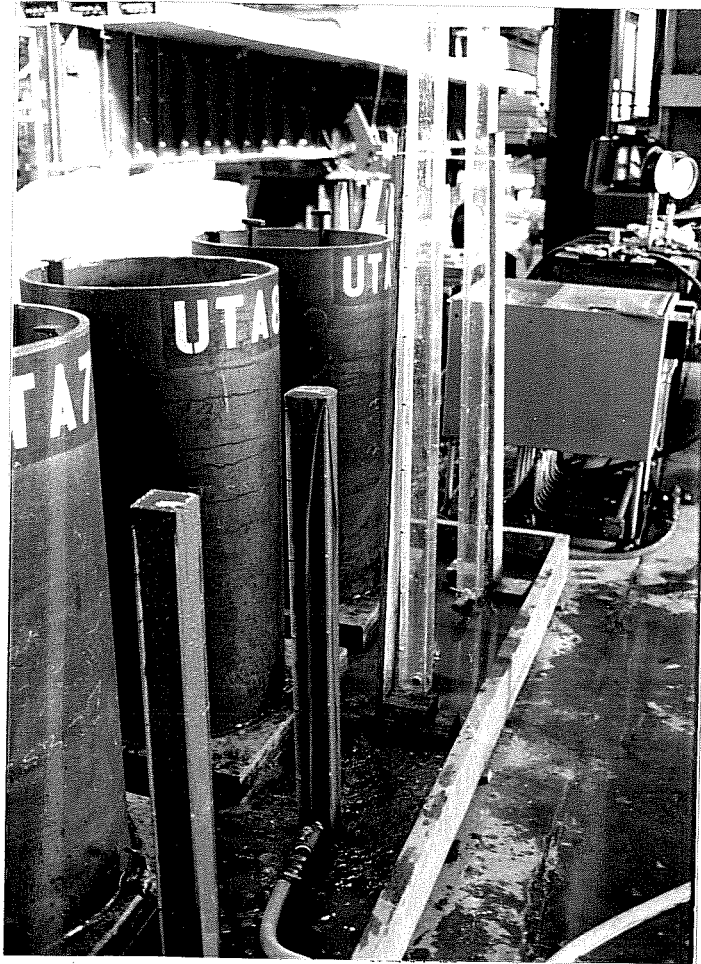


Fig. 2.11 Injection of grout into 2-in. x 2-in. grout columns





Fig. 2.12 Typical specimen storage during curing

the case of the 2-in. (50.8 mm) cubes, some cubes were placed into vapor barriers with water and stored next to the specimens, while others were placed in a lime bath in accordance with ASTM C192. For the series in which 3-in. (76 mm) cubes were cast, all cubes were stored in vapor barriers by the specimens. The 4 x 8 in. (101.5 x 203 mm) cylinders were stripped after 24 hours and stored inside one of the grouted connection specimens until testing. The six shrinkage specimens were divided into two groups; half the specimens were air cured while the other half were placed in a lime bath.

The grout columns were covered with vapor barriers, similar to those used on grouted connection specimens, immediately after pumping. Forms were usually stripped after five days. The columns were then moist cured in the vapor barriers until testing.

#### 2.2.6 Determination of Grouted Length and Grout Annulus.

After grouting there was some settlement of the grout in the annulus thus causing the exact height of the grout to vary around the annulus. Also, the width of the grouted annulus varied somewhat due to the initial out of roundness of the tubulars. After the grout had set, an average grouted length and average grout annulus were determined for each specimen. First the circumference of the pile was marked off into 12 equal divisions (4.75 in.). At each of these locations both the grout depth below the top of the pile and the annulus width were recorded. Next, the exact pile-sleeve offset was determined by taking the average value of three measurements 120° apart. By subtracting

the sum of the pile-sleeve offset and the grout depth below the top of the pile from the overall pile length, a grouted depth could be determined for each of the 12 locations. These values were averaged to determine the grouted length of a specimen. The results for both the average grouted length and grout annulus are listed in Table 2.9.

TABLE 2.9 Average Grouted Length and Annulus Properties

Specimen No.	Ave. Grouted Length (in.)	Annulus Width		
		Max. (in.)	Mini. (in.)	Ave. (in.)
UTA1	33.54	1.13	0.91	0.99
UTA2	34.45	1.09	0.88	0.98
UTA3	35.72	1.16	0.94	1.00
UTM1	35.10	1.09	0.88	0.97
UTM2	35.50	1.13	0.84	0.96
UTM3	34.70	1.16	0.91	0.99
UTA4	30.55	1.06	0.94	1.00
UTA5	30.86	1.06	0.88	0.97
UTA6	30.25	1.09	0.94	1.00
UTA13	18.12	1.06	0.88	0.99
UTM5	17.82	1.09	0.94	1.02
UTM6	18.51	1.00	0.88	0.95
UTA7	34.58	1.50	0.50	N/A
UTA8	34.05	1.56	0.56	N/A
UTA9	34.27	1.53	0.56	N/A
UTA10	18.91	1.06	0.84	0.97
UTA11	18.63	1.06	0.88	0.98
UTA12	18.65	1.19	0.88	1.00

## 2.3 Experimental Test Procedures

2.3.1 Test Frame. Grouted connections in offshore platforms are typically subjected to compressive axial forces and bending moments arising from a combination of dead and environmental loading. To simulate these loadings in the laboratory a test frame was designed in which a compressive axial load or combined compressive axial load and bending moment was applied to one end of the sleeve and these forces reacted on the pile at the opposite end.

A schematic of the test frame is shown in Fig. 2.13. The frame consisted of two circular steel platens connected together by high strength steel bars. The bottom platen was stiffened to reduce plate bending and to allow for easy access during the installation and removal of the high strength bars. The load was applied through the high strength bars by a combination of six 100 ton and one 200 ton hydraulic center hole rams.

2.3.2 Specimen Positioning. The specimens were lowered into position on the bottom loading platen using a manually operated overhead crane. The specimen (pile end) was centered on the bottom loading head and plumbed using three equally spaced leveling bolts which had been welded to the sleeve, Fig. 2.14. The position was marked and the specimen lifted off the loading head to allow for the application of a thin layer of hydrostone (high strength gypsum grout) under the specimen. The hydrostone was used to ensure a uniform bearing surface even though the tubular ends in contact with the

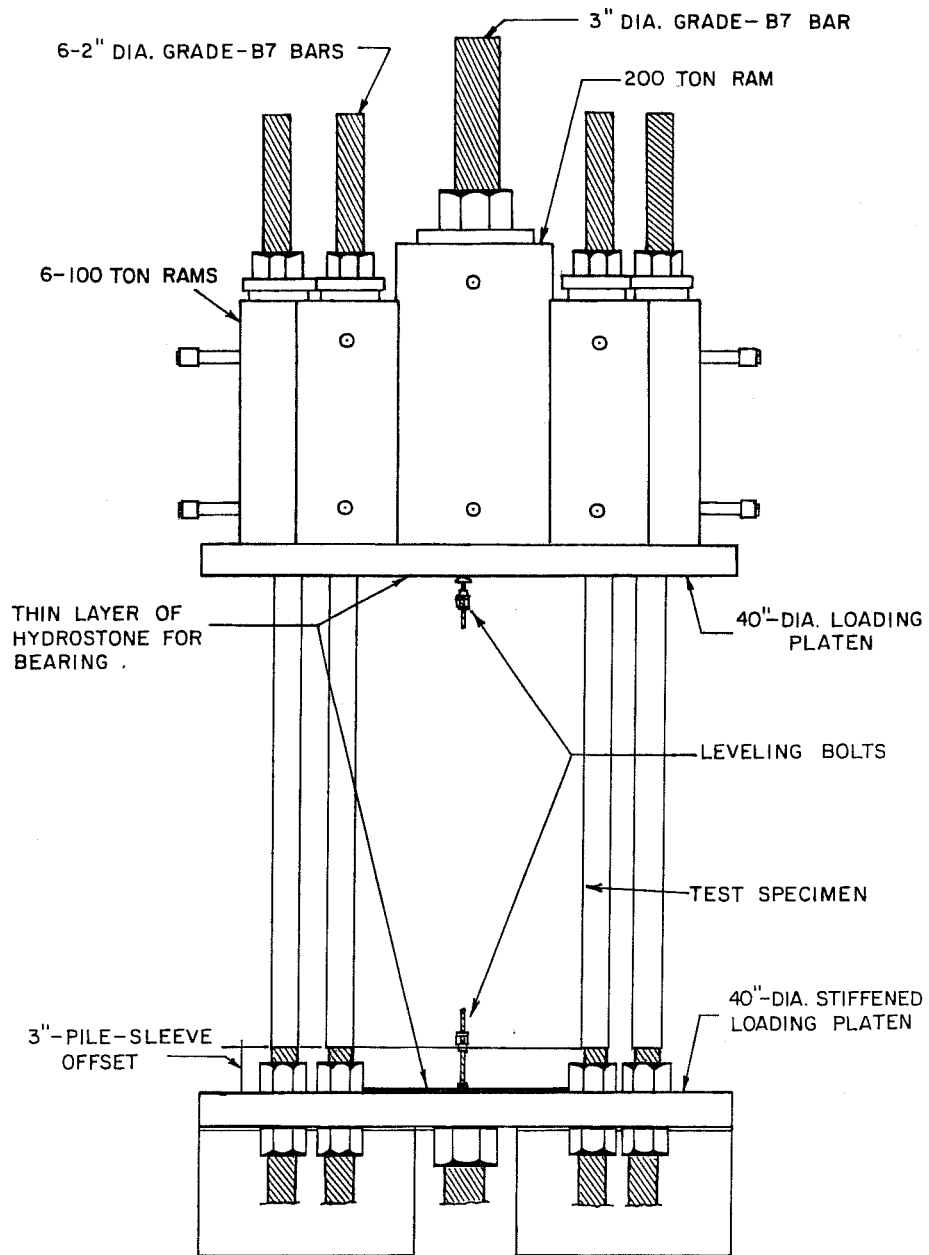


Fig. 2.13 Test frame schematic

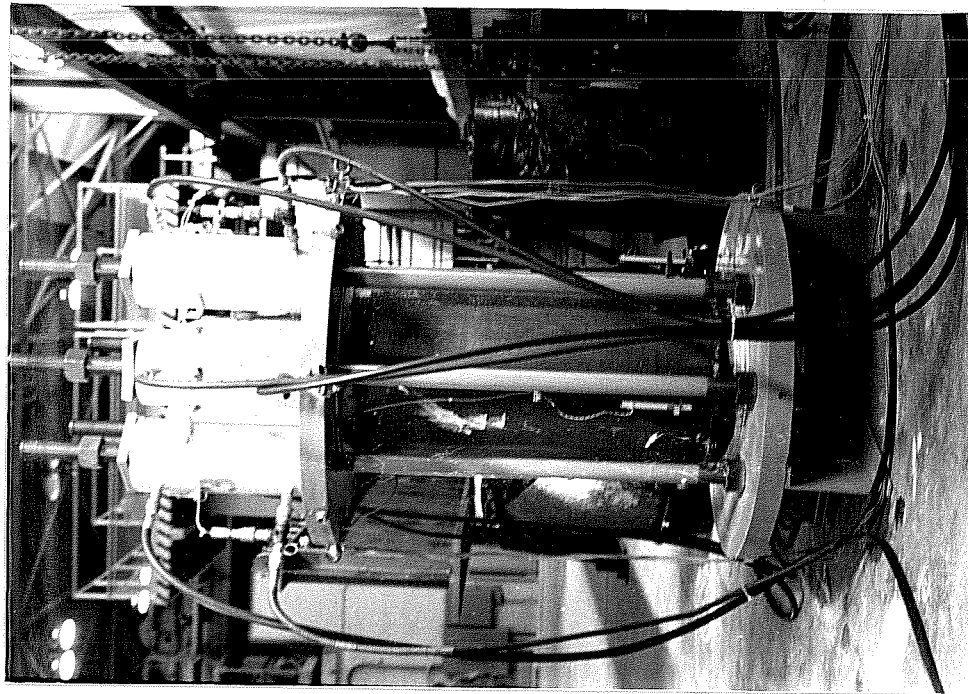


Fig. 2.15 Specimen in the test frame

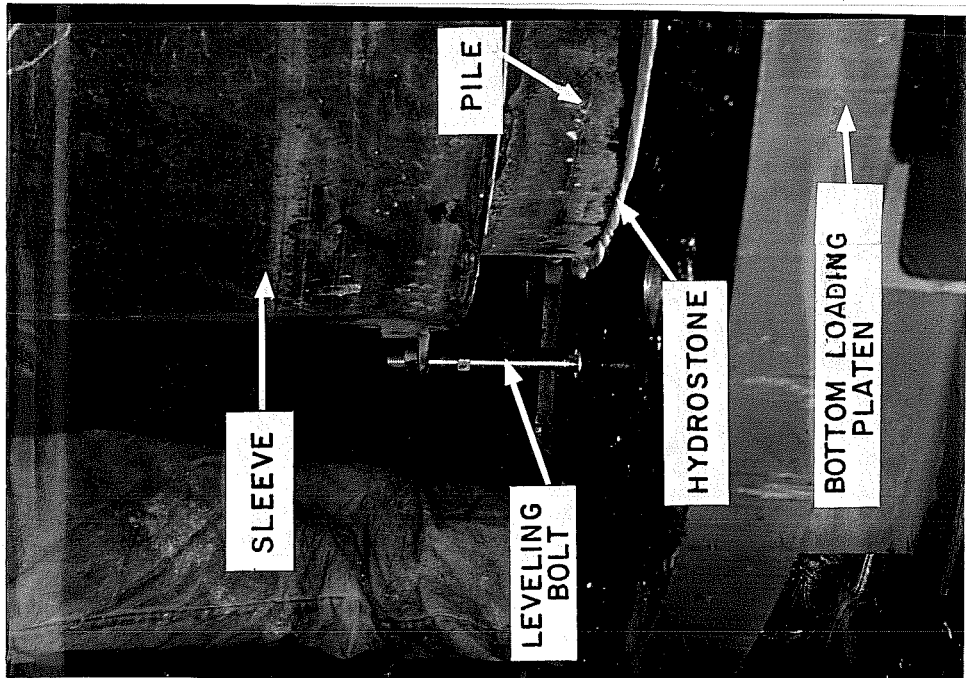


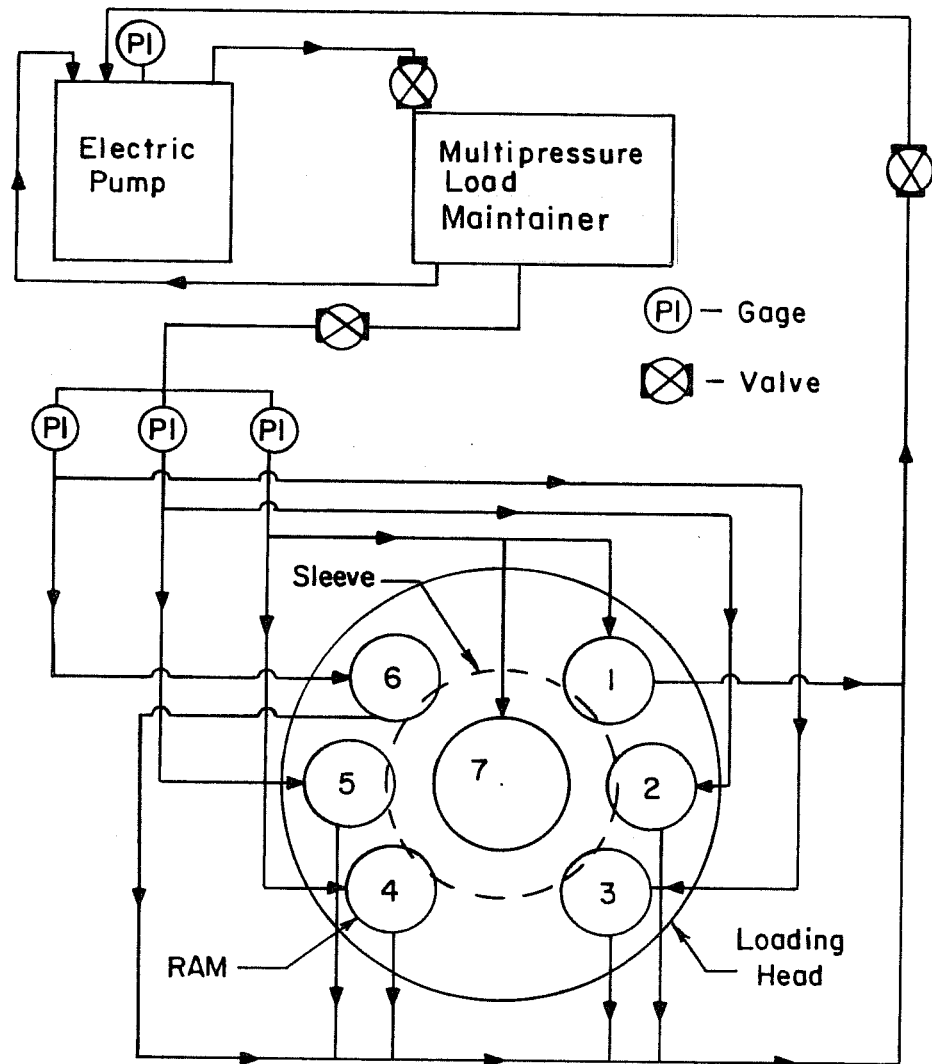
Fig. 2.14 Leveling bolt

loading head had been milled. The specimen was lowered back into position and realigned. After the hydrostone had set, a similar process was repeated for the upper loading platen (sleeve end). Next, the high strength bars were installed and the center hole rams were lowered into position. All bars were plumbed and leveling bolts turned back. In all tests the full penetration groove welds on the tubulars were positioned so they were at the bending neutral axis. Figure 2.15 shows a specimen in the test frame.

### 2.3.3 Loading System

Axial load system. A schematic drawing of the loading system used for axial load is shown in Fig. 2.16. The pressure required to load the system was provided by a single electric pump. The pressure in the rams was regulated by a multipressure load maintainer. The load maintainer and electric pump are shown in Fig. 2.17. All hydraulic equipment was connected by flexible pressure hoses. The multipressure load maintainer permitted the operator to control the rate of pressure increase and oil flow into the rams. To ensure uniformity of the load around the circumference of the specimen, all rams were fed from a common hydraulic manifold.

The main hydraulic line from the load maintainer was branched at a manifold with rams 1 and 4, (along with ram 7 when used), rams 2 and 5, and rams 3 and 6 put on three separate lines. Each branch line contained a 10,000 psi pressure gage. All return lines used a common manifold. A pressure gage was also installed on the return side of



Note:

RAM No. 1-6 100 TON RAM  
 RAM No. 7 200 TON RAM

Fig. 2.16 Schematic of axial load system



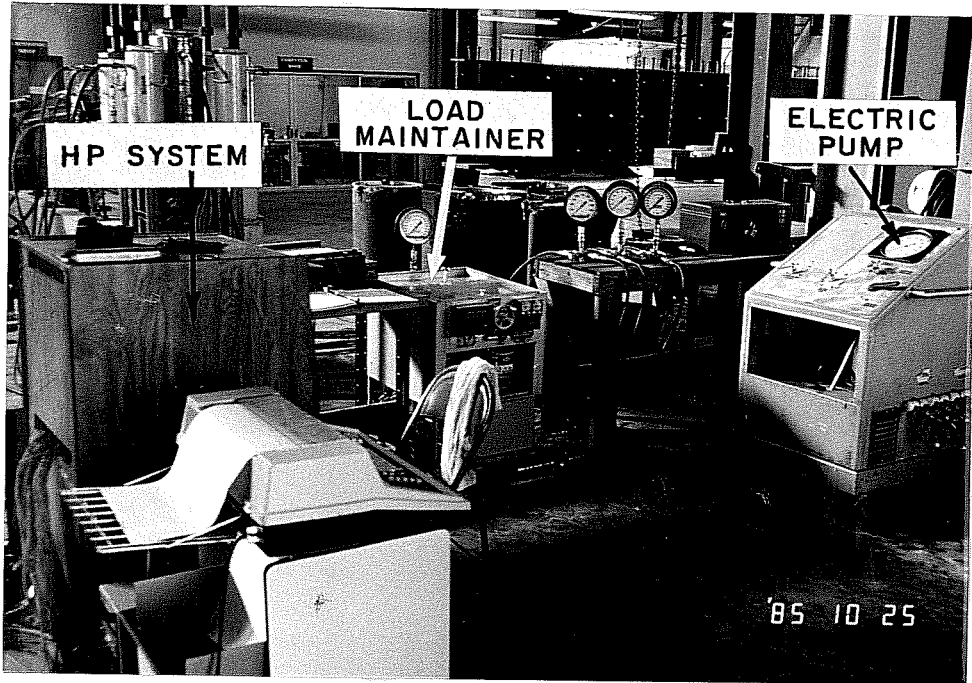


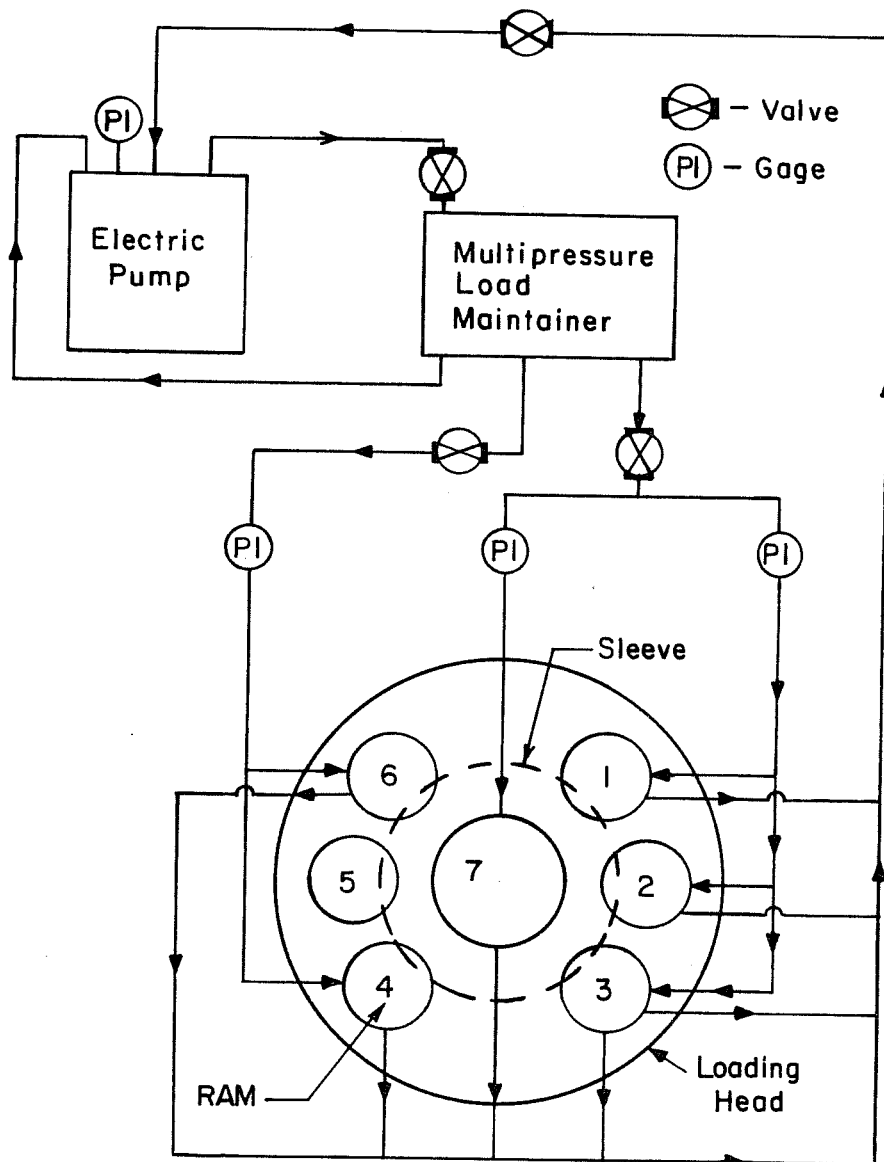
Fig. 2.17 Electric pump, load maintainer and HP system

the system at the pump to ensure that there was no back pressure in the system during the loading process.

Axial load and bending moment system. A schematic drawing of the loading system used for combined loading tests is shown in Fig. 2.18. Rams 1, 2, 3, and 7 were controlled by one load maintainer channel, while rams 4 and 6 were controlled by another channel. Ram 5 was not connected. The hydraulic line controlling rams 1, 2, 3, and 7 was branched with rams 1, 2, and 3 on one line and ram 7 on another line. The multipressure load maintainer allowed the operator to maintain a constant pressure difference between channels during the loading sequence, thus ensuring the desired stress distribution across the section.

2.3.4 Instrumentation. The loads were monitored using the 10,000 psi pressure gages, accurate to 25 psi, and pressure transducers accurate to 0.25%. The output from the pressure transducers was monitored using a Hewlett-Packard (HP) data acquisition system. The system automatically converted the voltage readings to pressure and then converted the pressure to load using the specified ram areas. The loads were corrected for the dead load of the loading system later.

For all tests, except UTAl, the relative displacement between the pile and sleeve was measured at four equally spaced positions around the circumference of the specimen using Linear Voltage Displacement Transducers (LVDT's) with 6-in. stroke as shown in Fig.



Note :

RAM No. 1-6 100 TON RAM  
 RAM No. 7 200 TON RAM

Fig. 2.18 Schematic of combined loading system

2.19. In test UTAl the LVDT's measured the displacement of the sleeve with respect to the bottom loading platen. Deflection measurements were also observed at two LVDT's locations using mechanical dial gages accurate to 0.001 in. The dial readings were used to verify the values recorded by the LVDT's. An X-Y plotter recorded the response of one of the pressure transducers and one of the LVDT's.

2.3.5 General Loading. The same general loading sequence was followed for all specimens. During the initial stages of the test, discrete load increments were applied and the resulting displacement recorded. As loading increased to ultimate the stiffness of the connection reduced, thus the loading sequence was switched to displacement control. At the higher load levels creep occurred. At this point in the loading sequence the oil flow from the load maintainer was stopped at the shut-off valve and readings taken. The specimen was then allowed to reach static equilibrium and readings were again taken.

After the initial failure, defined by a sudden slip or continually increasing displacement with no increase in load, the specimens continued to be loaded until there was a noticeable increase in deflection with decreasing load. Ultimate load was defined as the maximum static load achieved during the test.

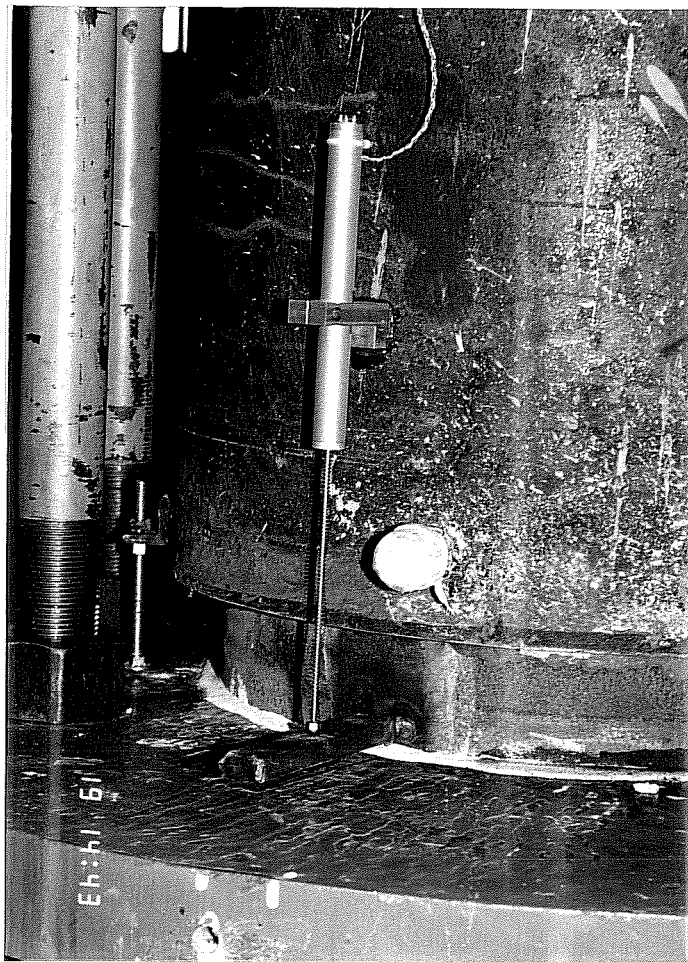


Fig. 2.19 Instrumentation used to obtain relative displacements with LVDT's

### 2.3.6 Determination of Grout Properties

Grout strength. To determine the unconfined compressive strength ( $f_{cu}$ ) of the grout, 2-in. (50.8 mm) cubes were cast in accordance with ASTM C109-80. The method of curing is reported in Section 2.2.5. A number of cubes were tested during the curing period to determine the rate of gain in grout strength and to assist in determining the time of testing where grout strength was critical. The grout strength curves determined in accordance with ASTM C109-80 are given in Appendix D. The mix designs are given in Tables 2.3 and 2.4 and the grout densities in Table 2.8. The remainder of the cubes were kept for testing at the time of a specimen test. For the first two series, specimens UTA1, UTA2, UTA3, UTM1, UTM2, and UTM3, the grout strength was based on ASTM C109-80 recommendations of three cubes. However, due to the scatter of cube test results, at least six cubes (whenever possible) were used on all subsequent tests to establish  $f_{cu}$ . A complete listing of the number of cubes used to determine  $f_{cu}$  for each test is given in Table 2.10.

A number of 2-in. (50.8 mm) cubes were also placed in a lime bath (See Section 2.2.5), to determine the effect of curing environment on the rate of strength gain of the grout. The strength curves are given in Appendix D.

In the development of Eq. 5, 3-in. (76 mm) cubes were used to determine  $f_{cu}$ . Consequently, to study the effect of cube size on  $f_{cu}$ , 3-in. (76mm) cubes were cast in Series 3 to 6. The strength

curves are given in Appendix D. As with the 2-in. (50.8 mm) cubes, at least six 3-in. (76 mm) (whenever possible) cubes were tested at the time of a specimen test.

TABLE 2.10 Size and Quantity of Grout Cubes Used to Determine  $f_{cu}$

Specimen No.	No. 2-in. Cubes	No. 3-in. Cubes	Specimen No.	No. 2-in. Cubes	No. 3-in. Cubes
UTA1	3	N/A	UTA13	3	3
UTA2	6	N/A	UTM5	6	6
UTA3	3	N/A	UTM6	3	3
UTM1	6	N/A	UTA7	3	6
UTM2	3	N/A	UTA8	6	6
UTM3	3	N/A	UTA9	3	3
UTA4	3	6	UTA10	6	6
UTA5	6	6	UTA11	6	6
UTA6	6	6	UTA12	6	6

Grout shrinkage/swell characteristics. These specimens were measured using a digital read-out length comparator accurate to 0.0001 in., shown in Fig. 2.20. The readings were taken at 24 hours, three days and seven days. After seven days the readings were taken at seven day intervals until 56 days. The initial 24 hour reading was used as the zero to which all other measurements are referenced. The readings from three specimens were used to determine the average amount of shrinkage/swell that occurred during a given recording

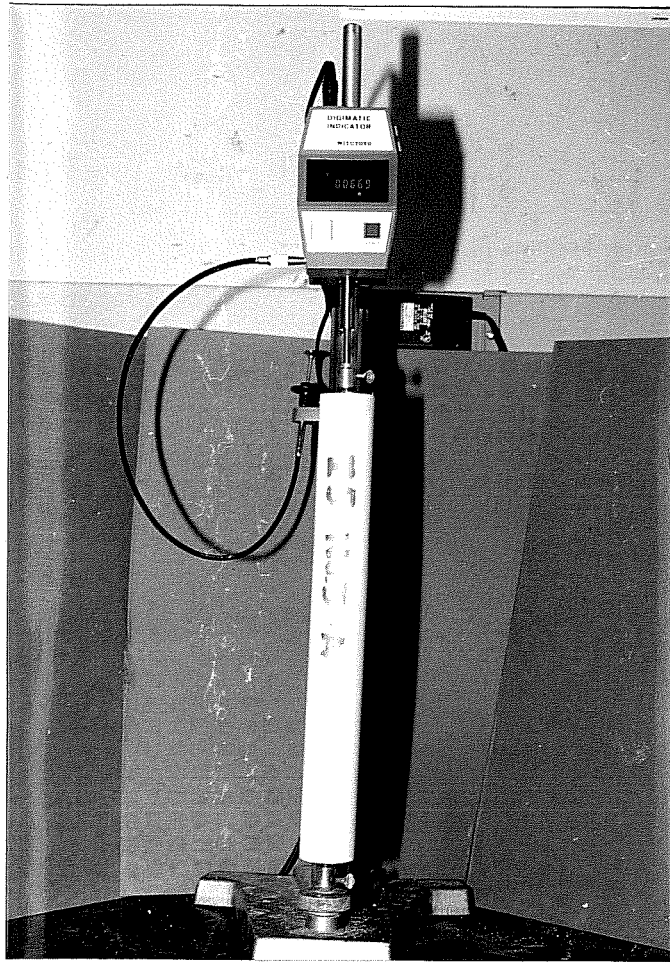


Fig. 2.20 Shrinkage specimen in digital length comparator



period. The shrinkage/swell plots for tests Series 3 to 6 are given in Appendix D.

Grout column cube strength. On the day of testing, the grout columns were removed from the vapor barriers, and 2 in. cubes were cut from the columns using a high speed rock saw, equipped with a 14-in. diamond tipped blade. Figures 2.20 and 2.21 show the typical cube locations for the 3 ft (914.4 mm) and 6 ft (1828.8 mm) columns, respectively. All cubes were tested in accordance with ASTM C109-80. However, for the grout columns the average value from the three cubes at a given location was taken as the unconfined compressive strength at that location. Results of column cube tests are given in Appendix D.

Determination of grout modulus and Poisson's ratio. The modulus of elasticity of the various grout mixes was determined in accordance with ASTM C469-75 using 4 x 8 in. (101.5 x 203 mm) grout cylinders. The modulus tests were carried out as soon after specimen testing as possible. Strains were measured using four 2.4-in. (60 mm) 120-ohm resistance strain gages. The gages were mounted in diametrically opposite pairs with one set longitudinal and the other set transverse. Strains were recorded at 2500 lb (11 KN) increments using a strain indicator and balance box. The average value for a given pair of strain gages was taken as the strain for the given load level. Appendix D contains all stress-strain curves for all the various mixes and pours.

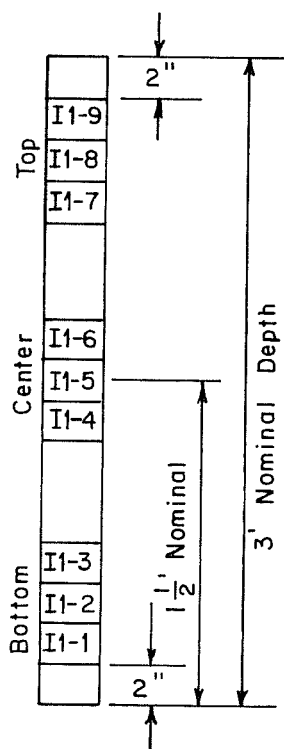


Fig. 2.21 Typical location of grout cubes for 3-ft column

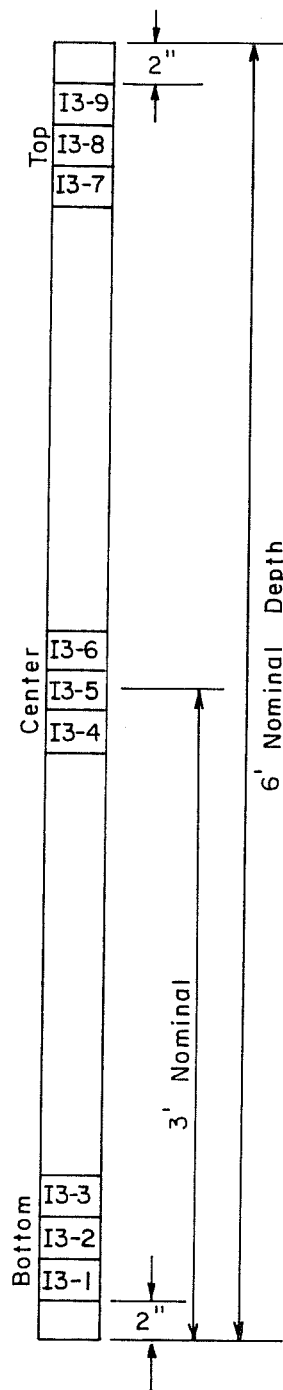


Fig. 2.22 Typical location of grout cubes for 6-ft column

2.3.7 Steel Coupon Test. Coupons were cut from two randomly selected 18-in. (457 mm) diameter piles and 21-in. (533 mm) diameter sleeves. The static yield strength,  $F_y$ , was taken as the average value obtained from the two coupons of a given pipe diameter. The standard test coupons were machined to ASTM A370-71 Specification for the Mechanical Testing of Steel Products [31]. Figure 2.23 shows a typical stress-strain plot for a tension coupon. The static yield point was determined using the 0.2% offset method. As discussed in Reference 32, the static yield plateau was determined by holding deformation constant for five minutes at three separate load levels. Strains were measured using a 2-in. (50.8 mm) extensometer capable of measuring strains of 0.0005 in./in. The strain indicator was removed once the static readings were recorded, and the tension coupon was then loaded to ultimate. Percent elongation was determined using a 2-in. (50.8 mm) gage length. The static yield stress is considered accurate to 0.3%. A summary of the tension coupon tests is given in Table 2.11.

TABLE 2.11 Summary of Tension Coupon Tests

Tube Dia. (in.)	Coupon No.	Static Yield (ksi)	Dynamic Yield (ksi)	Ultimate Strength (ksi)	% Elong. (2-in. gage)
18	P-1	45.7	46.3	75.7	15.0
	P-2	47.1	48.4	73.6	23.0
	Ave.	46.4	47.4	74.7	19.0
Mill report			51.0	72.7	26.0
ASTM A572			50.0	65.0	19.0
-----					
21	S-1	64.8	65.8	94.1	18.0
	S-2	61.8	62.8	91.7	20.0
	Ave.	63.3	64.3	92.9	19.0
Mill Report			73.8	93.8	17.0
ASTM A588			50.0	70.0	19.0

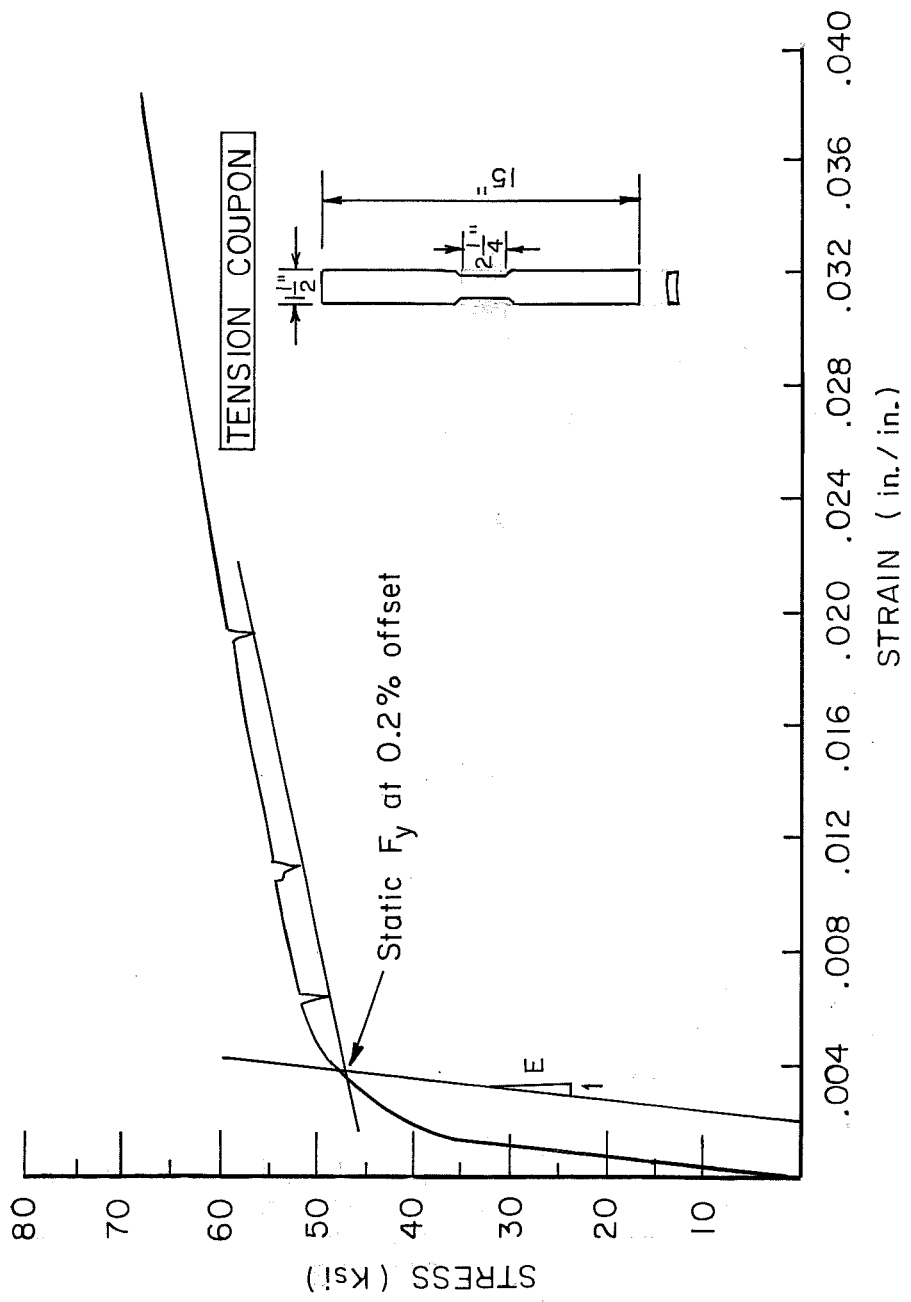


Fig. 2.23 Typical stress-strain plot for tension coupons

CHAPTER 3  
TEST RESULTS

3.1 General

Eighteen scale model grouted connections were tested. Thirteen of the tests specimens were subjected to pure axial loading (UTA) while the other five specimens were subjected to combined loading (UTM). For the test specimens under combined loading (axial and bending) the  $e/D_p$  ratio was 0.28. The combined loading produced a triangular stress distribution, zero stress on one extreme sleeve fiber and maximum compressive stress on the other extreme fiber. The type of test, grout mix,  $L/D_p$  ratio, age at testing, and loading conditions used in the test program are outlined in Table 3.1.

The unconfined compressive strength ( $f_{cu}$ ) of the grout listed in Table 3.1 was determined on the day of the test using the number and size(s) of cubes given in Table 2.10. Table 3.1 also contains the grout modulus,  $E_g$ , Poisson's ratio,  $\nu$ , and modular ratio,  $m$ . The stress-strain curves used to establish  $E_g$  and  $\nu$  are given in Figs. D-7 to D-15 of Appendix D.

Figure 3.1 shows a typical load-displacement curve in terms of average bond stress as defined in Section 1.3.2 versus relative axial displacement between pile and sleeve. Average bond stress displacement curves for each test are presented in Appendix E. The

TABLE 3.1 Test Program Results

Specimen No.	Parameter Investigated	L/Dp Ratio	Grout Age Mix Days	Loading	f <sub>cu</sub> 2-in cubes (psi)	f <sub>cu</sub> 3-in cubes (psi)	E <sub>g</sub> x 10 <sup>6</sup>	v	m	Ultimate Load (kips)	f <sub>bu</sub> (psi)	Displacement (in.)
UTA1	Reference	1.86	I3 20	Axial	3930	N/A	2.83	0.20	10.0	973	+513	0.34
UTA2*	Reference	1.91	I3 22	Axial	3970	N/A	2.83	0.20	10.0	1007	517	0.37
UTA3	Reference	1.98	I4 21	Axial	4020	N/A	2.21	0.21	13.2	960	475	0.24
UTM1*	Combined Loading	1.95	I3 23**	Axial/Bending	4380	N/A	2.83	0.20	10.0	1011	509	0.38
UTM2	Combined Loading	1.97	I4 23	Axial/Bending	4100	N/A	2.21	0.21	13.2	1119	557	0.25
UTM3*	Combined Loading	1.93	I4 26	Axial/Bending	4200	N/A	2.21	0.21	13.2	1150	586	0.31***
UTA4	Shear Key Loc.	1.70	I5 21	Axial	5990	7190	3.76	0.20	7.8	1094	633	0.54
UTA5	Shear Key Loc.	1.71	I5 23	Axial	5780	7380	3.76	0.20	7.8	1243	712	0.43
UTA6	Shear Key Loc.	1.68	I5 25	Axial	6110	6220	3.76	0.20	7.8	1143	668	0.46
UTA13	Reference	1.01	I6 21	Axial	4930	5670	3.15	0.21	9.1	524	511	0.08
UTM5	L/Dp Ratio	0.99	I6 23	Axial/Bending	5480	6140	3.15	0.21	9.1	857	850	0.41
UTM6	L/Dp Ratio	1.03	I6 25	Axial/Bending	5670	5670	3.15	0.21	9.1	737	704	0.17
UTA7	Eccentric Tubes	1.92	I7 21	Axial	4760	4790	3.19	0.22	8.8	1234	631	0.44
UTA8	Eccentric Tubes	1.89	I7 23	Axial	5010	5630	3.19	0.22	8.8	1055	548	0.29
UTA9	Eccentric Tubes	1.90	I7 25	Axial	5350	5730	3.19	0.22	8.8	1106	571	0.26
UTA10	Grout Strength	1.05	J2 2	Axial	6630	6690	3.54	0.21	8.3	537	502	0.17
UTA11	Grout Strength	1.04	J2 22	Axial	11120	10440	4.73	0.22	6.2	720	683	0.17
UTA12	Grout Strength	1.04	J2 23	Axial	10680	9440	4.73	0.22	6.2	692	656	0.24

\*Specimens were reloaded

\*\*Specimen was reloaded at 26 days, f<sub>cu</sub> - 4440 psi

\*\*\*Corresponds to axial failure load of 954 k; see test description for explanation

+See Appendix F for sample calculation

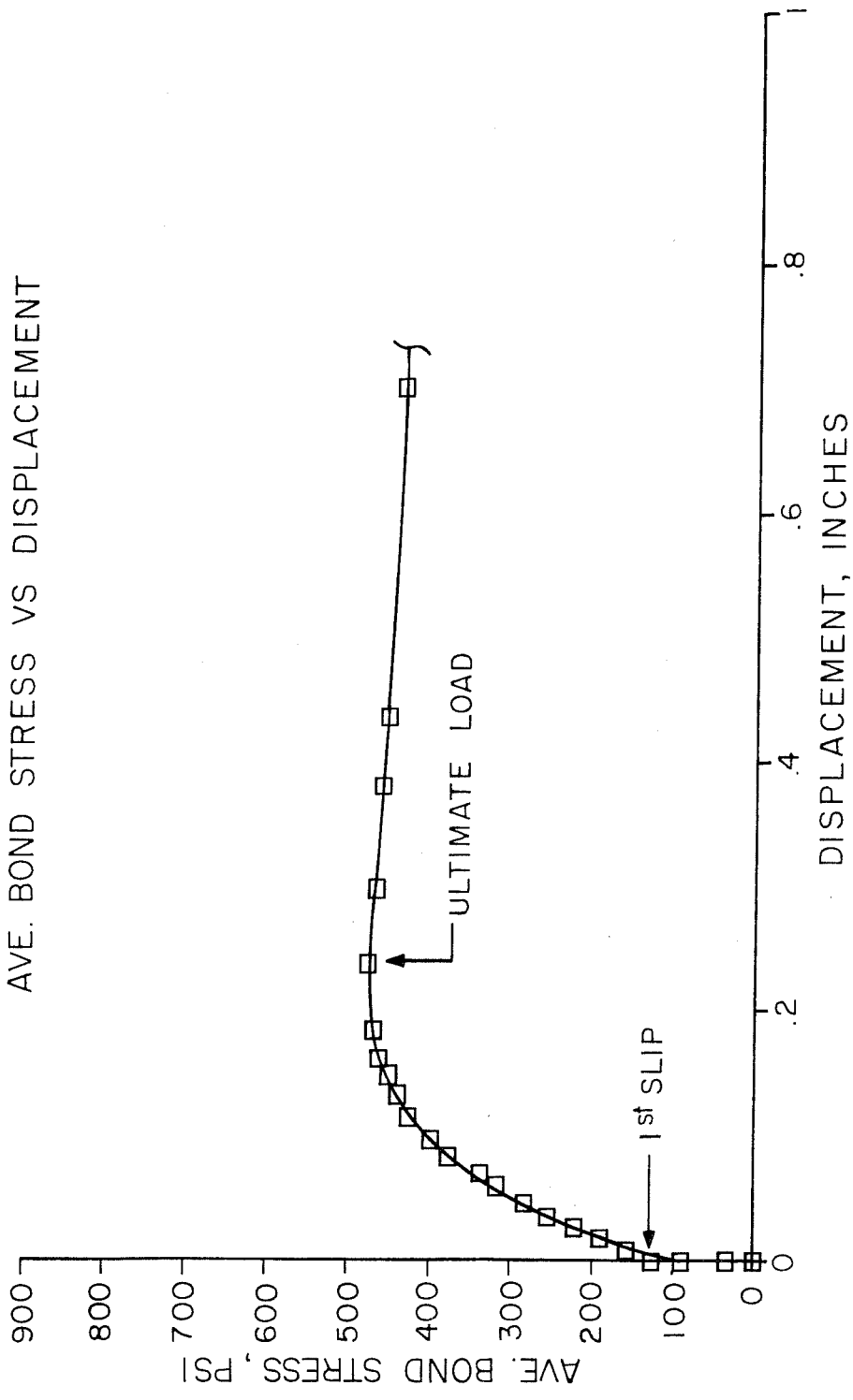


Fig. 3.1 Typical average bond stress versus displacement curve



displacements plotted for axial load represent an average value from the four LVDT's. For combined loading the displacement represents an average value of the two LVDT's located on the bending neutral axis. The ultimate static axial load, bond stress,  $f_{bu}$ , and displacement at ultimate are given in Table 3.1 for each test. A table of results by series is also included in each section. The series summary tables include the unconfined grout strength ( $f_{cu}$ ) based on 2 in. (50.8 mm) cubes, ultimate static axial load, corresponding ultimate bond stress and the ultimate bond stress normalized with respect to both  $\sqrt{f_{cu}}$  and  $f_{cu}$ . Sample calculations of calculated values are included in Appendix F.

The ultimate bond stress is given in two formats in the summary tables. The first method of calculating the ultimate bond stress, ( $f_{bu}^1$ ), is the standard method used by previous investigators, where the ultimate load is divided by  $\pi D_p L$  where  $L$  is the average grouted length from Table 2.9. The second method of calculating the ultimate bond stress ( $f_{bu}^2$ ) is based on the grout length between the first and last shear keys within the grouted length of the specimen. For experimental specimens the omission of the load transferred by bond before and after the last shear key can be considered insignificant in comparison with the load transferred by the shear keys. The second method of bond stress calculation yields a

constant grouted length value for each series. Therefore, unlike the standard method using  $L$ , the scatter of data remains constant in the conversion of ultimate load to ultimate bond stress. Table 3.2 gives the constant grouted lengths used for each series.

TABLE 3.2 Constant Grouted Lengths used for Calculation of  $f_{bu}^2$

Series No.	Grouted length (in.)	Series No.	Grouted length (in.)
1	31.9	4	14.9
2	31.9	5	31.9
3	29.8	6	14.9

The following sections describe individual test groups by series as listed in Section 2.1.1.

### 3.2 Series 1: Reference Tests

Three axial load tests were performed to establish a reference to which the other five series could be compared and also to allow for correlation with previous research. Ultimate load and bond stress are given in Table 3.3. The grout strength curves for Mixes I3 and I4 are given in Figs. D-1 and D-2 of Appendix D. The load-displacement graphs, in the form of the bond stress versus

TABLE 3.3 Results of Series 1: Reference Tests

Specimen No.	$f_{cu}$ (psi)	Ultimate Load	$*f_{bu}^1$ (psi)	$*f_{bu}^2$ (psi)	$f_{bu}^1/\sqrt{f_{cu}}$	$f_{bu}^1/f_{cu}$
UTA1	3930	973	513	540	8.18	0.131
UTA2	3970	1007	517	559	8.21	0.130
UTA3	4020	960	475	533	7.49	0.118
MEAN	3973	980	502	546	7.96	0.126
S.D.	45.1	24.3	23.2	13.5	0.41	0.007
%-DIF	2.2	4.7	8.1	4.7	8.8	9.9

\*See Appendix F for sample calculation

relative axial displacements between pile and sleeve are shown in Figs. E-1 to E-3 of Appendix E.

3.2.1 Test UTA1. The displacement for this first test was measured relative to the bottom loading platen, therefore, the displacement includes some plate bending. The first noticeable slip occurred at approximately 480 k (2135 KN). The maximum load was 973 k (4328 KN) at a displacement of 0.34 in. (8.64 mm). The valve between the load maintainer and the rams, shown in Fig. 2.16, was not installed for this test. Consequently, after the ultimate load was reached no lower equilibrium loads were obtained since the loading system continued to supply oil to the rams. At this point, the connection was allowed to slip until it was apparent that static equilibrium conditions could not be achieved. The connection was

then completely unloaded. The total recorded average displacement was 2.46 in. (62.5 mm).

3.2.2 Test UTA2. The specimen was loaded to 136 k (605 KN) then unloaded due to an instrumentation problem. First slip occurred at about 470 k (2091 KN). At a load of 1006 k (4475 KN) and a displacement of 0.18 in. (4.6 mm), the specimen experienced a sudden slip of 0.17 in. (4.3 mm). The specimen was unloaded and reloaded. Upon reloading the specimen reached a maximum load of 1007 k (4480 KN) at a displacement of 0.37 in. (9.4 mm). During the next load increment the specimen again experienced a sudden displacement (0.34 in.) after which the capacity continually decreased.

After testing a section of the sleeve was removed. Figure 3.2 shows the sleeve side of the grout surface. Arrows on the figures indicate the direction of applied load on the sleeve. The slippage on the sleeve side varied from 1.5 in. (38.1 mm) at the top of the specimen to 0.5 in. (12.7 mm) at the bottom. Figure 3.3 shows the pile side of the grout surface where the slippage was constant along the length and equal to the measured relative displacement of 1.8 in. (45.7 mm). Figure 3.4 is a profile of the grout showing the completely formed crack pattern.

3.2.3 Test UTA3. The specimen experienced no measurable displacement until a load of about 317 k (1410 KN). The specimen reached a maximum load of 960 k (4270 KN) with a corresponding



Fig. 3.3 Grout surface on pile side for Specimen UTA2



Fig. 3.2 Grout surface on sleeve side for Specimen UTA2

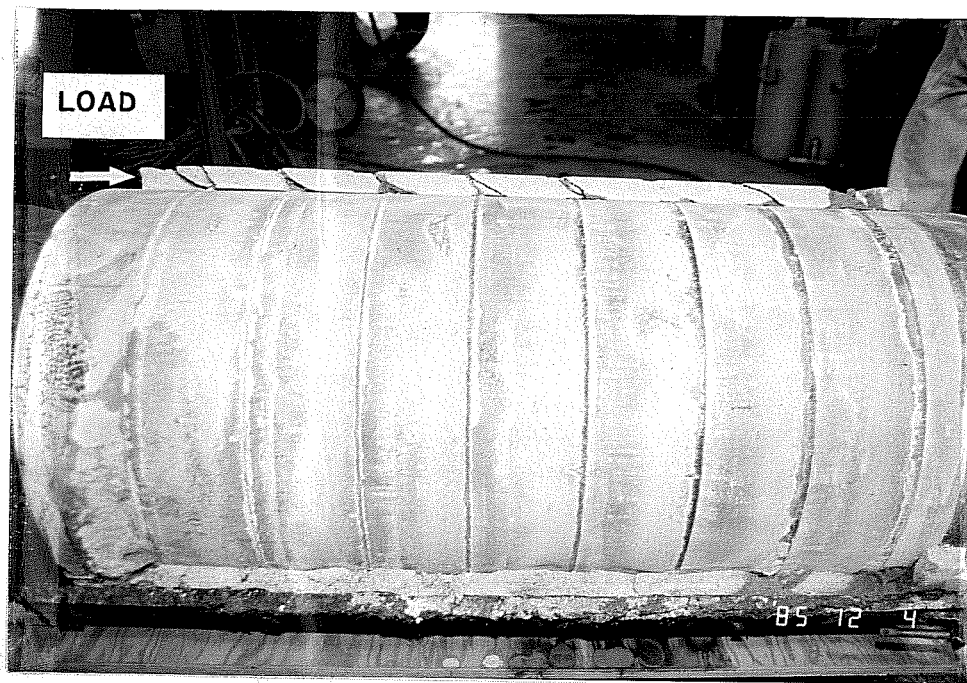


Fig. 3.4 Grout profile of Specimen UTA2 showing crack pattern

displacement of 0.24 in. (6.1 mm). The test was stopped with a final relative displacement of 1.33 in. (33.8 mm).

### 3.3 Series 2: Combined Loading

In Series 2, the behavior of specimens subjected to combined loading (axial and bending) was examined. Ultimate load and bond stress results are given in Table 3.4. The grout strength curves for Mixes I3 and I4 are given in Figs. D-1 and D-2 of Appendix D. The load-displacement plots, in the form of the bond stress versus relative axial displacement between pile and sleeve are shown in Figs. E-4 to E-6 of Appendix E.

TABLE 3.4 Results of Series 2: Combined Loading

Specimen No.	$f_{cu}$ (psi)	Ultimate Load	$f_{bu}^1$ (psi)	$f_{bu}^2$ (psi)	$f_{bu}^1/\sqrt{f_{cu}}$	$f_{bu}^1/f_{cu}$
UTM1	4380	*1011	*509	*561	*7.69	*0.116
UTM2	4100	1119	557	621	8.70	0.136
UTM3	4200	1150	586	638	9.04	0.140
MEAN	4227	1135	551	607	8.48	0.131
S.D.	141.9	21.9	38.9	40.5	0.70	0.013
%-DIF	6.4	2.7	4.9	2.7	3.8	2.9

\* Not included in calculation of mean, S.D. or %-difference since ultimate load represents pure axial loading

3.3.1 Test UTM1. For UTM1 rams 4, 5 and 6 shown in Fig. 2.18 were not used. The specimen exhibited minimal displacement until a load of about 274 k (1219 KN). At an axial load of 865 k (3848 KN), moment of 4298 in.-k (486 KN-m) and a relative displacement of 0.11 in. (2.8 mm) the hydraulic pump reached maximum capacity. The specimen was unloaded and the loading system altered to apply moment in the opposite direction. The specimen was again loaded up to the pump capacity. The relative axial displacement increased only 0.02 in. (0.5 mm). The specimen was unloaded and reloaded with the same results. The specimen was then reloaded in pure axial loading and failed at a load of 1011 k (4497 KN). The corresponding displacement was 0.38 in. (9.7 mm).

3.3.2 Test UTM2. The specimen reached a maximum axial load of 1119 k (4978 KN) and moment of 5520 in-k (623.7 KN-m) at a displacement of 0.25 in. (6.4 mm). The test was stopped at a final relative displacement of 1.31 in. (33.3 mm).

After testing the sleeve was removed exposing the grout surface which had been subjected to the highest compressive bending moment. Figure 3.5 shows the sleeve side of the grout surface. Figure 3.6 shows the corresponding pile side of the grout surface. Figure 3.7 is a profile of the grout showing the completely formed crack pattern.



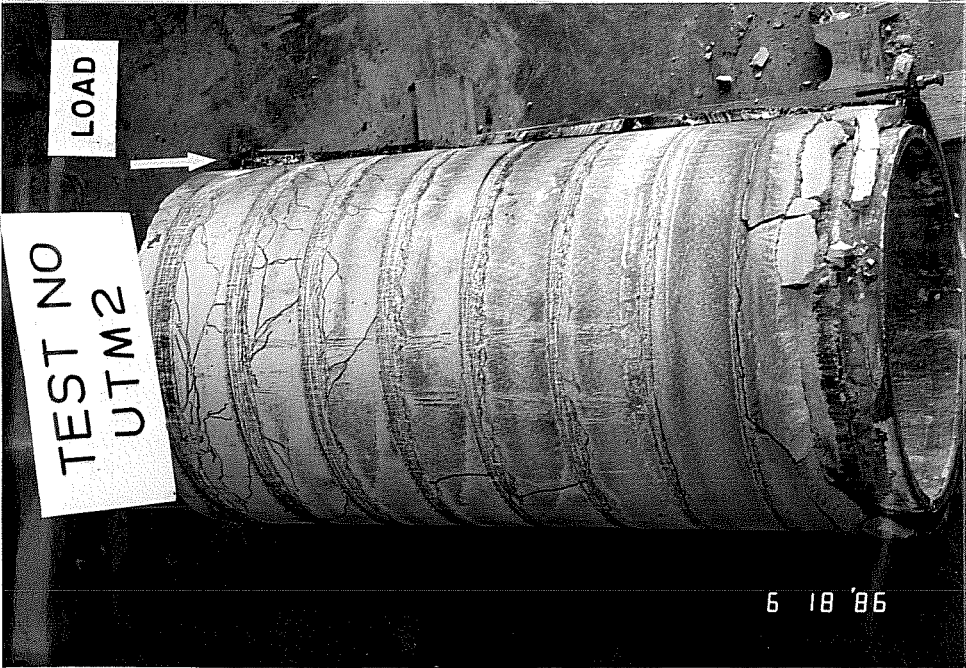


Fig. 3.5 Grout surface on sleeve side for Specimen UTM2

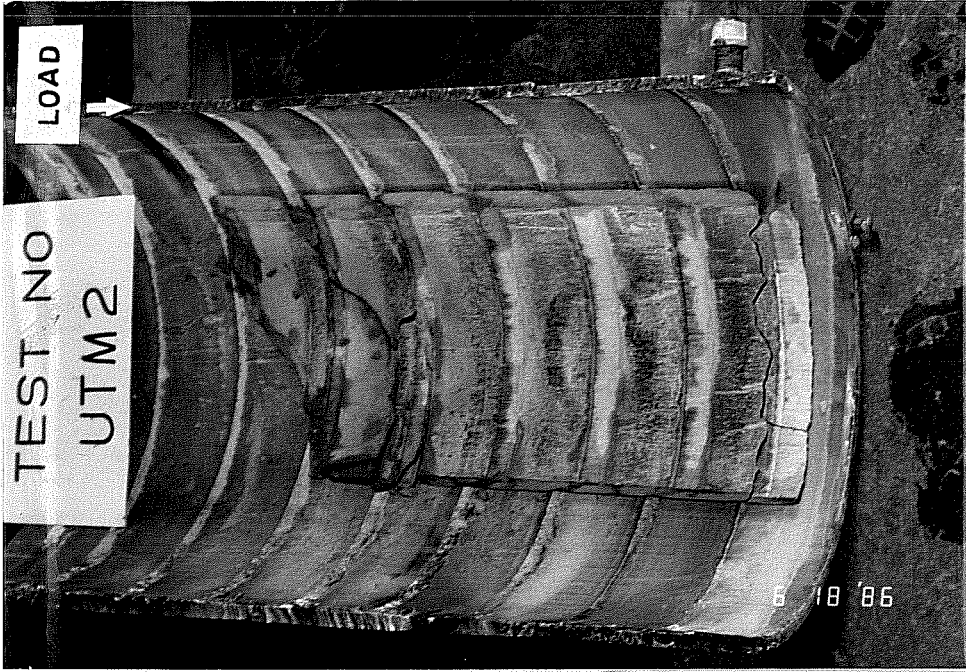


Fig. 3.6 Grout surface on pile side for Specimen UTM2

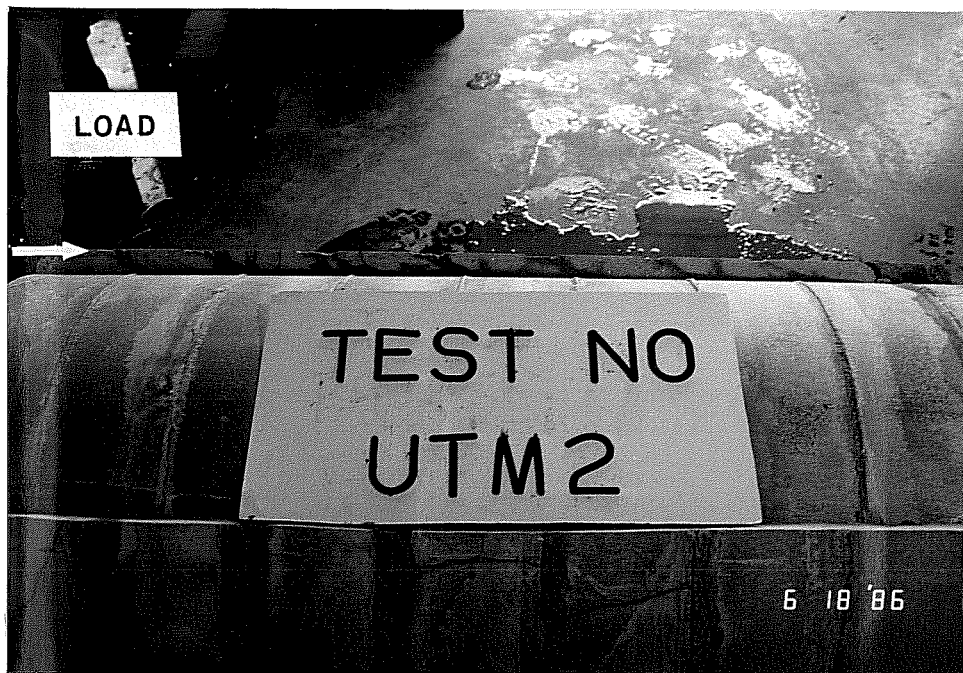


Fig. 3.7 Grout profile of Specimen UTM2 showing crack pattern

3.3.3 Test UTM3. The specimen was loaded up to an axial load of 1150 k (5116 KN) and moment of 5702 in.-k (644 KN-m), which was at the capacity of the hydraulic pump. On subsequent unloading and reloading there were slight increases in displacements, although the load remained fairly constant. However, due to possible damage to the pump and other equipment the specimen was unloaded. Pure axial load was then applied until failure at a load of 954 k (4244 KN). The corresponding displacement was 0.31 in. (7.9 mm).

#### 3.4 Series 3: Relative Shear-key Location

In Series 3, the effect of relative location of pile and sleeve shear keys was examined. The sleeves and piles were positioned with the shear keys directly across from each other. Ultimate load and bond stress results are given in Table 3.5. The grout strength curve for Mix I5 is given in Fig. D-3 of Appendix D. The load-displacement plots, in the form of the bond stress versus relative axial displacement between pile and sleeve are shown in Figs. E-7 to E-9 of Appendix E.

3.4.1 Test UTA4. The ultimate load of 1094 k (4867 KN) was reached at displacement of 0.54 in. (13.7 mm). During subsequent loading, the specimen experienced a sudden slip to 1.01 in. (25.7 mm).

TABLE 3.5 Results of Series 3: Relative Shear-Key Location

Specimen No.	$f_{cu}$ (psi)	Ultimate Load	$f_{bu}^1$ (psi)	$f_{bu}^2$ (psi)	$f_{bu}^1/\sqrt{f_{cu}}$	$f_{bu}^1/f_{cu}$
UTA4	5990	1094	633	650	8.18	0.106
UTA5	5780	1243	712	739	9.37	0.123
UTA6	6110	1143	668	679	9.01	0.109
MEAN	5960	1160	671	689	8.85	0.113
S.D.	167.0	75.9	39.6	45.4	0.61	0.009
%-DIF	5.4	13.6	12.5	13.6	12.7	13.8

The failure was accompanied by a loud bang as the specimen released stored energy.

3.4.2 Test UTA5. The specimen carried an ultimate load of 1243 k (5529 KN) with a displacement of 0.43 in. (10.9 mm). This test was stopped at the peak load so that the grout crack pattern at ultimate could be studied. The peak load was taken as that point at which three successive loading increments yielded less than a 1% increase in capacity. Figure 3.8 shows the sleeve side of the grout surface. The slippage on the grout surface varied from 11/16 in. (17.5 mm) at the top of the connection to 3/16 in. (4.8 mm) at the bottom. The figure also shows significant crushing of the grout ahead of the shear keys. Figure 3.9 shows the pile surface of the grout. The slippage varied from 1/4 in. (6.4 mm) at the top of the connection

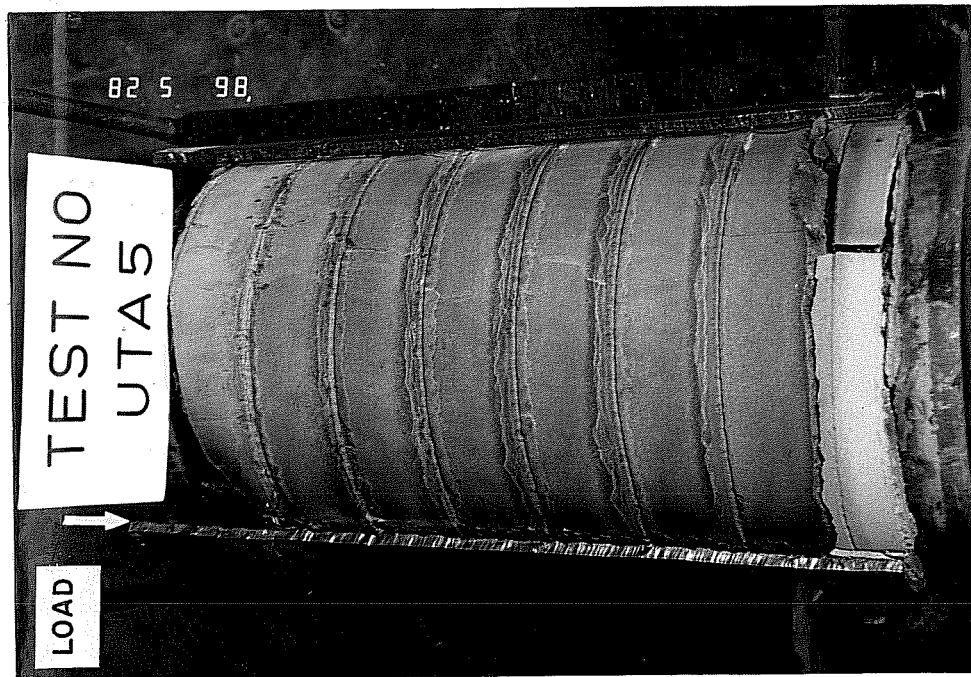


Fig. 3.8 Grout surface on sleeve side for Specimen UTA5

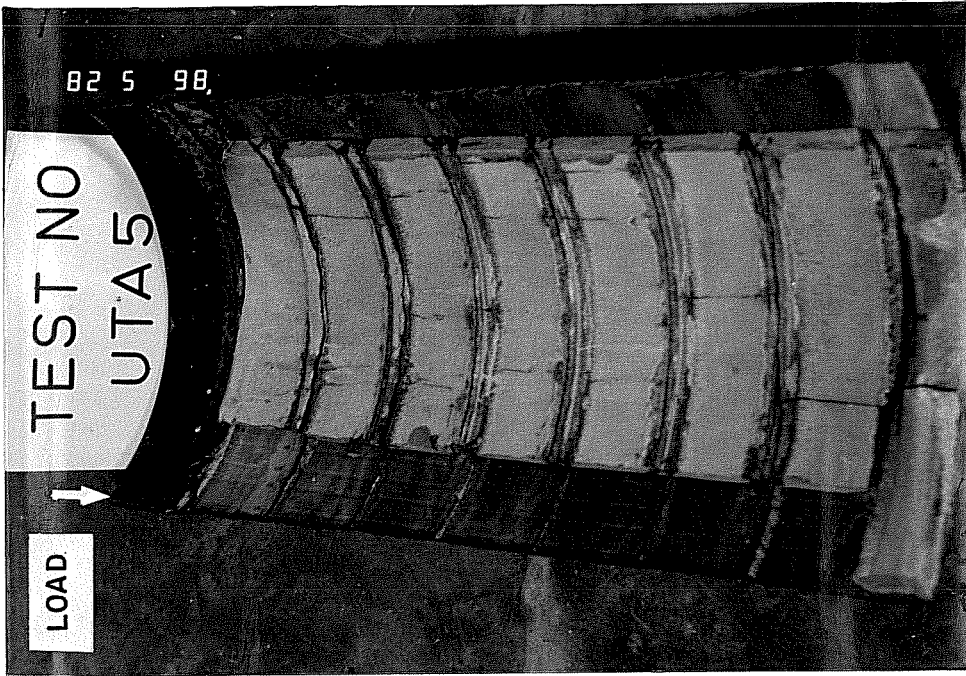


Fig. 3.9 Grout surface on pile side for Specimen UTA5

to 3/4 in. (19.1 mm) at the bottom. Figure 3.10 shows a profile of the crack pattern at ultimate load.

3.4.3 Test UTA6. The specimen carried an ultimate load of 1143 k (5085 KN) with a corresponding displacement of 0.46 in. (11.7 mm). The load-slip behavior was similar to that of UTA4 and UTA5.

### 3.5 Series 4: Length Effect on Combined Loading

In Series 4 the effect of length on connections under combined loading was examined. The  $L/D_p$  ratio for the specimens in Series 4 was 1.0 as compared to 2.0 for the previous three series; however, the  $e/D_p$  ratio of 0.28 was still maintained. Ultimate load and bond stress results are given in Table 3.6. The grout strength curves for Mix I6 are given in Fig. D-4 of Appendix D. The bond stress versus relative axial displacement between pile and sleeve, are shown in Figs. E-10 to E-12 of Appendix E.

3.5.1 Test UTA13. This specimen was a reference test for the other two specimens of the series, and was subjected to pure axial load. The specimen reached an ultimate load of 524 k (2331 KN) at a displacement of 0.08 in. (2.0 mm). The post ultimate behavior was similar to that of the axial specimens in Series 1 with  $L/D_p$  ratios of two.

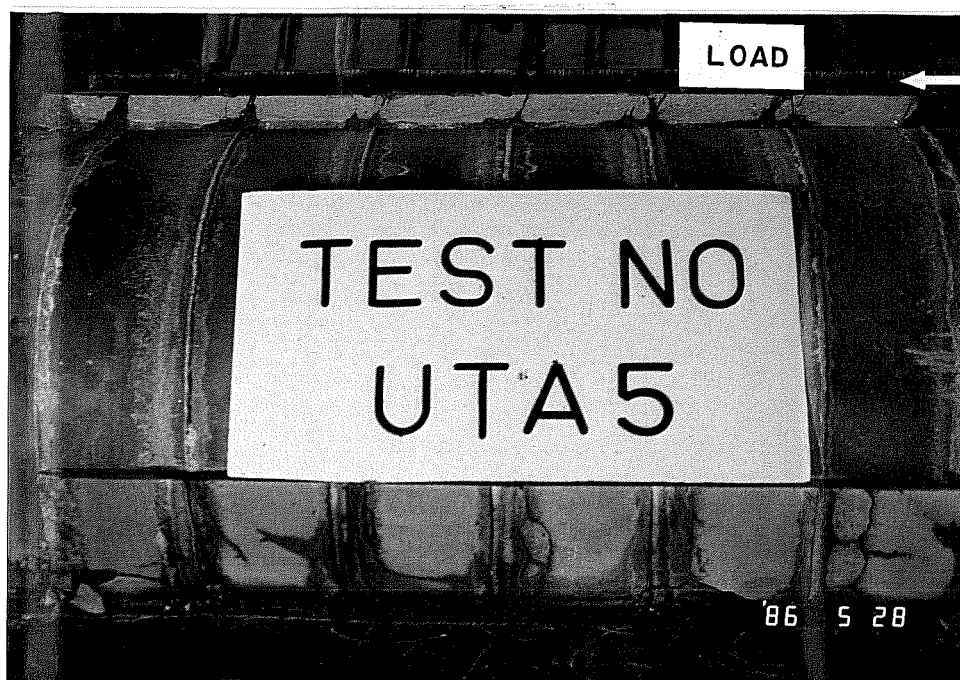


Fig. 3.10 Grout profile of Specimen UTA5 showing crack pattern

TABLE 3.6 Results of Series 4: Length Effect on Combined Loading

Specimen No.	$f_{cu}$ (psi)	Ultimate Load	$f_{bu}^1$ (psi)	$f_{bu}^2$ (psi)	$f_{bu}^1/\sqrt{f_{cu}}$	$f_{bu}^1/f_{cu}$
UTA13	4930	*524	*511	*623	*7.28	*0.104
UTM5	5480	857	850	1019	11.58	0.155
UTM6	5670	737	704	867	9.79	0.124
MEAN	5360	797	777	948	10.69	0.140
S.D.	384	84.9	103.2	107.5	1.27	0.02
%-DIF	13.1	14.0	17.2	14.0	15.5	20.0

\* Not included in calculation of mean, S.D. or %-difference since ultimate load represents pure axial loading

3.5.2 Test UTM5. The specimen carried an ultimate axial load of 857 k (3812 KN) and moment of 4331 in-k (489 KN-m). The corresponding displacement was 0.41 in. (10.4 mm). During the loading process there was noticeable rotation of the sleeve relative to the pile. The maximum recorded difference in displacement between the side of the sleeve under maximum compressive stress and the side with zero stress was 0.623 in. (15.8 mm). As the load approached ultimate the tubes tended to rotate back to their initial plumb positions and remained that way through post ultimate loading.

After testing the sleeve was removed exposing the grout surface which had been subjected to the highest bending moment. Figure 3.11 shows the sleeve surface of the grout. The slip varied



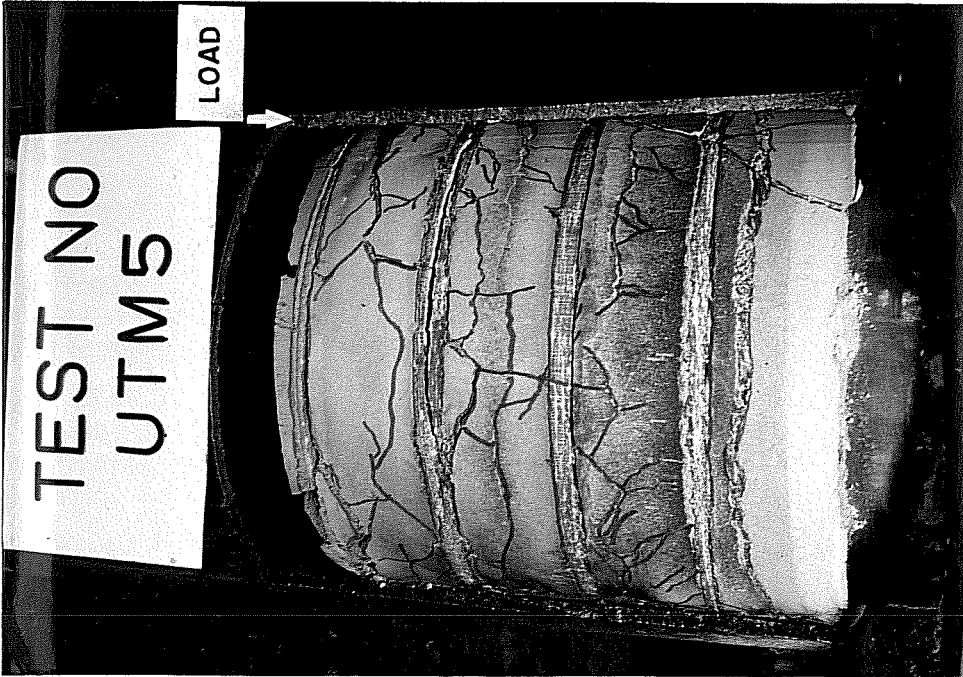


Fig. 3.11 Grout surface on sleeve side for Specimen UTM5

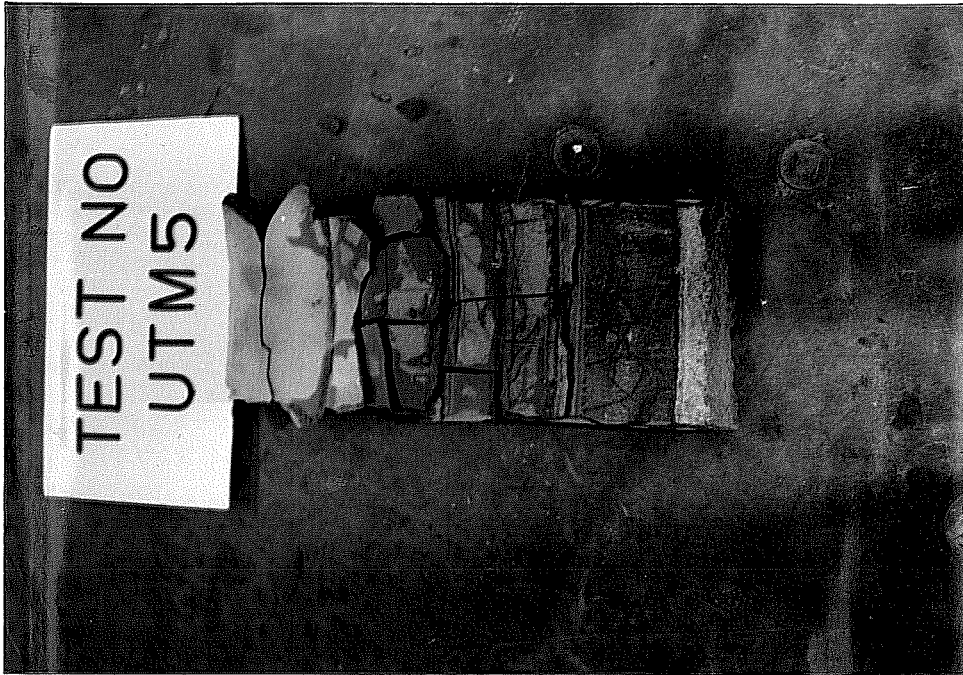


Fig. 3.12 Grout surface on pile side for Specimen UTM5

from 15/16 in. (23.8 mm) at the top of the connection to 5/8 in. (15.9 mm) at the bottom. Unlike the conditions under pure axial load (Figs. 3.2 and 3.8), Fig. 3.11 shows that a significant amount of cracking occurred between shear key locations. Figure 3.12 shows the pile surface of the grout. Due to the cracking no slip measurements could be taken. Figure 3.13 is a profile of the crack pattern.

3.5.3 Test UTM6. The behavior was similar to Test UTM5. The ultimate load obtained was 737 k (3278 KN) and moment of 3678 in-k (416 KN-m) with a corresponding displacement of 0.17 in. (4.3 mm). The post ultimate behavior, however, was accompanied by significant sudden slip, Fig. E-12, instead of the gradual decrease in capacity as in UTM5.

### 3.6 Series 5: Eccentric Pile and Sleeve

In Series 5, the effect of eccentrically placed piles and sleeves, shown in Fig. 3.14 was investigated. The width of the annulus varied from a minimum of 0.5 in. (12.7 mm) to a maximum of 1.5 in. (38.1 mm). The specimens were subjected to axial load, although some small amounts of moment developed due to the relative pile-sleeve alignment in the test frame. Ultimate load and bond stress results are given in Table 3.7. The grout strength curve for Mix I7 is given in Fig. D-5 of Appendix D. Bond stress versus

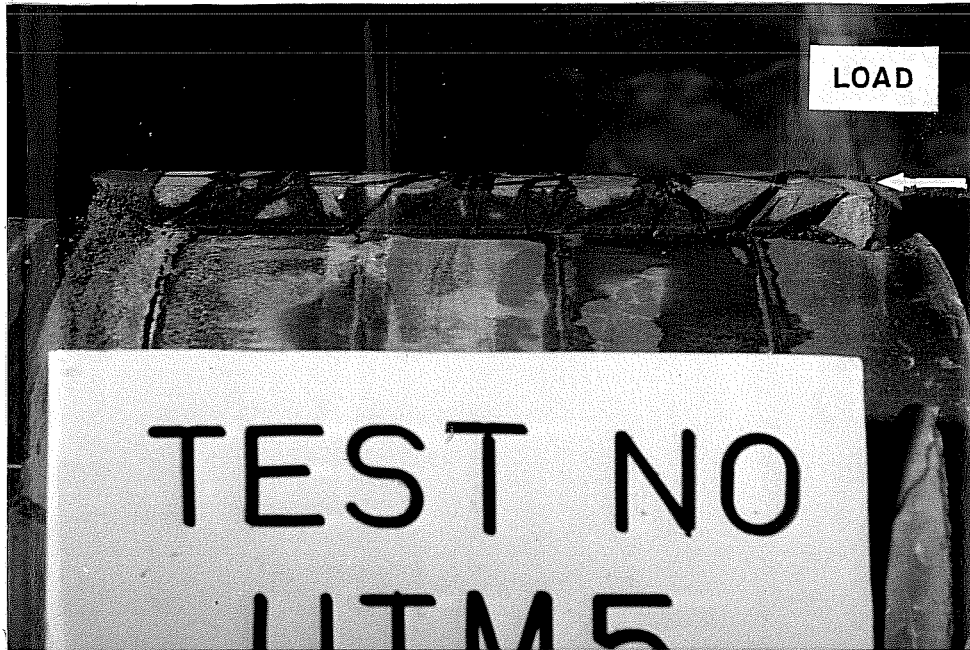


Fig. 3.13 Grout profile of Specimen UTM5 showing crack pattern



Fig. 3.14 Typical annulus for eccentrically placed pile and sleeve specimens

TABLE 3.7 Results of Series 5: Eccentric Pile and Sleeve

Specimen No.	$f_{cu}$ (psi)	Ultimate Load	$f_{bu}^1$ (psi)	$f_{bu}^2$ (psi)	$f_{bu}^1/\sqrt{f_{cu}}$	$f_{bu}^1/f_{cu}$
UTA7	4760	1234	631	685	9.15	0.133
UTA8	5010	1055	548	585	7.74	0.109
UTA9	5350	1106	571	614	7.81	0.107
MEAN	5040	1132	583	628	8.23	0.116
S.D.	296	92.2	42.9	51.4	0.79	0.014
%-DIF	11.0	17.0	15.1	17.1	15.4	19.5

relative axial displacement are shown in Figs. E-13 to E-15 of Appendix E.

3.6.1 Test UTA7. The first noticeable slip occurred at approximately 532 k (2367 KN). Post ultimate behavior was similar to Series 1 axial tests. The ultimate load was 1234 k (5489 KN) at a relative displacement of 0.44 in. (11.2 mm).

3.6.2 Test UTA8. The specimen carried an ultimate load of 1055 k (4693 KN) with a displacement of 0.29 in. (7.4 mm). This test was stopped at the peak load so that the grout crack pattern at ultimate could be studied. The peak load was taken as that point at which three successive loading increments yielded less than a 1% increase in capacity. Figure 3.15 shows the sleeve side of the grout surface. The slippage on the grout surface varied from 1/2 in. (12.7 mm) at the top of the connection to 1/4 in. (6.4 mm) at the bottom.

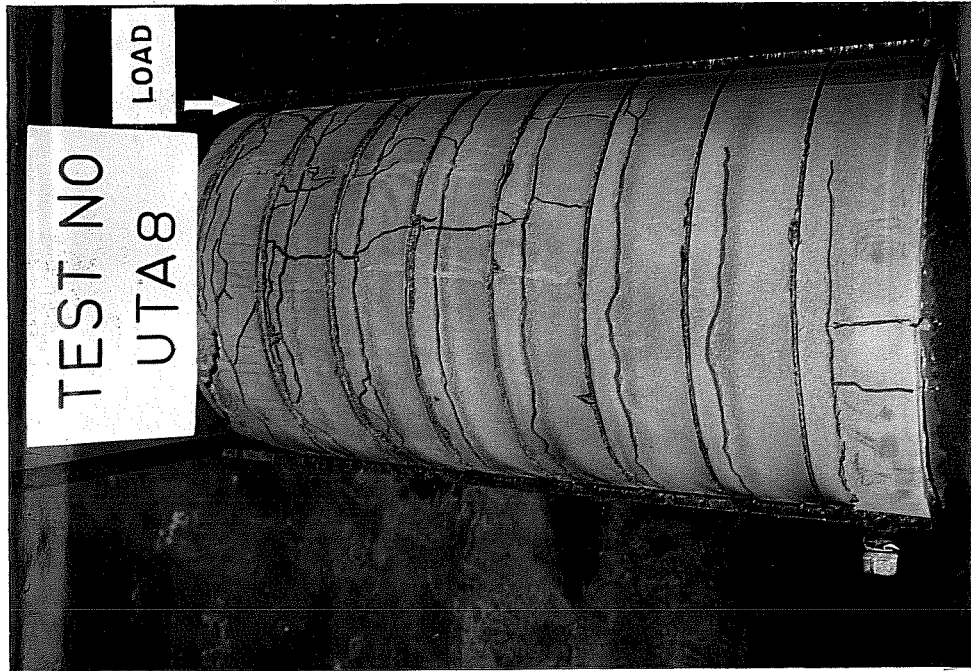


Fig. 3.15 Grout surface on sleeve side for Specimen UTA8

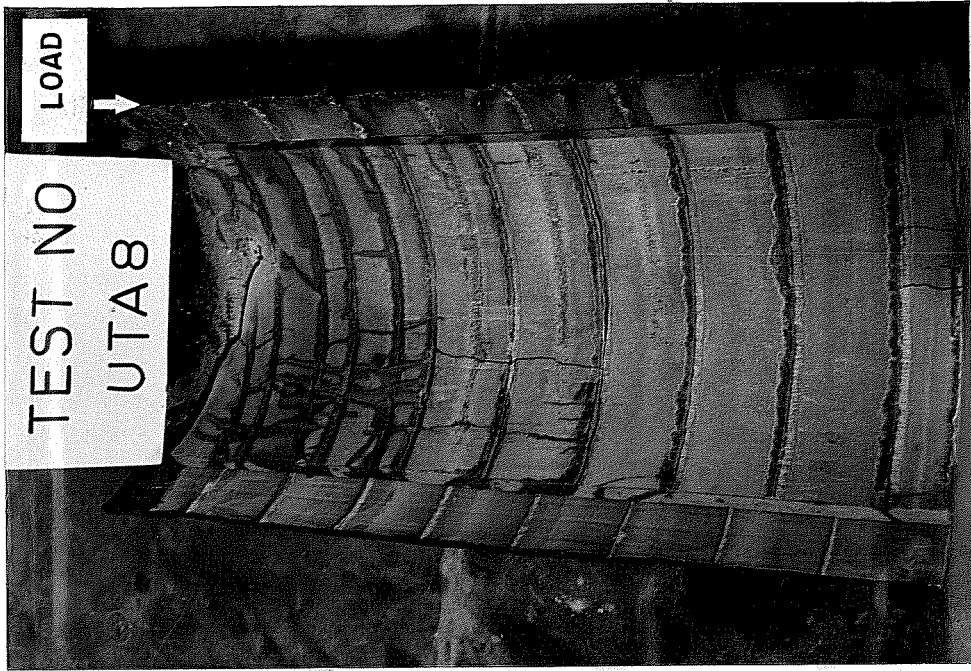


Fig. 3.16 Grout surface on pile side for Specimen UTA8

Figure 3.16 is a view of the pile side of the grout surface. The slippage on the grout surface varied from 5/16 in. (7.9 mm) at the top of the connection to 9/16 in. (14.3 mm) at the bottom. Figures 3.17 and 3.18 show profiles of the grout showing the crack pattern at ultimate, for both the 0.5 in. (12.7 mm) and 1.5 in. (38.1 mm) sides of the annulus, respectively.

3.6.3 Test UTA9. The behavior of specimen UTA9 was similar to UTA7 and UTA8. First noticeable slip occurred at approximately 527 k (2344 KN). The ultimate load obtained was 1106 k (4920 KN) at a relative displacement of 0.26 in. (6.6 mm).

### 3.7 Series 6: High Grout Strength

In Series 6 the behavior of specimens with high strength grout was examined. Other investigators have reported increases in connection capacity with grout strength, therefore, a  $L/D_p$  ratio of 1.0 was used to ensure that the connection capacity did not exceed the test frame capacity. Ultimate load and bond stress results are given in Table 3.8. The grout strength curves for Mix J2 are given in Fig. D-6 of Appendix D. The load-displacement plots, in the form of bond stress versus relative axial displacement between pile and sleeve are shown in Fig. E-16 to E-18 of Appendix E.

3.7.1 Test UTA10. The specimen was tested at an age of 2 days. At this time the grout strength  $f_{cu}$  was similar to specimen



Fig. 3.17 Grout profile of Specimen UTA8 showing crack pattern for side with 1/2-in. annulus

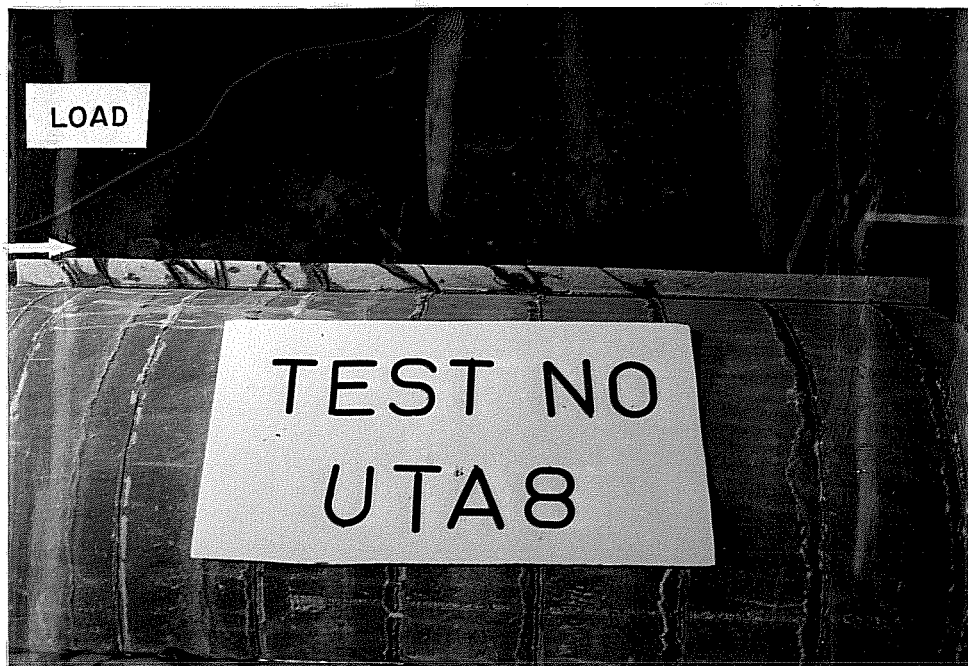


Fig. 3.18 Grout profile of Specimen UTA8 showing crack pattern for side with 1-1/2 in. annulus

TABLE 3.8 Results of Series 6: High Strength Grout

Specimen No.	$f_{cu}$ (psi)	Ultimate Load	$f_{bu}^1$ (psi)	$f_{bu}^2$ (psi)	$f_{bu}^1/\sqrt{f_{cu}}$	$f_{bu}^1/f_{cu}$
UTA10	*6630	*537	*502	*638	*6.17	*0.076
UTA11	11120	720	683	856	6.48	0.061
UTA12	10680	692	656	780	6.35	0.061
MEAN	10900	706	670	818	6.42	0.061
S.D.	311	19.8	19.1	53.7	0.09	0.00
%-DIF	4.0	3.9	4.0	8.9	2.0	0

\* Not included in MEAN, S.D. or %-DIF since these are 2-day results

UTA13, thus increasing the data base for the axial loaded specimens with  $L/D_p$  ratios of one. The behavior was similar to that of other axial loaded specimens. The ultimate load was 537 k (2389 KN) at a relative displacement of 0.17 in. (4.3 mm).

3.7.2 Test UTA11. The specimen behavior was similar to other axial tests although the post-ultimate capacity tended to decrease at a faster rate. The ultimate load was 720 k (3203 KN) with a relative displacement of 0.21 in. (5.3 mm).

3.7.3 Test UTA12. The specimen carried an ultimate load of 692 k (3078 KN) with a relative displacement of 0.24 in. (6.1 mm). The test was stopped at the peak load so that the grout crack pattern at ultimate could be studied. The peak load was taken as that point at which three successive loading increments yielded less than a 1% increase in capacity. Figure 3.19 is a view of the sleeve side of the



grout surface. The slippage on the grout surface along the length of the connection varied very little with a maximum slippage at the top of  $9/16$  in. (14.3 mm) and  $1/2$  in. (12.7 mm) at the bottom. Figure 3.20 is a view of the pile side of the grout surface, slippage along the length varied from  $5/16$  in. (7.9 mm) at the top of the connection to  $1/2$  in. (12.7 mm) at the bottom. Figure 3.21 shows a profile of the grout crack pattern at ultimate.

### 3.8 Measurement of Compressive Strength

At present, a number of different cube sizes are used to determine the unconfined compressive strength of grout. The most common cube sizes are 2-in. (50.8 mm), 3-in. (76 mm), and 4-in. (100 mm). The 2-in. (50.8 mm) cube is the size specified by ASTM 109-80 whereas the 3-in. (76 mm) and 4-in. (100 mm) cubes are standard sizes in the United Kingdom and Norway, respectively.

The recorded strength of a cementitious material has been shown to be dependent upon the size of the test specimen [21]. At the present time, there is no single factor relating the unconfined compressive strength determined from different size specimens; this is due to the fact that the strength is also dependent upon age and mix design. Thus, for Series 3 through 6 both 2-in. (50.8 mm) and 3-in.

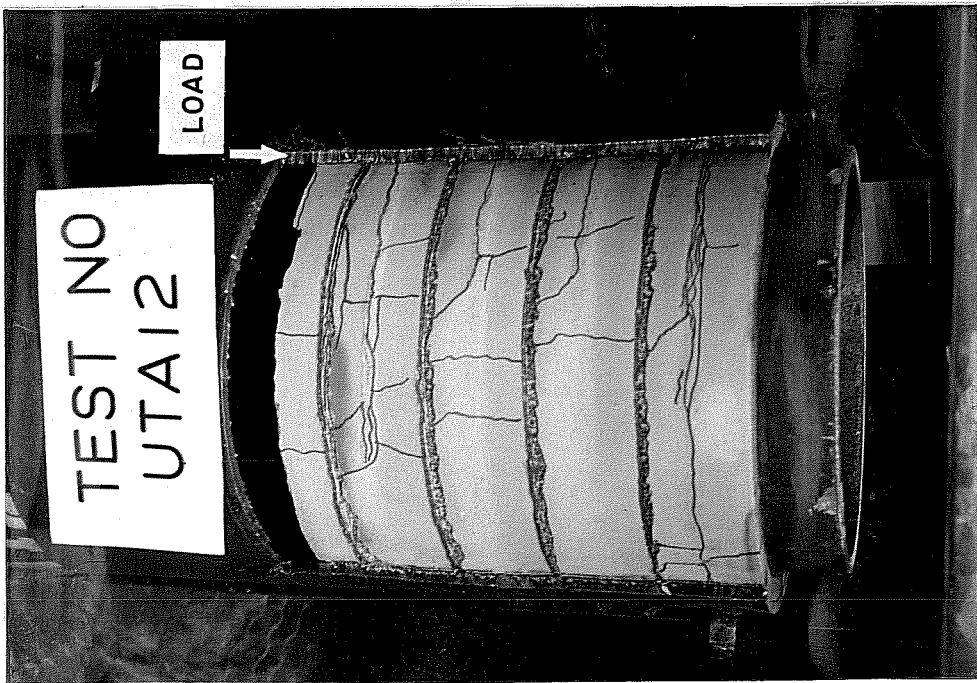


Fig. 3.19 Grout surface on sleeve side for Specimen UTA12



Fig. 3.20 Grout surface on pile side for Specimen UTA12

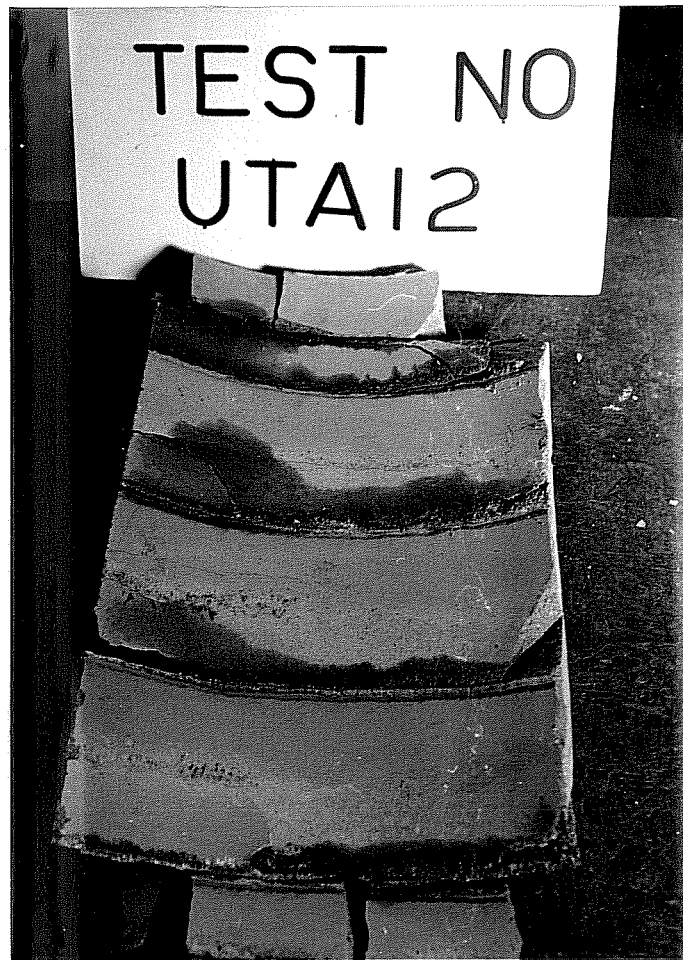


Fig. 3.21 Grout profile of  
Specimen UTA12 showing  
crack patterns

(76 mm) cubes were cast. The results of these strength curve tests are shown in Tables 3.9 through 3.11. The grout strength curve values were determined using the standard three cubes in accordance with ASTM C109-80. Table 3.9 lists the results of cubes using Mix Design I, given in Table 2.3, while Table 3.10 gives the results for cubes using Mix Design J, given in Table 2.4. Table 3.11 gives the comparison at the time of a grouted connection test. In all tables the ASTM C109 2-in. (50.8 mm) cube was used as the basis in establishing the multiplication factors. Although the results do not represent a statistical sampling they are comparable to results by other investigators [21, 33].

### 3.9 Grout Column Cube Results

Figure 3.22 shows a histogram of column cube strength normalized with respect to the ASTM C109 cubes for the six sets of grout columns injected using Mix Design I given in Table 2.3. The results of the individual column cube tests for the six sets of Mix I columns and one set of Mix J columns are given in Figs. D-20 through D-27 of Appendix D.

Table 3.9 Grout Compressive Strength for Mix I: Multiplication Factors with Respect to 2-in. Cubes

Age Days	*Mix 15		*Mix 16		*Mix 17		Ave. Mix I Ratio			
	f <sub>cu</sub> 2-in. cubes (psi)	Ratio 3-in. cubes (psi)	f <sub>cu</sub> 2-in. cubes (psi)	Ratio 3-in. cubes (psi)	f <sub>cu</sub> 2 in. cubes (psi)	f <sub>cu</sub> 3-in. cubes (psi)				
1	556	1058	1.90	1630	2261	1.39	1292	1699	1.32	1.54
3	2612	2761	1.06	3594	3687	1.03	2811	2777	0.99	1.03
7	4697	4640	0.99	4820	5022	1.04	3961	3655	0.92	0.98
14	6755	6676	0.99	5231	5015	0.96	3557	4627	1.30	1.08
21	5987	7190	1.20	5189	5667	1.09	4764	4791	1.01	1.10
28	5357	6196	1.16	6082	5552	0.91	5064	5706	1.13	1.07

\* See Table 2.3, for mix proportions

TABLE 3.10 Compressive Strength for Mix J: Multiplication Factors with Respect to 2-in. Cubes

Age, Days	$f_{cu}$ 2-in. cubes (psi)	$f_{cu}$ 3-in. cubes (psi)	Ratio
1	4581	5000	1.09
2	6630	6690	1.01
7	9214	7053	0.77
14	9648	10263	1.06
21	10350	8377	0.81
28	11381	8846	0.78

See Table 2.4, for mix proportions  
Strength curves were determined using 3 cubes

TABLE 3.11 Compressive Strength: Multiplication Factors on Day of Testing with Respect to 2-in. Cubes

Spec. No.	Ratio	Spec. No.	Ratio	Spec. No.	Ratio	Spec. No.	Ratio
UTA4	1.28	UTA13	1.15	UTA7	1.01	UTA10	1.01
UTA5	1.28	UTM5	1.12	UTA8	1.12	UTA11	0.94
UTA6	1.02	UTM6	1.00	UTA9	1.07	UTA12	0.88

# FCU' COL. CUBES VS. FCU ASTM CUBES

## GROUT MIX: I

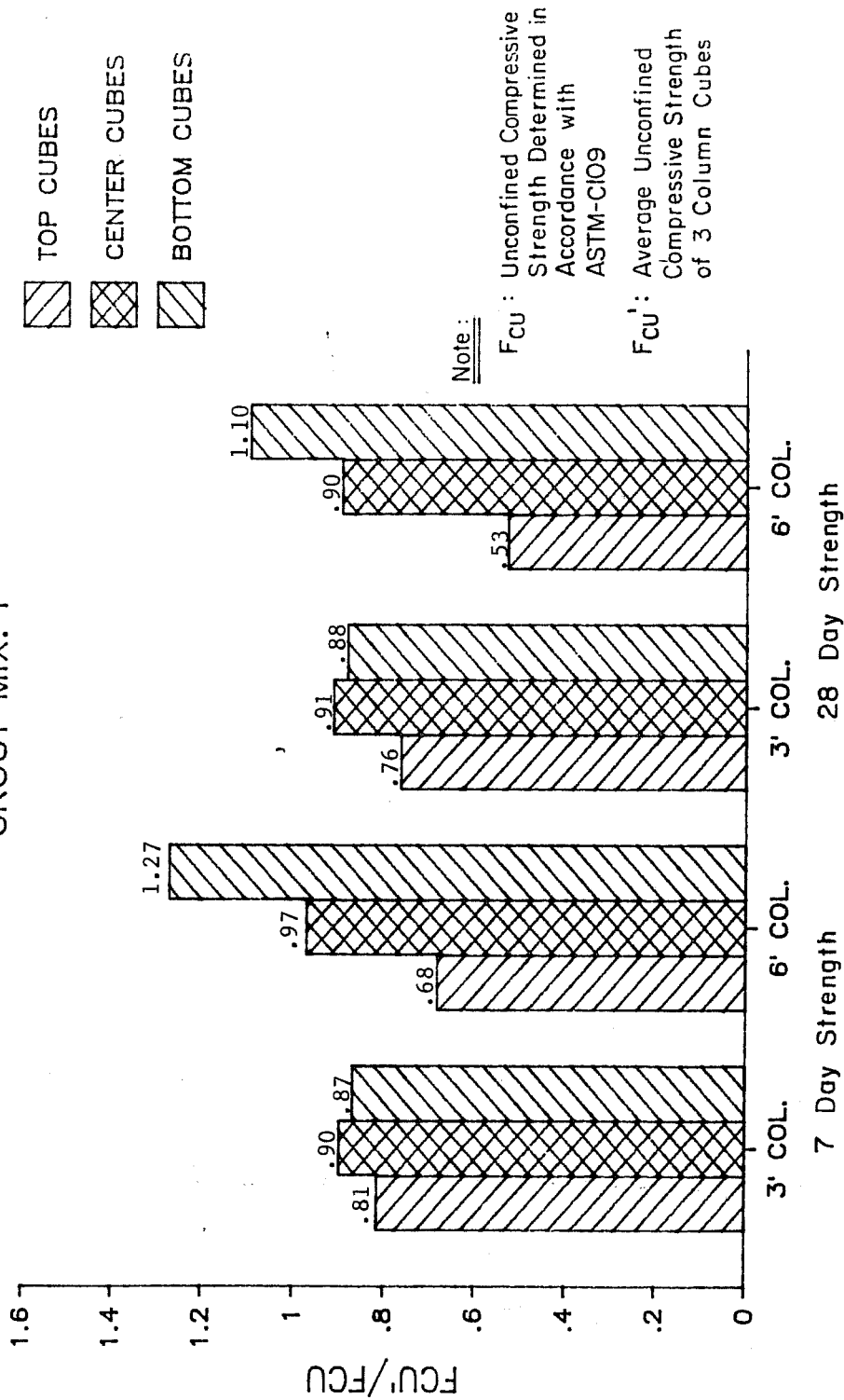


Fig. 3.22 Histogram of pumped grout column cubes vs ASTM C109 cubes for Mix Design I

## CHAPTER 4

### EVALUATION OF TEST RESULTS

#### 4.1 General

Before comparing the measured results with the values predicted by the empirical formulas given by Eqs. 5 and 9 of Chapter 1 the amount of scatter in the experimental  $f_{cu}$  and  $f_{bu}$  values will be discussed. Figure 4.1 shows a plot of the ultimate measured bond stress  $f_{bu}$  vs the unconfined compressive strength,  $f_{cu}$  times  $h/s$  for the 85 shear-keyed specimens listed in Table 2.1 and the seven pure axial specimens tested in the current test program. The figure shows in general that The University of Texas specimens exhibited a slightly higher  $f_{bu}$  for a given  $f_{cu}h/s$ . Other investigators [4,6,21,33] have shown that the grouted connection strength is a function of the tubes radial stiffness. The higher strength indicated in Fig. 4.1 is most likely due to the large radial stiffness of the specimens, as discussed in Section 2.1.2 of Chapter 2.

Figure 4.2 is a plot of  $f_{bu}$  vs  $f_{cu}h/s$  for the 18 specimens reported herein. The plot indicates that for Series 1, 2, 3 and 5 there was very little scatter in the ultimate connection strength for a given series. For the pure axial reference test there was only a 5% maximum difference in ultimate loads of three specimens. Series 2, 3 and 5 had maximum differences of 3%, 13% and 17%, respectively.



# FBU VS. FCU \* H/S

## 92 SPECIMENS WITH SHEAR KEYS

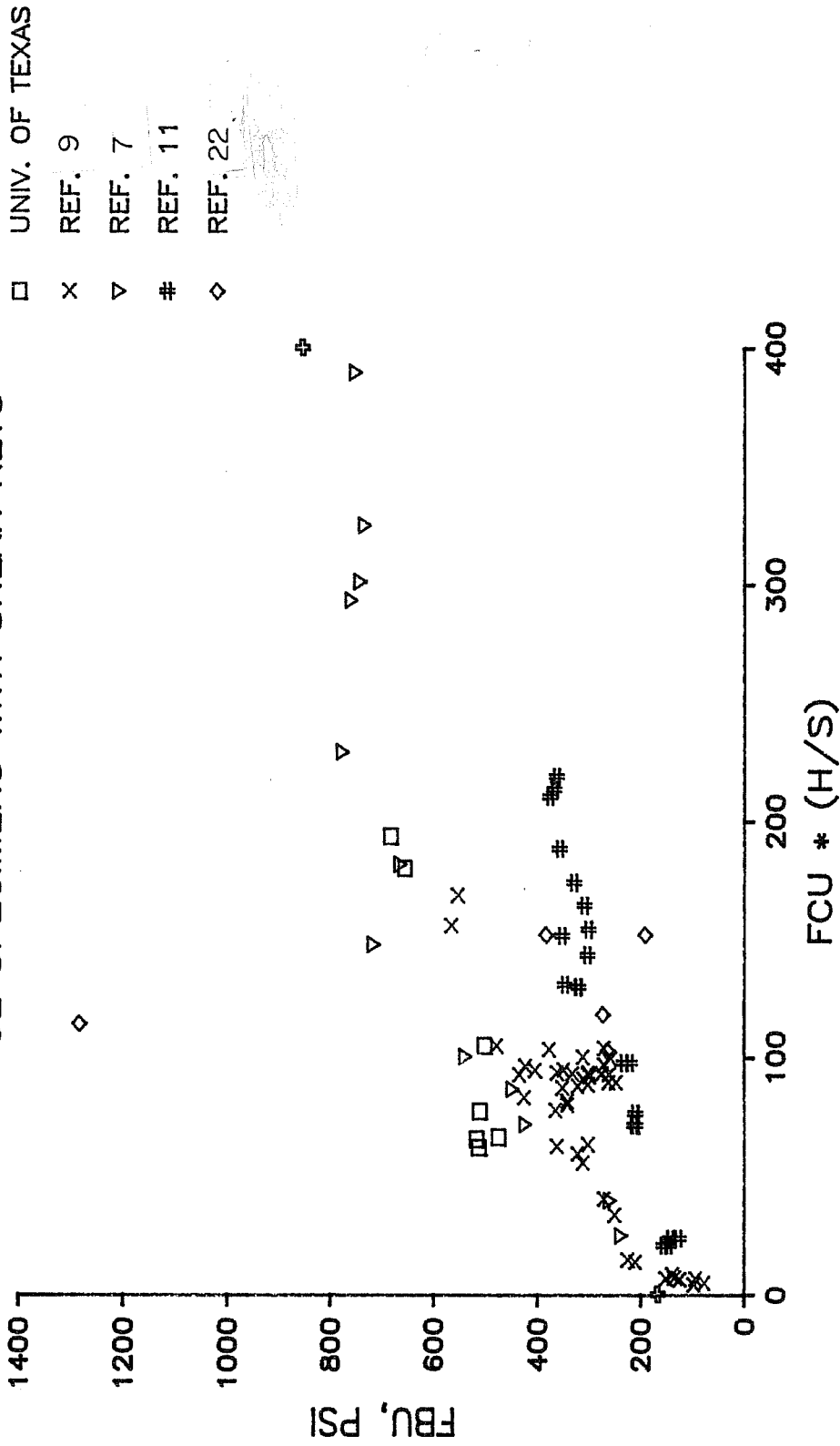


Fig. 4.1 Ultimate measured bond stress vs. unconfined compressive strength times (h/s) for 92 shear-key specimens

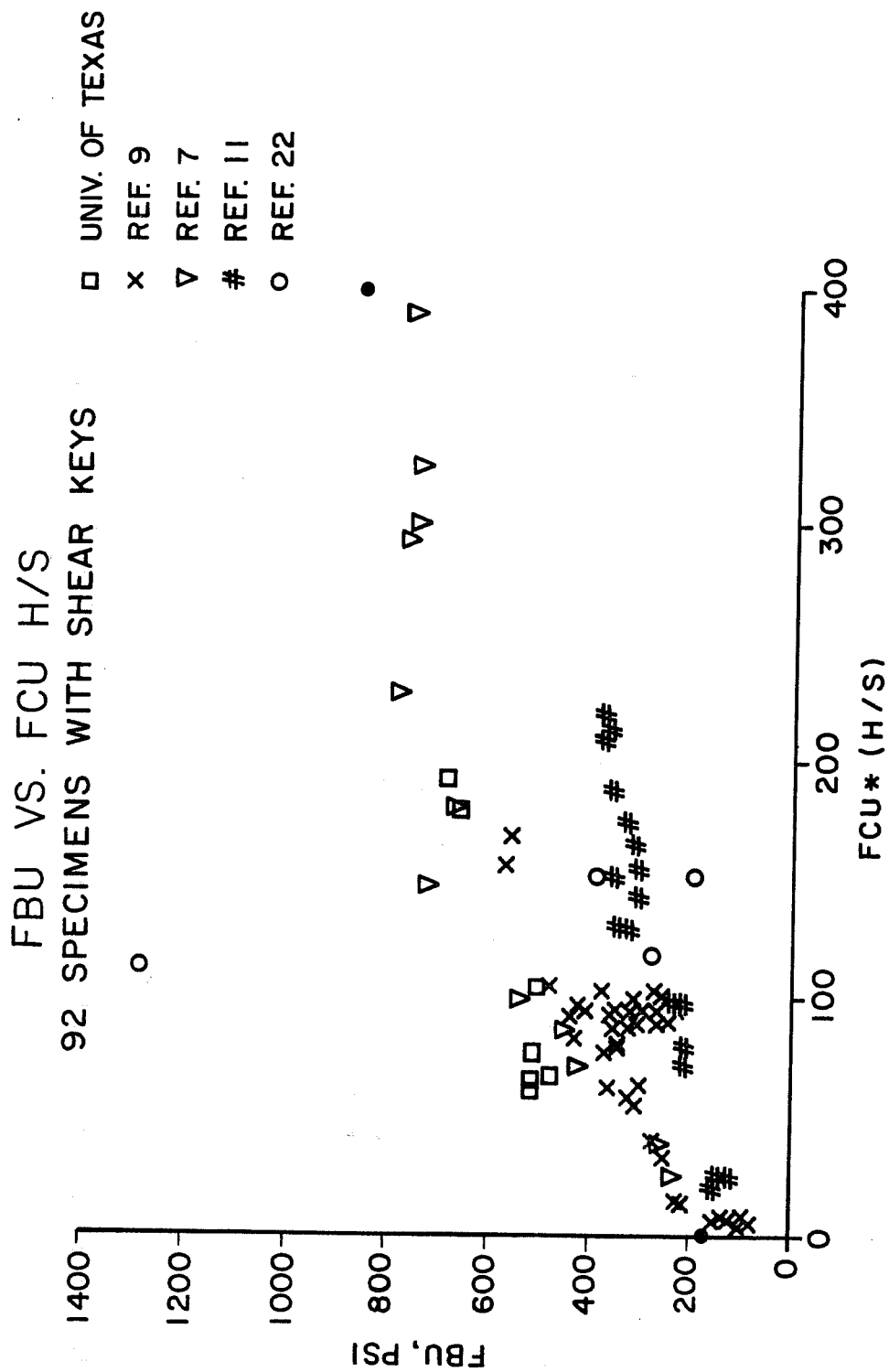


Fig. 4.2 Ultimate measured bond stress vs. unconfined compressive strength times (h/s) for 18 University of Texas shear-key specimens

Series 4 results for Specimens UTM5 and UTM6 indicate significantly higher bond stresses. These results, however, should not be considered as valid ultimate bond stresses since there is a significant length effect for specimens tested under combined loading. A substantial amount of the strength of these connections came from the prying action that developed between the tubes under the action of the applied bending moment.

Series 6 results are also not directly comparable since there was a significant difference in grout strengths. However, Fig. 4.2 does indicate that the grouted connection strength increases with increased grout strength.

#### 4.2 Repeatability Between Tests

Series 1: Reference Tests. This series of tests had three nominally identical grouted connections tested under the same axial loading conditions. Based on 2-in. cubes, the grout strength for the series can be considered constant since there was only a  $\pm 1\%$  variance from the mean value of 3973 psi, the respective scatter for tests UTA1, UTA2, and UTA3 from the mean ultimate bond strength,  $f_{bu}$  of 502 psi, as determined from 2-in. cubes was -5%, +2%, +3%, respectively. Specimen UTM1 should also be compared with this series since the ultimate bond stress is based on axial loading. For this test the

grout strength,  $f_{cu}$ , is 10% higher than the mean value of 3973 psi. The variation of  $f_{bu}$  from the mean is +1%.

Series 2: Combined Loading. The grout strength for Specimens UTM2 and UTM3 varied only  $\pm 1\%$  from the mean value of 4150 psi, established by 2-in. cubes. Specimen UTM1 will not be included here since the ultimate bond stress was based on axial load. The scatter from  $f_{bu}$  was -3% and +3% for Specimens UTM2 and UTM3, respectively.

Comparing Series 2 to 1 indicates that application of combined loading does not adversely effect the ultimate bond stress of the connection. In fact, the mean  $f_{bu}$  for combined loading increased 14% over that for axial load alone. This increase may be due in part to the slight increase in the mean grout strength of about 4%. However, the more likely explanation is that a horizontal force develops during loading due to the relative rotation of the pile and sleeve. As explained in Section 3.5 of Chapter 3, the rotation was very pronounced for the specimens under combined loading with  $L/D_p$  ratios of one.

Series 3: Relative Shear-Key Location. The mean grout strength for Series 3 specimens was 5960 psi, based on 2-in. cubes. The scatter in  $f_{cu}$  was +1%, -5%, and +3% for tests UTA4, UTA5, and UTA6, respectively. The variation from the mean,  $f_{bu}$ , of 671 psi was

-6%, 0%, and +6% for Specimens UTA4, UTA5, and UTA6. Comparison with Series 1 indicates a 34% increase in the mean  $f_{cu}$  for Series 3. The increase in bond strength is due to a 50% increase in  $f_{cu}$ , for Series 3 over Series 1.

Series 4: Length Effect on Combined Loading. The grout strengths for Specimens UTA13, UTM5, and UTM6 varied -8%, +2%, and -6%, respectively, from the mean value of 5360 psi established from 2-in. cubes. Comparison of  $f_{bu}$  for axially loaded Specimen UTA13 ( $L/D_p = 1$ ) with those axially loaded specimens of Series 1 ( $L/D_p = 2$ ) indicates there was a 24% increase in grout strength of UTA13 over the mean grout strength of 3973 psi for Series 1 and yet only a 2% increase in ultimate bond stress,  $f_{bu}$ . When  $f_{bu}$  is normalized with respect to  $\sqrt{f_{cu}}$  and  $f_{cu}$  UTA13 yields 10% and 26% decreases in the ultimate connection strength, respectively. This behavior indicates that there is a length effect for grouted connections with  $L/D_p = 1$ , which decreases the ultimate bond stress.

Specimens UTM5 and UTM6 exhibited significant increases in  $f_{bu}$  (+64%, +41%, respectively) over that for Specimen UTA13. As explained previously, this large increase is believed to be due to a locking force that developed at the ends of these short connections during moment application.

Series 5: Eccentric Pile and Sleeve. The mean grout strength, based on 2-in. cubes for Specimens UTA7, UTA8, and UTA9 was 5040 psi. The scatter in the respective  $f_{cu}$  values from the mean was -6%, -1%, and +6%. The mean  $f_{bu}$  was 583 psi with the scatter in data being +8%, -6%, and -2% for Specimens UTA7, UTA8, and UTA9, respectively.

Comparison of the mean  $f_{bu}$  of 583 psi with the mean  $f_{bu}$  of Series 1 (502 psi) indicates a 16% increase in strength. However,  $f_{cu}$  for Series 5 was 27% higher than Series 1. When the ultimate bond stress is normalized with respect to  $\sqrt{f_{cu}}$  (see Tables 3.3 and 3.7), Series 5 yields a 7% decrease in ultimate connection strength. This scatter is within the expected range of test scatter, thus pile-sleeve eccentric does not have an effect on the ultimate strength of a grouted connection.

Series 6: High Grout Strength. For Specimens UTA11 and UTA12 the mean grout strength,  $f_{cu}$  was 10,900 psi. The scatter of  $f_{cu}$  was +29% for UTA11 and -2% for UTA12. The mean ultimate bond strength,  $f_{bu}$ , was 760 psi, based on 2-in. cube results with scatter of 2%. Comparison with Specimen UTA10 ( $f_{cu} = 6630$  psi) indicates that a 1.64 increase in grout strength caused only a 1.33 increase in  $f_{bu}$ . This implies that  $\sqrt{f_{cu}}$  used in the UK Eq. 5 is a better indicator of the

relationship between the ultimate bond strength and the unconfined compressive strength than  $f_{cu}$  used in API Eq. 9.

#### 4.3 Comparison with Calculated Values

Table 4.1 lists the calculated values of  $f_{bu}$  for each test using mean UK Eq. 5 and API Eq. 9 given in Section 1.2 of Chapter 1. The values are calculated using both 2-in. and 3-in. cubes. In Eq. 5 the value of K was calculated using the modular ratio listed in Table 3.1, and the nominal (D/t) ratios from Table 2.2, the coefficient  $C_s$  was taken a 1.0 for shot-blasted surfaces. The length effect coefficient,  $C_L$ , was taken as 1 for specimens with  $L/D_p$  ratios of 2. For those specimens with  $L/D_p$  ratios of 1, the  $C_L$  value was taken as 0.72 as recommended in Ref. 9.

Table 4.2 lists the allowable values of bond stress,  $f_{ba}$  for each specimen using UK Eq. 8 and API Eq. 10 given in Section 1.2 of Chapter 1. Also, included in Table 4.2 is the factor of safety of  $f_{ba}$  with respect to the measured  $f_{bu}$  for each test. Sample calculations are given in Appendix F.

The results in Tables 4.1 and 4.2 can be summarized as follows:

- For the grout mixes, grout strength, and age of testing used in this test program there is no significant

TABLE 4.1 Comparison of Measured and Calculated  $f_{bu}$  Using Mean Eqs. 5 and 9

Specimen No.	K	Meas. $f_{bu}$ (psi)	Cal. $f_{bu}$ using		Cal. $f_{bu}$ using		Meas. $f_{bu}/Cal. f_{bu}$ 2-in. cubes Eq. 5	Meas. $f_{bu}/Cal. f_{bu}$ 3-in. cubes Eq. 9	Meas. $f_{bu}/Cal. f_{bu}$ 3-in. cubes Eq. 5	Meas. $f_{bu}/Cal. f_{bu}$ 3-in. cubes Eq. 9
			2-in. cubes Eq. 5 (psi)	3-in. cubes Eq. 9 (psi)	2-in. cubes Eq. 5 (psi)	3-in. cubes Eq. 9 (psi)				
UTA1	0.0191	513	510	275	N/A	N/A	1.01	1.87	N/A	N/A
UTA2	0.0190	517	510	276	N/A	N/A	1.01	1.87	N/A	N/A
UTA3	0.0179	475	483	278	N/A	N/A	0.98	1.71	N/A	N/A
UTM1	0.0190	509	535	288	N/A	N/A	0.95	1.77	N/A	N/A
UTM2	0.0178	557	505	287	N/A	N/A	1.10	1.94	N/A	N/A
UTM3	0.0179	586	535	297	N/A	N/A	1.10	1.97	N/A	N/A
UTA4	0.0205	633	675	332	740	365	0.94	1.91	0.86	1.73
UTA5	0.0203	712	684	336	773	383	1.04	2.12	0.92	1.86
UTA6	0.0205	668	710	346	717	349	0.94	1.93	0.93	1.91
UTA13	0.0196	511	422	303	452	323	1.21	1.69	1.13	1.58
UTM5*	0.0197	850	447	318	473	336	1.90	2.67	1.80	2.53
UTM6*	0.0193	704	427	313	427	313	1.65	2.45	1.65	2.25
UTA7	0.0198	631	605	306	607	307	1.04	2.06	1.04	2.06
UTA8	0.0198	548	572	296	606	312	0.96	1.85	0.90	1.76
UTA9	0.0198	571	642	323	664	335	0.89	1.77	0.86	1.70
Mean**							1.01	1.88	0.95	1.80
S.D.							0.086	0.128	0.100	0.157
% C.V.							8.5	6.8	10.6	8.7
UTA10	0.0200	502	499	349	499	351	1.01	1.44	1.01	1.43
UTA11	0.0220	683	740	492	717	472	0.92	1.39	0.95	1.45
UTA12	0.0220	656	726	479	682	443	0.90	1.37	0.96	1.48
Mean**							0.94	1.40	0.97	1.45
S.D.							0.059	0.036	0.032	0.025
% C.V.							6.2	2.6	3.3	1.7

\*Not included in calculation of mean, S.D., or % C.V.  
 \*\*Specimens grouped according to grout mix. First group used Mix I (Table 2.3) and second group used Mix J (Table 2.4)



TABLE 4.2 Comparison of Measured and Allowable Bond Stresses Using UK Eq. 8 and API Eq.10

Specimen No.	Measured $f_{bu}$ (psi)	Allowable Eq. 8 (psi)	Safety Factor	Allowable Eq. 10 (psi)	Safety Factor
UTA1	513	63.8	8.0	51.4	10.0
UTA2	517	63.8	8.1	51.8	10.0
UTA3	475	60.4	7.9	52.2	9.1
UTM1	509	66.9	7.6	55.0	9.3
UTM2	557	63.1	8.8	54.9	10.1
UTM3	586	66.9	8.8	57.8	10.1
UTA4	633	84.4	7.5	67.9	9.3
UTA5	712	85.5	8.3	69.1	10.3
UTA6	668	88.8	7.5	71.9	9.3
UTA13	511	52.8	9.7	59.4	8.6
UTM5*	850	55.9	15.2	63.8	13.3
UTM6*	704	53.4	13.2	62.5	11.3
UTA7	631	75.6	8.3	60.5	10.4
UTA8	548	71.5	7.7	57.6	9.5
UTA9	571	80.3	7.2	65.5	8.7
Mean**			8.1		9.6
S.D.			0.70		0.60
% C.V.			8.6		6.2
UTA10	502	62.4	8.0	73.0	6.9
UTA11	683	92.5	7.4	114.5	6.0
UTA12	656	90.8	7.2	110.8	5.9
Mean**			7.5		6.3
S.D.			0.42		0.55
% C.V.			5.5		8.9

\*Not included in calculation of mean, S.D., or % C.V.

\*\*Specimens grouped according to grout mix. First group used Mix I (Table 2.3) and second group used Mix J (Table 2.4)

difference in the calculated  $f_{bu}$  values when using either 2-in. or 3-in. cubes in Eq. 5 or Eq. 9.

- For normal strength Mix I, Eqs. 5 and 9 yielded an average decrease in the calculated ultimate bond stress,  $f_{bu}$  of 5.8% for the 2-in. (50.8 mm) cubes when compared with the strength obtained using 3-in. (76 mm) cubes, with a range of 0.3% to 13.8%.
- For high strength Mix J the 2-in. (50.8 mm) cubes yielded a calculated ultimate bond stress 2.3 and 3.7% higher from Eqs. 5 and 9, respectively, than those values predicted using 3-in. (76 mm) cubes, with a range of -0.6% to 7.6%.
- The API mean ultimate bond strength formulation given by Eq. 9 is more conservative in all cases. The Wimpey Laboratories mean formulation given by Eq. 5 yields solutions that are in better agreement with the measured values, although the solutions may not always be conservative.
- Allowable,  $f_{ba}$  from both UK Eq. 8 and API Eq. 10 yielded factors of safety greater than the recommended value of 6 for both the normal and high strength grout mixes. However, API Eq. 10 showed a significant difference of

34% between the mean factor of safety for the two mixes, whereas UK Eq. 8 gave similar mean factors of safety for the two mixes.

#### 4.4 Grout Cube Size Effects

As mentioned previously, there are a number of different size test cubes used in the determination of the unconfined compressive strength of grout. Investigators [21,33,34] have shown that the recorded strength from a cube test is a function of size, age and mix design.

A comparison of results listed in Tables 3.9 and 3.10 for the unconfined compressive strength obtained using 2-in. (50.8 mm) and 3-in. (76 mm) grout cubes, showed the following trends.

The most significant strength differences existed in the early stages for the normal strength Mix I. However, as the strength curve flattened out the ratio tended to stabilize with the 3-in. (76 mm) cubes yielding an approximately 8 to 10% higher strength. On the day of testing the unconfined compressive strength of the 3-in. (76 mm) cubes had a 12% higher mean strength, a standard deviation of 0.107 and a coefficient of variation of 9.6% with respect to the 2-in. (50.8 mm) cubes.

The ratio for high strength grout Mix J tended to stabilize with the 3-in. (76 mm) cubes yielding an unconfined compressive

strength approximately 20% lower than that of the 2-in. (50.8 mm) cubes. On the day of testing, Specimens UTA11 and UTA12, the unconfined compressive strength of the 3-in. (76 mm) cubes had a 9% lower mean strength, a standard deviation of 0.042 and a coefficient of variation of 4.7% with respect to the 2-in. (50.8 mm) cubes.

Table 4.3 lists the mean, standard deviation and coefficient of variation of the unconfined compressive strength for all batches of 2-in. (50.8 mm) and 3-in. (76 mm) cubes. The limited results show the coefficient of variation was greater for the 2-in. (50.8 mm) cubes in all cases, except for Mix J at 28 days where the 3-in. (76 mm) cubes had a higher coefficient of variation. The coefficient of variation obtained from these limited sample sizes are comparable with the results obtained by Wimpey Labs [33] using larger sample populations. The Wimpey investigation indicated an average coefficient of variation of 19.5%, with a range of 8.3% to 30.0% on a sample population of 1712 3-in. (76 mm) cubes.

The results of The University of Texas cube tests indicate that the coefficient of variation within a given cube size population is comparable with the coefficient of variation between the 2-in. (50.8 mm) and 3-in. (76 mm) cubes. Also, the percent difference between the unconfined compressive strength determined with respect to the 2-in. (50.8 mm) and 3-in. (76 mm) cubes is comparable with the scatter of the ultimate grouted connection strength obtained from

TABLE 4.3 Summary of Cube Unconfined Compressive Strength Scatter

Mix I	7 day		28 day	
	2-in.	3-in.	2-in.	3-in.
No cubes	21	9	21	9
Mean $f_{cu}$ (psi)	3800	4428	5152	5818
S.D. (psi)	763	736	628	385
% C.V.+	20.1	16.6	12.2	6.6
Mix J				
No. cubes	6	6	6	6
Mean	8646	7032	10988	9931
S.D. (psi)	790	607	605	1166
% C.V.	9.1	8.6	5.5	11.7

tests results. For the specimens tested and grout mixes used in this test program the selection of cube size used for the calculation of grouted connection strength had no significant effect. Furthermore, the test results shown in Tables 3.3 through 3.8 indicated that  $\sqrt{f_{cu}}$  better fit the data than  $f_{cu}$ , which would further reduce the significance of the cube size effect. Until further testing has been done on cube size effects these statements must be qualified by the fact that the unconfined compressive strength results are dependent upon age, and specific mix design and no single factor has been established relating the strength determined from different cube sizes.

#### 4.5 Comparison of Injected Grout Column Cubes with ASTM C109 Cubes

Tables 4.4 and 4.5 give the mean, standard deviation and coefficient of variation at 7 and 28-days for Mix I column pours with respect to the mean of each pour. The locations indicated in the tables correlate with those shown in Figs. 2.21 and 2.22, respectively.

The histogram shown in Fig. 3.22 along with Tables 4.4 and 4.5 indicate the following trends with respect to injected grout cubes vs standard ASTM C109 grout cubes.

- As the height of the grout column increased from 3 ft (914.4 mm) to 6 ft (1828.8 mm), the variation of the unconfined compressive strength through the column height also increased.
- The standard deviation and coefficient of variation of injected grout cubes increased with increasing grout column height.
- The unconfined compressive strengths of the injected grout column cubes were less than those of the ASTM C109 cubes for all locations except the bottom cube sets of the 6-ft (1828.8 mm) columns. These cubes showed a 10% to 30% increase in unconfined compressive strength over that obtained from the ASTM C109 cubes. This increased

TABLE 4.4 Summary of 7-Day Column Cube Results using Mix I

	Nominal 3-ft Column			Nominal 6-ft Column		
	Top	Center	Bottom	Top	Center	Bottom
Mean	0.82	0.90	0.87	0.68	0.97	1.27
S.D.	0.072	0.010	0.066	0.090	0.278	0.221
% C.V.	8.8	11.1	7.6	13.2	28.6	17.3

TABLE 4.5 Summary of 28-Day Column Cube Results Using Mix I

	Nominal 3-ft Column			Nominal 6-ft Column		
	Top	Center	Bottom	Top	Center	Bottom
Mean	0.77	0.91	0.88	0.53	0.90	1.10
S.D.	12.1	0.211	0.141	0.173	0.189	0.309
% C.V.	15.9	23.1	16.0	32.6	21.2	28.1

strength at the lower end of the grout column is consistent with the behavior seen in normal concrete columns where core samples usually indicate stronger concrete at the bottom of the column because of increased density.

- The coefficient of variation of the means of the injected grout column cubes is similar to that obtained for ASTM grout cubes listed in Table 4.3.

#### 4.6 Orientation of Crack Patterns in Tested Specimens

Figure 4.3 shows a profile schematic of the crack pattern observed for axial specimen UTA2, as shown in Fig. 3.4. The cracks shown in the figure are those that were observed at final displacement and not at the ultimate load. The grout strength of UTA2 was  $f_{cu} = 3970$  psi. The schematic indicates that cracks formed at the shear key locations on the pile or sleeve and ran across the 1-in. grout annulus at approximately a  $60^\circ$  angle from the horizontal. The range of measured angles was from  $27^\circ$  to  $68^\circ$  with an average inclination of  $50^\circ$ . Both Figs. 4.2 and 3.4 show that a series of grout compression struts developed between the shear keys which enabled the sleeve to transfer the load into the pile or vice versa. The grout which had formed the compression struts was completely



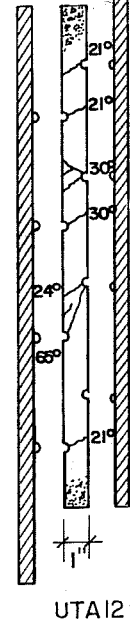
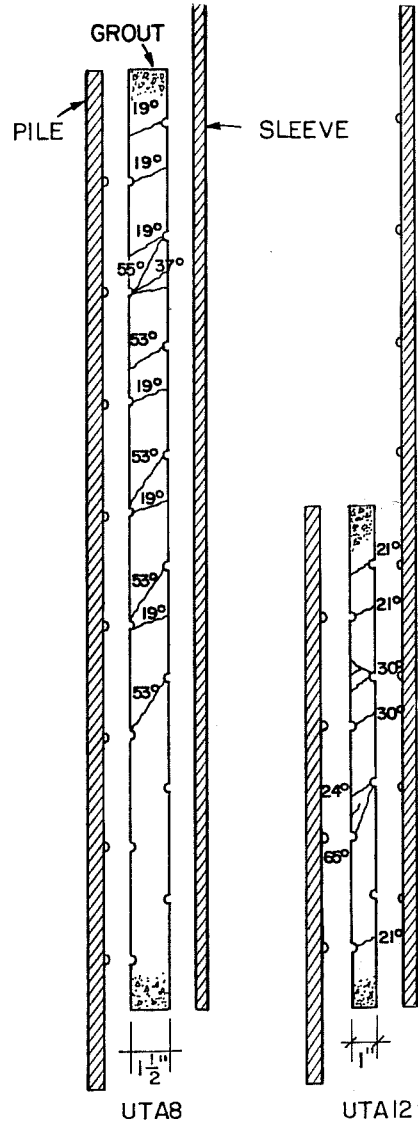
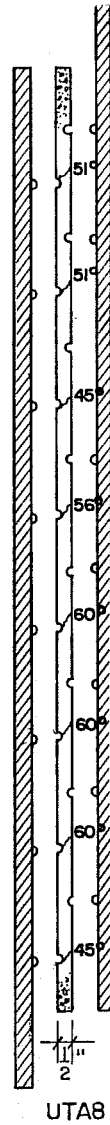
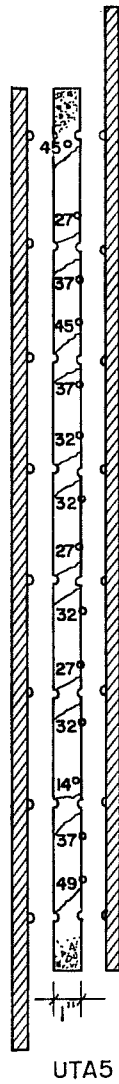
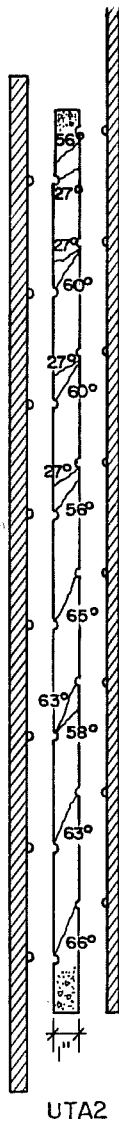


Fig 4.3

Fig. 4.4

Fig. 4.5

Fig. 4.6

Fig. 4.7

Schematic drawings showing crack orientation for Specimens UTA2, UTA5, 1/2" annulus side of UTA8, 1-1/2" side of UTA8 and UTA12

crushed at final displacement whereas the grout between the struts showed almost no noticeable damage.

Figure 4.4 shows a profile schematic of UTA5's crack pattern at ultimate load, shown in Fig. 3.10, where the ultimate load is defined as that load at which three successive load increments caused less than a 1% increase in load. For this specimen of Series 3 the shear keys were placed directly across from each other as described in Section 2.1.1. UTA5 had a grout strength of  $f_{cu} = 5780$  psi. The cracks initiated at the shear key locations on the pile and sleeve and propagated across the grout annulus at an average inclination from the horizontal of  $35^\circ$  with a range of  $14^\circ$  to  $51^\circ$ . It is important to note that the cracks did not run from shear keys on the pile to those on the sleeve or vice versa, indicating that the orientation of the cracks in a grouted connection is not controlled by the relative location of the shear keys on the pile and sleeve.

Specimen UTA8 had eccentrically placed tubes as explained in Section 2.1.1. Figure 4.5 and 4.6 show profile schematics of the crack patterns for the 1/2" and 1-1/2" side of the annulus at ultimate load, as defined previously. These patterns correspond to those shown in Figs. 3.17 and 3.18. Figure 4.5 shows the crack pattern for the 1/2" annulus. On this side of the annulus the cracks had an average angle of inclination of  $55^\circ$  with a range of  $45^\circ$  to  $60^\circ$ .

On the side with the 1-1/2" annulus, Fig. 4.6, the average angle of inclination was  $38^\circ$  with a range from  $19^\circ$  to  $53^\circ$ . On this side, however, there seemed to be both primary cracks and secondary cracks which developed at a lower angle of inclination. When considering only the primary cracks the average angle of inclination was approximately  $53^\circ$ , while the secondary cracks had an average inclination of about  $20^\circ$ . If the secondary cracks are ignored the resulting crack profiles indicate that crack inclination is independent of annulus width for the two widths examined here. The results also further the trend which was observed between UTA2 ( $f_{cu} = 3973$  psi) and UTA5 ( $f_{cu} = 5780$  psi), that the inclination of the crack in the grout annulus is dependent upon the grout strength with a higher grout strength causing a lower inclination of crack.

Figure 4.7 shows the schematic of the crack profile shown in Fig. 3.21 for specimen UTA12, with a 1" grout annulus. Again this crack profile is the crack pattern at ultimate load as defined previously. UTA12 had a grout strength of  $f_{cu} = 10680$  psi. The average crack inclination was 24 with a range of approximately 21 - 30, again indicating that there is a decrease in crack orientation with increasing grout strength. All cracks initiated at the shear key locations and propagated across the annulus independent of the shear key location on the other tube.

Of the specimens which were examined no two were exactly alike in all respects except for grout strength. Consequently, no final conclusion will be drawn with regard to the relationship between crack orientation and grout strength.

Based on the above discussion the following conclusions may be drawn about crack patterns in grouted connections.

- The cracks at the shear key locations formed grout compression struts which acted as a mechanism to transfer load between the steel tubes.
- Inclination of annulus cracks is independent of relative shear key location between the sleeve and pile.
- Angle of cracking in the grout is independent of grout annulus thickness for the range of thicknesses examined in this investigation.

## CHAPTER 5

### PREDICTING ULTIMATE AXIAL STRENGTH OF GROUTED CONNECTIONS

#### 5.1 General

The development of an analytical model to predict the ultimate strength of a grouted connection is a substantial task. The analytical model must account for the many factors which affect connection strength, e.g. the elastic and inelastic deformations of the grout which is subjected to triaxial states of stress, the load transfer mechanism and connection geometry. Indeed, grouted connection failure is a complex phenomenon and the tendency towards empirical models rather than theoretical solutions is understandable.

Empirical models can accurately predict the ultimate strength, if a large valid data base exists and the parameters used to describe the behavior are selected judiciously. The parameters affecting grouted connection strength and two recent empirically determined strength equations were discussed in Chapter 1. Empirical equations such as these could become obsolete as the data base changes. Analytical solutions are not a function of any data base and therefore indicate theoretically which parameters are significant to behavior. Experimental data, however, must support a theoretical solution for it to be valid. The purpose of this chapter is to isolate the principal components of the ultimate static axial strength of grouted connections through the use of a simple analytical

model. Once the proper constitutive equations governing the grouted connection behavior have been determined or developed, more refined models using techniques such as the finite element method can be justified. The experimental data from the investigation described in the preceding chapters along with other investigators' data are used to determine the validity of the proposed analytical model. Finally, suggestions are given for further research that would aid in understanding grouted connection behavior.

## 5.2 The Failure Mechanism

The axial load transfer mechanism of a grouted connection can be considered as the sum of two basic components. These components are:

- Coulomb friction: when  $\tau < \mu\sigma_n$ , where  $\tau$  is the shear stress which develops at the grout-steel interface,  $\sigma_n$  the normal compressive stress which develops due to the confinement of the grout by the steel tubes and  $\mu$  the coefficient of friction.
- Grout compression struts: grout compression struts develop at the shear key locations and transfer load from the sleeve (pile) to the pile (sleeve). As discussed in Section 4.6, the size and inclination of

these grout struts is a function of shear key spacing,  $s$  and grout strength,  $f_{cu}$ .

Adhesive bond could be included, however, the adhesive bond which develops at the steel-grout interface can be considered insignificant in comparison with the other two components and once exceeded plays no further role in the strength of the connection, therefore it will be neglected.

Development of the load transfer mechanism begins after adhesion at the grout-steel interfaces is exceeded. At the top end of the connection the sleeve is carrying the entire load. Cracks initiate at the lower side of the shear key on the sleeve and extend across the annulus until they reach the pile surface. At the lower end of the connection a similar process occurs; however, here the cracks initiate at the top side of the shear-keys on the pile and extend across the grout annulus to the sleeve surface, see Fig. 5.1a. As discussed in Section 4.6 the angle of inclination of these cracks is a function of the grout strength,  $f_{cu}$ , and is not a function of the relative spacing between the pile and sleeve shear keys. The initial development of cracks and the breakdown in the adhesive bond corresponds to initial slip on the load-deflection plots shown in Appendix E.

In the next stage of development of the load-carrying mechanism, cracks develop at other shear key locations along the

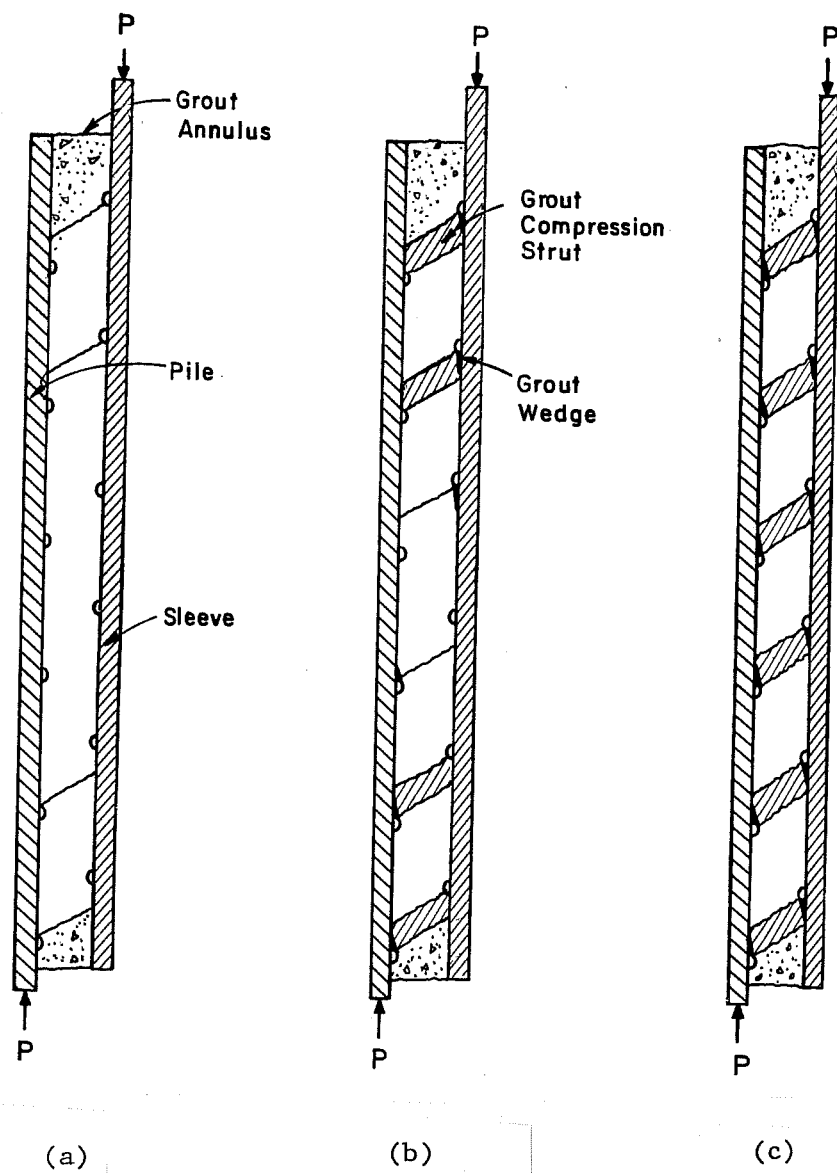


Fig. 5.1 a) Idealized stage 1 development of failure mechanism  
 b) Idealized stage 2 development of failure mechanism  
 c) Idealized stage 3 development of failure mechanism



length of the connection creating compression struts in the grout which transfer a major portion of the load between the steel tubes. As the load increases, grout at the ends of the struts begins to crush and form wedges at shear key locations where stresses are highest, see Fig. 5.1b. The Coulomb friction component increases as normal forces at the boundary increase due to the increase in axial stress in the grout and development of a wedging action from the grout compression struts. Wedges of grout continue to form at shear key locations throughout the length of the connection as load increases. Once these wedges have developed throughout the length of the connection, as shown in Fig. 5.1c, the tubes begin to slip significantly relative to each other and the ultimate strength of the connection has been obtained.

Grouted connection strength is governed by crushing of the grout at the tips of the compression struts and not by failure of the strut itself. Connection capacity is directly related to the state of triaxial stress in the grout. Based on this failure mechanism and results from other investigations, an analytical model should include the following main parameters:

- Radial connection stiffness
- Grout strength and stress state
- Shear key height
- Shear key spacing

The data which is presently available does not include all the required material and geometric properties for a given set of tests to predict ultimate strength. Consequently, a qualitative examination of each of the parameters will be used to establish reasonable bounds of their effects on the ultimate strength of a grouted connection.

### 5.3 Qualitative Effects of Parameters Affecting Grouted Connection Strength

5.3.1 Radial Connection Stiffness. The steel tube geometry of a grouted connection is important since it determines the amount of lateral confinement in the grout. Many experimental investigations have shown that the compressive strength of a cementitious material increases with increasing confinement.

In an actual grouted connection, the pile thickness is usually significantly greater than the sleeve thickness as discussed in Chapter 1. Consequently, the radial stiffness of the sleeve is the most important component in determining the amount of lateral confinement in the grout.

For the load application method used by Wimpey Labs [10], with the pile in tension and the sleeve in compression, Chivlers [27] assumed that, due to Poisson's effect, there is a decrease in confinement of the grout, thus causing a decrease in connection strength. The series A tests described in Section 1.4.2.1, however, do not substantiate this assumption and, in fact, indicate that

Poisson's effect is minimal, with the results of the different load applications being well within the expected scatter of the data. The method of load application used in experimental investigations is to apply the load directly to the ends of the specimen whereas in an actual grouted connection the load is transferred over a finite distance via shear plates or structural brace(s), which further reduces Poisson's effect. In the development of the analytical model, Poisson's effect will be considered as a secondary effect which can be neglected without significantly affecting the results. Thus the level of confinement of the grout along the length of a grouted connection may be considered constant.

Figure 5.2 illustrates the effect of radial connection stiffness on the ultimate strength of a grouted connection. The data represent the results of 24 tests (Series P and R) performed at Wimpey Labs [34] in which all parameters were kept constant except for the tube wall thickness. The abscissa represents the connection stiffness,  $K$ , as defined in Eq.4 of Section 1.3.1. The ordinate represents the ultimate bond stress,  $f_{bu}$  normalized with respect to  $\sqrt{F_{cu}}$ . Engineers at Wimpey assumed that for the range of data investigated there was a linear increase in grouted connection strength with an increase in radial connection stiffness. Figure 5.2 indicates that, for the range of radial stiffnesses investigated,

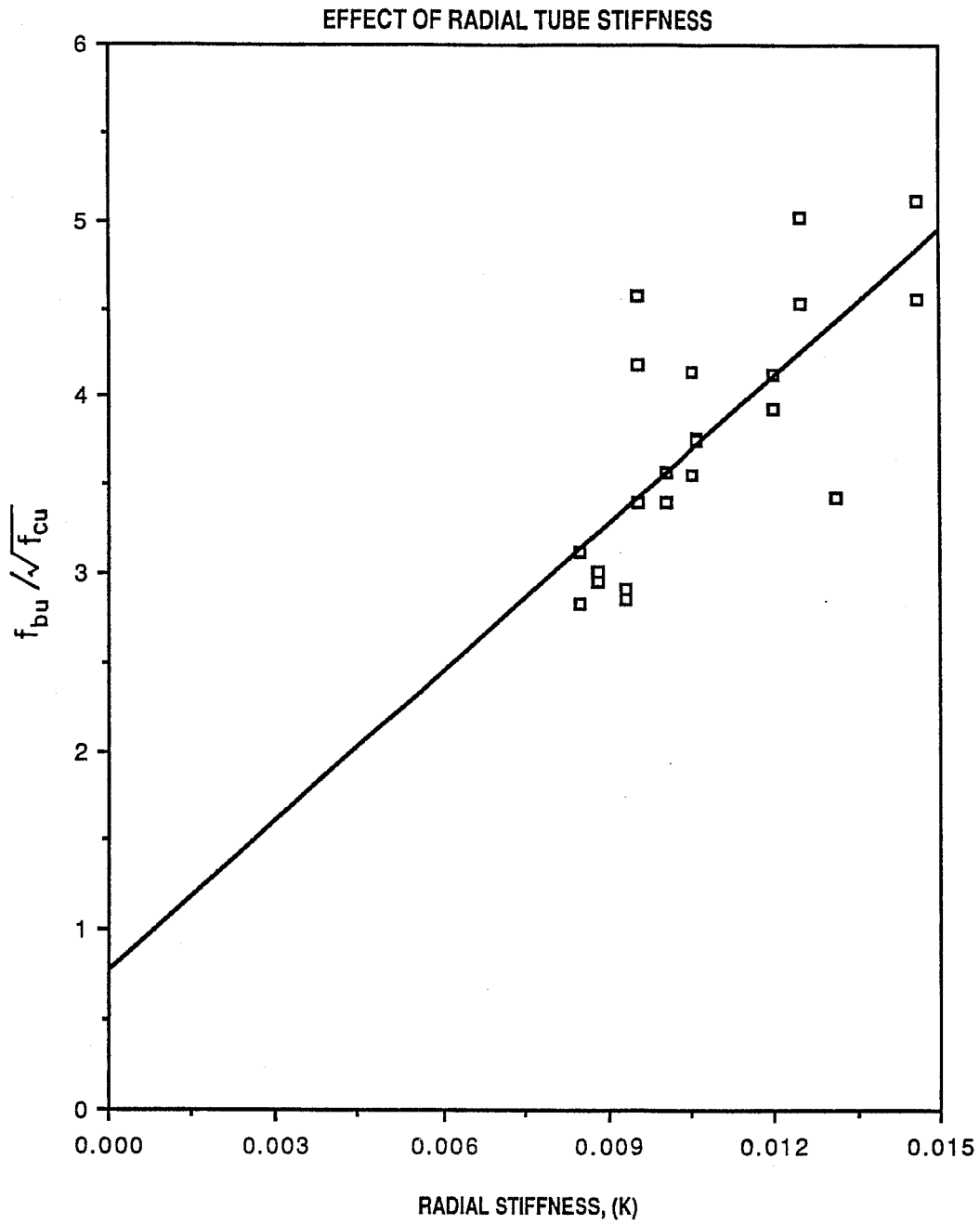


Fig. 5.2 Effect of radial connection stiffness on ultimate bond strength for Wimpey Labs series P and R

doubling the radial stiffness approximately doubles the ultimate grouted connection strength.

An infinitely stiff tube represents an upper bound in which the highest stresses would develop in the grout. It may be assumed that the steel tubes need be considered only infinitely stiff relative to the grout which becomes less stiff as the load approaches ultimate. The level of radial stiffness required for a tube to be considered infinitely stiff is a function of grout strength, shear key height and spacing.

A lower bound on the effect of radial stiffness on the connection strength is represented by a flexible sleeve which offers little or no lateral confinement to the grout. For this type of system failure occurs when the axial compressive stress in the grout approaches the unconfined compressive strength,  $f_{cu}$ .

5.3.2 Grout Strength. In Fig. 5.3 the effect of ultimate bond stress,  $f_{bu}$  versus increasing grout strength,  $f_{cu}$  is shown for seven axial tests performed at The University of Texas and reported in Chapter 3. The figure clearly indicates that there is an increased connection capacity with increased grout strength. Investigators at Wimpey Labs [34] have stated that this relationship can be expressed as a function of  $f_{cu}$ , as shown in Fig. 5.4. The upper bound on the effect of grout strength is controlled by limitations on development

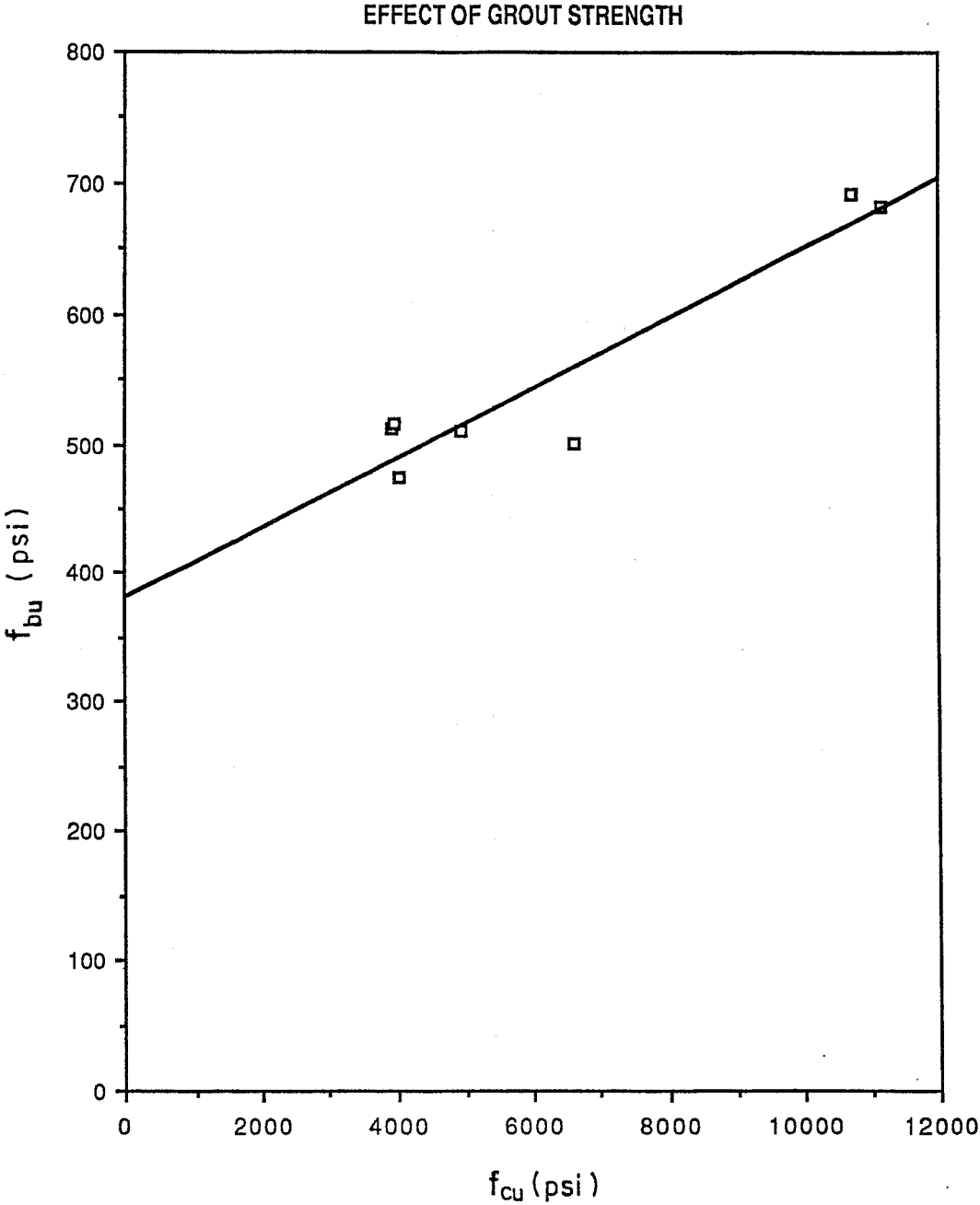


Fig. 5.3 Effect of grout strength on ultimate bond strength for seven University of Texas axial specimens

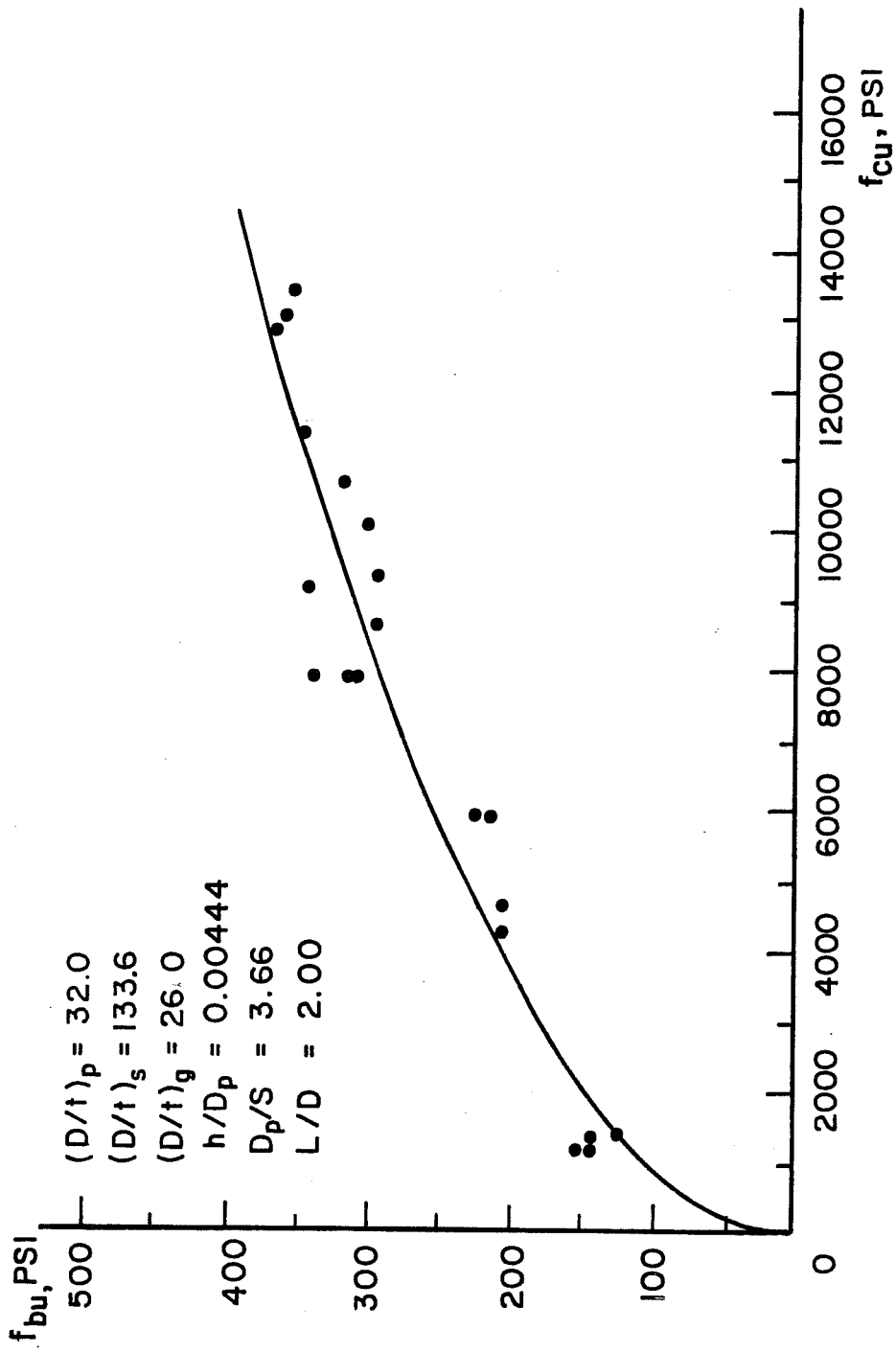


Fig. 5.4 Parabolic relationship between ultimate bond strength and cube strength

of a workable high-strength mix. An analytical model should include the effect of grout strength and, based on experimental results, predict increases in ultimate connection strength which is between  $\sqrt{f_{cu}}$  and the  $f_{cu}$  for a given increase in grout strength.

5.3.3 Shear Key Height. The lower bound on shear key height would be the plain pipe connection where all the load is carried by Coulomb friction that develops at the steel-grout interface. The upper limit on shear key height would theoretically be one-half the annulus width. However, in practice, the actual height would be considerably less to allow for field clearance during pile installation.

At Wimpey Labs [34] three pairs of specimens (R1-R4, R9-R10) with differing  $h/D_p$  ratios were tested, but all other geometric parameters were constant. Figure 5.5 shows the ultimate bond stress,  $f_{bu}$  normalized with respect to  $\sqrt{f_{cu}}$  versus the  $h/D_p$  ratios. The figure indicates a linear relationship between ultimate connection strength and the shear key height, for the range of data shown.

As the height of the shear key increases, the bearing stress in the grout at the key reduces. Also, the size of the grout wedge which forms before failure can occur increases.

If the shear key height is increased, while all other parameters are kept constant, the magnitude of the shear stress which



## EFFECT OF SHEAR KEY HEIGHT

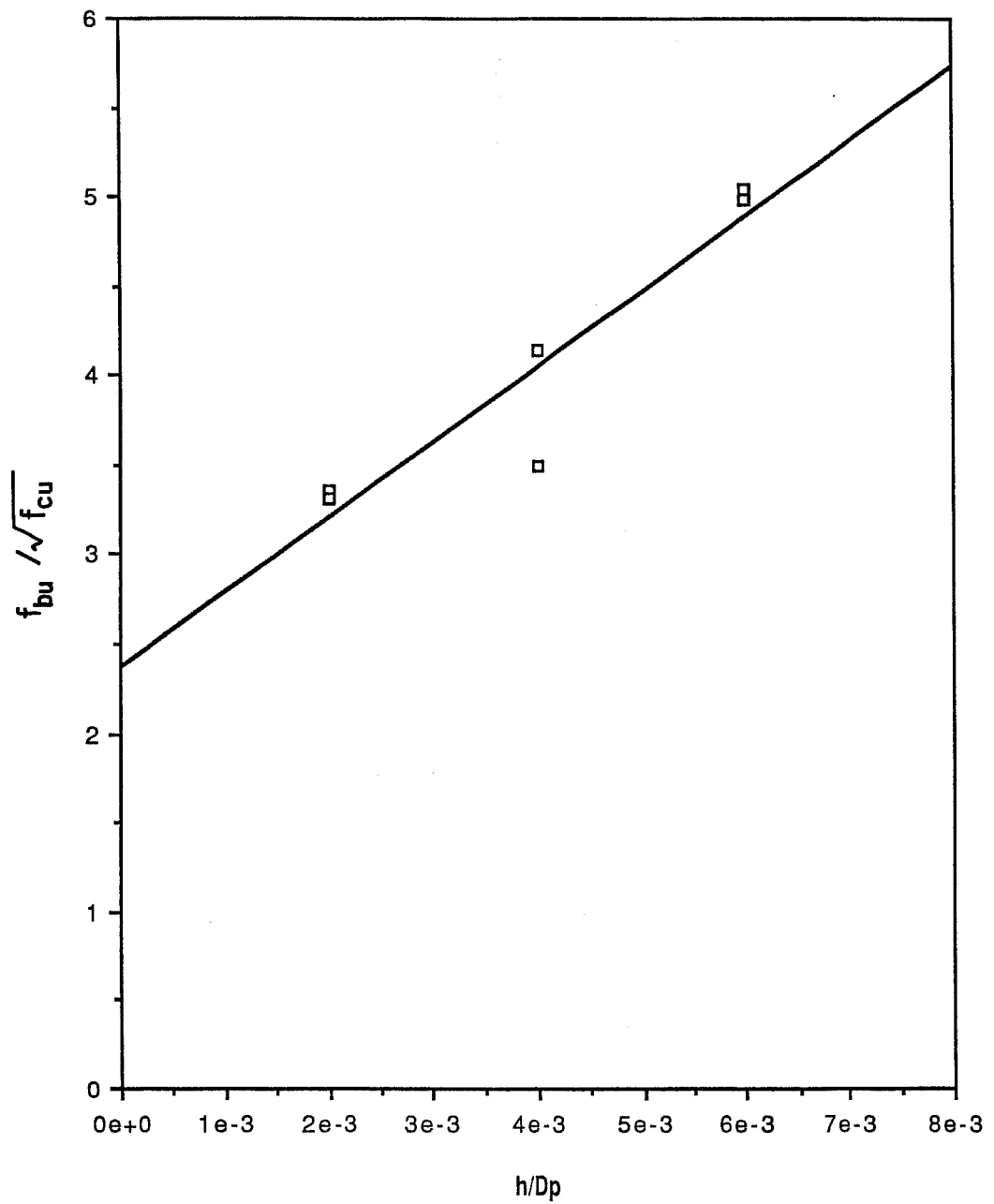


Fig. 5.5 Effect of shear key height on ultimate bond strength for Wimpey Labs series R

develops in a grout strut will increase. At some point, this combination of key bearing stress and increasing shear stress, due to increasing shear key height will cause a decrease in grouted connection strength. In an analytical model, the critical combination of stress causing failure in the confined grout should be considered. The stress state will be a function of the radial stiffness, grout strength and shear key spacing.

5.3.4 Shear Key Spacing. If the spacing between shear keys is infinite the grouted connection is a plain tube which relies totally on Coulomb friction at the steel-grout interface. The strength of the connection is a function of the surface roughness of the steel tubes, shrinkage/swell characteristics of the grout and the radial connection stiffness. When shear keys are added, the strength of the connection increases, since the strength of the connection no longer relies totally on Coulomb friction but on the mechanical action of the shear keys and the development of the grout compression strut mechanism. The shear keys, also, cause the Coulomb friction to increase due to the wedging action of the compression struts against the steel tubes.

If the shear key spacing is reduced while all other geometric parameters are kept constant, the capacity of the connection increases since more compression struts can develop. Wimpey Labs [34] performed a series of six tests (Q1-Q6) using three pairs of specimens

with different shear key spacings but with all other geometric ratios kept constant. The results are shown in Fig. 5.6, with the ultimate bond stress  $f_{bu}$  normalized with respect to  $\sqrt{f_{cu}}$  versus  $D_p/s$ . Within the range of shear-key spacings examined, there is a linear increase in ultimate connection strength with decreasing shear key spacing. Yet, as the shear-key spacing continues to decrease there should be some point at which the strength will begin to decrease. For example, if the shear keys were placed continuously along the length of the connection the strength of the connection should again roughly coincide with a plain pipe connection whose surface roughness would be a function of the shear key height. Based on this concept there is an optimum shear key spacing which will maximize the ultimate strength of the grouted connection. An analytical model should therefore predict such a point for a given set of geometric parameters.

5.3.5 Summary of the Effect of Basic Parameters Affecting the Ultimate Strength of Grouted Connections. The previous discussions have indicated that the ultimate strength of a grouted connection is dependent upon four basic parameters. These parameters are the radial stiffness, grout strength, shear key spacing and the shear key height. Though all parameters have certain limits of applicability, the following general statement may be made for

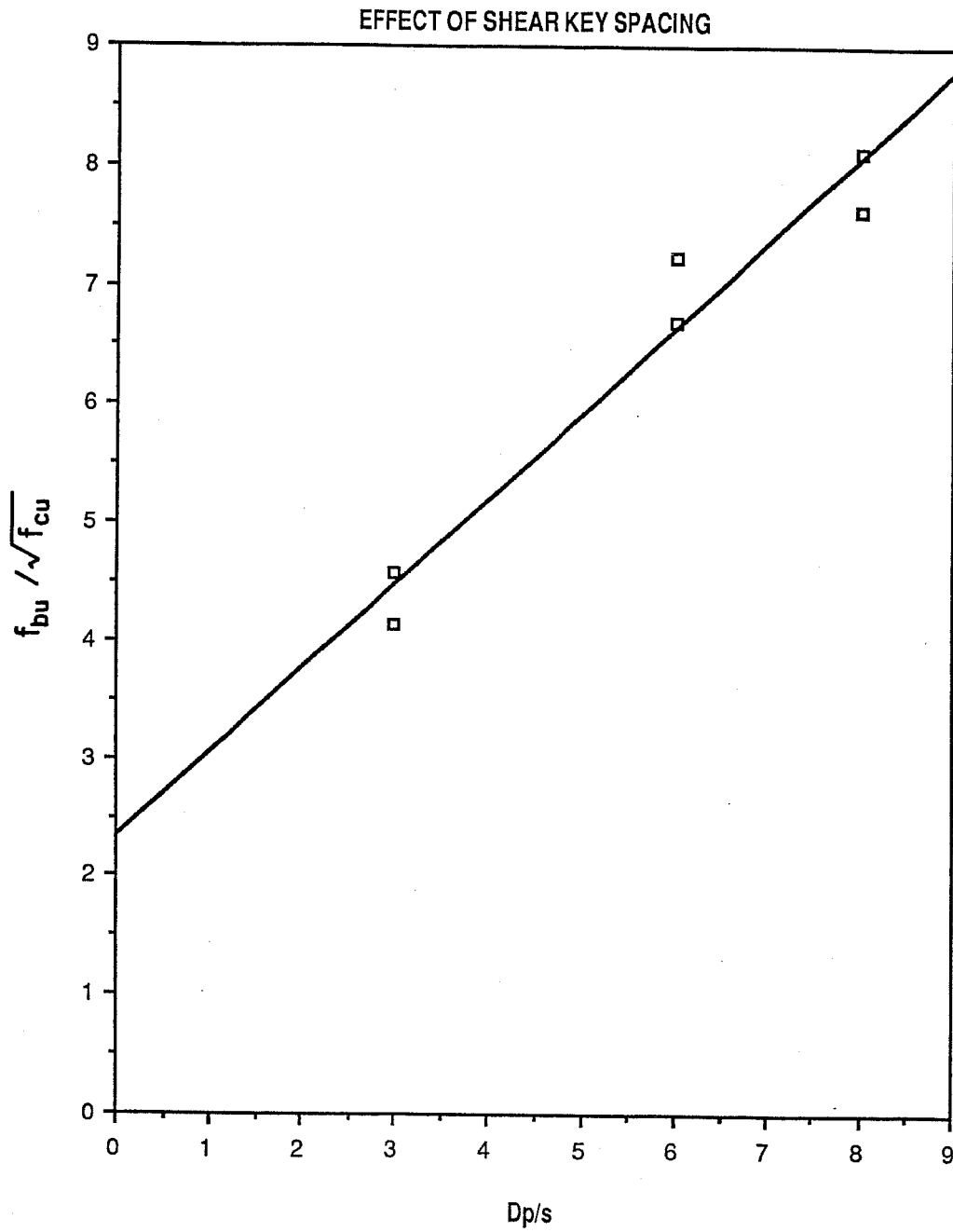


Fig. 5.6 Effect of shear key spacing on ultimate bond strength for Wimpey Labs series Q

grouted connections within the range of practical limits: increasing radial stiffness, grout strength, shear key height and/or decreasing shear key spacing will increase the ultimate strength of a grouted connection. The formation of a grout wedge followed by sliding or failure by shearing along some plane is dependent upon these parameters.

#### 5.4 Modeling the Grouted Connection

As discussed previously the axial load transfer mechanism of a grouted connection can be divided into two load-resisting components: the Coulomb friction that develops along the length of the connection due to the normal forces in the grout and the grout compression struts. The exact distribution of normal stresses and corresponding frictional forces along the length of the connection is extremely difficult to access. An examination of specimen UTA2, shown in Fig. 3.3, indicated that the grout between the compression struts had no noticeable damage. The amount of normal and frictional stress developed in this region is probably relatively low when compared with the stresses developed in the strut region. The Coulomb friction load will therefore be considered to be transferred over the depth of grout compression strut at the steel-grout interface.

In an attempt to simplify the analysis of the grouted connection it will be assumed that at ultimate load all grout compression struts will carry exactly the same ultimate load. This

allows the model to consist of only one strut and the total contribution from all struts can be obtained by multiplying the load per strut times the total number of struts in the grouted connection. Figure 5.7 shows the single grout compression strut which will be used in the development of the analytical model.

Figure 5.8 is an exploded view of Fig. 5.7 showing the forces on the grout compression strut. In the analysis all bending effects will be ignored. The inclination and width of a strut is controlled by the grout compressive strength,  $f_{cu}$  and the spacing of the shear keys. In the discussion to follow the shear keys will be assumed to be staggered as shown in Fig. 2.2a of Chapter 2.

The force  $P_k$  in Fig 5.8 represents the contribution to strut strength due to shear key action. The force  $P_f$  represents the strength due to Coloumb friction which is a function of the normal force,  $N$  and the coefficient of friction  $\mu$  for the steel tubes. The total strength of an individual strut is

$$P_i = P_k + P_f \quad (26)$$

The key contribution  $P_k$  will be calculated using the constitutive relations developed in the following sections. Using Fig. 5.8 with the frictional force,  $P_f$  given as

$$P_f = \mu N \quad (27)$$

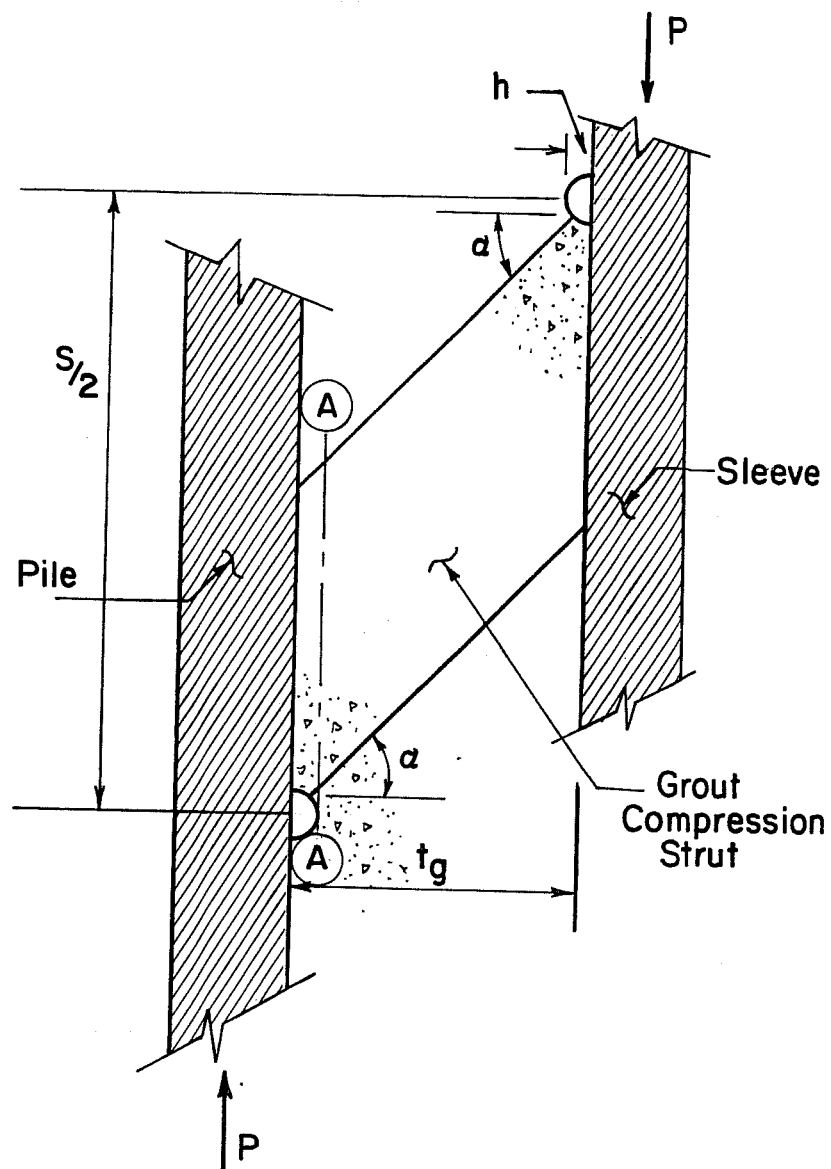


Fig. 5.7 Idealized grout compression strut

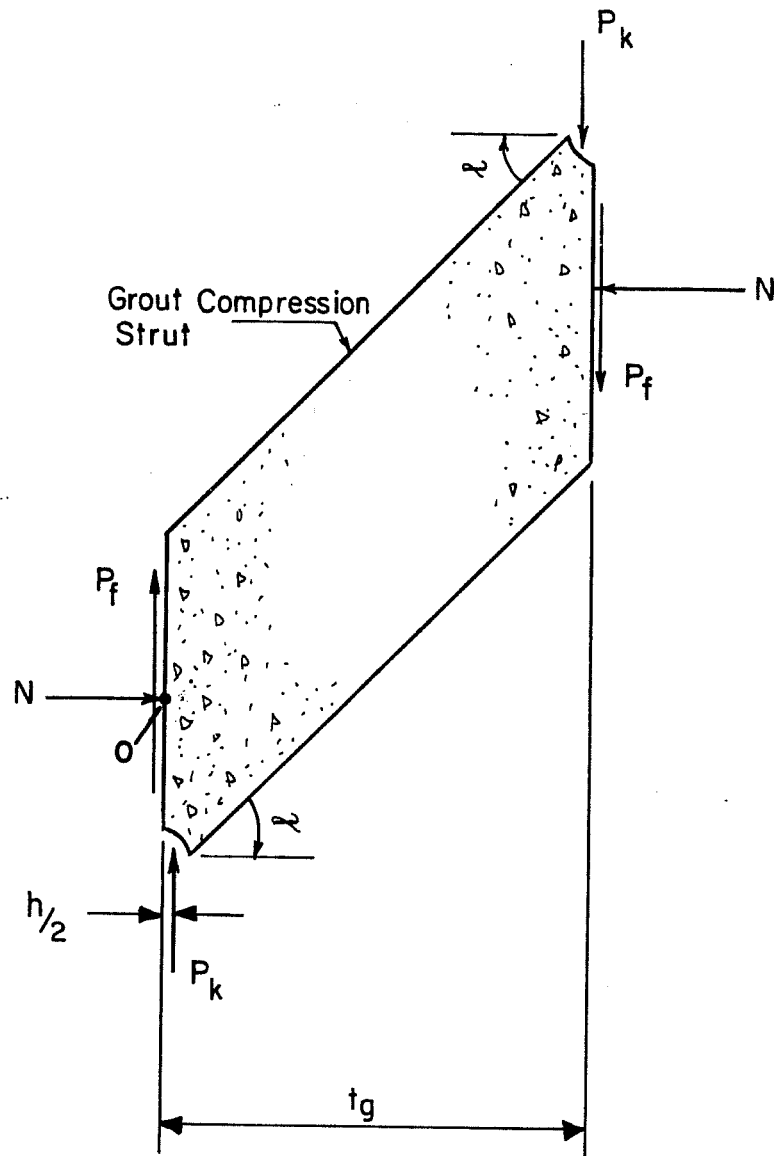


Fig. 5.8 Forces acting on idealized grout compression strut



The normal force,  $N$  causes the frictional force,  $P_f$  to develop where the normal compressive force,  $N$  can be defined by taking  $M_o = 0$  which gives

$$N = P_k [t_g - h] / [t_g (\tan \alpha - \mu)] \quad (28)$$

All the unknown forces shown in Fig. 5.8 can now be determined and the total strength of a grouted connection is

$$P = \sum_{i=1}^n P_i \quad (29)$$

where  $n =$  number of compression struts in the grouted connection  
(usually equal to number of shear keys on the pile)

#### 5.4.1 Shear Key Force Component of Overall Strut Strength.

To obtain the component of the load due to shear key action,  $P_k$  the constitutive relations developed in the sections to follow will be used. These relations, however require a knowledge of the relationship between the applied load,  $P$  and the resulting stresses.

The controlling failure region of the strut is where the grout wedge forms. In this region the grout is subjected to high levels of triaxial stress. If a small element is removed from this region of grout wedge formation, the state of stress would be as shown in Fig. 5.9. The normal stress  $\sigma_{33}$  (longitudinal stress) is a function of the applied key load divided by the area over which the

load is considered to act. The amount of radial and hoop stress ( $\sigma_{11}$ ,  $\sigma_{22}$ ) which develop are controlled by the radial stiffness, grout strength, material properties and the normal stress,  $\sigma_{33}$ . The shear stresses  $\tau_{12}$  and  $\tau_{23}$  are zero due to symmetry. The shear stress  $\tau_{13}$  is a function of the area over which the shear is considered to act and the inclination angle of the grout strut which controls the width of the strut. In general the unknown stresses may be expressed as:

$$\sigma_{33} = P_k/A_1 \quad (30)$$

$$\sigma_{11} = f(K, f_{cu}, \sigma_{33}) \quad (31)$$

$$\sigma_{22} = f(K, f_{cu}, \sigma_{33}) \quad (32)$$

$$\tau_{12} = P/A_2 \quad (33)$$

The exact values of these stresses are dependent upon the location in the grout wedge which is chosen as critical. The state of stress in the grout wedge region causes crushing of the grout at the grout-steel interface first due to the combination of high shear and normal stresses. This crushing of the grout corresponds to the gradual increase in relative displacement shown on the load-displacement plots of Appendix E. Before ultimate strength is obtained, a complete grout wedge must form. For this simplified model the last point to form will be the most critical and govern the computed ultimate strength.

The normal stress,  $\sigma_{33}$  will be assumed to be constant along the height of the shear key. The shear stress will be taken at the

tip of the shear key. The value of the normal stress,  $\sigma_{33}$  at this point will be equal to the applied key load  $P_k$  divided by the bearing area under the shear key and can be expressed as

$$\sigma_{33} = P_k / \left[ \pi (R_p + h)^2 R_p^2 \right] \quad (34)$$

The corresponding average shear stress  $\tau_{13}$  will conservatively be taken as constant in the region under the shear key and will be equal to the total applied load,  $P$  divided by the area of the cylindrical surface A-A shown in Fig. 5.7

$$\tau_{13} = P / \left[ \pi (D_p + 2h) (s/2 - t_g - \tan\alpha) \right] \quad (35)$$

$$\text{where } P = \mu N + P_k \quad (35a)$$

At any load level there are four unknown strains ( $d\epsilon_{11}$ ,  $d\epsilon_{22}$ ,  $d\epsilon_{33}$ ,  $d\epsilon_{13}$ ) and two unknown stresses ( $d\sigma_{11}$ ,  $d\sigma_{22}$ ). To obtain an upper bound solution both  $d\epsilon_{11}$  and  $d\epsilon_{22}$  will be taken equal to zero. This assumption implies that the tubes confining the grout are infinitely stiff. This simplification allows a solution to be obtained without the implementation of a full-scale analysis. The assumption also allows a check of the validity of the constitutive relations being used to model the grouted connection. If the solution obtained using this simplified model is not in reasonable comparison with the experimental results, then there would be little reason to expect that applying the constitutive laws in a more sophisticated analysis

such as a finite element approach would yield improved solutions. For the actual case of tubes without infinite radial stiffness an empirical coefficient can be developed which is a function of the radial stiffness for given  $D/t$  ratios.

The angle  $\alpha$  given in Eq. 35 and shown in Fig. 5.7 seems to be a function of grout strength,  $f_{cu}$  as shown in Section 4.6. The discussion indicated that  $\alpha$  and  $f_{cu}$  are inversely related with an increasing grout strength causing a decrease in the strut angle,  $\alpha$ . The limited amount of data, however, would not justify more than a simple linear relationship within the bounds of the grout strengths used. For the schematics shown in Section 4.6 there are no two specimens which were exactly alike in all respects except for grout strength. Therefore a constant angle of  $\alpha = 45^\circ$  will be used in all calculations. This angle is within the range of measured crack orientations for all the specimens examined except, UTA12 which had high strength grout and a  $L/D_p = 1$ .

#### 5.4.2 Coulomb Friction Component of Overall Strut Strength

The Coulomb friction that develops at the steel-grout interface is  $\mu N$ . Once the load due to strut action has been determined, using the constitutive relations developed in the following sections, Eq. 28 can

be used to determine the normal force required for Eq. 27. The only remaining unknown is the coefficient of friction,  $\mu$ .

Rabbat [35] performed a series of fifteen tests on 14 x 28 in. specimens to establish the coefficient of static friction,  $\mu$  between rolled steel plate and cast-in-place concrete or grout. For normal stresses of between 20 psi to 100 psi, Rabbat found the coefficient of static friction to be in the range of 0.64 to 0.70 for concrete with a wet steel-concrete interface and recommended a value of  $\mu = 0.65$ . For dry steel-concrete or grout interface with the same range of normal stresses Rabbat found the coefficient of friction to be slightly lower, and recommended a value of  $\mu = 0.57$ .

The normal compressive stresses developed at the grout-steel interface of a grouted connection can be 5 to 10 times greater than those used in Rabbat's investigation. The shot-blasted surface condition of the grouted connection tubes would increase the surface roughness, over the cleaned rolled steel plates used by Rabbat. However, since there is currently a lack of data to indicate whether the coefficient of friction is dependent upon the level of normal compressive stress, a value of  $\mu = 0.65$  will be used. The selection of  $\mu = 0.65$  instead of  $\mu = 0.57$  is not based on whether the steel-grout interface is wet or dry but is an allowance for the increased surface roughness due to the shot-blasted condition of the steel tubes.

### 5.5 Constitutive Relations for Grout

The state of high triaxial stress which the grout is subjected to implies that the behavior is highly nonlinear and any material model used to govern its behavior must account for this nonlinearity. To the author's knowledge there are no constitutive relations reported in the literature for grout as such, but rather are based on concrete behavior. Therefore it will be assumed that the behavior of grout and concrete are the same under triaxial stress-states.

Information on the multiaxial stress-strain relations and the failure criterion of concrete is essential for predicting the nonlinear material behavior of a grouted connection. In recent years a large number of investigations have been carried out and various models proposed to characterize the multiaxial stress-strain behavior of concrete [36,37,38,39,40]. The models vary from simple equivalent stress-strain relationships for the multiaxial stress-strain behavior of concrete to complex models based on plasticity theory.

In the following sections two constitutive relations will be examined and applied to the problem of the grouted connection. Theoretical details will be omitted unless they are useful in explaining certain aspects of the models. The interested reader is referred to the following articles [41,42,43,44].

The two models selected are the one by Chen and Chen [36] which was among the first to be proposed for concrete and another developed by Fardis et. al. [37]. These models were arrived at phenomenologically from experimental data. One basic difference between the two models is that Chen's model is based on the results of uniaxial and biaxial test data whereas the Fardis model also includes the results of triaxial experimental data. It should be noted that these models do not necessarily represent optimum models but were selected solely to indicate the degree of variance in solution which can be obtained using different constitutive relations. Also, the two models selected represent two basic types of models, those which are developed from uniaxial and biaxial data and those which also include triaxial data.

#### 5.6 Development of Chen's Constitutive Relations for Concrete

As stated previously the constitutive relations developed by Chen and Chen [36] were among the first proposed for modeling concrete using classical plasticity theory. Chen's model uses the flow theory of plasticity with isotropic hardening to construct a three-parameter model for the description of the behavior of concrete under multiaxial states of stress. In the formulation, Chen assumes the concrete to be a continuous, isotropic linearly elastic-plastic strain hardening-fracturing material. On the basis of uniaxial and biaxial experimental data, Chen proposed two different but similar functions for the failure surface. The failure surface is defined in stress

space such that once the stress state reaches this surface the material will completely rupture and cannot resist any further loading. In the compression-compression region the failure surface is defined

$$f_u(\sigma_{ij}) = J_2 + A_u I_1/3 - \tau_u^2 = 0 \quad (36a)$$

where  $J_2 =$  the second deviatoric stress invariant

$$= s_{ij} s_{ij} / 2 \quad (i, j = 1, 2, 3)$$

$I_1 =$  the first stress invariant

$$= \sigma_{ii} \quad (i = 1, 2, 3)$$

and in the tension-tension or tension-compression region

$$f_u(\sigma_{ij}) = J_2 - I_1^2 \pm A_u I_1/3 - \tau_u = 0 \quad (36b)$$

Then assumed the initial discontinuous surface to take the same form as the failure surface. The initial discontinuous surface is a surface that can only be reached by elastic action, and is mathematically equivalent to the initial yield surface of metals. In the compression-compression region the initial discontinuous surface is defined

$$f_o(\sigma_{ij}) = J_2 + A_o I_1/3 - \tau_o^2 = 0 \quad (37a)$$



and in the tension-tension or tension-compression region

$$\bar{f}_o(\sigma_{ij}) = J_2 - I_1^2/6 + A_o I_1/3 - \tau_o^2 = 0 \quad (37b)$$

The material constants  $A_o$ ,  $\tau_o$ ,  $A_u$  and  $\tau_u$  are experimentally determined values which are functions of the ultimate stresses under uniaxial compression,  $f'_c$  uniaxial tension,  $f'_t$ , equal biaxial compression,  $f'_{bc}$  and of the initial yield stresses under similar conditions  $f_c$ ,  $f_t$  and  $f_{bc}$ . In the compression-compression region the material constants are

$$\frac{A_o}{f'_c} = \frac{\bar{f}'_{bc}{}^2 - \bar{f}'_c{}^2}{2\bar{f}'_{bc} - \bar{f}'_c} \quad (38a)$$

$$\frac{A_u}{f'_c} = \frac{\bar{f}'_{bc}{}^2 - 1}{2\bar{f}'_{bc} - 1} \quad (38b)$$

$$\left(\frac{\tau_o}{f'_c}\right)^2 = \frac{\bar{f}'_c \bar{f}'_{bc} (2\bar{f}'_c - \bar{f}'_{bc})}{3(2\bar{f}'_{bc} - \bar{f}'_c)} \quad (38c)$$

$$\left(\frac{\tau_u}{f'_c}\right)^2 = \frac{\bar{f}'_{bc} (2 - \bar{f}'_{bc})}{3(2\bar{f}'_{bc} - 1)} \quad (38d)$$

and for the tension-tension or tension-compression region

$$\frac{A_o}{f'_t} = \frac{\bar{f}'_c - \bar{f}'_t}{2} \quad (39a)$$

$$\frac{A_u}{f'_c} = \frac{1 - \bar{f}'_t}{2} \quad (39b)$$

$$\left(\frac{\tau_o}{f'_c}\right)^2 = \frac{\bar{f}'_c \bar{f}'_t}{6} \quad (39c)$$

$$\left(\frac{\tau_u}{f'_c}\right)^2 = \frac{\bar{f}'_t}{6} \quad (39d)$$

The bar in Eqs. 38 and 39 denotes dimensionless quantities (division by  $f'_c$ ). As recommended by Chen [36],  $\bar{f}'_{bc}$  for biaxial compression will

be taken as  $1.16f'_c$  and  $\bar{f}_t$  for uniaxial tension as  $0.09f'_c$ . Figure 5.10 shows the shape of the initial and failure surfaces for Chen's constitutive relations in principal-stress space. Both the initial and failure functions have different expressions depending on the state of stress. The criteria for defining where the state of stress lies are given by Eqs. 40a - 40d and are illustrated in Fig. 5.11.

compression-compression region

$$I_1 < 0 \text{ and } J_2 + I_1/3 < 0 \quad (40a)$$

compression-tension

$$I_1 < 0 \text{ and } J_2 + I_1/3 > 0 \quad (40b)$$

tension-compression

$$I_1 > 0 \text{ and } J_2 - I_1/3 > 0 \quad (40c)$$

tension-tension

$$I_1 > 0 \text{ and } J_2 - I_1/3 > 0 \quad (40d)$$

Chen assumes that the subsequent loading surfaces as shown in Fig. 5.11 are similar in form to the initial discontinuous and failure surfaces. According to the kinematics of the loading surfaces adopted by Chen [36], the loading surface both translates along the  $\sigma_1=\sigma_2=\sigma_3$  axis and expands isotropically simultaneously. Consequently, the loading function is a combination of kinematic hardening and isotropic hardening models used frequently in classical plasticity.

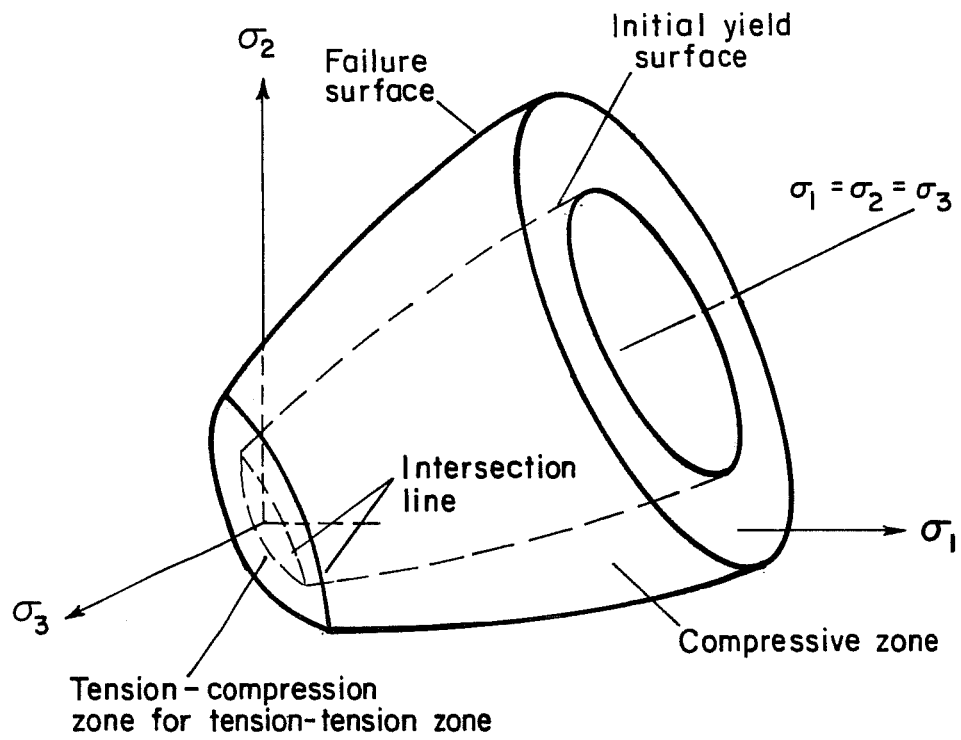


Fig. 5.10 Chen's initial yield and failure surfaces in principal-stress space ref. [36]

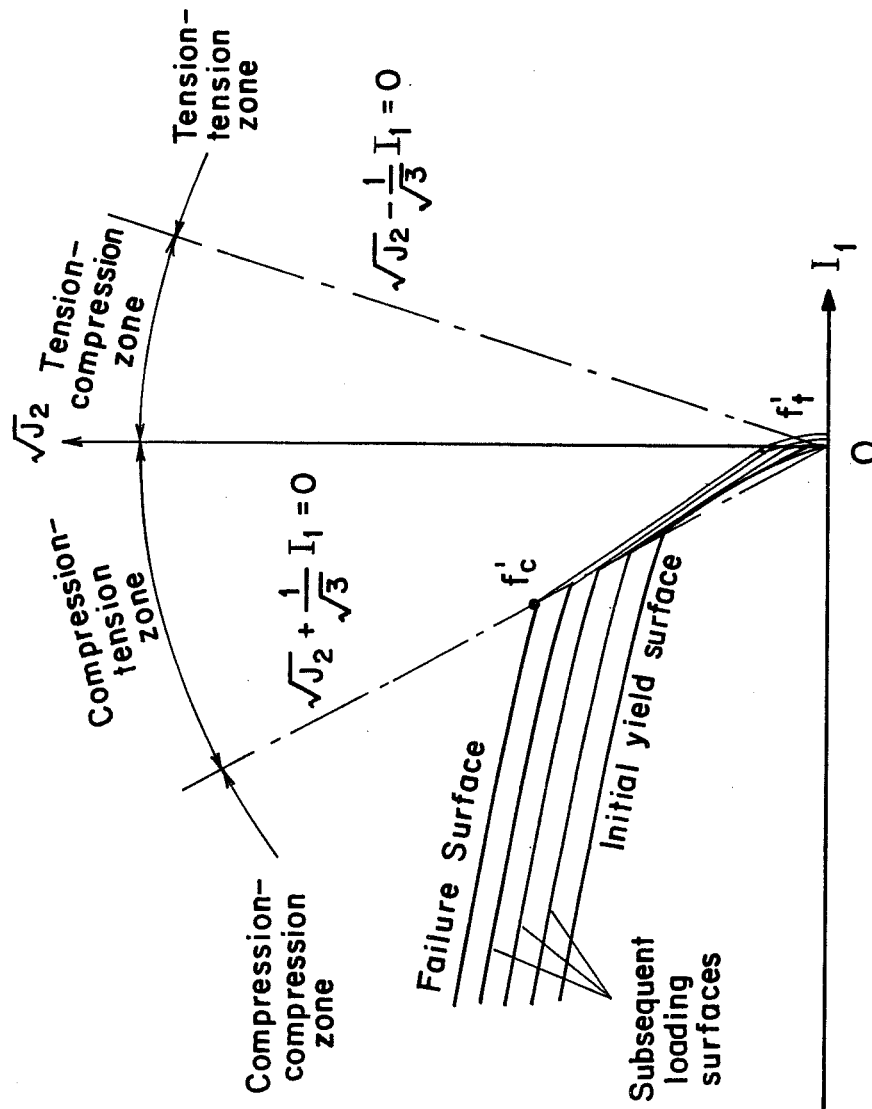


Fig. 5.11 Chen's subsequent loading surfaces in  $I_1, J_2$  space ref. [36]

In the compression-compression region, the loading function takes the form

$$F(\sigma_{ij}) = \frac{J_2 + (\beta/3)I_1}{1 - (\alpha/3)I_1} = \tau^2 \quad (41a)$$

and in tension-compression or tension-tension region

$$F(\sigma_{ij}) = \frac{J_2 - I_1^2/6 + (\beta/3)I_1}{1 - (\alpha/3)I_1} \quad (41b)$$

where  $\alpha = \frac{A_u - A_o}{\tau_u^2 - \tau_o^2}$  (41c)

$$B = \frac{A_o \tau_u^2 - A_u \tau_o^2}{\tau_u^2 - \tau_o^2} \quad (41d)$$

Having defined the loading function, Chen derives the incremental stress-strain relationships from the loading surface using the normality condition. The normality condition requires that the plastic-deformation-rate vector be normal to the yield surface. Constitutive relations, such as Chen's [36], derived on the normality principle of plasticity will predict volume expansion or dilatancy in the concrete at failure. The normality condition also imposes strong implications with respect to uniqueness of solution for work hardening and perfectly plastic bodies.

The increment of strain is given by:

$$d\epsilon_{ij} = d\epsilon_{ij}^e + d\epsilon_{ij}^p \quad (i, j = 1, 2, 3) \quad (42)$$

The elastic response is governed by Hooke's Law

$$d\sigma_{ij} = D_{ijkl}^e d\epsilon_{kl} \quad (i, j, k, l = 1, 2, 3) \quad (43)$$

where  $D_{ijkl}^e$  is the elastic tangential stiffness matrix. Thus, the stress increment is determined as:

$$d\sigma_{ij} = D_{ijkl}^e (k\epsilon_{kl} - d\epsilon_{kl}^p) \quad (i, j, k, l = 1, 2, 3) \quad (44)$$

During plastic loading, both initial yield and subsequent stress states must satisfy the yield condition  $f(\sigma_{ij}, \epsilon_{ij}^p, \kappa) = 0$ . Plastic flow is then governed by the consistency condition

$$df = \frac{\partial f}{\partial \sigma_{ij}} d\sigma_{ij} + \frac{\partial f}{\partial \epsilon_{ij}^p} d\epsilon_{ij}^p + \frac{\partial f}{\partial \kappa} d\kappa = 0 \quad (45)$$

where the hardening parameter  $\kappa$  is a function of the plastic strain.

By using Eq. 44 along with the flow rule given by

$$d\epsilon_{ij}^p = d\lambda \frac{\partial f}{\partial \sigma_{ij}} \quad (46)$$

the consistency condition can be expressed as

$$\frac{\partial f}{\partial \sigma_{ij}} D_{ijkl}^e \left( d\epsilon_{kl} - d\lambda \frac{\partial g}{\partial \sigma_{kl}} \right) + \frac{\partial f}{\partial \epsilon_{ij}^p} d\lambda \frac{\partial g}{\partial \sigma_{ij}} + \frac{\partial f}{\partial \kappa} \frac{\partial \kappa}{\partial \epsilon_{ij}^p} d\lambda \frac{\partial g}{\partial \sigma_{ij}} = 0 \quad (47)$$

Thus the scalar function  $d\lambda$  is given by:

$$d\lambda = \frac{\left( \frac{\partial f}{\partial \sigma_{ij}} \right) D_{ijkl}^e d\epsilon_{kl}}{h + \left( \frac{\partial f}{\partial \sigma_{mn}} \right) D_{mnpq}^e \frac{\partial g}{\partial \sigma_{pq}}} \quad (48)$$

where  $h$  denotes the hardening parameter

$$h = \frac{-\partial f}{\partial \epsilon_{ij}^p} \frac{\partial g}{\partial \sigma_{ij}^p} - \frac{\partial f}{\partial \kappa} \frac{\partial \kappa}{\partial \epsilon_{ij}^p} \frac{\partial g}{\partial \sigma_{ij}^p} \quad (49)$$

The plastic-strain increment  $d\epsilon_{ij}^p$  is a function of the total strain increment  $d\epsilon_{ij}^p$  and the gradients of the initial yield and subsequent loading surfaces

$$d\epsilon_{ij}^p = \frac{\left(\frac{\partial f}{\partial \sigma_{rs}}\right) D_{rskl}^e d\epsilon_{kl}}{h + \left(\frac{\partial f}{\partial \sigma_{mn}}\right) D_{mnpq}^e \frac{\partial g}{\partial \sigma_{pq}}} \frac{\partial g}{\partial \sigma_{ij}} \quad (50)$$

The stress-strain relation for Chen's assumed concrete behavior of an elastic-work hardening-plastic solid are obtained by substitution of  $d\epsilon_{ij}^p$  into the expression for the stress increment given by Eq. 44.

$$d\sigma_{ij} = \left( D_{ijkl}^e + D_{ijkl}^p \right) d\epsilon_{kl} \quad (51)$$

where the plastic-stiffness tensor has the form

$$D_{ijkl}^p = \frac{-D_{ijtu}^e \left(\frac{\partial f}{\partial \sigma_{rs}}\right) \left(\frac{\partial g}{\partial \sigma_{tu}}\right) D_{rskl}^e}{h + \left(\frac{\partial f}{\partial \sigma_{mn}}\right) D_{mnpq}^e \frac{\partial g}{\partial \sigma_{pq}}} \quad (52)$$

When the loading functions of Eq. 41 are substituted into Eq. 52, the incremental elastoplastic stress-strain relation given by Eq. 51 is fully defined by  $f$  with the associated-flow-rule condition  $f=g$ . In the three dimensional case, the incremental relationship is given as

$$(d\sigma) = \frac{E_g}{((1+v)(1-2\nu))} [\sigma](d\epsilon) \quad (53)$$

where

$$(d\sigma)^T = (d\sigma_{11} \ d\sigma_{22} \ d\sigma_{33} \ d\sigma_{12} \ d\sigma_{23} \ d\sigma_{31})$$

$$[\sigma] = 6 \times 6 \text{ symmetric elastoplastic stiffness matrix}$$

$$(d\epsilon)^T = \{d\epsilon_{11} \ d\epsilon_{22} \ d\epsilon_{33} \ d\epsilon_{12} \ d\epsilon_{23} \ d\epsilon_{31}\}$$

As previously stated for an upper bound solution of infinitely stiff tubes both  $d\epsilon_{11}$  and  $d\epsilon_{22}$  are zero. From symmetry, the shear stresses  $d\sigma_{12}$  and  $d\sigma_{23}$  are also zero as are the corresponding shearing strains  $d\epsilon_{12}$  and  $d\epsilon_{23}$ . Eliminating these rows and columns and partitioning the matrix into knowns and unknowns yields:

$$\begin{bmatrix} d\sigma_{33} \\ d\sigma_{13} \\ d\sigma_{11} \\ d\sigma_{22} \end{bmatrix} = \begin{bmatrix} \Phi_{33} & \Phi_{36} \\ \Phi_{63} & \Phi_{66} \\ \Phi_{13} & \Phi_{16} \\ \Phi_{23} & \Phi_{26} \end{bmatrix} \begin{bmatrix} d\epsilon_{33} \\ d\epsilon_{13} \end{bmatrix} \quad (54)$$

where

$$\begin{aligned} \Phi_{13} &= v - \omega [(1-2\nu)(s_{11} + \rho) + 3\nu\rho] [(1-2\nu)(s_{33} + \rho) + 3\nu\rho] \\ \Phi_{16} &= -\omega [(1-2\nu)(s_{11} + \rho) + 3\nu\rho] [(1-2\nu)\tau_{31}] \\ \Phi_{23} &= v - \omega [(1-2\nu)(s_{22} + \rho) + 3\nu\rho] [(1-2\nu)(s_{33} + \rho) + 3\nu\rho] \\ \Phi_{26} &= -\omega [(1-2\nu)(s_{22} + \rho) + 3\nu\rho] [(1-2\nu)\tau_{31}] \\ \Phi_{33} &= 1 - v - \omega [(1-2\nu)(s_{33} + \rho) + 3\nu\rho]^2 \end{aligned}$$



$$\begin{aligned}\Phi_{36} &= -\omega [(1-2\nu)(s_{33} + \rho) + 3\nu\rho] [(1-2\nu)\tau_{31}] \\ \Phi_{66} &= \frac{1-2\nu}{2} - \omega [(1-2\nu)\tau_{31}]^2 \\ 1/\omega &= [(1-2\nu)(2J_2 + 3\rho^2) + 9\nu^2] \\ &\quad + \frac{2\tau H(1+\nu)((1-2\nu)}{E} \sqrt{(2J_2 + 3\rho^2)} \left(1 - \frac{a}{3} I_1\right) \\ \rho &= nI_1 + \frac{\beta + \alpha\tau^2}{3} \\ H &= d\tau/de_p = \text{slope from uniaxial compression test}\end{aligned}$$

For a specified load step the change in stresses  $d\sigma_{33}$  and  $d\sigma_{13}$  at the critical point can be determined using Eqs. 34 and 35 of Section 5.4.1. Substituting these values into Eq. 54, the upper partition of the matrix can then be solved for the unknown strains  $d\epsilon_{33}$  and  $d\epsilon_{13}$ . Once these strains are known the values of  $d\sigma_{11}$  and  $d\sigma_{22}$  can be solved for using the lower partition of Eq. 54.

To apply Chen's constitutive relations in determining the ultimate strength of a grout compression strut, shown in Fig. 5.7 the initial discontinuous surface must be defined. Chen states [36] that the values of the discontinuous function used by various investigators range from 0.30 - 0.75 of that of the failure function. Chen found, however, that the choice of the initial discontinuous surface has no major influence on the values of the loading function, but that a value of 0.60 more closely satisfies the normality condition. For this investigation a value of 0.40 will be selected since this is a commonly accepted limit for elastic behavior of concrete or grout.

The value of  $P$  required to reach the initial discontinuous surface can be calculated directly using Eq. 37 in conjunction with Eqs. 38 or 39 since the linear-elastic relation between the stresses  $d\sigma_{33}$  and  $d\sigma_{13}$  are known.

An incremental load step size must then be selected to take the load from the initial discontinuous surface to the failure surface. Chen's model like most plasticity models is very path-dependent; thus, care must be exercised in selecting a sufficiently small load step to accurately model the path. For this simple model of a single grout compression strut a load step size of 25 lbs. was found to yield sufficiently accurate solutions.

At the beginning of each increment the initial values of the unknown stresses  $d\sigma_{11}$  and  $d\sigma_{22}$  are assumed to be zero. Updated stresses are then determined using Eq. 54. When the assumed and calculated values of the stresses are within the prescribed tolerance convergence for the load step has been achieved and the load, stress and strain vectors are updated. The value of  $r$  is then calculated using Eq. 41 to determine if the load step is at or beyond the failure surface defined in Eq. 36, in which case the failure load  $P$ , for the grout compression strut has been obtained. A flow chart for Chen's plasticity model is given in Fig. 5.12 and 5.13 and a program listing is given in Appendix G.

### 5.7 Development of Fardis' Monotonic Constitutive Law for Concrete

A pivotal component of the Fardis model [37] is a surface in stress space, called a bounding surface, which for a given stress and strain history always encloses the current stress point. For monotonic, nearly proportional loading, the bounding surface is the usual failure surface, defined as the locus of stress-points corresponding to ultimate strength. The stress point must always lie within or on the bounding surface and its distance from the latter determines the value of the tangent plastic modulus.

Strain components are considered entirely plastic and are computed by superposition of an isotropic component, proportional to the hydrostatic stress increment, and deviatoric and isotropic components, proportional to the octahedral shear stress increments. The plastic modulus for calculation of the latter strain components is a function of the distance of the stress point from the failure surface, measured along the direction of the current stress increment, and of  $\epsilon_{\max}$ , the maximum compressive strain ever experienced by the material. Thus the bounding surface is taken to depend on  $\epsilon_{\max}$  and is given by an equation of the form

$$F(\sigma_{ij}, \epsilon_{\max}) = 0 \quad (55)$$

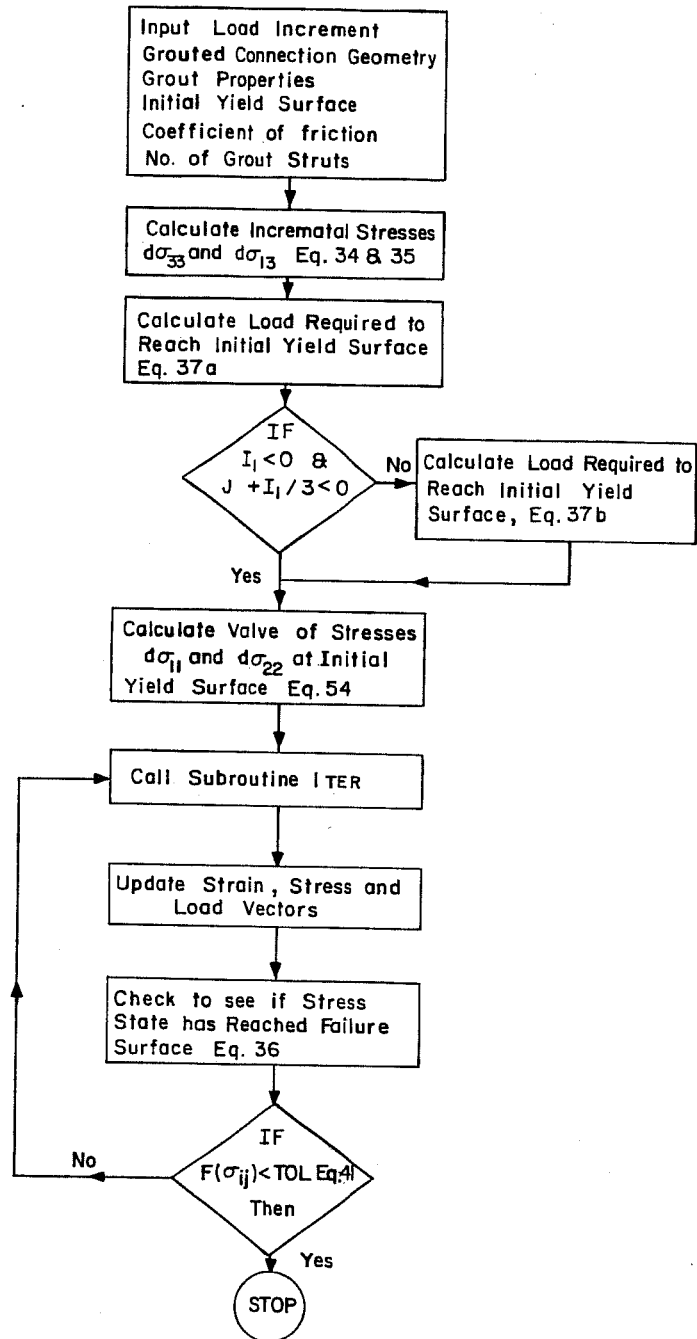


Fig. 5.12 Flow chart for Chen's constitutive relations

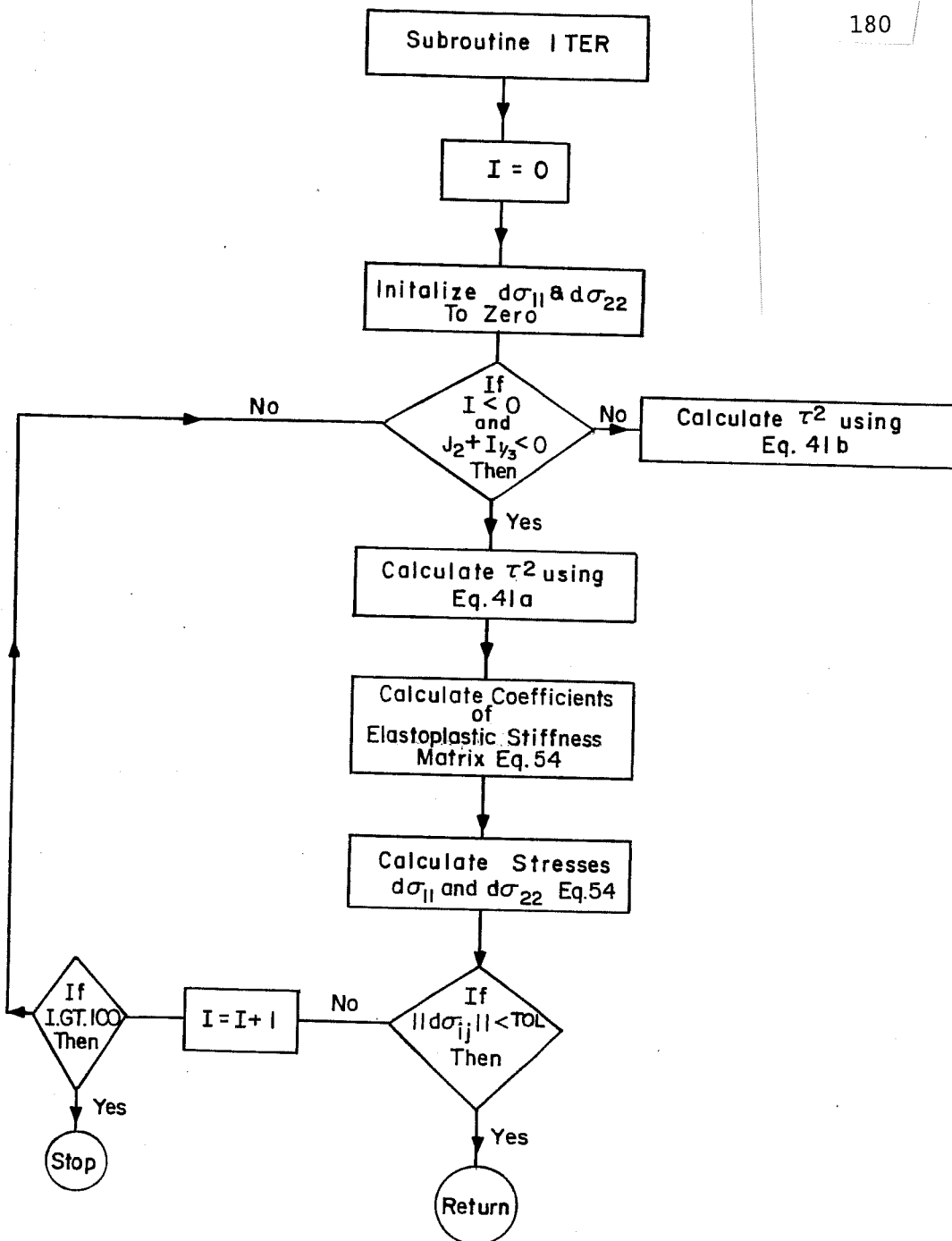


Fig. 5.13 Flow chart of subroutines for Chen's constitutive relations

For any arbitrary  $\epsilon_{max}$ , the bounding surface is a surface in nine-dimensional stress space. If the material (grout) is considered isotropic then the bounding surface can be described in three-dimensional principal stress space and  $F(\omega_{ij}, \epsilon_{max})$  can be considered as a function of the stress invariants.

Fardis selected the first stress invariant  $I_1 = \omega_{ii}$  ( $i = 1, 2, 3$ ) and the second and third deviatoric stress invariants  $J_2 = s_{ij} s_{ij} / 2$  and  $J_3 = s_{ij} s_{jk} s_{ki}$  ( $i, j, k = 1, 2, 3$ ), in which  $s_{ij} \omega_{ij} - \delta_{ij} I_1 / 3$  where  $s_{ij}$  is the deviatoric stress tensor and  $\delta_{ij}$  is the Kronecker delta. These invariants were selected because of their geometric meaning. The projection of the position vector of the stress point onto the hydrostatic axis equals  $I_1 / \sqrt{3}$ , the distance from the hydrostatic axis equals  $\sqrt{2J_2}$ . If the stress space is projected on the deviatoric plane,  $I_1 = 0$ , then the angle  $\theta$  between the position vector and the projection of any semiaxis is such that  $\cos 3\theta = \frac{-3\sqrt{3}J_3}{2J_2^{3/2}}$ . The final form of the monotonic failure surface, serving as an outer limit to the bounding surface, as proposed by Fardis is given by

$$\left( \frac{I_1}{f_{cu}} + 0.30 \right) - (12 + 11 \cos 3\theta)^{1/6} \left[ 0.7 \left( \frac{\sqrt{J_2}}{f_{cu}} \right)^2 + 1.85 \frac{\sqrt{J_2}}{f_{cu}} \right] = 0 \quad (56)$$

The monotonic failure surface possesses all the desirable characteristics, such as convexity, smoothness, curved meridians and deviatoric sections which have  $60^\circ$  symmetry and change from nearly triangular to nearly circular with increasing  $I_1$ .

The stress-strain response of concrete is nonlinear from the beginning thus the model assumes the strain component  $d\epsilon_{ij}$  to be completely inelastic. The strain increment is decomposed into its deviatoric and volumetric parts

$$d\epsilon_{ij} = d\epsilon_{ij} + \delta_{ij}d\epsilon_{jj}/3 \quad (k = 1,2,3) \quad (57)$$

where  $d\epsilon_{ij}$  = deviatoric strain increment

$d\epsilon_{kk}$  = volumetric strain increment

Fardis assumed that  $d\epsilon_{ij}$  is caused only by changes in the deviatoric stress tensor,  $s_{ij}$  i.e. a purely isotropic stress increment does not affect the deviatoric components of strain. The volumetric portion of  $d\epsilon_{ij}$  is caused both by isotropic and by deviatoric stress increments (shear compaction/dilatancy).

Determination of the components of  $d\epsilon_{ij}$  for the monotonic stress-strain law will be considered next. The term monotonic is defined by Fardis to mean a loading history which has no reversals in either the isotropic or the deviatoric stresses. Fardis assumed that  $d\epsilon_{ij}$  is proportional to  $s_{ij}$ . The proportionality yields

$$d\epsilon_{ij}/s_{ij} = d\gamma_o/\tau_o \quad (58)$$

where

$$\tau_o = \text{octahedral shear stress} = \sqrt{1/3 s_{ij} s_{ij}}$$

$$\gamma_o = \text{octahedral shear strain} = \sqrt{1/3 e_{ij} e_{ij}}$$

$(i, j = 1, 2, 3)$

Assuming incremental linearity

$$d\gamma_o = d\tau_o/H \tag{59}$$

where H is the generalized shear modulus, which is a function of the stress and strain at the point. The determination of H was based on the observation that the shape of the stress-strain curves in multiaxial compression with shear stresses predominant, resembles those obtained in uniaxial compression to the extent that, in approximation, one set of multiaxial curves can be obtained from the appropriate scaling of the stress-strain axes of corresponding uniaxial results. The tangent modulus determined from any such curve will decrease gradually to zero as the stress point approaches the bounding surface. Fardis assumed the shear modulus as a monotonic function of the ratio of the distance d, of the current stress point from the bounding surface measured in stress space along the instantaneous load direction,  $d\sigma_{ij}$ , to  $d_{\max}$ , which is the value of d at the beginning of the current loading process, see Fig. 5.14. In addition, both uniaxial cyclic data and the multiaxial monotonic results show that for a constant value of  $d/d_{\max}$ , the tangent modulus decreases with the maximum compressive strain ever experienced by the



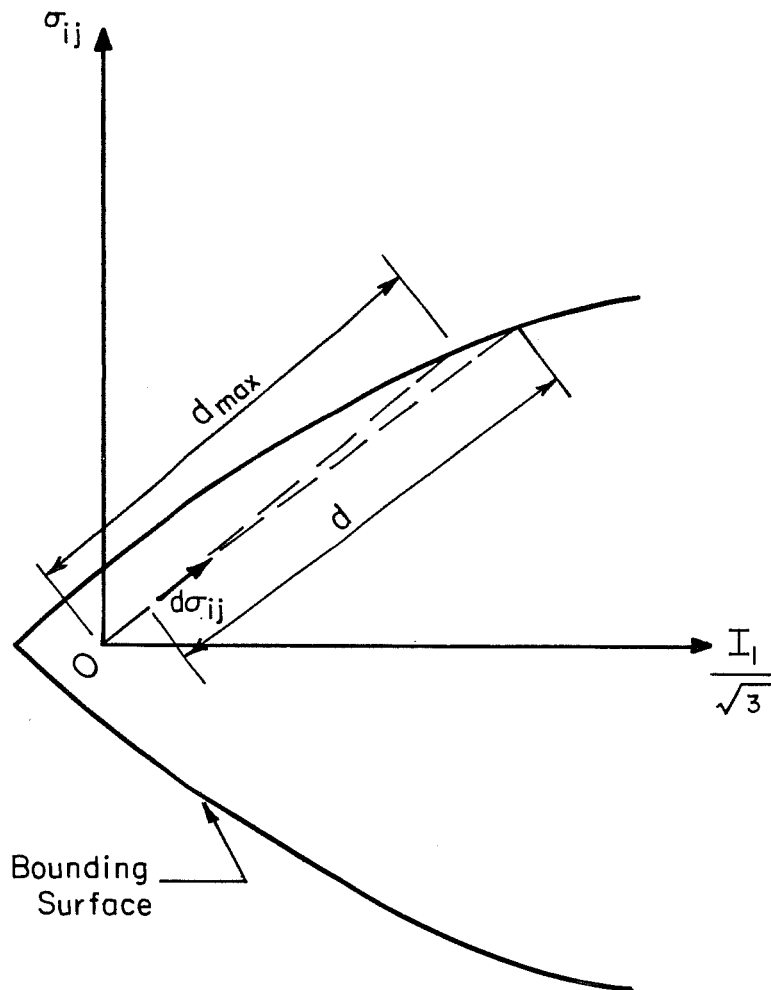


Fig. 5.14 Definition of Fardis' parameters,  $d$  and  $d_{\max}$  for generalized shear modulus

material,  $\epsilon_{\max}$  up until that time. On the basis of these observations Fardis assumed that  $H$  depends on  $\sigma_{ij}$  and on the strain history only through  $d/d_{\max}$  and  $\epsilon_{\max}$ , and can be expressed as

$$H = 16f_{cu} \left( (d/d_{\max} \epsilon_{\max}) \right)^{0.55} \quad (60)$$

With a limiting value of  $H$  equal to  $850f_{cu}$  for large values of  $d/d_{\max} \epsilon_{\max}$ . This value of  $H$  corresponds to a secant Young's modulus  $E_g$  at  $0.40f_{cu}$  equal to  $1000f_{cu}$  and an initial Poisson's ratio,  $\nu$  of 0.17.

As stated previously,  $d$  is the distance in stress space from the current  $\sigma_{ij}$  to the bounding surface, measured in the direction,  $d\sigma_{ij}$ . The value of  $d$  at the beginning of the current loading process is  $d_{\max}$ . In general,  $d$ , decreases from  $d_{\max}$  to zero during the loading process, however if, due to a gradual or discontinuous change in direction of  $d\sigma_{ij}$ ,  $d$  becomes greater than  $d_{\max}$ , then  $d_{\max}$  assumes this new value, and  $d/d_{\max}$  starts again from 1. The value of  $d$  is computed as the distance in stress space from the last calculated stress point in the direction of  $d\sigma_{ij}$  to the intersection of the bounding given by Eq. 56. In general this involves the solution of a system of nonlinear equations.

Fardis calculated the portion of the volumetric strain increments  $d\epsilon_{kk}$  caused by the isotropic component of  $d\sigma_{ij}$ ,  $\delta_{ij}dI_1/3$  as

$$d\epsilon_{kk,o} = dI_1/3\kappa_t \quad (k = 1,2,3) \quad (61)$$

A simple expression for the tangent modulus  $\kappa_t$  given by Eq. 62 was obtained by fitting to hydrostatic compression data.

$$\kappa_t = \kappa_o / (1 + I_1 / 3 f_{cu}) \quad (62)$$

The initial value of  $\kappa_t$ ,  $\kappa_o$  was determined to be  $550f_{cu}$ . This value corresponds to a secant modulus of  $0.40f_{cu}$  with the values of  $E_g$  and  $\nu$  cited previously.

The remaining portion of the volumetric strain increment  $d\epsilon_{kk}$  is associated with deviatoric strains. By assuming incremental linearity this relationship can be expressed as

$$d\epsilon_{kk,d} = \beta d\delta_o \quad (k = 1,2,3) \quad (63)$$

Based on triaxial data with  $I_1$  constant, Fardis selected the expression given by Eq. 64 to represent the shear compaction/dilantancy factor,  $\beta$ .

$$\beta = 9\epsilon_{max}^{1/4} (d/d_{max} - 0.1) \quad (64)$$

Combining Eq. 57-59, 61 and 63

$$d\epsilon_{ij} = \left[ \frac{s_{ij}}{\tau_o} + \delta_{ij} \frac{\beta}{3} \right] \frac{d\tau_o}{H} + \delta_{ij} \frac{dI_1}{9\kappa_t} \quad (i,j = 1,2,3) \quad (65)$$

Now expressing  $d\tau_o$  as

$$\partial\tau_o/\partial\sigma_{km} d\sigma_{km} = s_{km} d\sigma_{km}/3\tau_o \quad (k = 1, 2, 3)$$

a linear relationship between  $d\epsilon_{ij}$  and  $d\sigma_{ij}$  can be expressed

$$d\epsilon_{ij} = \frac{1}{3H\tau_o} \left[ \frac{s_{ij}}{\tau_o} + \delta_{ij} \frac{\beta}{3} \right] s_{km} d\sigma_{km} + \delta_{ij} \frac{d\sigma_{kk}}{9\kappa_t} \quad (k, m = 1, 2, 3) \quad (66)$$

Equation 66 is in the form of an incremental compliance relationship.

In matrix form, the relation is

$$\{d\epsilon\} = [C] \{d\sigma\} \quad (67)$$

$$\text{where } \{d\epsilon\}^T = (d\epsilon_{11} \quad d\epsilon_{22} \quad d\epsilon_{33} \quad d\epsilon_{12} \quad d\epsilon_{13} \quad d\epsilon_{23})$$

$$[C] = \text{nonsymmetric compliance matrix}$$

$$\{d\sigma\}^T = (d\sigma_{11} \quad d\sigma_{22} \quad d\sigma_{33} \quad d\sigma_{12} \quad d\sigma_{13} \quad d\sigma_{23})$$

For the grouted connection the incremental stresses  $d\sigma_{33}$  and  $d\sigma_{13}$  are specified by Eqs. 34 and 35 of Section 5.4.1. Due to symmetry  $d\sigma_{12}$  and  $d\sigma_{23}$  are zero and examination of Eq.66 shows that the corresponding strains  $d\epsilon_{12}$  and  $d\epsilon_{23}$  are also zero. The compliance matrix thus reduces to a 4x4 matrix

$$\begin{Bmatrix} d\epsilon_{11} \\ d\epsilon_{22} \\ d\epsilon_{33} \\ d\epsilon_{31} \end{Bmatrix} = \begin{Bmatrix} C_{11} & C_{12} & C_{13} & C_{16} \\ C_{21} & C_{22} & C_{23} & C_{26} \\ C_{31} & C_{32} & C_{33} & C_{36} \\ C_{61} & C_{62} & C_{63} & C_{66} \end{Bmatrix} \begin{Bmatrix} d\sigma_{11} \\ d\sigma_{22} \\ d\sigma_{33} \\ d\sigma_{31} \end{Bmatrix} \quad (68)$$

For  $d\epsilon_{11} = d\epsilon_{22} = 0$  the stresses  $d\sigma_{11}$  and  $d\sigma_{22}$  are equal and the incremental stress change  $d\sigma_{11}$  is

$$d\sigma_{11} = -(C_{23} d\sigma_{33} + C_{26} d\sigma_{13}) / (C_{12} + C_{22}) \quad (69)$$

where

$$C_{23} = \frac{1}{3H\tau_o} \left[ \frac{s_{22}}{\tau_o} + \frac{\beta}{3} \right] s_{33} + \frac{1}{9\kappa_t}$$

$$C_{26} = \frac{2}{3H\tau_o} \left[ \frac{s_{22}}{\tau_o} + \frac{\beta}{3} \right] d\sigma_{13}$$

$$C_{12} = \frac{1}{3H\tau_o} \left[ \frac{s_{22}}{\tau_o} + \frac{\beta}{3} \right] s_{11} + \frac{1}{9\kappa_t}$$

$$C_{22} = \frac{1}{3H\tau_o} \left[ \frac{s_{22}}{\tau_o} + \frac{\beta}{3} \right] s_{22} + \frac{1}{9\kappa_t}$$

Once these stresses are obtained the unknown incremental strains can be obtained using Eq. 66. The calculation of the ultimate strength of a grout compression strut is then obtained by the following steps.

1. Select an incremental load step size, which establishes the incremental stresses  $d\sigma_{33}$  and  $d\sigma_{13}$  from Eqs. 34 and 35. It is worth noting at this point that plasticity models are in general very path dependent thus care should be exercised in selecting a sufficiently small load increment.
2. Determine the stresses for the first increment of load. For the first increment Eq. 66 can not be used since  $\tau_o = 0$ , however, Eq. 65 can be put in an alternative form

$$d\epsilon_{ij} = \frac{ds_{ij}}{H} + \frac{\delta_{ij}\beta}{3H} d\tau_o + \delta_{ij} \frac{d\sigma_{kk}}{9\kappa_t} \quad (i, j, k = 1, 2, 3) \quad (70)$$

where  $d\tau_o = \sqrt{1/3 ds_{ij} ds_{ij}}$

For the first load increment  $\beta=0$  in a grouted connection since  $\epsilon_{\max}=0$  and Eq. 70 reduces to

$$d\epsilon_{ij} = ds_{ij}/H + \delta_{ij} d\sigma_{kk}/9\kappa_t \quad (71)$$

This relation is justified by the fact that  $d\epsilon_{ij}$  is proportional to  $d\sigma_{ij}$ . Equation 71 can be solved directly for  $d\sigma_{11}$  and  $d\sigma_{22}$  since  $d\epsilon_{11}=d\epsilon_{22}=0$ . The value of  $d_{\max}$  for this increment can then be calculated in the direction of  $d\sigma_{ij}$  using Eq. 56.

In subsequent increments, the direction and the value of the stress increment are unknown. This makes the incremental stress-strain relation nonlinear and requires, in general, iterations within each load increment. The basic process used is to assume the value of  $d\sigma_{ij}$  of the last increment as the initial guess of  $d\sigma_{ij}$  for the current increment. Based on these assumed values of  $d\sigma_{ij}$ , calculate the value of  $d$  in this direction which then allows the calculation of updated values of  $d\sigma_{ij}$ . When the assumed values of  $d\sigma_{ij}$  are within the prescribed tolerance of the calculated values convergence has been obtained and the load can be updated and the procedure repeated for the next load increment. Failure is defined as the point at which the

value of  $F(\sigma_{ij}, \epsilon_{max})$  given by Eq. 56 becomes negative, i.e.  $F(\sigma_{ij}, \epsilon_{max}) < 0$  implies that we have gone outside the bounding surface. The flow charts for Fardis model are given in Figs. 5.15 and 5.16 and a complete program listing is given in Appendix G.

5.7.1 Modification of Constants for Grout. Before the Fardis constitutive relations can be implemented for grouted connections the constants representing the maximum allowable generalized shear modulus,  $H_{max}$ , and the initial tangent modulus,  $K_o$  must be adjusted to represent the material properties of the grout used in a given connection. As discussed previously the current generic values are valid for normal strength concrete (3000 - 5000 psi) with a Poisson's ratio of  $\nu = 0.17$  and a secant modulus,  $E_g$  at  $0.40f_{cu}$ . For grout,  $E_g$  will be taken at  $0.40f_{cu}$  thus the maximum value of the generalized shear modulus and the initial tangent stiffness are

$$H_{max} = 2G = E_g / (1 + \nu) \quad (72)$$

$$\kappa_o = E_g / 3(1 - 2\nu) \quad (73)$$

The value of Poisson's ratio used will be those determined for a specific grout mix. Recommendations as to the generalized values of these material constants will be discussed later.

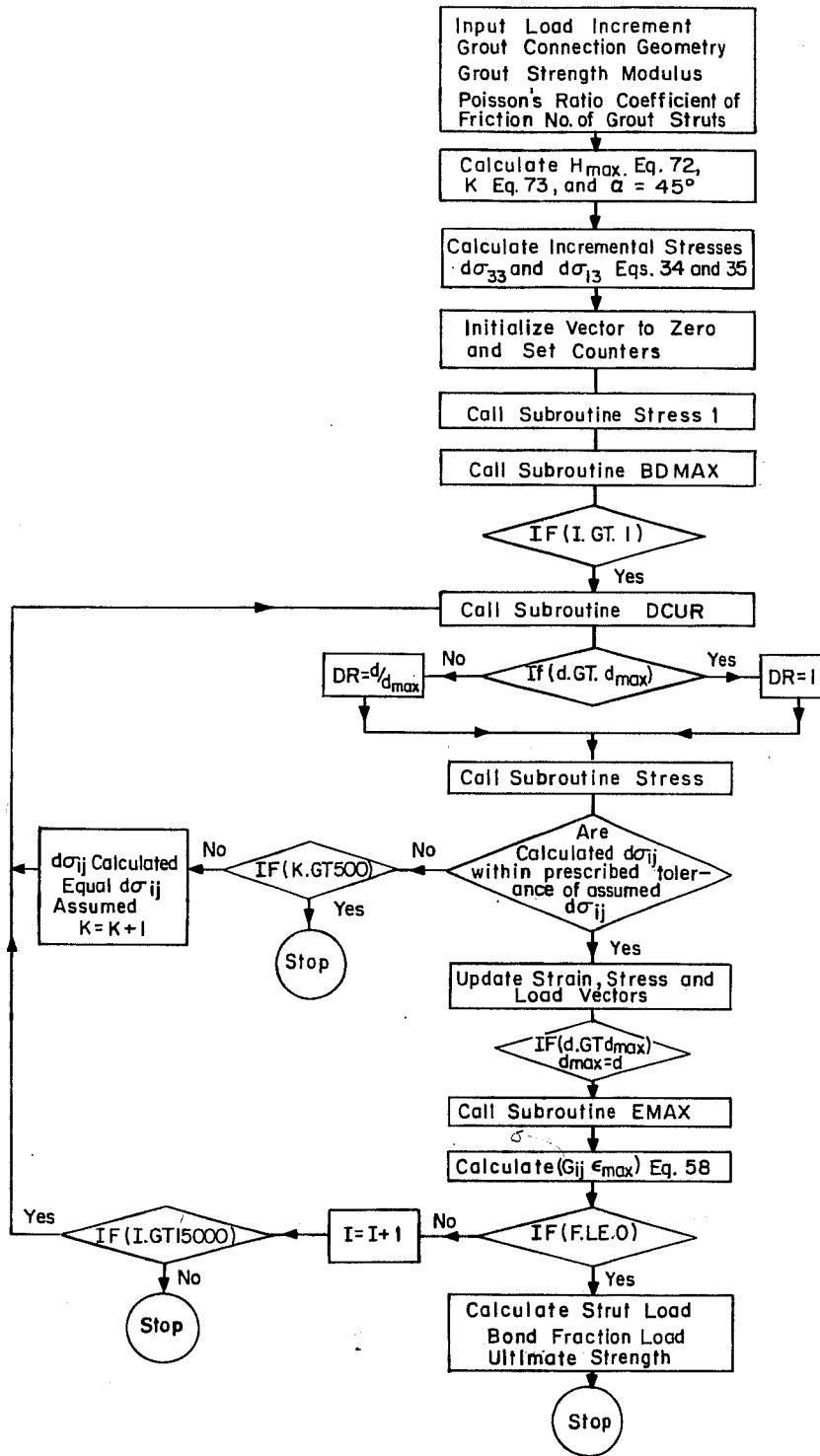


Fig. 5.15 Flow chart for Fardis' constitutive relations



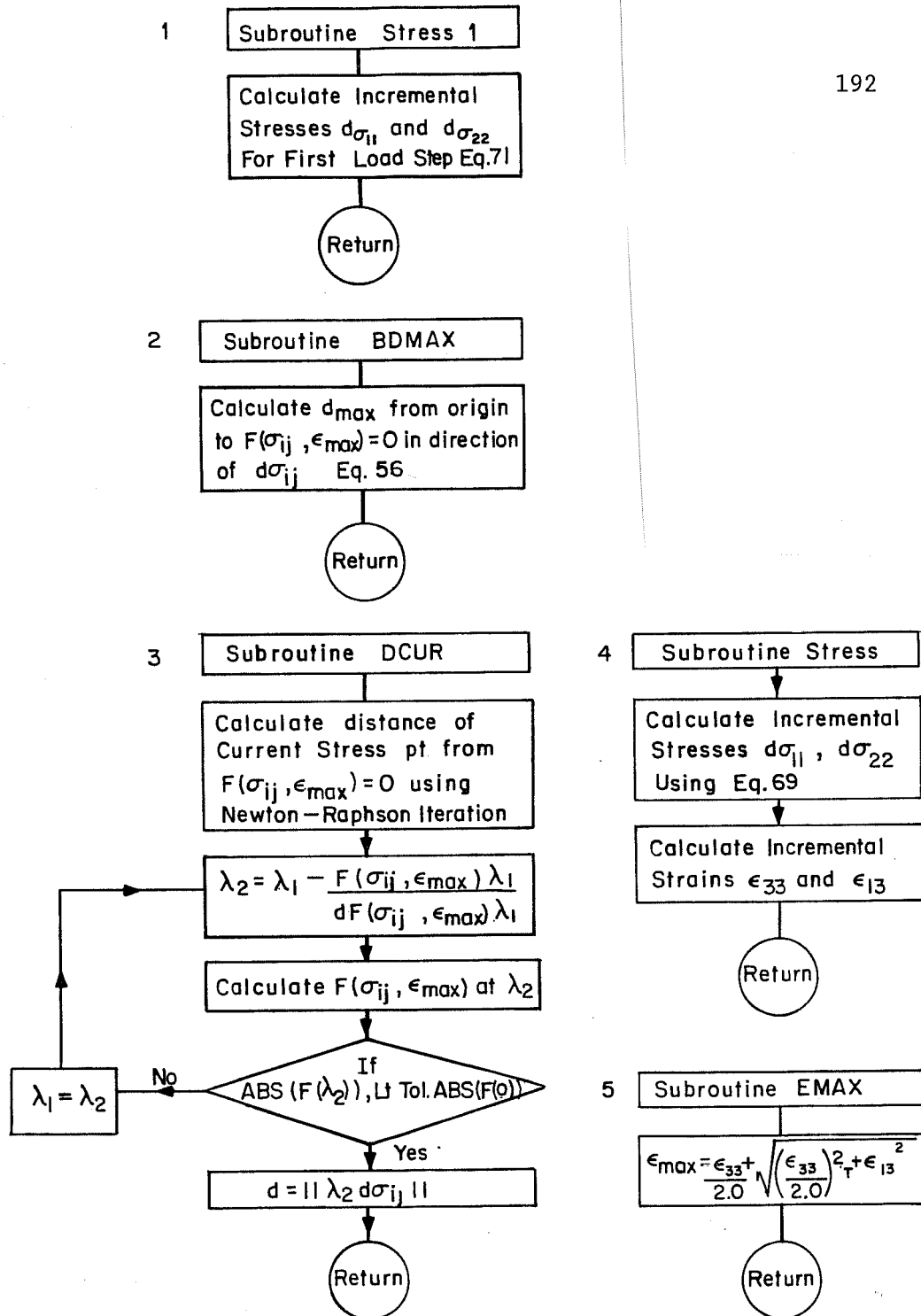


Fig. 5.16 Flow chart of subroutines for Fardis' constitutive relations

## 5.8 Application of Constitutive Relations to Axial Specimens with Normal Strength Grout

5.8.1 General. To determine the ultimate strength of a grouted connection using Chen's and Fardis' constitutive relations developed in Sections 5.6 and 5.7 the following general steps are required. First an incremental load step size must be selected. As mentioned previously plasticity models are incremental in nature and thus dependent upon the load path. For the simple model proposed here the computational time is minimal even for very small load steps therefore, a step size of 25 lbs was used. The stress-state at the critical location (tip of shear key) is defined using Eqs. 34 and 35 of Section 5.4.1 and the condition that  $d\epsilon_{11}$  and  $d\epsilon_{22}$  are zero, i.e. infinitely stiff tubes. The load is then incremented until the state of stress reaches the failure or bounding surface as defined by Eq. 36 for Chen's constitutive relations or Eq. 56 for Fardis' relations. The strength due to key action,  $P_k$ , is calculated by the plasticity model since the number of load steps required to reach the failure or bounding surface is known. The component of the strength attributed to Coulomb friction can then be obtained using Eqs. 27 and 28. The total strength of an individual strut is then obtained using Eq. 26 and the ultimate strength of the grouted connection by Eq. 29.

In applying Chen's and Fardis' constitutive relations the basic grout material properties  $f_{cu}$ ,  $E_g$  and  $\nu$  are required. The only

grout property reported by other investigators is,  $f_{cu}$ . This limits the checking of the model to the test specimens reported in Chapters 2 - 4 with the added restriction of infinitely stiff tubes. The model, however will provide an upper bound solution on the strength of a grouted connection for a given set of material properties and geometric parameters. The model can be used to determine general trends as the parameters, such as grout strength and shear key spacing and height are changed. Furthermore, the model can be used to illustrate the effect of different constitutive relations on the predicted strength of the grouted connection.

5.8.2 Predicted Strength of Series 1 Axial Specimens Using Chen's Constitutive Relations. In applying Chens' constitutive relations the complete uniaxial compression test curve must be known, for the work hardening parameter H of Eq. 54 to be evaluated. Of the stress-strain curves obtained in Appendix D only Mix I3 was taken to ultimate. The model can therefore only be checked against the experimental results of specimens UTA1 and UTA2. The complete stress-strain curve of Mix I3 is shown in Fig. 5.17. A least squares fit to the data was used to obtain Eq. 74 which will be used to represent the slope of the stress-strain curve in the inelastic region of Chen's model.

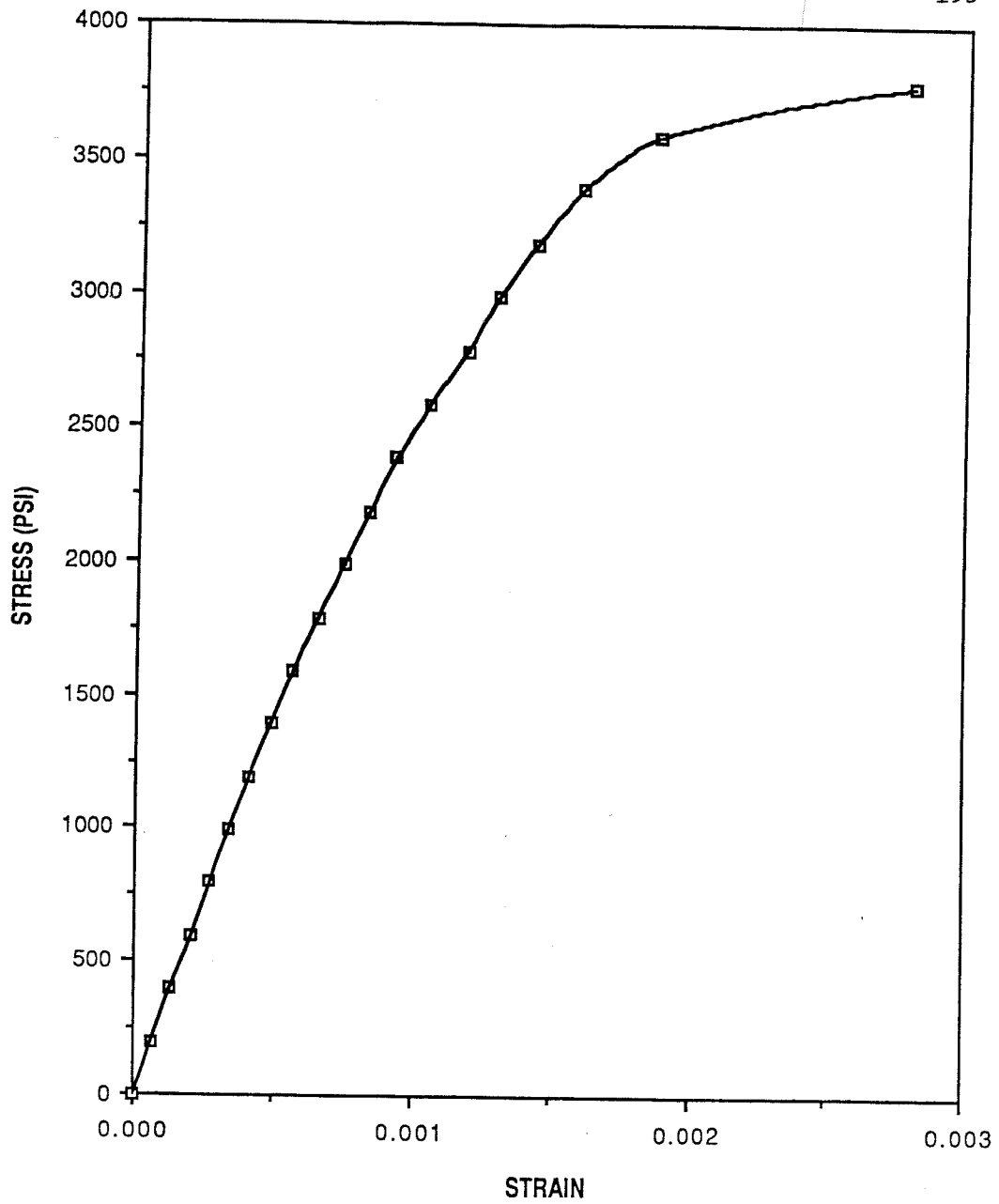


Fig. 5.17 Uniaxial stress-strain curve for grout mix 13

$$\sigma_u = 3.07E6\epsilon_u + 5.99E8\epsilon_u^2 \quad (74)$$

The required geometric and material properties for the calculation of the load due to key action are given in the following tables; shear-key geometry Table 2.5, annulus properties Table 2.9,  $E_g$  and  $\nu$  Table 3.1. Table 5.1 gives the predicted ultimate strengths for specimens UTA1 and UTA2 using Chen's constitutive relations. These specimens had eight grout compression struts (eight shear keys).

The ultimate strengths obtained using Chen's constitutive relations are approximately 60% of the experimental values. It is important to remember that loads obtained using Chen's constitutive relations were for infinitely stiff tubes which means the predicted values should actually be higher than the measured values since the experimental tubes were not infinitely stiff. The results in Table 5.1 indicate that approximately 36% of the load is carried by shear key action while the remaining 64% is carried by bond friction. Thus it would seem that under such severe boundary conditions, i.e. infinitely stiff tubes, the inclusion of triaxial data in the development of the constitutive relations may be essential. Another reason for the large discrepancy between the predicted and measured values could be that the assumed state of stress at the critical location is not valid. However, it would seem that with the boundary condition of infinitely stiff tubes the predicted solution should be

Table 5.1 Predicted Axial Strengths for Series 1 Using Chen Constitutive Relations

Specimen No.	Key Load	Bond Friction Load	Cal. Load	Meas. Load
	(kips)	(kips)	(kips)	(kips)
UTA1	220	390	610	973
UTA2	210	380	590	1007
Ave.	215	385	600	990

Table 5.2 Predicted Axial Strengths for Series 1 Using Fardis' Constitutive Relations

Specimen No.	Key Load	Bond Friction Load	Cal. Load	Meas. Load
	(kips)	(kips)	(kips)	(kips)
UTA1	370	670	1040	973
UTA2	370	660	1020	1007
UTA3	420	750	1160	960
Ave.	380	690	1075	980

greater than 60% of the measured values, even if the assumed stress-state is not strictly valid.

5.8.3 Predicted Strength of Series 1 Axial Specimens Using Fardis' Constitutive Relations. The required geometric and material properties for the calculation of the load due to key action,  $P_k$  are given in the following tables; shear-key geometry Table 2.5, annulus properties Table 2.9,  $E_g$  and  $\nu$ , Table 3.1. The Fardis model yields the strengths as shown in Table 5.2 for the Series 1 specimens. These specimens had eight grout compression struts (eight shear keys).

The predicted loads indicate that approximately 36% of the load is carried by shear key action and the remaining 64% by bond friction. The predicted ultimate strengths using Fardis' constitutive relations are approximately 10% higher than the measured values. As discussed previously the predicted ultimate strengths are for grouted connections with tubes which are infinitely stiff radially. The results shown would indicate that the steel tubes used in the experimental work were radially very stiff when compared to the grout stiffness.

5.8.4 Discussion of Predicted Series 1 Strengths Using Chen's and Fardis' Constitutive Relations. A comparison of the results shown in Tables 5.1 and 5.2 indicate that the ultimate strengths predicted by Fardis' relations are almost double those predicted by Chen's relations. The values from the Fardis relations

also compare more favorably with the measured results. The reason that the predicted ultimate strengths of the Fardis' relations are higher than the measured strengths can be attributed to the boundary conditions, i.e. infinitely stiff tubes. However, as stated previously these results would tend to indicate that the tubes used in the experiments had large radial stiffnesses when compared with the grout.

In the Fardis' model the portion of the load carried by bond friction would indicate a bond stress of approximately 1500 psi developed at the interface of the grout compression strut and the steel tube. This value is approximately 5 to 10 times higher as that developed in a plain pipe connection where the normal force is a function of Poisson's ratio of the grout and steel tubes. This higher bond stress in a grouted connection with shear keys can be attributed to the wedging of the grout compression struts between the shear keys which allows for higher normal forces and consequently higher bond friction forces.

The results also indicate that care must be taken in the selection of constitutive relations used in modeling the behavior of grout in a grouted connection since considerable variation in predicted ultimate strengths may be obtained. In the case of the grouted connections, where the grout is subjected to high levels of



triaxial stress, the results indicate that the constitutive relations used should include triaxial data in their development.

#### 5.9. Effect of Load Step, Material and Geometric Parameters Using Fardis' Constitutive Relations

In this Section the effect of load step and various material and geometric parameters; i.e. grout cube strength, grout modulus, Poisson's ratio, and shear key height and spacing, on the ultimate axial strength of grouted connections will be investigated using the Fardis' constitutive relations.

5.9.1 Effect of Load Step Size. As stated previously, the loads listed in Table 5.2 were obtained using a load increment of 25 lbs. In Table 5.3, the results of the analysis for specimen UTAl with various load step sizes are listed. The results indicate that for the "small" load step sizes used in the analysis there is only about a 8% range in the calculated strengths. An examination of the shear key and bond friction components making up the total strength indicate that both components have the same 8% change in estimated strength over the range of step sizes shown. Fardis constitutive relations, as with all plasticity models, are incremental in nature and thus dependent upon the load path. For this simplified model the computational time is minimal even for very small load step sizes, therefore a load step size of 25 lbs will be used in all future calculations. In larger models the decision of the proper load step

Table 5.3 Effect of Load Step Size on Calculated Strength of Axial Specimen UTA1

Load Step Size	Key Load	Bond Friction Load	Calculated Strength
(lbs.)	(kips)	(kips)	(kips)
5000	400	720	1120
1000	384	691	1075
500	376	677	1053
100	371	668	1039
50	371	667	1038
25	371	667	1038
10	371	667	1038

size should be based on convergence of the ultimate strength and the stress-path traversed in stress space. The stresses along the stress-path to the failure (bounding) surface will also converge to the "exact" solution as the load step size is reduced. Convergence occurred for the grouted connection model using the Fardis constitutive relations in the range of 25-50 lbs.

Figure 5.18 shows the ratio of the calculated lateral confining pressure to key bearing stress versus the key bearing stress. The Fardis model predicts an initial compaction (volume decrease) of the material with a corresponding value of the ratio of about 0.175. This is followed by a region in which there is compaction at an increasing rate leading to a decrease of the ratio to about 0.15. This coincides with the onset of substantial inelastic behavior in the grout and suggests a collapse of the void structure in the grout. Beyond this point, dilatancy (volume increase) occurs and the ratio begins to increase until a maximum ratio of about 0.389 is obtained. Past the peak, grout is compacted with an associated decrease of the ratio until failure is obtained. It is worth noting here, that Chen's model predicts dilatancy from initial loading until failure. The initial ratio is the elastic value of 0.25 and the value increases to 0.489 at failure.

5.9.2 Effect of Radial Stiffness. As mentioned earlier, the tubes used in The University of Texas experimental

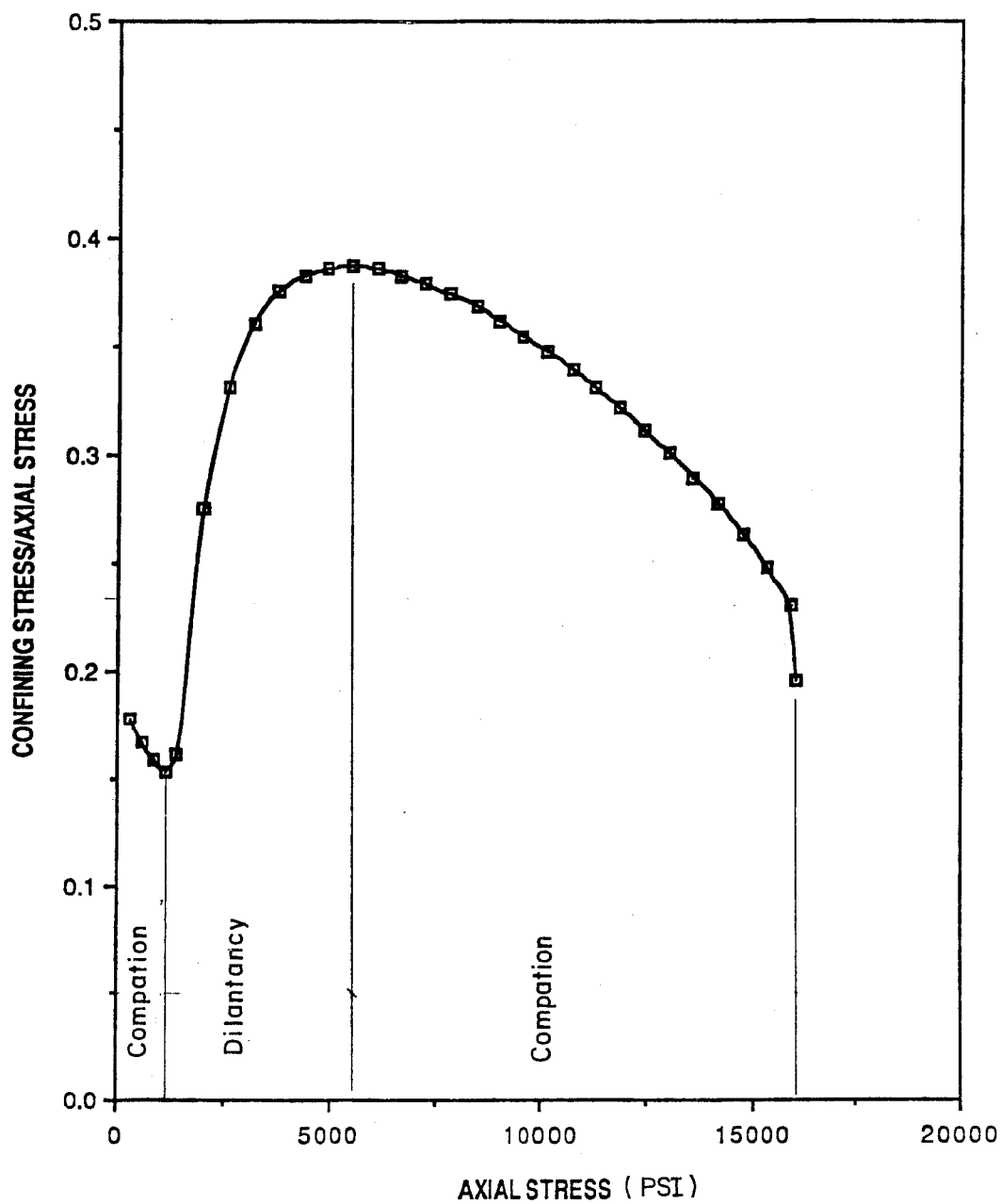


Fig. 5.18 Ratio of the calculated lateral confining stress to bearing stress vs bearing stress as predicted by the Fardis constitutive relations

program appear to be fairly stiff radially since the measured loads are close to those obtained for infinitely stiff tubes. Figure 5.19 shows the variation of radial stiffness of a steel tube as a function of  $D/t$ . The value of  $D/t = 20$  was arbitrarily assigned the value of one since normal  $D/t$  ratios in piles are greater than 20 and it is the limiting value for thin-walled tubes. The sleeves, which are the main tubes controlling the amount of lateral confinement to the grout normally have  $D/t$  ratios greater than 40. In The University of Texas program the pile  $D/t = 28.8$  and sleeve  $D/t = 42$ . The stiffness of the sleeve tubes is approximately 5 times that of the grout in the elastic range and increases during loading since the sleeves remained elastic whereas the stiffness of the grout reduced as it became inelastic. Although it is very difficult to establish conditions that would constitute an infinitely stiff sleeve, the tubes used in The University of Texas tests are reasonable represented by assuming infinite stiffness. Since the radial stiffness of a tube can be expressed as a function of  $D/t$  it should be possible to develop an empirical relationship between the infinitely stiff tubes used in the model and the actual radial stiffness of the test specimens. Wimpey Labs Series P and R tests shown in Fig. 5.2 would be one such series which could be used in conjunction with The University of Texas Series 1 in establishing such a relationship. The model, however

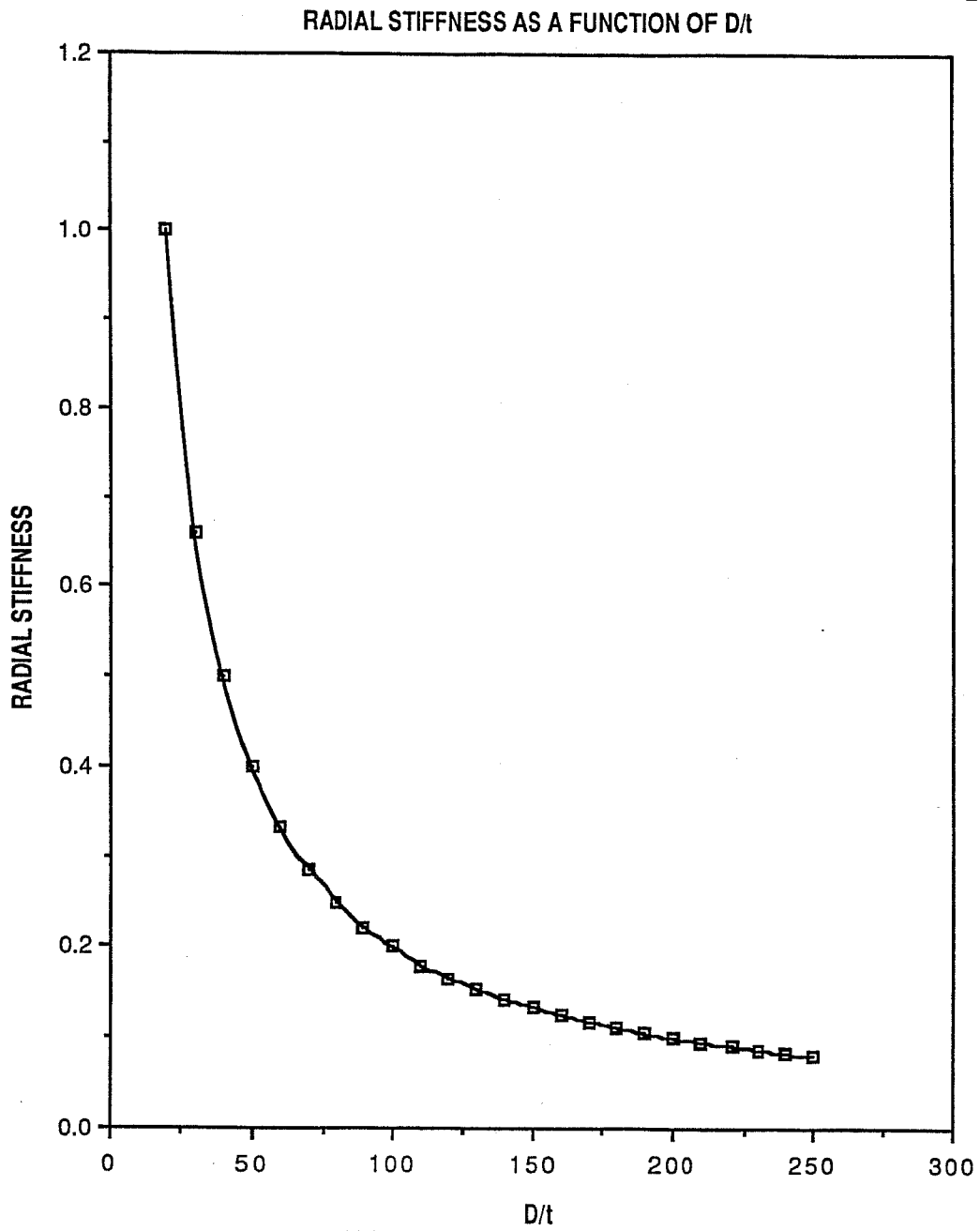


Fig. 5.19 Variation of radial stiffness of steel tube as a function of  $D/t$

requires both  $E_g$  and  $\nu$  values, yet the only grout property reported by Wimpey Labs or by other investigators is the unconfined compressive strength of the grout,  $f_{cu}$ . This makes the development of an empirical relationship for tubes with radial stiffness less than infinity impossible at the present time. The model, therefore, provides an upper bound solution to strength of a grouted connection for a given set of geometric parameters.

5.9.3 Effect of Cube Strength Variation. The cube tests used to determine the unconfined compressive strength of the grout  $f_{cu}$  were discussed in Section 4.4. The results of The University of Texas and Wimpey Labs [21,33] studies on cube strengths indicated that there is an average coefficient of variation of between 10% - 20% for both 2" and 3" cubes. Figure 5.20 illustrates the effect of cube strength variation on the ultimate strength predicted by the model for Test UTA1. If the recorded  $f_{cu}$  had been 80% of  $f_{cu}$ , the ultimate calculated strength correspondingly would decrease 17%. If the grout strength recorded had been 20% higher, then the calculated ultimate load would increase 16%. These results show that the model predicts a linear relationship between  $f_{cu}$  and predicted ultimate strength, i.e. a 10% increase/decrease in  $f_{cu}$  will cause a slightly lower increase/decrease in the ultimate strength. The variation of ultimate strength with cube strength indicates that for

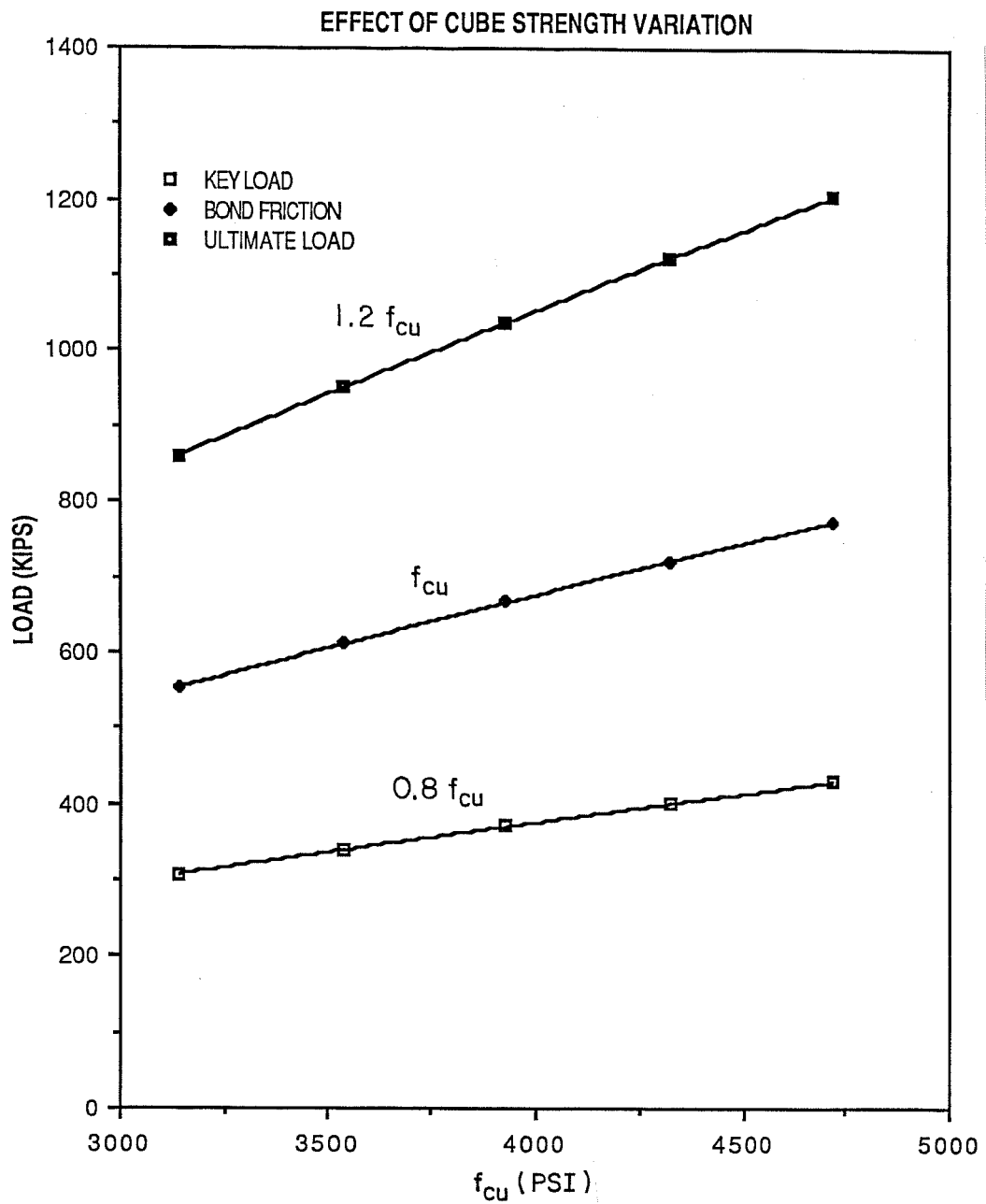


Fig. 5.20 Effect of cube strength variation on predicted ultimate strength



the observed coefficient of variation of cube strength the ultimate load predicted by the model could vary by as much as  $\pm 20\%$ .

5.9.4 Effect of Poisson's Ratio. Figure 5.21 shows the effect of varying the value of Poisson's ratio, while keeping all other parameters constant. For specimen UTAl, a 5% decrease in  $\nu$  results in a 8% decrease in strength. Alternatively a 5% increase in  $\nu$  results in a strength increase of 8.7%. If the two components, key load and bond friction are examined separately, both components increase at the same rate for a given increase in  $\nu$ . The dependence of the model on Poisson's ratio is not unexpected since it affects the volume changes that the grout undergoes which determines the amount of confining pressure that develops. The lateral pressure is related to the ultimate load through Coulomb friction.

For the grouts used in The University of Texas program  $\nu$  ranged between 0.20 and 0.23. Based on the limited experimental data, Poisson's ratio of the higher strength grout, appears to be comparable with the values for normal strength grout. This trend is comparable with that found for concrete [46,47,48]. The range of expected values of  $\nu$  for grout is between 0.20 and 0.23 but even with this narrow range, large differences in the ultimate strength of a grouted connection can be obtained. A lower value of  $\nu$ , however, will always yield a lower estimate on the upper bound strength.

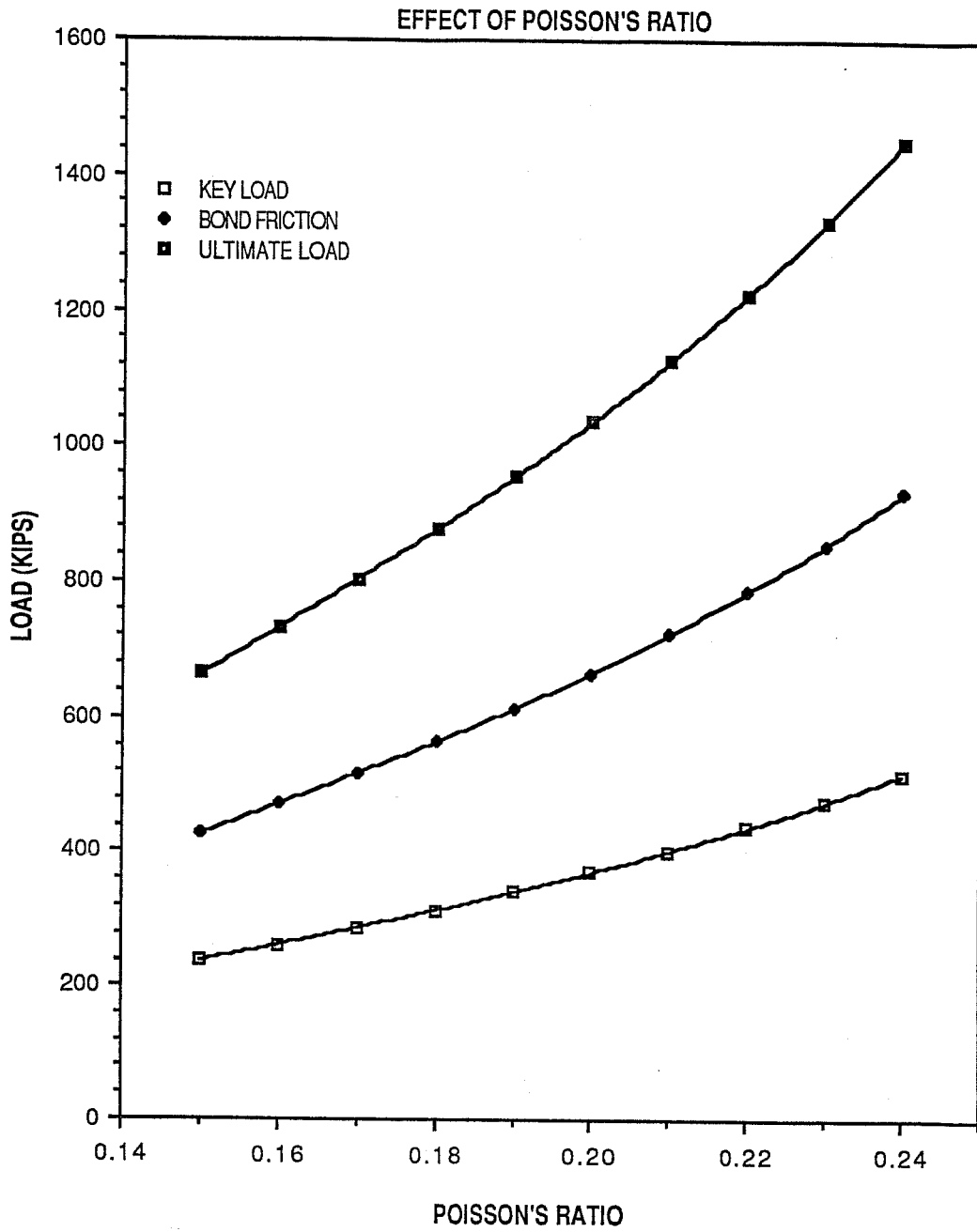


Fig. 5.21 Effect of Poisson's ratio on predicted ultimate strength

5.9.5 Effect of Grout Modulus. The modulus of elasticity,  $E_g$  was determined using 4" x 8" cylinders as described in Section 2.3.6. Figure 5.22 shows the variation in calculated ultimate strengths using varying grout moduli while keeping all other variables constant. For specimen UTA1 a 50% decrease in  $E_g$  decreases the predicted ultimate axial load 19.8%. Similarly a 50% increase in  $E_g$  causes only an 6.6% increase in the calculated strength. In each case Fig. 5.22 indicates that the components are affected similarly by the change in grout modulus. Experimental results of replicate modulus tests on a given batch of grout indicate very consistent results, with variations of less than 2% in all cases. This consistency indicates that within practical ranges of grout moduli the computed values can be considered almost independent of  $E_g$ .

Figure 5.23 shows the variations of Young's modulus,  $E_g$ , Generalized shear modulus,  $H$  and the initial tangent stiffness,  $\kappa_o$  with grout strength for the different grout batches listed in Appendix D. For the range of grout cube strengths used in The University of Texas test program (4000 - 11000 psi) there is a linear relationship, within the scatter of the data, between  $f_{cu}$  and  $E_g$ .

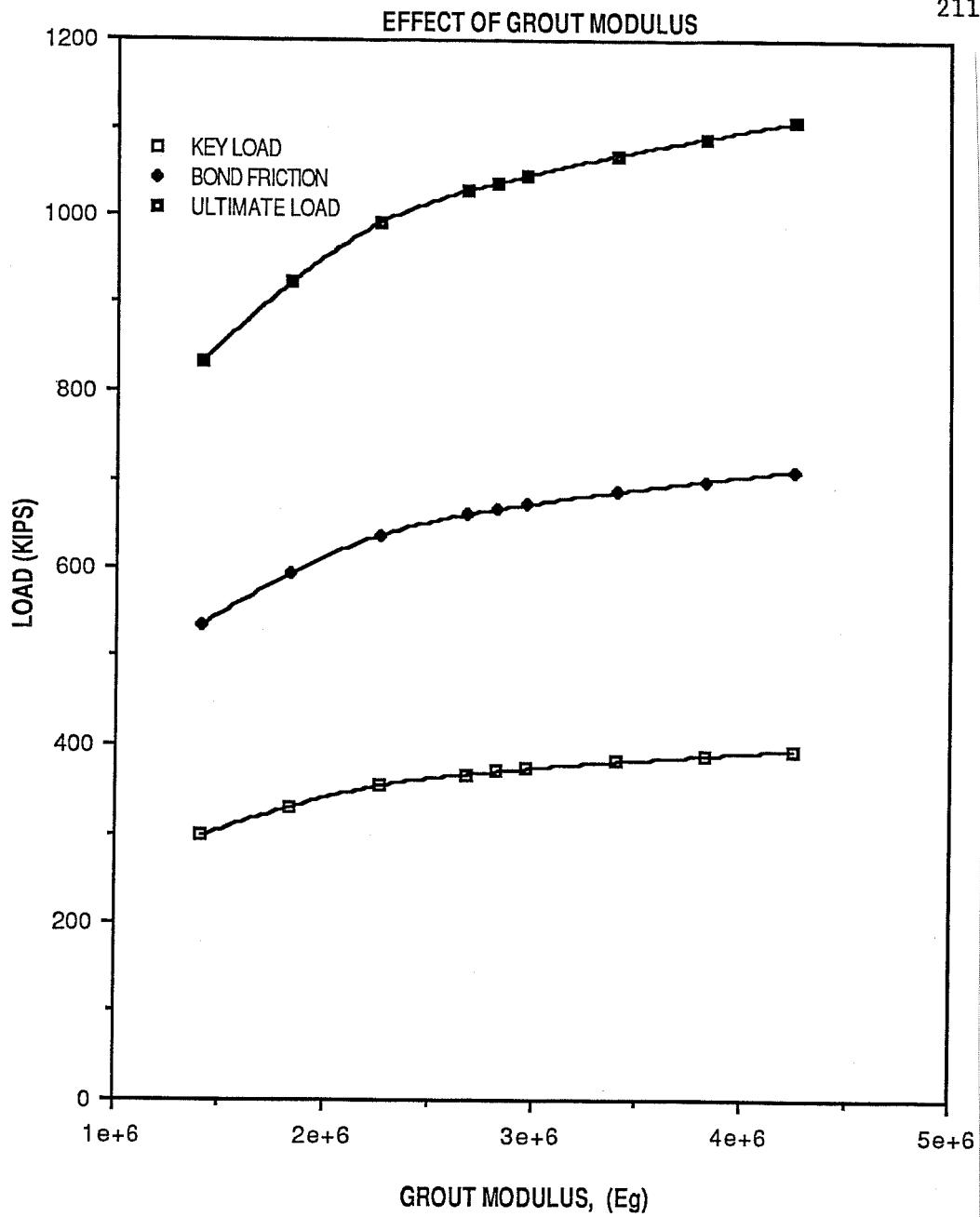


Fig. 5.22 Effect of grout modulus on predicted ultimate strength

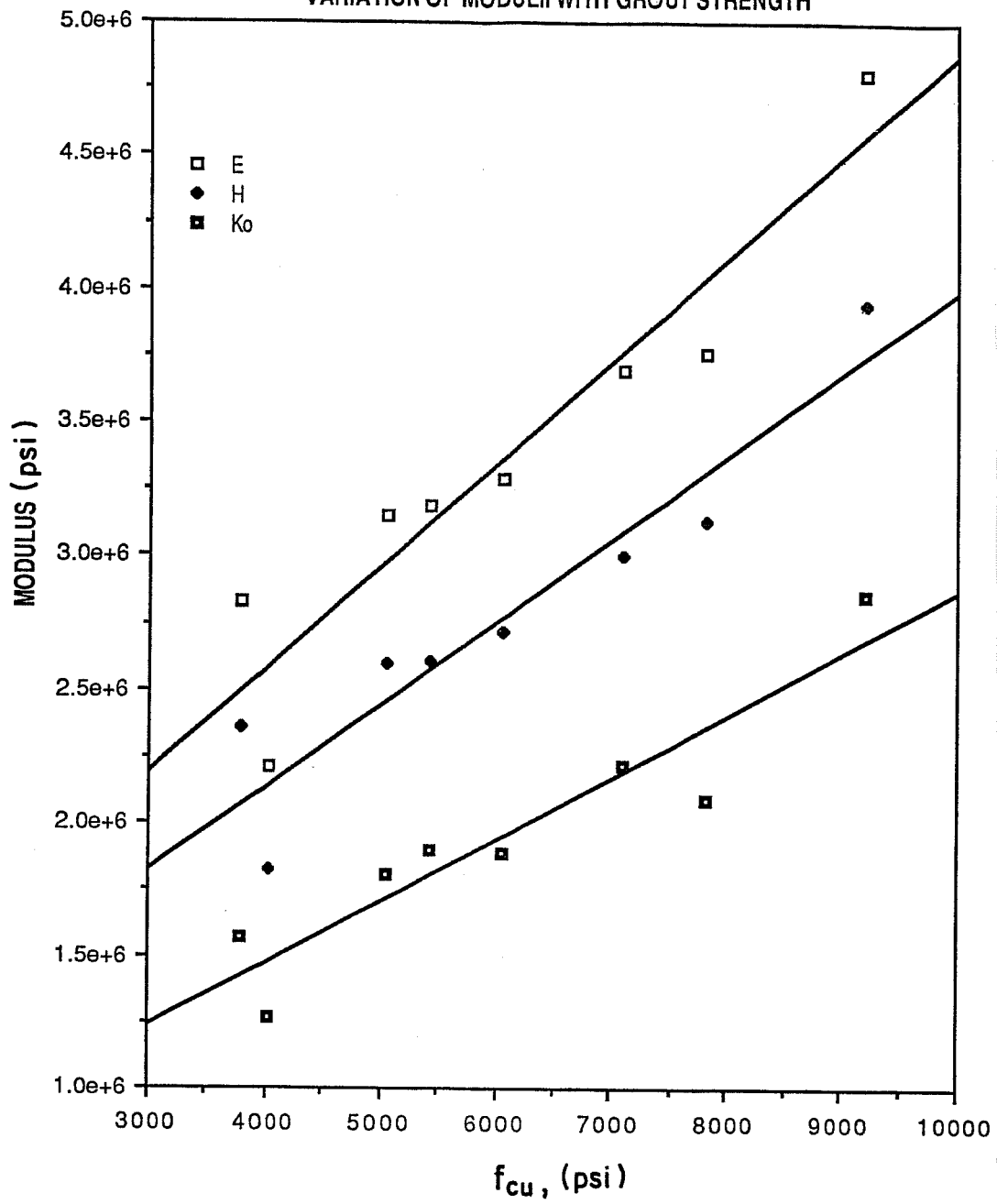


Fig. 5.23 Variation of moduli with grout strength

5.9.6 Effect of Shear Key Height. Figure 5.24 shows the effect of changing shear key height for specimen UTAl while keeping all other parameters constant.

The initial linear behavior in the range of  $h/D_p$  from 0.00 to 0.005 is similar to the trend shown in Fig. 5.5 for the Wimpey Lab tests, with increasing ultimate strength as  $h$  increases. The slope of the initial linear region, shown in Fig. 5.24, is a function of the shear key spacing. Unlike Fig. 5.5, Fig. 5.24 indicates that there is an upper limit on shear key height. For specimen UTAl with  $t_g = 1.0$ " and  $s = 4.25$ " the optimum  $h/D_p$  is approximately 0.007 ( $h = 0.125$ " ). For heights greater than about 0.125" the ultimate strength decreases. As discussed in Section 5.3.3 this decrease in capacity is due to the combination of high key bearing stress and increasing shear stress in the grout caused by increasing  $h$ . It is worth noting here that of the current test results available all have had shear key heights less than optimal.

5.9.7 Effect of Shear Key Spacing. Figure 5.25 shows the effect of varying shear key spacing on the ultimate strength of specimen UTAl. The values of  $D_p/s$  shown in Fig. 5.25 varied from 2 to 17 ( $s = 1.0625$ " to 8.5" ). If  $D_g/s$  is reduced from the current value of 4.2 ( $s = 4.25$ " and 8 struts) for specimen UTAl to 2.1 ( $s = 8.5$  and 4 struts) Fig. 2.25 indicates an ultimate strength decrease

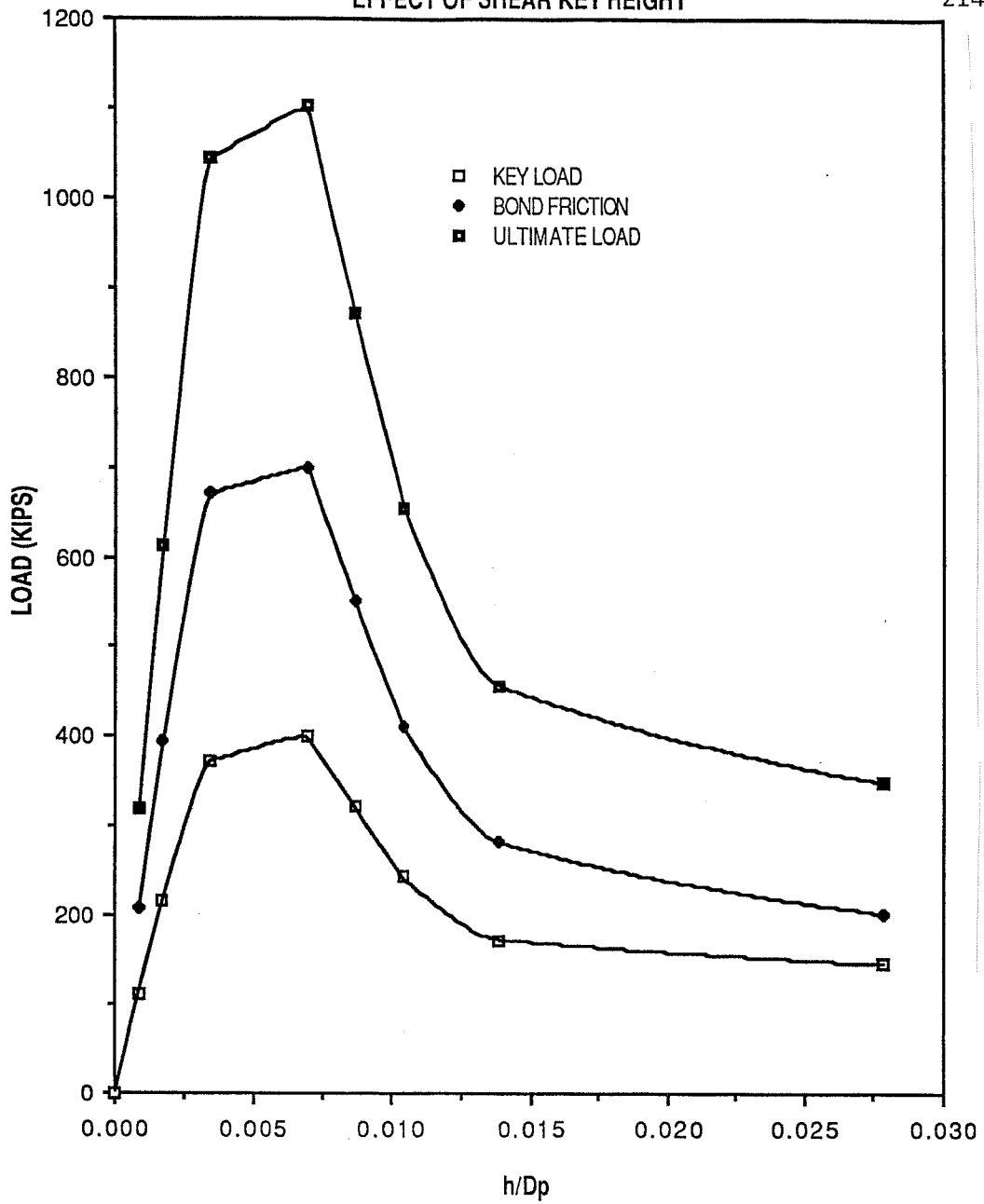


Fig. 5.24 Effect of shear key height on predicted ultimate strength

## EFFECT OF SHEAR KEY SPACING

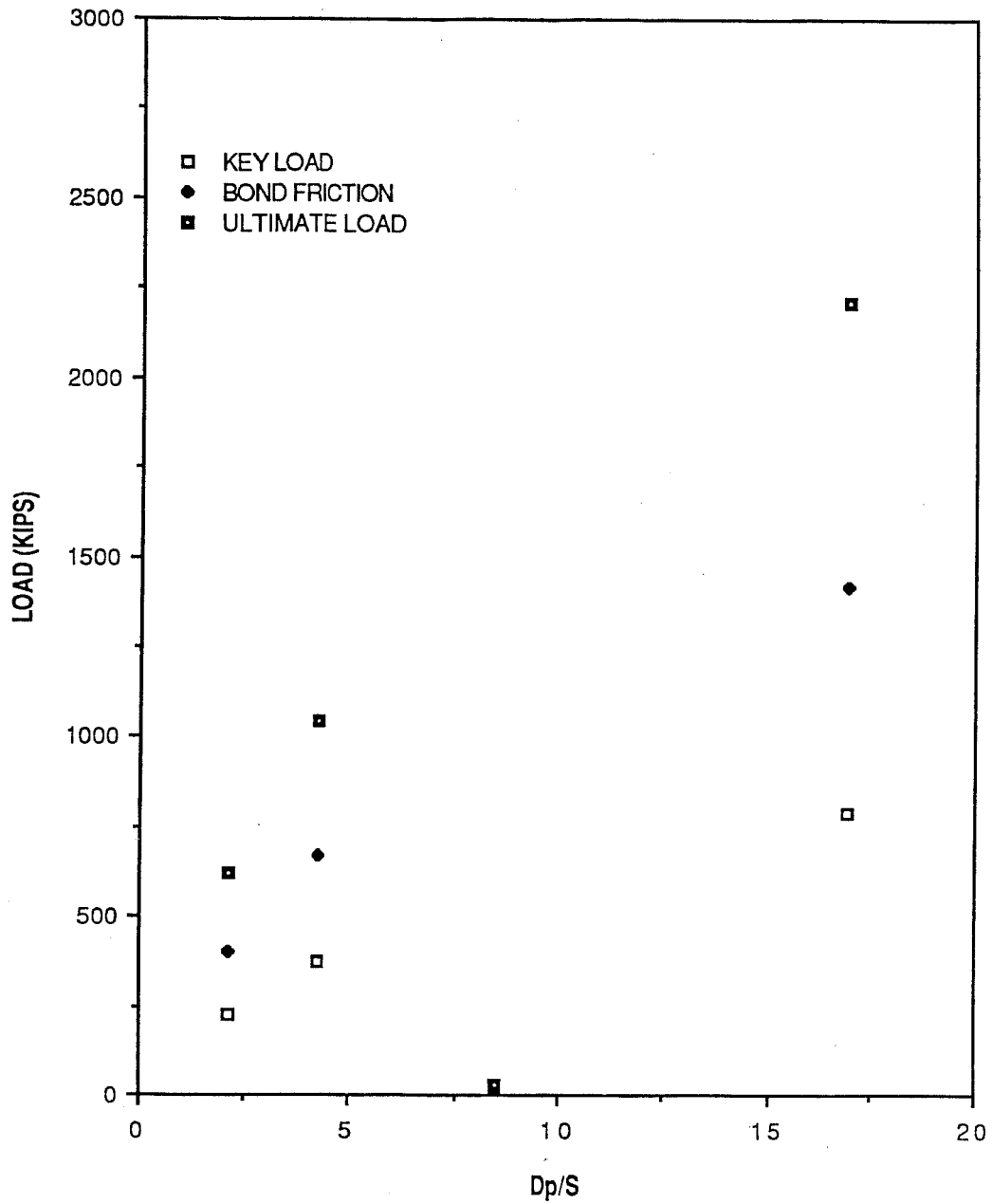
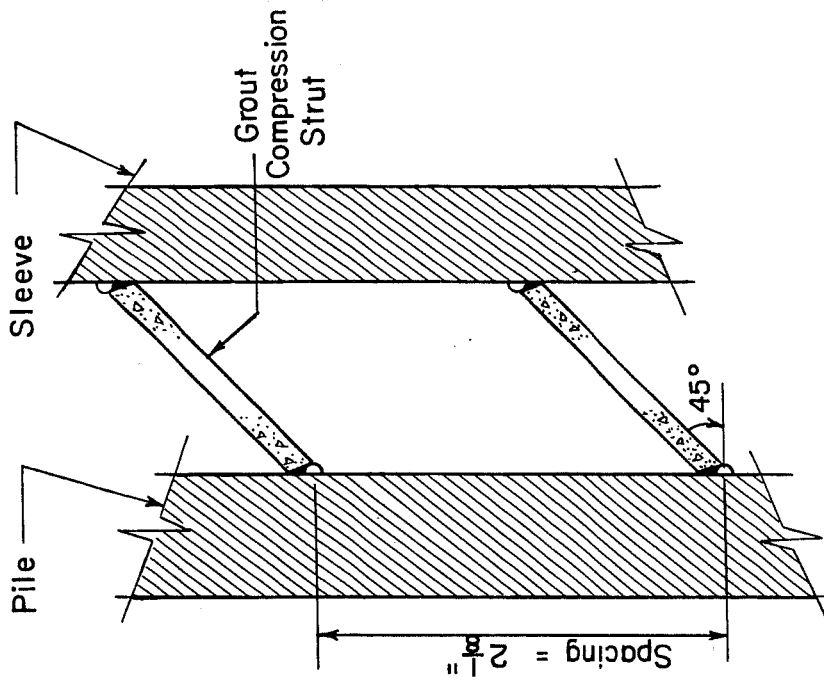


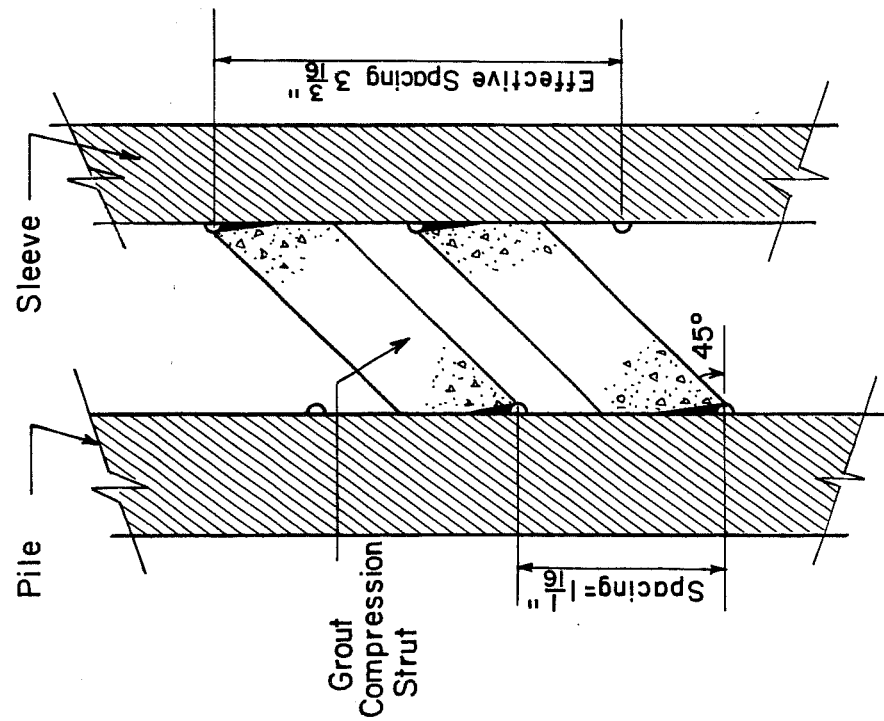
Fig. 5.25 Effect of shear key spacing on predicted ultimate strength



of 40.2%. Similarly increasing  $D_p/s$  to 16.9 ( $s = 1.0625"$  and 30 struts) causes a strength increase of 113%. These results indicate a nearly linear relationship between ultimate strength and shear key spacing and is comparable with the results shown in Fig. 5.6. Figure 5.25 indicates that if  $D_p/s$  was 8.5 ( $s = 2.125"$  and 16 struts) the predicted strength would be approximately 30 k. This predicted strength can be explained by the assumed crack angle of  $45^\circ$ . As discussed in Section 4.6 the orientation of the cracks in a grouted connection are independent of the relative location of the shear keys on the pile and sleeve. Thus for a spacing of 1.0625", the assumed angle of cracking ( $\alpha=45^\circ$ ) caused the strut to step over the closest shear key on the opposing tube as shown in Fig. 5.26a. Thus the effective shear key spacing used in calculating the strut width is 3.1875" instead of 1.0625". For the case of 2.125" spacing the crack does not step over the closest shear key on the opposing tube. This causes the strut width to become extremely small at only 0.0625", see Fig. 5.26b and with all the material between the struts ignored the load required to fail the strut is minimal. This implies that for certain shear key spacing the grouted connection strength would be only slightly higher than that of a plain pipe connection. The angle used to establish strut orientation is extremely important in determining the ultimate strength, since it controls the width of the strut.



(a)



(b)

Fig. 5.26 Effect of assumed strut orientation in establishing effective shear key spacing

5.9.8 Optimal Shear Key Height and Spacing. As stated in Sections 5.3.4 and 5.3.5 there should be an optimal combination of shear key height and spacing for a given grout strength and radial stiffness. Figure 5.27 shows the results of varying  $h$  and  $s$  for specimen UTA1 while keeping all other variables constant. As the spacing of the shear keys is reduced, the strength of the grouted connection increases due to the increase in the number of grout compression struts. The figure indicates, however, that the optimal value of  $h/D_p$  also decreases with decreasing shear key spacing. As shear key spacing is decreased the maximum useful height of the shear key also decreases. Table 5.4 lists the optimal shear key height and corresponding loads for the spacings shown in Fig. 5.27. As the shear key spacing is reduced the magnitude of the shear stress along the cylindrical surface A-A, shown in Fig. 5.7a will increase due to the decrease in the strut width. Thus the critical combination of stresses occurs at lower shear key heights and reduced spacings. Figure 5.27 clearly shows that arbitrarily increasing shear key height and reducing shear key spacing may not always lead to higher ultimate strengths in a grouted connection.

5.9.9 Application of Fardis' Constitutive Relations to Axial Specimens with High Strength Grout. Table 5.5 lists the results for axial specimens of Series 6 using high strength grout and axial specimen UTA13 of Series 4.

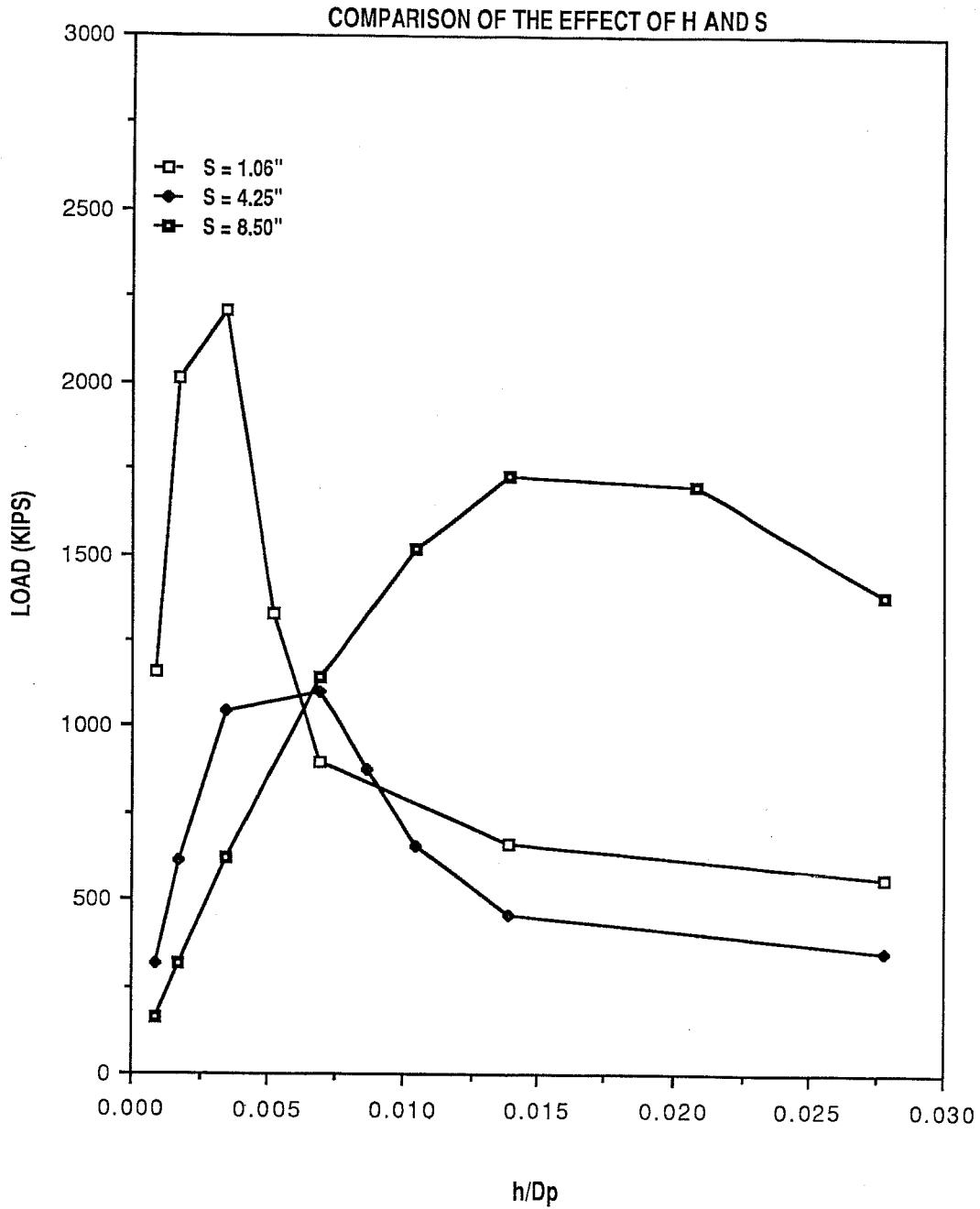


Fig. 5.27 Optimal shear key height for given shear key spacing

TABLE 5.4 Optimal Shear Key Heights for Different Shear Key Spacings

Shear key Spacing	Shear key Height	Key Load	Bond Friction Load	Ultimate Load
(in.)	(in.)	(kips)	(kips)	(kips)
1.06	0.0625	790	1420	2210
4.25	0.125	400	700	1100
8.50	0.250	660	1070	1730

TABLE 5.5 Calculated Loads for Specimens with High Strength Grout and  $L/D_p = 1$

Spec. No.	$f_{cu}$ (psi)	Key Load (kips)	Bond Friction Load (kips)	Cal. Load (kips)	Adj. Load (kips)	Meas. Load (kips)
UTA13	4930	240	440	680	490	524
UTA10	6630	320	580	900	650	537
UTA11	11120	600	1070	1670	1200	720
UTA12	10680	560	1000	1560	1120	693

The computed ultimate strength seems high when compared with the experimental values. There are two main reasons why the calculated ultimate strengths are high. First, the specimens listed in Table 5.5 all had values of  $L/D_p = 1$ . Wimpey Lab has stated that there is a significant length effect [9] in test specimens with  $L/D_p = 1$ . A coefficient  $C_L$ , (Eq. 5 in Chapter 1) of 0.72 for this length specimen is recommended. If this reduction factor is applied to the loads, then the ultimate strength calculated for UTA13 reduces to 490 k.

To obtain a clearer picture of how the proposed model behaves with increasing grout strengths, Table 5.6 lists the calculated loads for specimen UTA1 using grout mixes I4, I5, I6 and J2 (properties are given in Appendix D).

The results are plotted in Fig. 5.28. The plot indicates a linear relation between  $f_{cu}$  and calculated strength. This type of behavior is not unexpected since the constitutive relations were developed for normal strength concretes (3000 - 5000 psi). The experimental results, however indicate that the relationship between grout strength and ultimate strength is closer to  $\sqrt{f_{cu}}$  than to  $f_{cu}$  as currently predicted by Fardis' constitutive relations.

Ideally, functions representing the generalized shear modulus, tangent stiffness, and shear compaction/dilatancy factors in

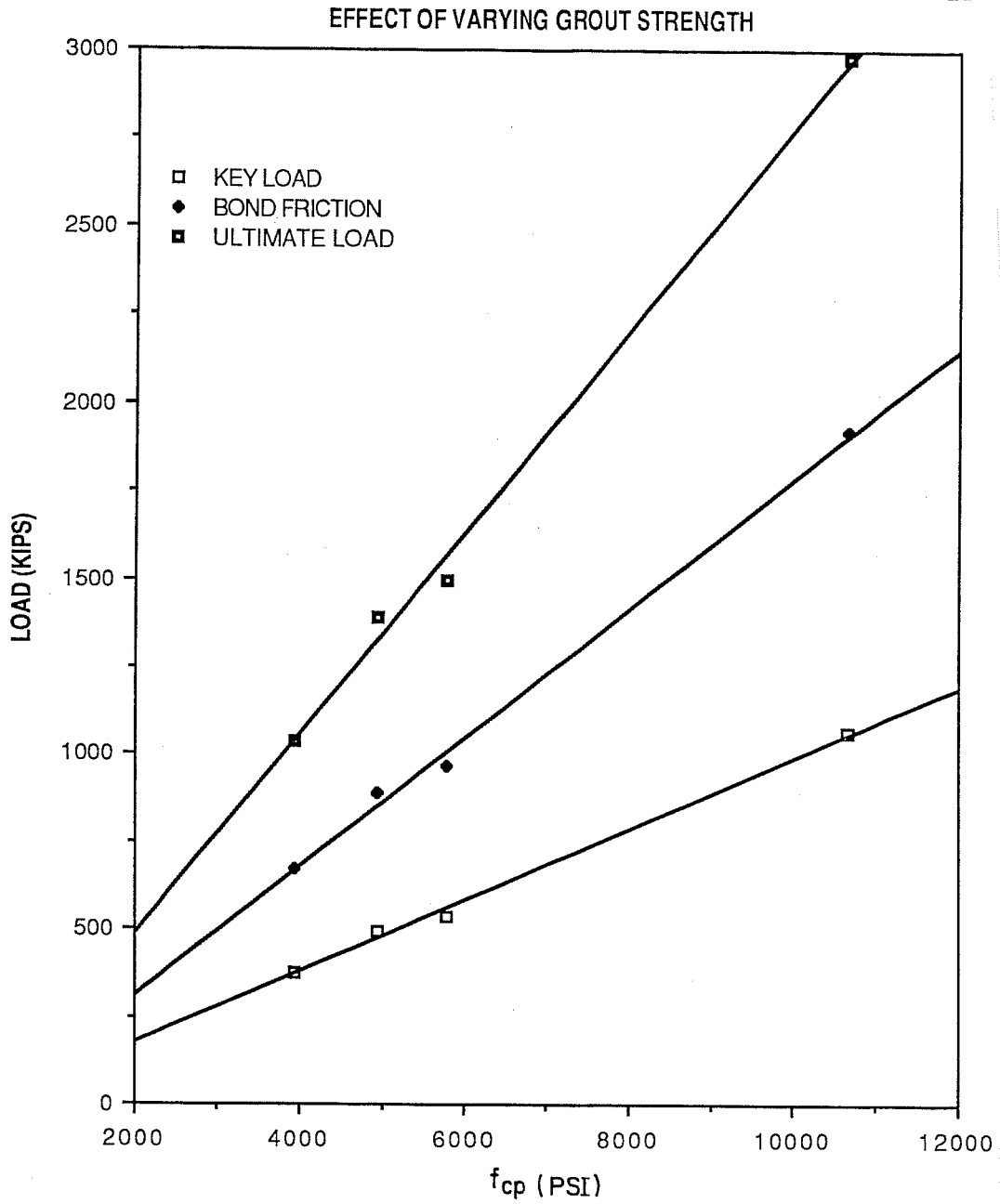


Fig. 5.28 Effect of increasing grout strength on predicted ultimate strength

TABLE 5.6 Effect of Increasing Grout Strength on the Ultimate Strength of UTAl

$f_{cu}$ (psi)	Strut Load (kips)	Bond Friction Load (kips)	Total Load (kips)
3930	370	670	1040
4930	500	890	1390
5780	540	960	1500
10680	1060	1920	2980



the model should be redeveloped or adjusted for all ranges of concrete/grout strengths using a family of uniaxial, biaxial, and triaxial stress-strain curves for a wide range of concrete/grout strengths. The uniaxial stress-strain curves given in Appendix D can not be used since these are not to ultimate. Without this information, only simple somewhat crude adjustments can be made in modifying the model for high strength concrete/grout. Work by Carrasquillo [47] contains stress-strain curves for a high-strength gravel concrete which has properties similar to the high strength grout Mix J2, (Table 2.4). The properties of the mix, hereafter referred to as Mix G1, are  $f_{cu} = 10571$  psi,  $E_g = 3720000$ ,  $\nu = 0.20$ ,  $w/c = 0.47$  and  $\epsilon_{max} = 0.0036$  at ultimate stress. The behavior of high strength grout will be assumed to be similar to that of high strength concrete.

Figure 5.29 shows a plot of the experimental axial and lateral strains of Mix G1 as obtained by Carrasquillo [47] versus those calculated using the Fardis constitutive relations for uniaxial compression. The plot shows that for the axial strains, the constitutive relations underestimate the initial stiffness of the concrete and overestimate the strain at failure. In the case of the lateral strains, the computed values are significantly less than the measured values, however, the failure strains are approximately

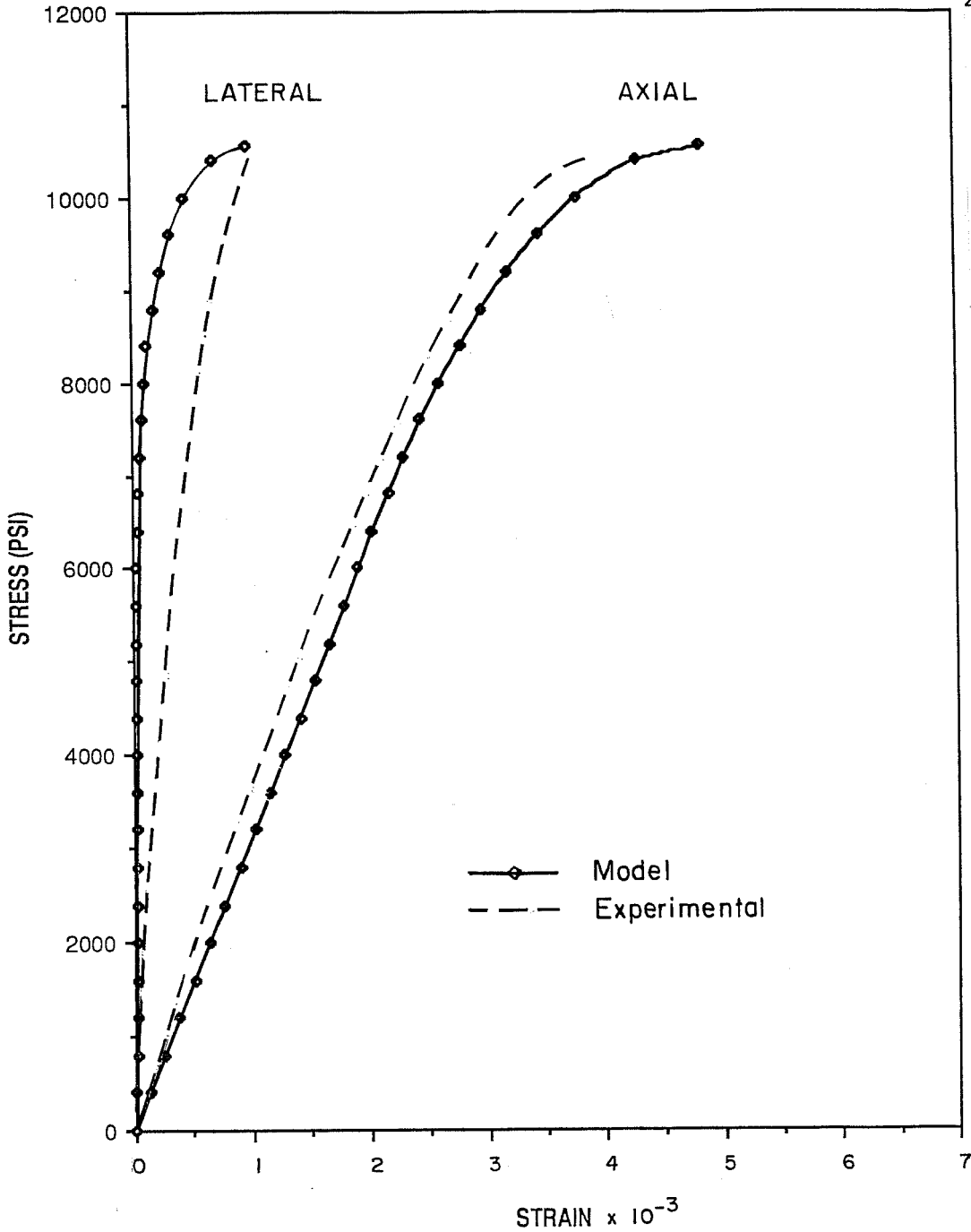


Fig. 5.29 Comparison of Carrasquillo's experimentally obtained uniaxial compression test strains with those predicted using Fardis' constitutive relations, for high strength gravel concrete

equal. The calculated axial and lateral strains can be adjusted by modifying or changing the form of Eqs. 60 and 64 used to represent the generalized shear modulus and shear compaction/dilatancy. In general, the generalized shear modulus controls the initial slope of the axial strain curve. One simple method of modifying Eq. 60 is to change the constant 16 to a larger value which in turn will increase the value of  $H$  at any given load level. Increasing  $H$  will also decrease the ultimate strength calculated for grouted connections since both the axial and lateral strains at failure will be reduced. The amount of lateral strain and corresponding dilatancy that is calculated by Fardis relations is controlled by the  $\beta$  function given in Eq. 64. For normal strength concrete, volume becomes minimum at approximately 90% of the monotonic strength ( $0.90f_{cu}$ ). It is worth noting that Eq. 64 indicates that for  $d/d_{max}=0.1$ , i.e.  $0.90f_{cu}$   $\beta$  becomes zero. Results of Carrasquillo's work [47] indicate that for both high strength concrete and mortar there is continuous volume decrease until failure. This suggests that for high strength concrete  $\beta=0$ . By letting  $\beta=0$  the amount of lateral strain that occurs at any given load level will increase, thus moving the calculated strains towards the experimental results. The effects of  $\beta$  and  $H$  are not, however, independent. For example, if  $\beta = 0$  and the function representing  $H$  is left in its original form the calculated ultimate

strength will increase since the confining stress which develops is larger due to the increased lateral strains. Thus the procedure followed will be to let  $\beta=0$  and then change the constant in front of Eq. 64 until the calculated axial failure strain of the model corresponds with that obtained experimentally from the uniaxial compression test. Figure 5.30 show the results of this process with the final form of  $\beta$  and H given in Eqs. 75 and 76.

$$\beta=0 \quad (75)$$

$$H = 29f_{cu}(d/d_{\max}\epsilon_{\max})^{0.55} \quad (76)$$

The plot shows that initial experimental and calculated stiffnesses now coincide, yet the model does tend to underestimate the strains at high levels of stress. The amount of lateral straining predicted by the model has also increased, but at the higher stress levels the model again underestimates the strain.

If the modified constitutive relations are now applied to UTA1 with  $f_{cu} = 10680$  psi the resulting strut load = 800 k, bond friction load = 1440 k and ultimate strength = 2240 k, these compared with the the loads given in Table 5.6 for the original constitutive relations. Comparison of the modified and original loads show that the calculated strut load and bond friction load decreased by 25%. By using the modified form of the constitutive relations the

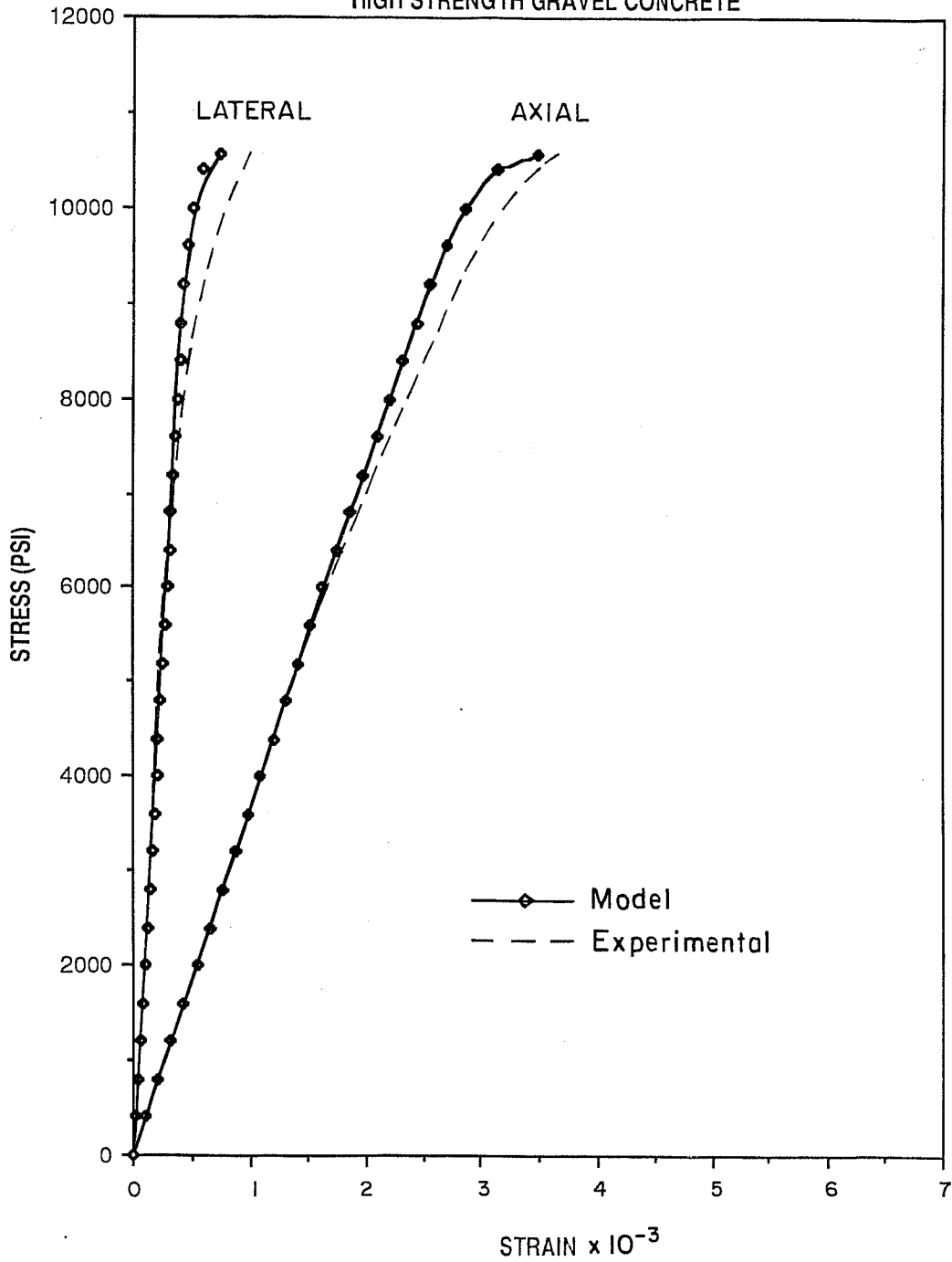


Fig. 5.30 Comparison of Carrasquillo's experimentally obtained uniaxial compression test strains with those predicted using Fardis' modified constitutive relations, for high strength gravel concrete

calculated ultimate strength now changes between the  $\sqrt{f_{cu}}$  and  $f_{cu}$  and thus more closely matches the experimental results.

For those cases and only those cases in which the high-strength concrete/grout exhibits compaction until failure will the above simple approach work in modifying Fardis constitutive relations. Carrasquillo's work [46] indicated that for the concrete mixes that he used this did not occur for concrete up to at least 8000 psi. If Fardis' constitutive relations are applied to concrete of this strength in their present form the ultimate capacity of the grouted connection would be greatly overestimated since the model would predict ultimate strengths which would increase linearly with  $f_{cu}$  while the experimental results show a variation closer to  $\sqrt{f_{cu}}$ . If  $\beta$  is left in its original form as given in Eq. 64 and only H given in Eq. 60 is modified the calculated loads become even more unconservative.

The main problem that exists then, is what exactly constitutes high-strength concrete/grout and what procedure is applicable for all ranges of concrete/grout strengths. To the author's knowledge there have been no constitutive relations developed for high-strength concrete nor have any of the existing models been compared to uniaxial, biaxial and triaxial experimental results, if they exist. All constitutive relations available for concrete at the present time were developed in the most part from concretes with strengths in the

range of 3000 - 5000 psi and their application to strengths beyond this range is questionable. Until further research is done and constitutive relations modified or developed for concrete with  $f_{cu} > 6000$  psi the author would recommend that existing constitutive relations be applied with caution.

#### 5.9.10 Summary of Computed Grouted Connection Strength.

At the present time the lack of published data on the basic grout material properties such as  $E_g$  and  $\nu$  do not allow for the correlation of theoretical and experimental results for conditions other than grout confined by infinitely stiff tubes. The Fardis et. al. [37] constitutive relations yield reasonable results for an upper bound solution of the ultimate strength of a grouted connection using normal strength grout. Based on the results of the simple model developed using one grout compression strut it would seem justified to apply the Fardis constitutive relations in a more sophisticated analysis such as finite element and expect good results. One reason that Fardis relations were able to model the high level of triaxial stress which the grout was subjected to in this analysis was the inclusion of triaxial data in its development.

The effect of the parameters such as radial stiffness, grout strength and material properties, shear key height and shear key spacing were examined and the following conclusions and

recommendations can be made. The model showed that the calculated ultimate grouted connection strength is linearly related to grout cube strength,  $f_{cu}$ . A conservative estimate on the upper bound ultimate strength of a grouted connection can be obtained using a lower bound estimate of the cube strength, which was shown to have a coefficient of variation of between 10% and 20%.

The parameter most affecting the calculated strength of a grouted connection is Poisson's ratio, even though results of experimental investigations show that the practical range of Poisson's ratio for grout is between 0.20 and 0.23. Conservative ultimate grouted connection strengths can always be obtained however by using a lower bound on Poisson's ratio. The effect of the other basic grout property  $E_g$  is not nearly as significant and in fact within the practical limits of application the calculated loads may be considered independent of  $E_g$ . For example, a +20% change in  $E_g$  causes less than a 5% change in the calculated strength for grouts exhibiting moduli in the range of 2000000.0 - 3000000.0 psi. As  $E_g$  increases the effect of varying  $E_g$  is even further reduced.

Increasing the shear key height of a grouted connection increases the ultimate strength of the connection. Figure 5.24 showed, however, that for a given spacing and grout annulus there is an optimal shear key height beyond which connection strength decreases due the combination of high axial and shear stresses.



In most cases decreasing the shear key spacing in a grouted connection increases the calculated strength since more grout compression struts will develop. For example, halving the spacing of the shear keys will cause the calculated load to approximately double. However, whether the load increases with decreasing shear key spacing is dependent upon the angle  $\alpha$  chosen for the crack orientation, since the angle establishes the strut width. Figure 5.29 showed that for any given spacing of shear keys there is an optimal height and that decreasing shear key spacing will cause this optimal shear key height to decrease. Again this is directly related to the combination of axial and shearing stress for a given shear key spacing and height.

The application of the present set of constitutive relations to grout strengths exceeding 6000 psi is not recommended unless extreme care is taken to assure the validity of the results. A simple approach for modifying the present form of Fardis relations was shown to yield reasonable solutions for grouts which exhibit compaction until failure.

## CHAPTER 6

### SUMMARY AND CONCLUSIONS

#### 6.1 General

Eighteen grouted pile-to-sleeve connection tests were conducted to examine the influence of moment, relative shear key location between pile and sleeve, eccentric piles and sleeves and grout strength on axial strength. These tests along with three reference tests were divided into six test series each containing three replicates. The measured strengths were compared with the current empirical equations recommended by the API and United Kingdom Department of Energy for determining the ultimate strength of a grouted pile-to-sleeve connection. These equations are expressed in terms of an ultimate bond stress as

$$\text{API: } f_{bu} = 167 + 1.72f_{cu}h/s$$

$$\text{UK: } f_{bu} = 16K C_L (9C_s + 1100h/s) f_{cu}^{0.5}$$

where  $K = 1/m(D/t)_g + [(D/t)_s + (D/t)_p]^{-1}$

A simple model, based on classical plasticity, was developed to provide an upper bound solution, i.e. a solution based on infinitely stiff tubes, for the strength of a grouted pile-to-sleeve connection. The model was then used to investigate the sensitivity of various material and geometrical parameters on the ultimate strength of a grouted pile-to-sleeve connection.

## 6.2 Summary of Experimental Results

6.2.1 Pile-to-Sleeve Connection Tests. The results of the tests reported herein, showed that moment had no detrimental effect on the ultimate axial strength of grouted pile-to-sleeve connections. For short connections ( $L/D_p = 1$ ) the axial strength increased due to prying forces that developed at the ends of the connection. The API and United Kingdom Department of Energy equations given above need not be modified to account for moment.

Two distinct pile-sleeve shear key arrangements were investigated. The results showed the relative position of the shear keys on the pile and sleeve had no affect on connection strength.

Eccentric pile-sleeve connections were investigated in which the grout annulus varied from a minimum of 1/2 in. to a maximum of 1-1/2 in. When compared with identical specimens having a constant 1 in. annulus the connection strength was found to be unaffected by the variations in annulus thickness.

The strength of a grouted pile-to-sleeve connection was found to be a function of the unconfined compressive strength,  $f_{cu}$  with the relationship better represented by  $\sqrt{f_{cu}}$  rather than  $f_{cu}$ .

The measured results were compared with the empirical equations given previously, the API equation was found to be more conservative in all cases. The United Kingdom Department of Energy

formulation yielded strengths that were in better agreement with the measured values, although the solutions were not always conservative.

6.2.2 Effect of Cube Size on Grout Strength. Limited studies showed the effect of cube size on the unconfined compressive strength of grout,  $f_{cu}$ . Two cube sizes, 2 in. (50.8 mm) and 3 in. (76 mm), were investigated using two different grout mixes. The results of these investigations indicated: (1) the coefficient of variation within a given cube size population is comparable with the coefficient of variation between cube sizes; and, (2) the difference between the unconfined compressive strength determined by 2-in. (50.8 mm) and 3-in. (76 mm) cubes is within the scatter of the measured grouted pile-to-sleeve connection strengths. For the cube sizes and grout mixes examined in the test program, cube size had no significant effect on the ultimate connection strength using the current empirical equations.

6.2.3 Injected Grout Column Cubes vs ASTM C109 Cubes.

A series of tests was conducted in which grout was injected into two different height grout columns of 3 ft (914.4 mm) and 6 ft (1828.8 mm). The unconfined compressive strength was determined from 2 in. (50.8mm) cubes cut from these columns. The results showed that the unconfined compressive strength of injected grout is generally less than that of ASTM C109 cubes. The standard deviation and coefficient of variation of injected grout cubes increased with increasing column

height. The coefficient of variation of the means of the injected grout column cubes is in the same range as that obtained for ASTM C109 grout cubes.

### 6.3 Summary of Analytical Study

The behavior of the grouted pile-to-sleeve connection was analyzed in order to develop a simple analytical solution for the ultimate connection strength. The main focus of the analytical study was to determine which parameters are important in the analysis of the grouted pile-to-sleeve connection and to establish the sensitivity of ultimate connection strength to these parameters. The simple model defined failure based a grout failure at a critical point and not on an overall structural analysis. Classical plasticity theory was used to determine the ultimate strength of the grout under states of triaxial stress. Two major components were assumed to resist the load; shear key bearing and Coulomb friction at the steel-grout interface. The model did not account for the effect of radial stiffness but provided an upper bound solution, i.e. infinitely stiff tubes, for the strength of a grouted pile-to-sleeve connection. The analytical study showed that the selection of constitutive relations used in modeling the behavior of a grouted connection is an extremely important consideration since considerable variations in predicted strength may be obtained. For grouted pile-to-sleeve connections,

where grout is subjected to high levels of triaxial stress, constitutive relations should include triaxial data in their development.

The sensitivity analysis using constitutive relations developed by Fardis et. al. indicated that predicted connection strength was linearly related to grout cube strength,  $f_{cu}$ . The experimental coefficient of variation of cube strength is between 10% and 20%. The material parameter most affecting the strength of a grouted connection was Poisson's ratio, even though results of experimental investigations showed that the practical range of Poisson's ratio for grout is between 0.20 and 0.23. The reliance of ultimate strength on Poisson's ratio is unfortunate because it is not a material parameter which can be readily controlled by mix design. Within practical limits of application the strength of a grouted pile-to-sleeve connection was shown to be independent of grout modulus.

For the geometric parameters of shear key spacing and height, the model trends are similar to those found by experimental investigators. Increasing the shear key height or decreasing spacing, in general, increases connection strength. However, the model showed that there are optimal shear key heights for a given spacing beyond which connection strength decreases due to the combination of high axial and shearing stresses in the grout. The model also showed that

the assumed angle of grout strut orientation is important and in certain instances can lead to lower strengths for decreasing shear key spacing. This behavior is caused by a decrease in the width of the compression strut which leads to a higher shearing stress in the strut and consequently lower predicted strengths.

Constitutive relations are currently based on normal strength concretes (3000 psi - 5000 psi) and the application of these to strengths beyond 6000 psi is not recommended unless extreme care is taken to assure the validity of the results. A simple approach for modifying the Fardis constitutive relations was shown to yield reasonable solutions for those high-strength grouts which exhibit compaction until failure.

#### 6.4 Recommendations for Future Work

The results of the experimental program indicate that for a given specimen geometry and grout strength the scatter in the ultimate strength of a grouted pile- to-sleeve connection with shear keys is in the range of 5% to 15%. Yet, when the results are converted to a bond stress the scatter of the data increases significantly. Therefore, a comprehensive study of the existing data should be done and the current methods used to convert loads to stresses should be investigated so that the data presentation does

not show more scatter than the ultimate loads determined during testing.

The injected column cube results indicated that there may be a length effect on the ultimate strength of a grouted pile-to-sleeve connection. Consequently, a series of experiments should be conducted to determine the relationship between ultimate connection strength and connection length.

Based on the results of the parameter study and sensitivity analysis using the simple model developed herein, it would seem justified to next apply the Fardis constitutive relations in a more sophisticated overall structural analysis using a finite element approach and to expect good results.

Past experimental programs have targeted the geometric parameters which effect the strength of grouted pile-to-sleeve connections. The current analytical study, however, has shown that for a fully reliable analytical model to be developed there must now be investigations into the mechanism of load transfer in the connection.

The test program reported herein, indicated that the inclination of the grout compressive struts may be related to the grout compressive strength. The angle of cracking is an important parameter since it establishes the width of the strut for a given



connection geometry, therefore, parameters effecting grout strut orientation should be investigated.

A major component of connection strength is contributed to frictional resistance. Thus there is a need to establish the coefficient of static friction at the grout-steel interface. Results of Rabbat's testing [35] yielded a coefficient of static friction for grout cast against cleaned rolled steel plate and low levels of normal stresses. This testing should be extended to see if the coefficient of friction changes or remains constant for high levels of normal stresses which develop in a grouted pile-to-sleeve connection and to determine the coefficient of static friction for shot-blasted surfaces.

The analytical study also revealed the need for current constitutive relations to be modified or redeveloped to account for the behavior of high strength concretes and/or grouts. Also, it would seem useful to develop constitutive relations which do not have a large dependency on material parameters, such as Poisson's ratio, over which designers have little or no control.

APPENDIX A



TEST REF.	SLEEVE		PILE		GROUT		SHEAR KEY		K	KM	L	L/D	AGE	FCU LOAD		FBU
	D in.	t in.	D/t	D in.	t in.	D/t	h in.	f in.						h/s	psi	
Q5	22.59	20	13.75	20.00	.63	31.99	22.00	1.00	22.02	.080	2.50	.0320	7.0	5265	557.9	
Q6	22.59	20	13.75	20.00	.63	31.99	22.00	1.00	22.02	.080	2.50	.0320	7.0	4864	566.1	
R1	22.59	20	13.75	20.00	.63	31.99	22.00	1.00	22.02	.040	6.67	.0060	7.0	5539	250.0	
R2	22.59	20	13.75	20.00	.63	31.99	22.00	1.00	22.02	.040	6.67	.0060	7.0	6663	270.4	
R3	22.59	20	13.75	20.00	.63	31.99	22.00	1.00	22.02	.120	6.67	.0181	7.0	5163	362.1	
R4	22.59	20	13.75	20.00	.63	31.99	22.00	1.00	22.02	.120	6.67	.0181	7.0	5174	377.4	
R5	22.59	20	108.67	20.00	.63	31.99	21.00	.50	42.06	.080	6.67	.0120	7.0	4928	321.4	
R6	21.59	20	108.67	20.00	.63	31.99	21.00	.50	42.06	.080	6.67	.0120	7.0	6663	341.8	
R7	24.59	20	123.91	20.00	.63	31.99	24.00	2.00	12.00	.080	6.67	.0120	7.0	5197	362.7	
R8	24.59	20	123.91	20.00	.63	31.99	24.00	2.00	12.00	.080	6.67	.0120	7.0	6466	364.7	
R9	22.59	20	13.75	20.00	.63	31.99	22.00	1.00	22.02	.080	6.67	.0120	7.0	6768	341.8	
R10	22.59	20	13.75	20.00	.63	31.99	22.00	1.00	22.02	.080	6.67	.0120	7.0	7361	301.0	
BPA1	7	13.78	16	87.50	12.38	37.33	13.46	.54	24.78	.060	1.65	.0364	1.00	677	337.5	
BPA2	7	13.78	16	87.50	12.38	37.33	13.46	.54	24.78	.060	1.65	.0364	1.99	2377	449.1	
BPA3	7	13.78	16	87.50	12.38	37.33	13.46	.54	24.78	.060	1.65	.0364	1.99	1083	259.3	
BPA4	7	13.78	16	87.50	12.38	37.33	13.46	.54	24.78	.060	1.65	.0364	1.99	2759	539.7	
BPA5	7	13.78	16	87.50	12.38	37.33	13.46	.54	24.78	.060	1.65	.0364	1.99	4058	717.0	
BPA6	7	13.78	16	87.50	12.38	37.33	13.46	.54	24.78	.060	1.65	.0364	1.99	1965	433.3	
BPA7	7	13.78	16	87.50	12.38	37.33	13.46	.54	24.78	.060	1.65	.0364	1.99	4392	665.2	
BPA8	7	13.78	16	87.50	12.38	37.33	13.46	.54	24.78	.060	1.65	.0364	1.99	6295	777.4	
BPA9	7	13.78	16	87.50	12.38	37.33	13.46	.54	24.78	.060	1.65	.0364	1.99	8059	760.1	
BPA10	7	13.78	16	87.50	12.38	37.33	13.46	.54	24.78	.060	1.65	.0364	1.99	8270	734.3	
BPA11	7	13.78	16	87.50	12.38	37.33	13.46	.54	24.78	.060	1.65	.0364	1.99	8270	734.3	
BPA12	7	13.78	16	87.50	12.38	37.33	13.46	.54	24.78	.060	1.65	.0364	1.99	10703	732.8	
B1.1	11	19.76	15	133.87	17.99	56.32	19.47	.74	26.37	.080	4.92	.0132	2.00	1250	147.2	
B1.2	11	19.76	15	133.87	17.99	56.32	19.47	.74	26.37	.080	4.92	.0132	2.00	1250	147.2	
B2.1	11	19.76	15	133.87	17.99	56.32	19.47	.74	26.37	.080	4.92	.0132	2.00	4388	210.2	
B2.2	11	19.76	15	133.87	17.99	56.32	19.47	.74	26.37	.080	4.92	.0132	2.00	4388	210.2	
B3.1	11	19.76	15	133.87	17.99	56.32	19.47	.74	26.37	.080	4.92	.0132	2.00	9476	300.4	
B3.2	11	19.76	15	133.87	17.99	56.32	19.47	.74	26.37	.080	4.92	.0132	2.00	9476	300.4	
C1.1	11	19.76	15	133.87	17.99	56.32	19.47	.74	26.37	.080	4.92	.0132	2.00	8808	302.5	
C1.2	11	19.76	15	133.87	17.99	56.32	19.47	.74	26.37	.080	4.92	.0132	2.00	8808	302.5	
C2.1	11	19.76	15	133.87	17.99	56.32	19.47	.74	26.37	.080	4.92	.0132	2.00	1445	128.5	
C2.2	11	19.76	15	133.87	17.99	56.32	19.47	.74	26.37	.080	4.92	.0132	2.00	1445	128.5	
C3.1	11	19.76	15	133.87	17.99	56.32	19.47	.74	26.37	.080	4.92	.0132	2.00	4693	240.2	
C3.2	11	19.76	15	133.87	17.99	56.32	19.47	.74	26.37	.080	4.92	.0132	2.00	4693	240.2	
C4.1	11	19.76	15	133.87	17.99	56.32	19.47	.74	26.37	.080	4.92	.0132	2.00	10104	308.4	
C4.2	11	19.76	15	133.87	17.99	56.32	19.47	.74	26.37	.080	4.92	.0132	2.00	9507	352.4	
D1.1	11	19.76	15	133.87	17.99	56.32	19.47	.74	26.37	.080	4.92	.0132	2.00	10695	346.4	
D1.2	11	19.76	15	133.87	17.99	56.32	19.47	.74	26.37	.080	4.92	.0132	2.00	10695	346.4	
D2.1	11	19.76	15	133.87	17.99	56.32	19.47	.74	26.37	.080	4.92	.0132	2.00	6003	231.3	
D2.2	11	19.76	15	133.87	17.99	56.32	19.47	.74	26.37	.080	4.92	.0132	2.00	6003	231.3	
D3.1	11	19.76	15	133.87	17.99	56.32	19.47	.74	26.37	.080	4.92	.0132	2.00	7980	220.3	
D3.2	11	19.76	15	133.87	17.99	56.32	19.47	.74	26.37	.080	4.92	.0132	2.00	7980	220.3	
D4.1	11	19.76	15	133.87	17.99	56.32	19.47	.74	26.37	.080	4.92	.0132	2.00	13122	319.4	
D4.2	11	19.76	15	133.87	17.99	56.32	19.47	.74	26.37	.080	4.92	.0132	2.00	13122	319.4	
D4.3	11	19.76	15	133.87	17.99	56.32	19.47	.74	26.37	.080	4.92	.0132	2.00	11574	356.5	
D4.4	11	19.76	15	133.87	17.99	56.32	19.47	.74	26.37	.080	4.92	.0132	2.00	11574	356.5	
MPA2	22	10.175	15	133.87	17.99	56.32	19.47	.74	26.37	.080	4.92	.0132	2.00	12951	362.6	
MPA3	22	10.175	15	133.87	17.99	56.32	19.47	.74	26.37	.080	4.92	.0132	2.00	12951	362.6	
MPA4	22	10.175	15	133.87	17.99	56.32	19.47	.74	26.37	.080	4.92	.0132	2.00	12951	362.6	
MPA5	22	10.175	15	133.87	17.99	56.32	19.47	.74	26.37	.080	4.92	.0132	2.00	12951	362.6	
MPA6	22	10.175	15	133.87	17.99	56.32	19.47	.74	26.37	.080	4.92	.0132	2.00	12951	362.6	
MPA7	22	10.175	15	133.87	17.99	56.32	19.47	.74	26.37	.080	4.92	.0132	2.00	12951	362.6	
MPA8	22	10.175	15	133.87	17.99	56.32	19.47	.74	26.37	.080	4.92	.0132	2.00	12951	362.6	
MPA9	22	10.175	15	133.87	17.99	56.32	19.47	.74	26.37	.080	4.92	.0132	2.00	12951	362.6	
MPA10	22	10.175	15	133.87	17.99	56.32	19.47	.74	26.37	.080	4.92	.0132	2.00	12951	362.6	
MPA11	22	10.175	15	133.87	17.99	56.32	19.47	.74	26.37	.080	4.92	.0132	2.00	12951	362.6	
MPA12	22	10.175	15	133.87	17.99	56.32	19.47	.74	26.37	.080	4.92	.0132	2.00	12951	362.6	
1.1	9	13.94	16	88.50	12.76	37.34	11	.43	31.45	.076	2.30	.0333	7.0	7174	536	
1.2	9	13.94	16	88.50	12.76	37.34	11	.43	31.45	.076	2.30	.0333	7.0	6342	551	
1.3	9	13.94	16	88.50	12.76	37.34	11	.43	31.45	.076	2.30	.0333	7.0	8273	582	

TEST REF.	SLEEVE		PILE		BROUT		SHEAR KEY		K	KM	L	L/D	AGE	FCU	LOAD	FEU	
	D	t	D	t	D	t	D	t									h
	in.	in.	in.	in.	in.	in.	in.	in.									
2-1	13.34	.16	88.50	D/t	13.62	.43	31.45	.076	2.30	.0333	50.9	3.99	5.0	4646	1337	949.6	
3-1	13.34	.16	88.50	D/t	13.62	.43	31.45	.076	2.30	.0333	111.6	8.75	1.3	1958	1185	265.7	
3-2	13.34	.16	88.50	D/t	13.62	.43	31.45	.076	2.30	.0333	92.0	8.76	1.3	1372	1205	425.4	
3-3	13.34	.16	88.50	D/t	13.62	.43	31.45	.076	2.30	.0333	111.8	8.77	1.3	1481	1293	400.8	
4-1	13.34	.16	88.50	D/t	13.62	.43	31.45	.076	2.30	.0333	12.6	.98	7.0	785	791	776.8	
4-2	13.34	.16	88.50	D/t	13.62	.43	31.45	.076	2.30	.0333	12.8	.98	7.0	720	732	559.4	
4-3	13.34	.16	88.50	D/t	13.62	.43	31.45	.076	2.30	.0333	12.8	1.01	7.0	705	732	752.4	
5-1	36.50	.39	92.70	D/t	35.71	1.12	31.82	.137	5.91	.0333	33.1	1.99	2.0	275	1532	456.2	
6-1	80.08	.87	92.45	D/t	73.35	2.17	33.87	.134	12.99	.0303	73.2	1.00	2.0	3029	5881	318.5	
6-2	80.08	.87	92.45	D/t	73.35	2.17	33.87	.134	12.99	.0303	74.2	1.00	2.0	3470	6005	415.7	
6-3	80.08	.87	92.45	D/t	73.35	2.17	33.87	.134	12.99	.0303	74.2	1.00	2.0	3470	6005	415.7	
7-1	13.34	.16	88.50	D/t	13.62	.43	31.45	.076	2.30	.0333	12.6	1.96	7.0	812	476	450.1	
7-2	13.34	.16	88.50	D/t	13.62	.43	31.45	.076	2.30	.0333	12.6	1.96	7.0	812	476	450.1	
7-3	13.34	.16	88.50	D/t	13.62	.43	31.45	.076	2.30	.0333	12.6	1.96	7.0	812	476	450.1	
CUR1	22.40	.20	113.80	D/t	22.01	1.00	21.32	.080	6.65	.0120	.011	2.03	9.0	10309	286	753.6	
CUR2	22.40	.20	113.80	D/t	22.01	1.00	21.32	.080	6.65	.0120	.010	2.03	12.0	9583	284	765.2	
CUR3	22.40	.20	113.80	D/t	22.01	1.00	21.32	.080	6.65	.0120	.010	2.03	9.0	10309	286	753.6	
CUC	27.14	.24	113.90	D/t	26.65	1.33	27.33	.080	6.65	.0120	.015	2.03	9.0	10309	286	753.6	
CUD	27.14	.24	113.90	D/t	26.65	1.33	27.33	.080	6.65	.0120	.015	2.03	9.0	10309	286	753.6	
CUE	27.25	.23	92.95	D/t	22.01	1.00	21.32	.080	6.65	.0120	.027	2.03	4.0	6244	241.0	241.0	
CUF	27.25	.23	92.95	D/t	22.01	1.00	21.32	.080	6.65	.0120	.016	2.03	7.0	7841	376.1	376.1	

APPENDIX B

## APPENDIX B

$$f_{bu} \propto f_{cu} \quad (1)$$

$$F_{bu} = \frac{f_{bu}}{1.105} \left[ \frac{50}{f_{cu}} \right]^{0.5} \quad (2)$$

$$F_{bu} = k C_L (AC_s + Bh/s) \quad (3)$$

$$F_{bu} = k C_L (76 C_s + 9468 h/s) \quad (4)$$

$$f_{bu} = 4/3 k C_L (9C_s + 1100 h/s) f_{cu}^{0.5} \quad (5)$$

$$f_{bd} = k C_L (9C_s + 1100 h/s) f_{cu}^{0.5} \quad (6)$$

$$F_{bd} = k C_L (57 C_s + 7100 h/s) \quad (7)$$

$$f_{ba} = 1/6 k C_L (9C_s + 1100 h/s) f_{cu}^{0.5} \quad (8)$$

$$f_{bu} = 1.15 + 1.72 f_{cu} h/s \quad (9)$$

$$f_{ba} = 0.138 + 0.5 f_{cu} h/s \quad (10)$$

$$\sigma_k = 5.5 f_{cu} \quad (11)$$

$$f_{bu} = C + \mu\sigma_n + \sigma_m h/s \quad (12)$$

$$\bar{\sigma}_n = k_n (u_m - \Delta') > 0 \quad (13)$$

$$\sigma_o = \bar{\sigma}_n r/t \quad (14)$$

$$\sigma_o = k_r (u_m - \Delta') t \quad (15)$$

$$\epsilon_o = \delta/r = (\sigma_o - \nu\sigma_z) / E_s \quad (16)$$

$$\sigma_z = f_{bu} \pi r_p L / (2 \pi r_s t_s + \Delta_s) \quad (17)$$

$$\Delta'_s = r_s [k_n r_s (u_m - \Delta') + \nu f_{bu} \pi r_p / (2 \pi r_s t_s + \Delta_s)] / t_s E_s \quad (18)$$

$$\Delta'_p = r_p [k_n r_p (u_m - \Delta') + \nu f_{bu} L/2] / t_p E_s \quad (19)$$

$$\Delta' = (\Delta'_s + \Delta'_p) / 2 \quad (20)$$

$$\Delta' = (k_n u_m \gamma + \nu f_{bu} L r_p \theta / 2) / (2E_s + k_n \gamma) \quad (21a)$$

$$\gamma = \frac{r_s^2}{t_s} + \frac{r_p^2}{t_p} \quad (21b)$$

$$\theta = \frac{\pi r_s}{(\pi r_s t_s + A_s/2)} + \frac{1}{t_p} \quad (21c)$$

$$f_{bu} = \frac{2E_s[\mu k_n u_m + \sigma_m h/s] + \sigma_m k_n \gamma h/s}{2E_s + k_n \gamma + \mu k_n v(L/D_p) r_p^2 / \theta} \quad (22)$$

$$f_{bu} = \frac{4 \times 10^5 [3.75 + 100 h/s] + 2500 \gamma h/s}{4 \times 10^5 + 25 \gamma + 22.5(L/D_p) r_p^2 \theta} \quad (23)$$

$$f_{bu} = \frac{5.66 \times 10^4 [3.75 + 100 h/s] + 3.54 \gamma h/s}{4 \times 10^5 + 25 \gamma + 22.5(L/D_p) r_p^2 \theta} \quad (24)$$

$$f_{bu} = \frac{5.66 \times 10^4 [3.75 + 100 h/s] 3.54 \gamma h/s}{4 \times 10^5 + 25 \gamma + 22.5(L/D_p) r_p^2 \theta} \quad (25a)$$

$$\gamma = \frac{r_p^2}{t_p} - \frac{r_s^2}{t_s} \quad (25b)$$

$$\theta = \frac{1}{t_p} - \frac{\pi r_s}{\pi r_s t_s + \Delta_s/2} \quad (25c)$$



APPENDIX C

## APPENDIX C

## OFFSHORE GROUTING METHODS, MATERIALS, AND MIX DESIGN

C.1 General

Cement grouting has been used in construction projects for more than 100 years. In the broadest sense, grouting can be defined as injecting chemical grouts or suspended solids into voids or compatible material to consolidate, compact, strengthen, stabilize or reduce permeability of the host medium; to lift, move and/or support structures; or to provide for load transmission between structures or between structures and rock or soil. Only recently, however, industry, government, and academia formally recognized the need for a cooperative research program in this area. In 1981, the American Concrete Institute (ACI) organized ACI committee 552, cement grouting, to perform the task of studying and reporting on the applications and uses of cement grouting.

C.2 Offshore Oil Industry Applications

In the offshore industry, grouting is used in the foundations of all types of structures to ensure efficient transfer of load from the structure to the sea-bed. Typical grout areas are the annuli between the skirts and leg jacket, and the driven piles, and the annuli around insert piles in drilled holes.

The most popular form of construction for fixed offshore platforms in the North Sea and the Gulf of Mexico is the piled steel

jacket, shown in Fig. 1.1. The pile is usually driven through each leg and extends to the top of the leg, grout is pumped into the annulus between the jacket and the pile. The grout in this application serves only to transmit the lateral forces between the pile and the jacket and is not normally required to support vertical loads. Bond stresses, between the steel-grout interface, are low and any local debonding is unlikely to compromise the overall stability of the structure.

In deeper water, piles generally do not extend to the surface and are either distributed around the base of the structure or grouped in sleeve clusters around the main legs as shown in Fig. 1.2a and 1.2b. In these cases the grouted annulus forms the only structural connection between the jacket and the foundation, with the grout transmitting all the forces arising from both dead weight and any environmental live loads.

### C.3 Offshore Grouting Methods

There are at least three common methods used in grouting sleeve-pile connections with variations existing within each method [49,50,51,52,53,]. Terms for each of these methods, although not standard are: (1) conventional two-stage, (2) packer and (3) balanced pressure method.

The conventional two-stage placement technique, shown in Fig. C.1, involves the use of a mechanical grout seal at the bottom of the

leg/skirt to help prevent mud contamination of the annulus as the pile is driven , and also to help support the first stage grout plug. The procedure requires two grout inlets into the leg/skirt pile. The lower inlet is for placement of the first stage grout, which is normally five to thirty feet in depth. First stage grout is normally a quick setting type of grout. However, if desired the same slurry that will be used for the upper portion can be used for the plug. After the grout plug has hardened, the remainder of the leg/skirt pile annulus can be filled using the plug to support the hydrostatic grout head.

The packer method, shown in Fig. C.2, utilizes a high pressure seal which may allow the grouting operation to be completed in one stage. The water in the annulus is displaced by the grout which enters just above the packer. In skirt piles, packers can also be placed at the top of the skirt sleeves to seal the annulus, this allows the grout to be pumped to the surface through a return line for sampling. The advantages of this method are that grouting in one stage eliminates the time required for the plug to set, and also the increased hydrostatic head of the grout may increase the bonding of the grout to the steel tubulars.

One of the major objections to the displacement method of grout injection, used in both the two-stage and the packer method is the dilution of the grout by water. To compensate for this, up to 50% additional material is usually pumped into the annulus, or

multiple grout entry ports are provided around the circumference of the leg/skirt.

Balanced pressure method, shown in Fig. C.3, relies on balancing the hydrostatic pressure of the grouting material inside the sleeve-pile annulus, with the hydrostatic pressure at the mudline outside the bottom end of the annulus. The top of the sleeve is sealed using a plate or packer and then compressed air is injected just below the seal at sufficient pressure to displace the seawater out of the bottom of the sleeve. After the annulus is dewatered, the air pressure is maintained and the grout is injected below the top seal and free falls down the annulus to the base of the sleeve. As the annulus is filled with grout, the air pressure is gradually released, compensating for the increase in hydrostatic pressure in the annulus. Injection continues until the grout head balances the depth of seawater. Once this grout reaches initial set, the remaining portion of the annulus is filled. The main disadvantages to this method are that by letting the grout free fall in the annulus the chances of mix segregation and void formation increase. Also, the failure of a seal can cause major problems in the grouting process.

#### C.4 Grouting Materials

Grouted connection grouts are normally formulated with some type of inorganic hydraulic cement which yields a high early strength to ensure the stability of the structure [54,55,56,57,58,59]. Since

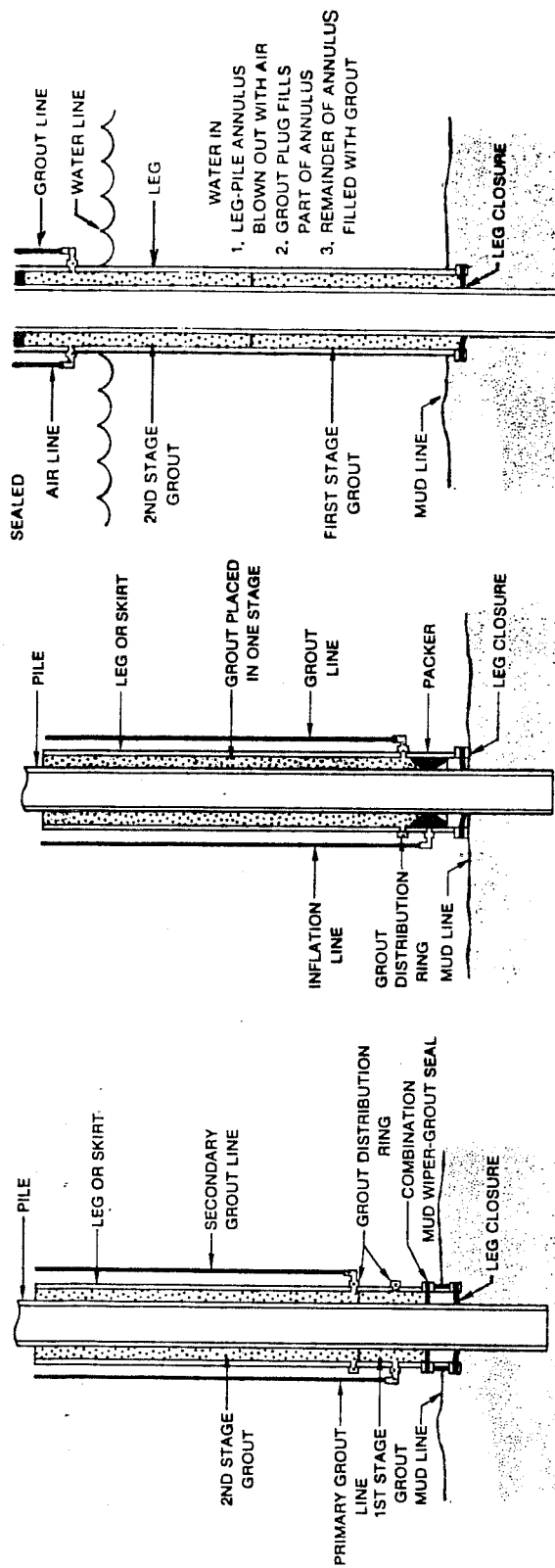


Fig. C.1 Conventional two-stage Method

Fig. C.2 Packer Method

Fig. C.3 Balanced Pressure Method

the platform load is transferred from the sleeve to the pile via the grout, specific grout properties vary for a given platform design and installation process. Table C.1 [59] shows some examples of offshore sleeve-to-pile connection grouts. The grout slurries are usually simple mixes, while still being compatible with required strength and pumpability. The most commonly used grout is a Portland cement with a low water/cement ratio and one or more admixtures, used to impart specific grout properties. High Alumina Cement grout is used when exceptionally high early strengths are required, since in the seawater environment High Alumina Cement doesn't seem to have the conversion problems which are present in other environments. Gypsum cements are occasionally used, but only for quick set plugs.

C.4.1 Cement Classes and Types. The API, in Specification 10-84, [59] uses the following classification of cements for use in offshore structures.

Class A: (ASTM Type I) Available only in ordinary type.

Class B: (ASTM Type II) Intended for use when conditions require moderate to high sulfate resistance.

Class C: (ASTM Type III) Used when conditions require early strength. Available in ordinary and moderate strength and high sulfate resistance types.

Class G and H: No additions other than Calcium Sulfate or water or both shall be interground or blended with the clinker

TABLE C.1 Typical Offshore Grout Formulations Ref. 59

Grout Composition (psi)	$f_{cu}$	Remarks
Neat Portland Cement 44% Water	6000	Normal High Early Easily mixed with jet mixer
Portland Cement HSP Aggr./Dispersant 37% Water	10000	Normal/High Early RCM needed for continuous mixing Pressurized Density measurements recommended
API Class A Cement 6% Expansive admix. 50% Water	5000	Normal Easily mixed with jet mixer
API Class H Cement 6% Expansive admix. 44% Water	8000	Normal RCM at reduced rates for 50% HSP Aggr. continuous mixing Pressurized Density measurements recommended
API Class A-Pozmix (56-44) Calcium Chloride 60% HSP Aggr. 42% Water	8000	Normal/High Early RCM at reduced rates for continuous mixing Pressurized Density measurements recommended
Expansive Cement 59% water	5000	Normal Easily mixed with jet mixer Density 14.8 lbs/gal
Calcium Aluminate Cement 40% Fresh Water	8000	Very/High Early Do not mix with sea water
API Class A Cement 4% Expansive Admix. 26% High Strength and dispersant 50% water	4000	Normal Density 12.5 lbs/gal Low density/high strength microspheres

## Notes:

1. Percentages are by weight of cement
2. Slurry densities range from 15.7 to 16.7 lbs/gal
3. Strengths listed are 28 day at 75 F or 90 day at 45 F
4. HSP Aggr. - 4 mesh to dust high strength porous aggregate with ca 14% water absorbency
5. Pozmix - High Silica Fly Ash



during the manufacture of Class G and H cement.

Available in moderate and high sulfate resistance types.

C.4.2 Admixtures. The most frequently used admixtures mixed with the cements given in Section C.4.1 are as follows.

Calcium Chloride: Normal dosage 1 to 3 percent by weight of cement.

The Calcium Chloride is used to increase the early (1 to 3 day) strength. Non-chloride accelerators are available but have seen little use in offshore platform grouts. Blending Portland cement with gypsum cement or High Alumin cement is also used to accelerate strength, but such blends are normally limited to quick set or flash set plugs.

Super-plasticizers: Normal dosage is between 0.05 and 0.1 percent.

Most common are the Sodium Naphthalene Sulphonates. They reduce the friction pressure when pumping through small diameter grout lines, reduce water/cement ratio, and improve early and final compressive strengths.

Retarders: Normal dosage is 0.10 percent. These small amounts are sometimes required to extend the pumping time of high strength expansive grouts.

Bentonite/Attapulgate: Normal dosage is 2 to 16 percent. These materials are used to formulate low density and high yield grouts. They are considered lightweight water extending types, which lower density by enabling the grout to be mixed

at higher water ratios without free water separation. However, strength decreases as density decreases.

Sodium Silicate: Normal dosage is 1 to 6 percent. This chemical is used to formulate low density and high yield grouts. Sodium Silicate is considered a lightweight water extending type of admixture which also has accelerating effect. Again, strength decreases as density decreases.

Gilsonite: Normal dosage is 5 to 50 percent. This is a lightweight solid hydrocarbon ground to a particle size compatible with dry blending with cement. Gilsonite lowers the grout density due to a low specific gravity and a required higher mixing water content. Strength is usually 10 to 50 percent higher than for grouts using water extending admixtures.

C.4.3 Fine Aggregate and Solids. The purpose of fine aggregates, used in a specific grout, varies with the exact application and type of aggregate.

Sand: Normal dosage is 20 to 300 percent. Sand is the most common type of fine aggregate with sizes usually being smaller than a ASTM 20 mesh. Sand generally increases grout density, decreases shrinkage, and reduces temperature of hydration. Sand also imparts a degree of toughness or fracture resistance to high strength grouts and normally results in a slight improvement in bond strength. However, excessive sand, above 100 percent,

can result in blockages and potentially poorly grouted zones due to water filtration.

**Extra Fine Inorganic Solids:** Normal dosage is 10 to 100 percent.

Examples are flyash, natural pozzolans, ground slag, and silica flour. They are normally used to lower the cost of grout, since reduced cement volume is required, and/or in the formulation of low heat of hydration grouts.

**High Strength Microspheres:** Normal dosage 5 to 50 percent. Hollow

spheres (10 to 100 um) formed from a fused inorganic material, compatible with all commonly used cements. Grouts using microspheres offer low density and vastly improved strength development when compared to other type of low density grouts.

APPENDIX D

# STRENGTH CURVE

GROUT MIX: 13

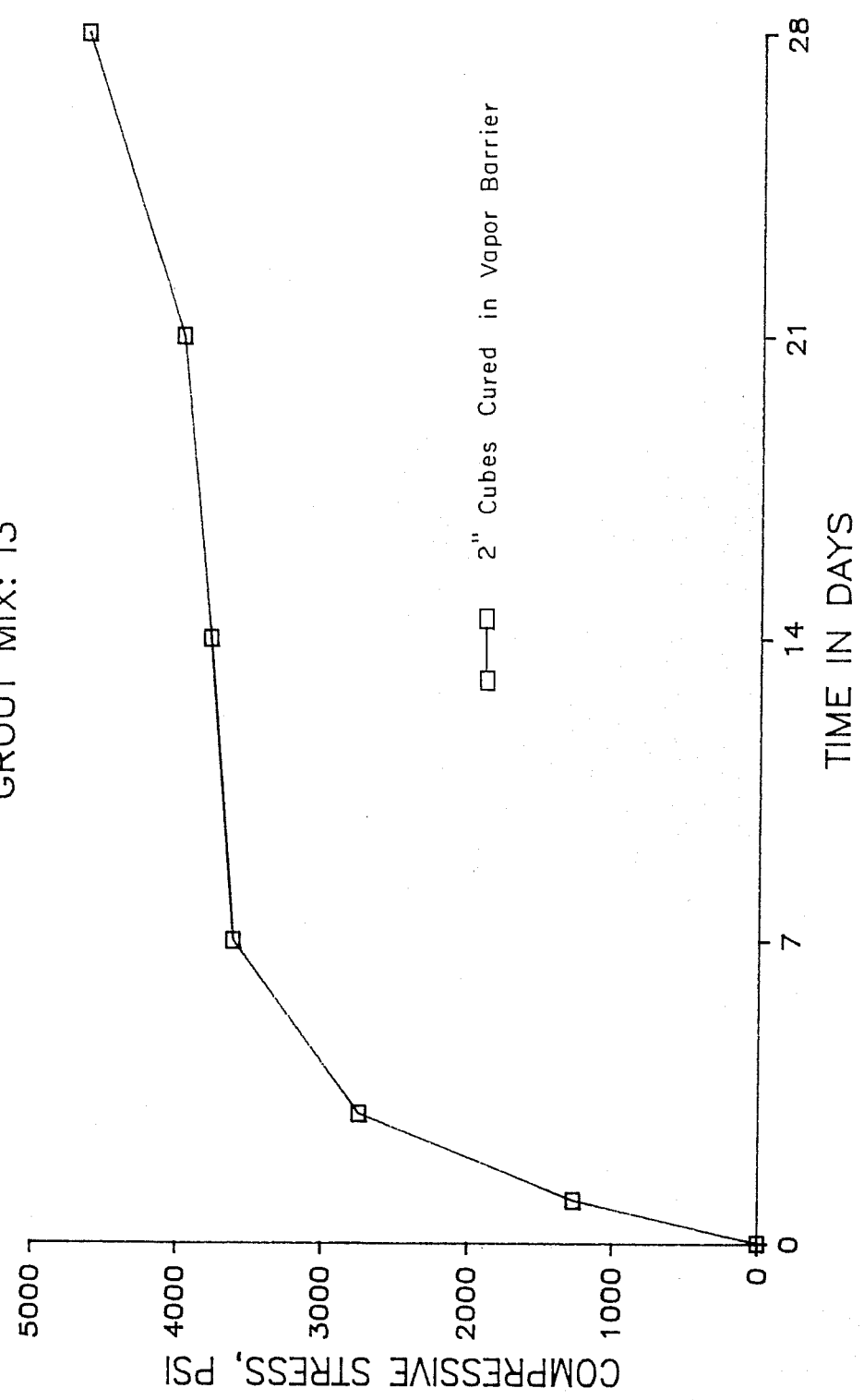


Fig. D.1

# STRENGTH CURVE

GROUT MIX: 14

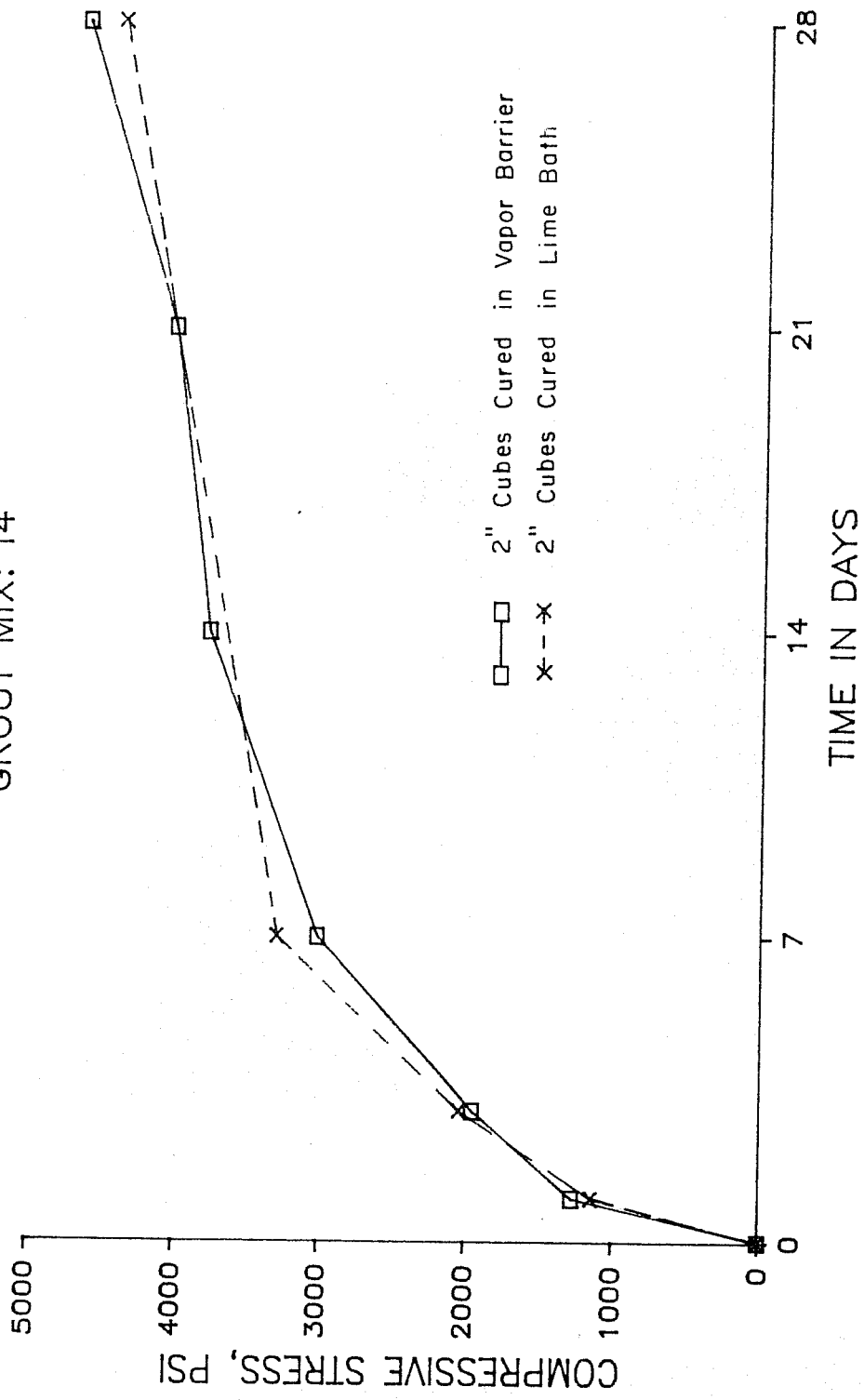


Fig. D.2

# STRENGTH CURVE

GROUT MIX: 15

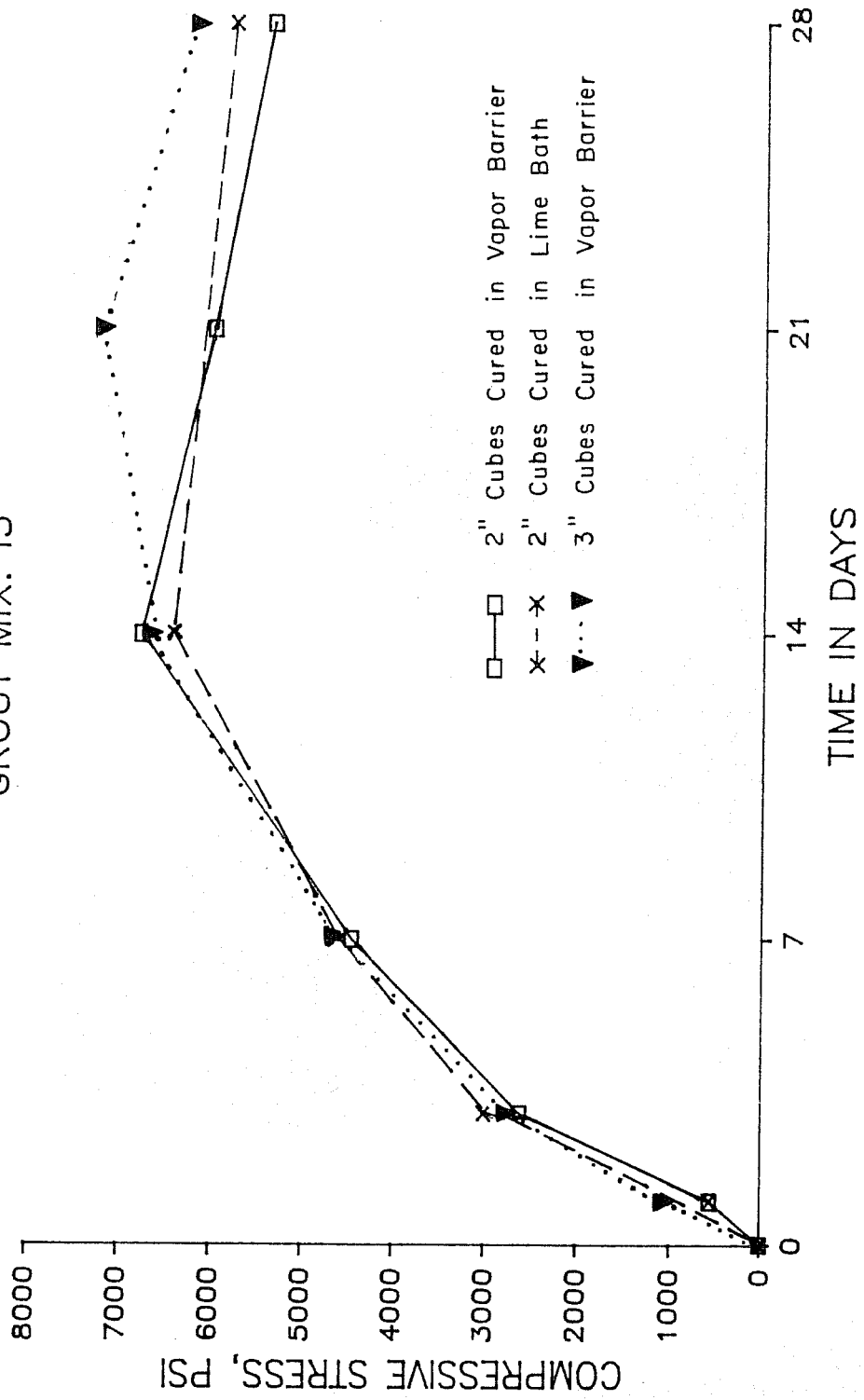


Fig. D.3

# STRENGTH CURVE

GROUT MIX: 16

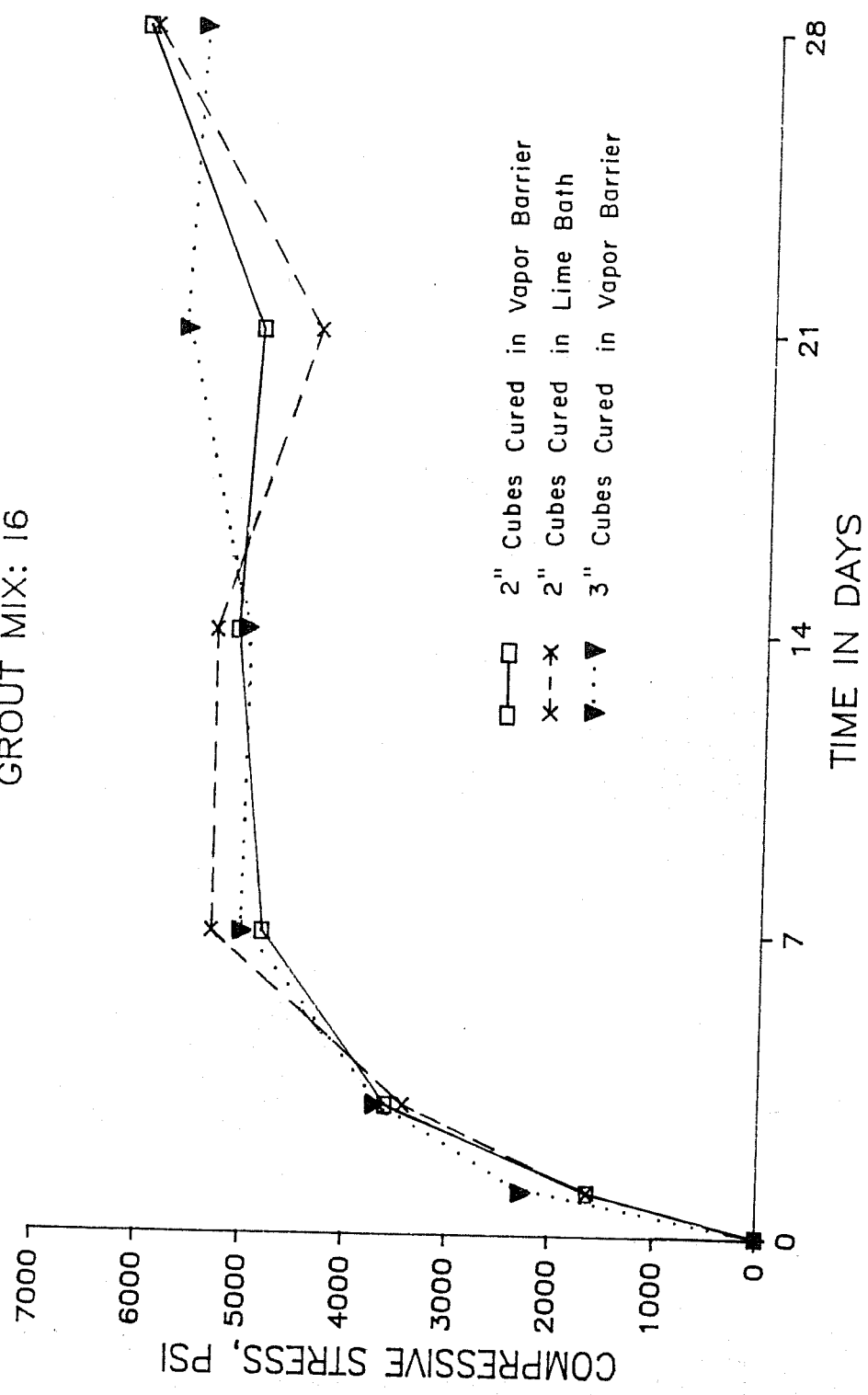


Fig. D.4



# STRENGTH CURVE

GROUT MIX: 17

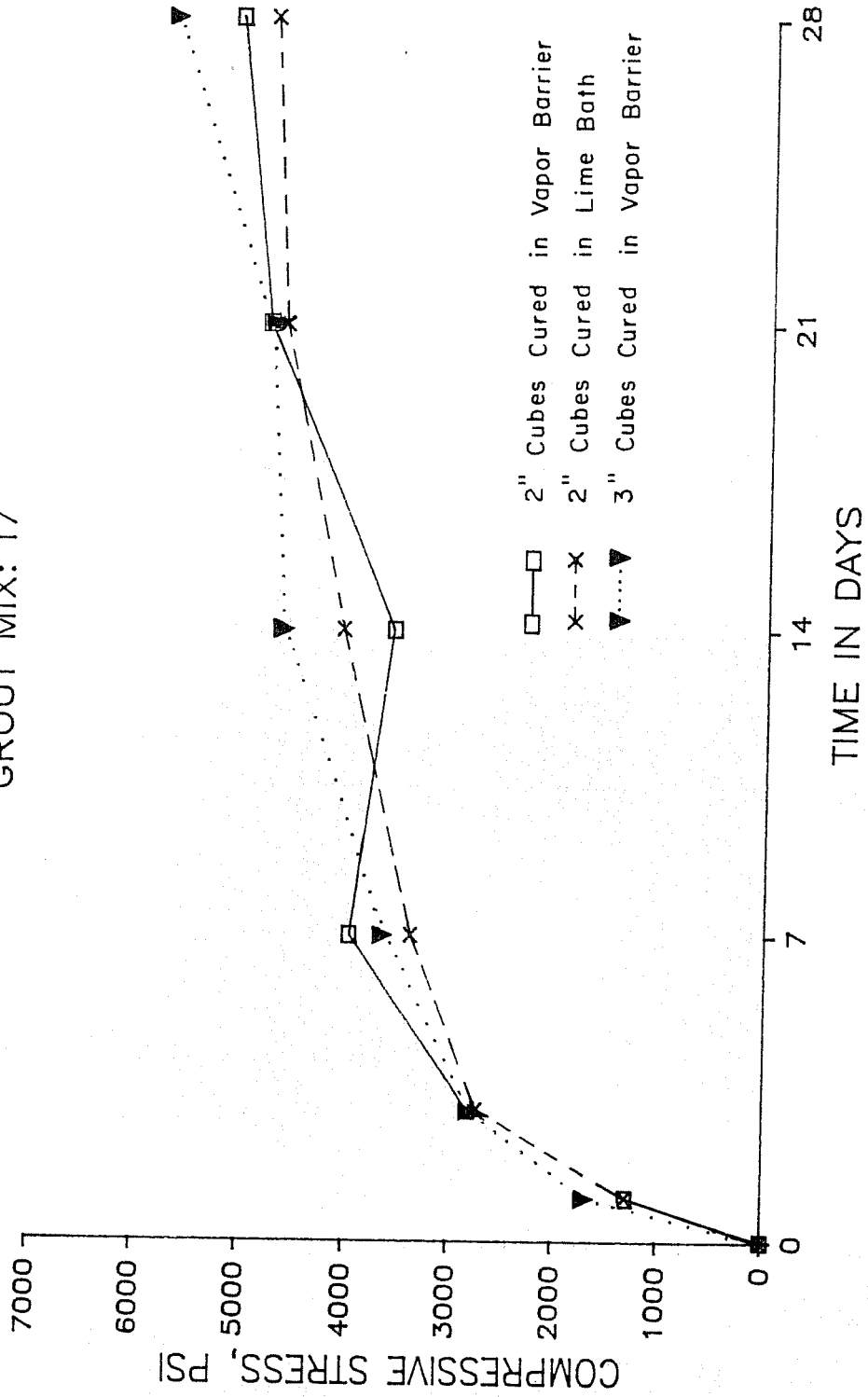


Fig. D.5

# STRENGTH CURVE

GROUT MIX: J2

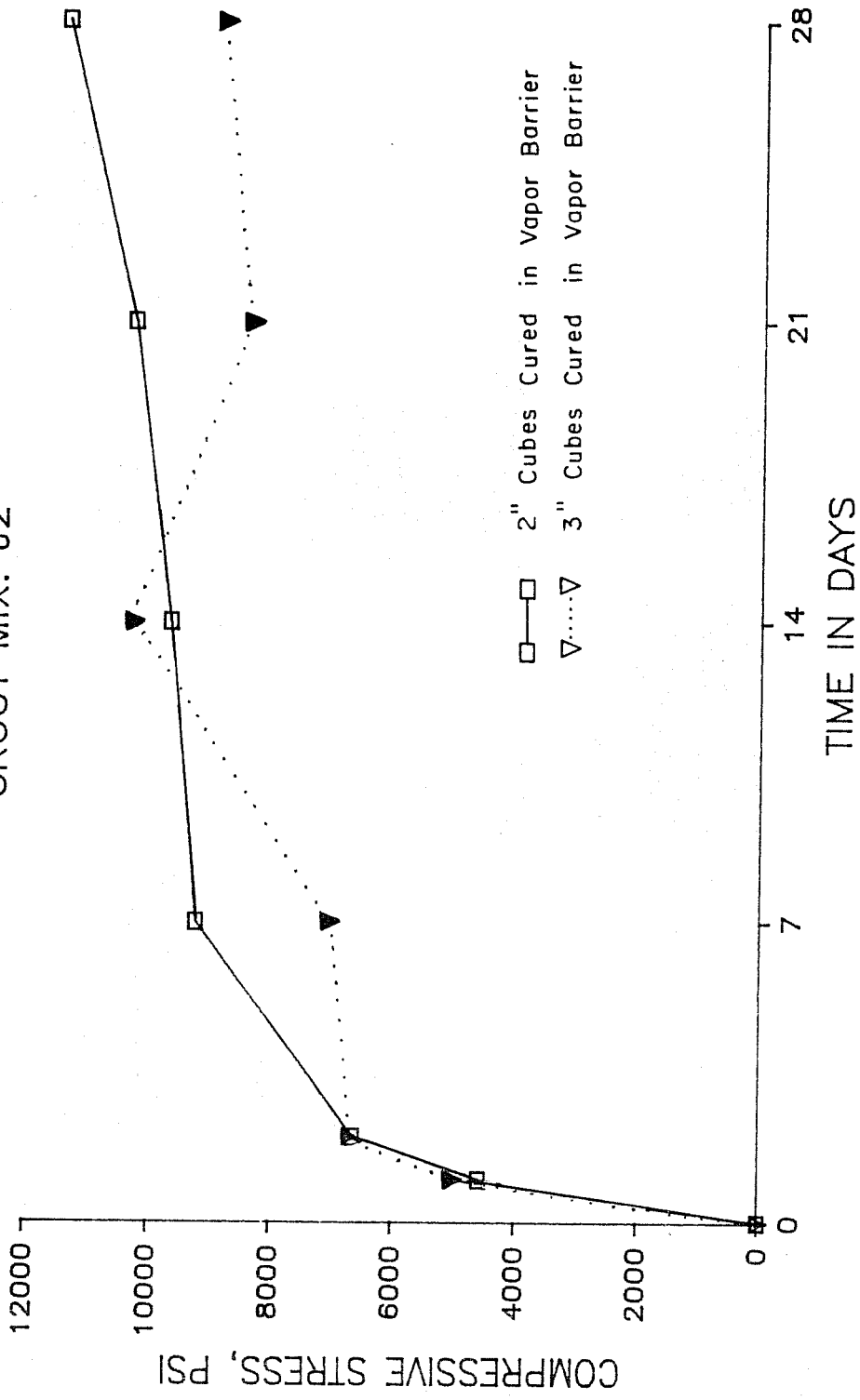


Fig. D.6

# STRESS VS STRAIN

GROUT MIX: 13 AGE= 28 DAYS

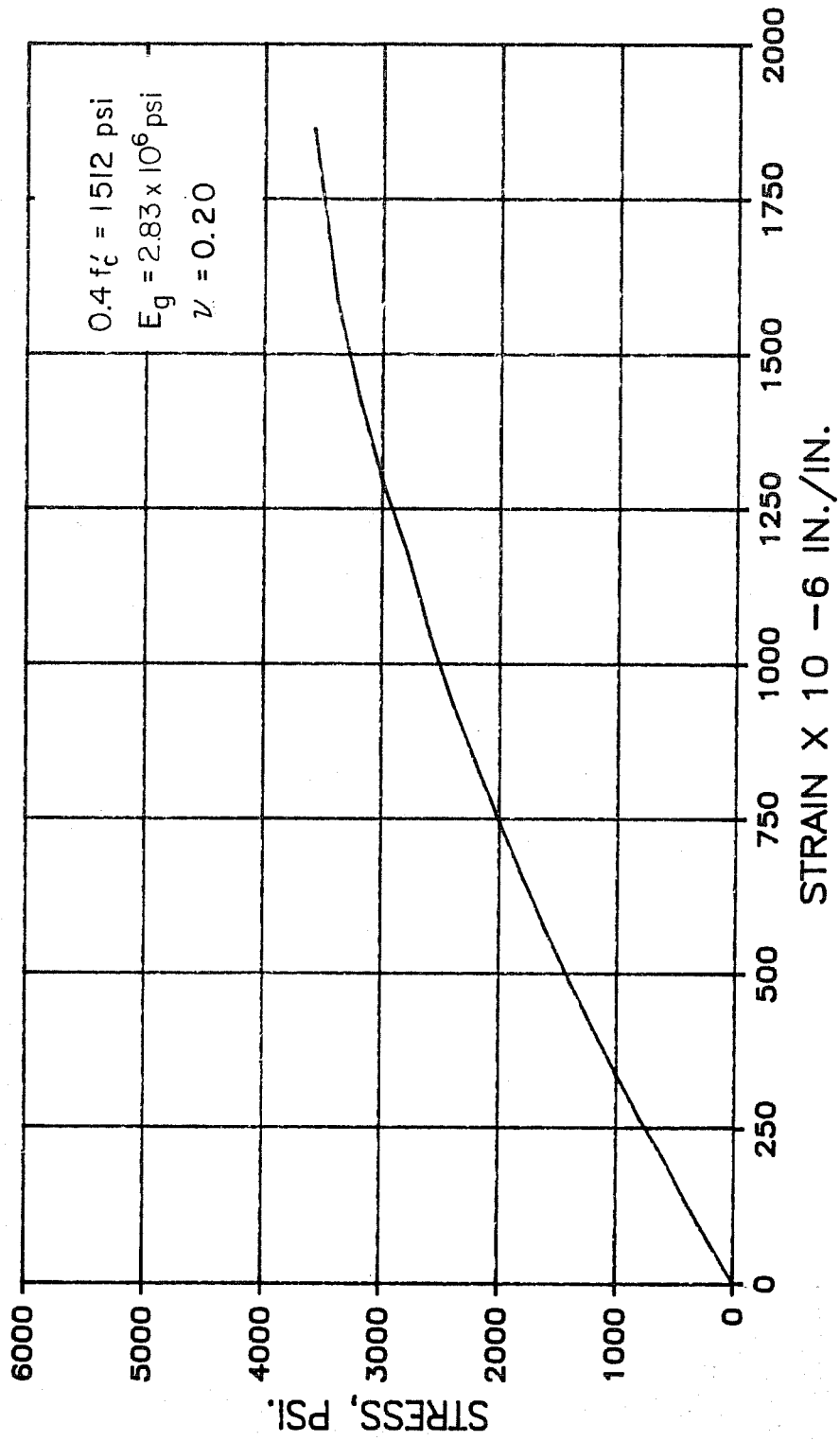


Fig. D.7

# STRESS VS STRAIN

GROUT MIX: 14 AGE= 26 DAYS

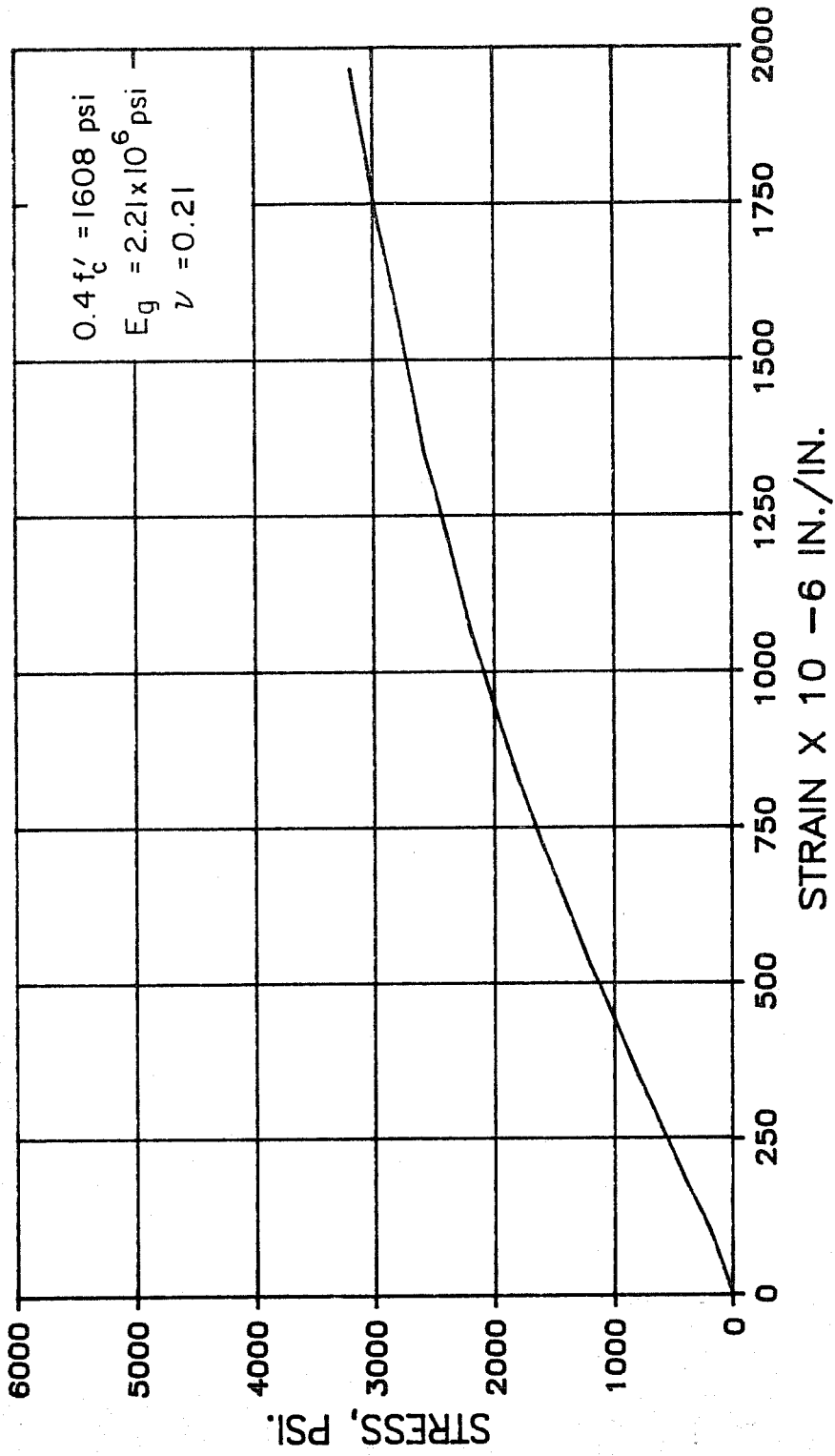


Fig. D.8

# STRESS VS STRAIN

GROUT MIX: 15 AGE= 25 DAYS

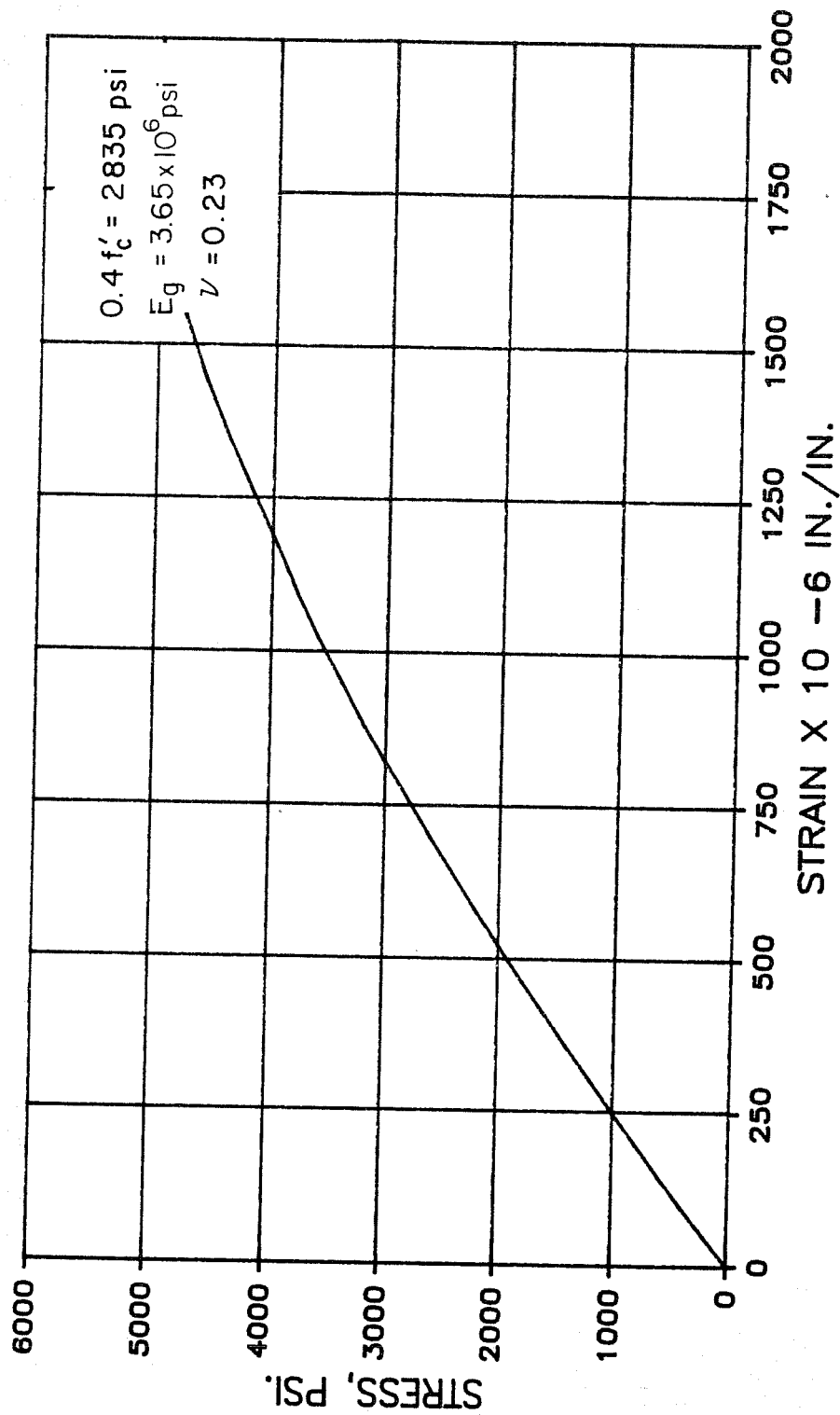


Fig. D.9

# STRESS VS STRAIN

GROUT MIX: 15 AGE= 25 DAYS

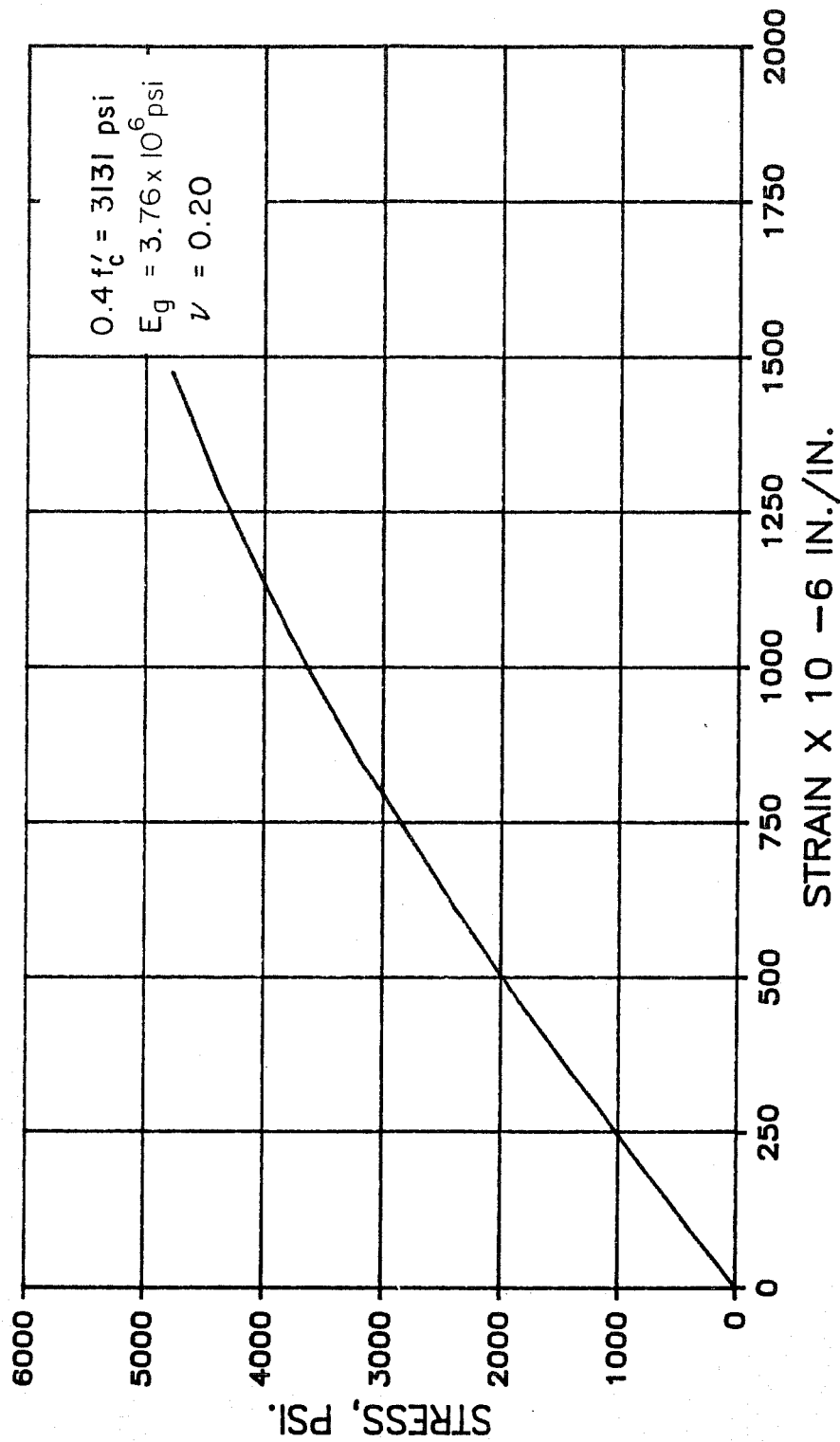


Fig. D.10

# STRESS VS STRAIN

GROUT MIX: 16 AGE= 23 DAYS

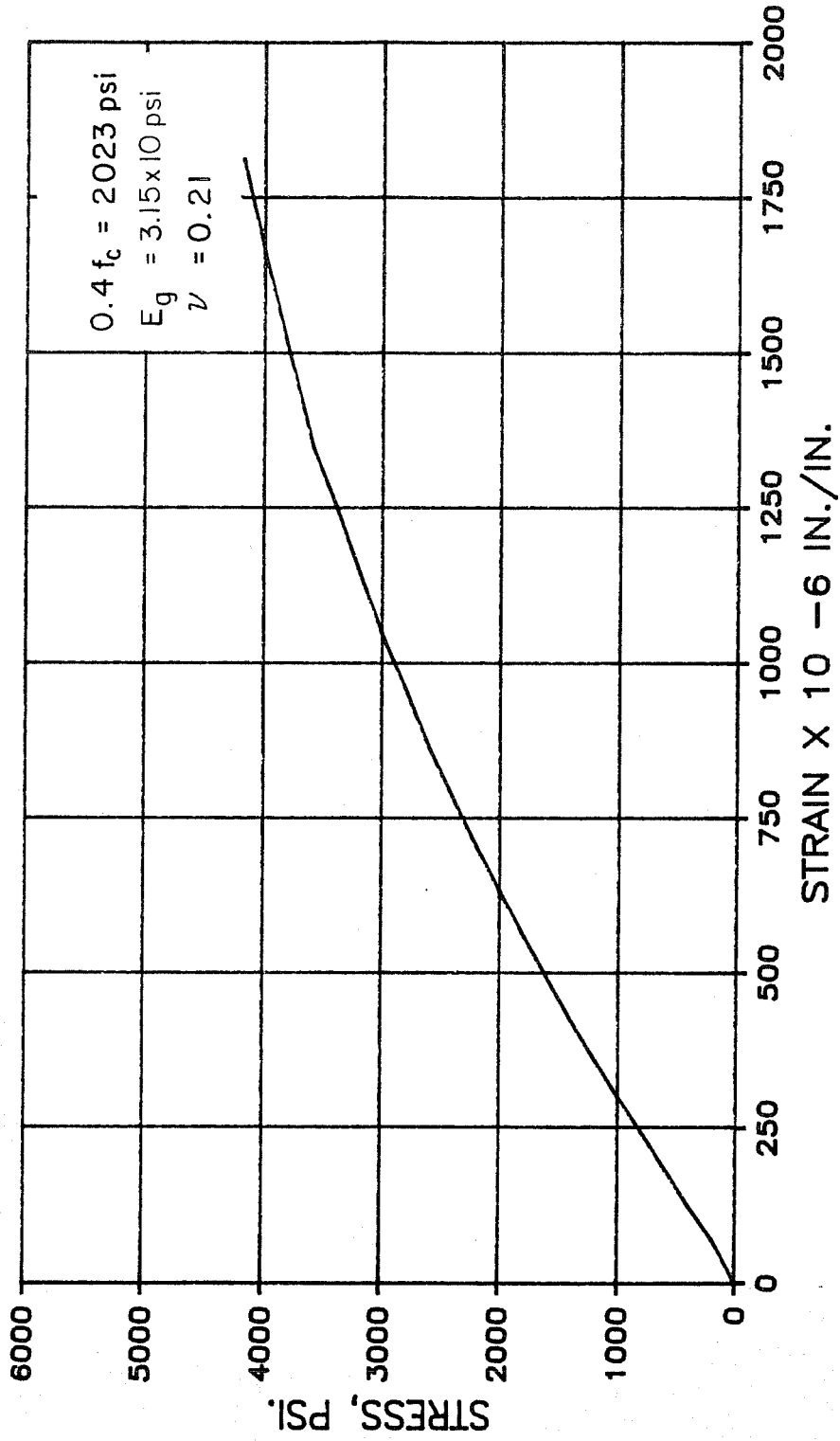


Fig. D.11

# STRESS VS STRAIN

GROUT MIX: 17 AGE= 22 DAYS

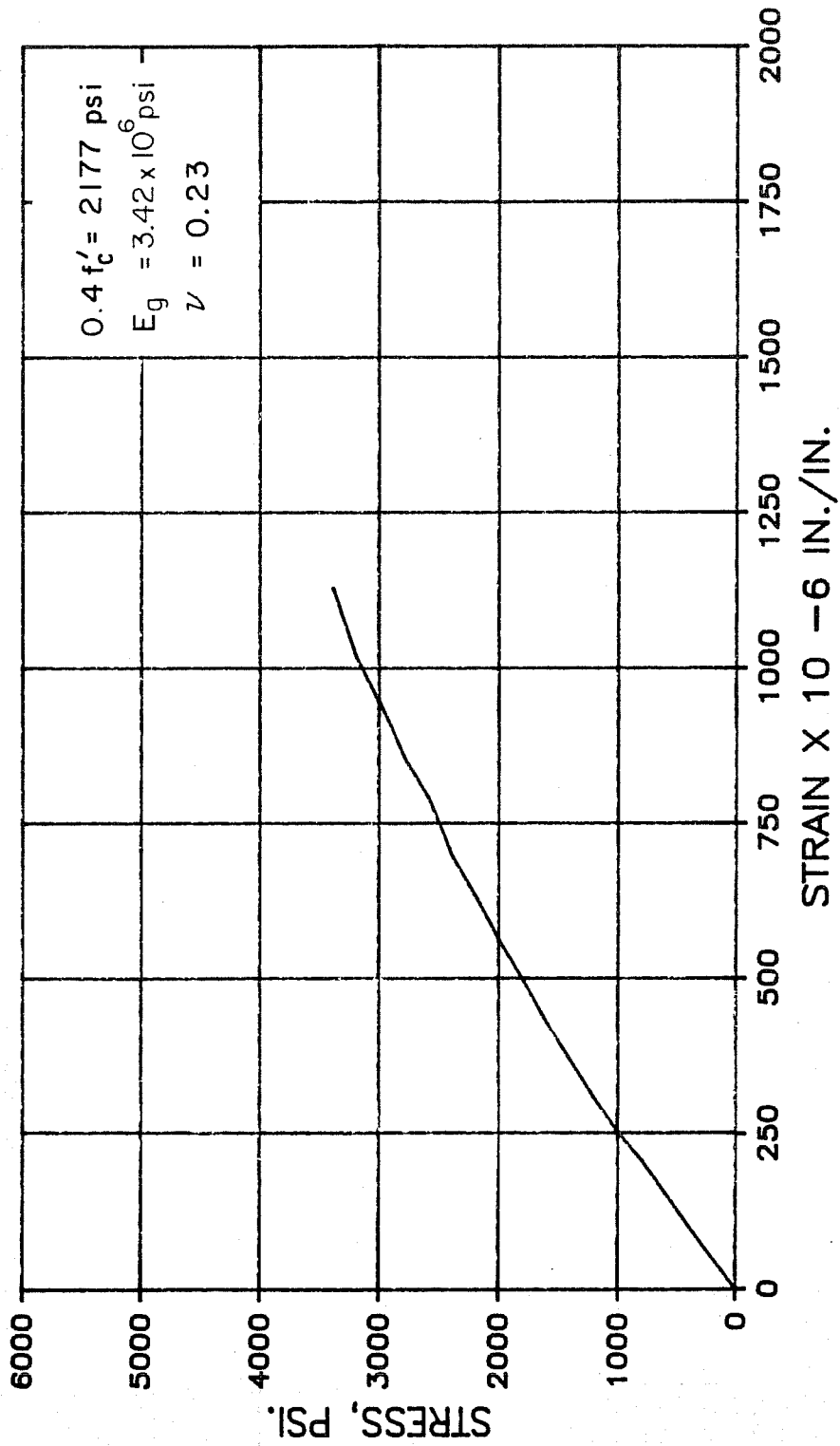


Fig. D.12



# STRESS VS STRAIN

GROUT MIX: 17 AGE= 22 DAYS

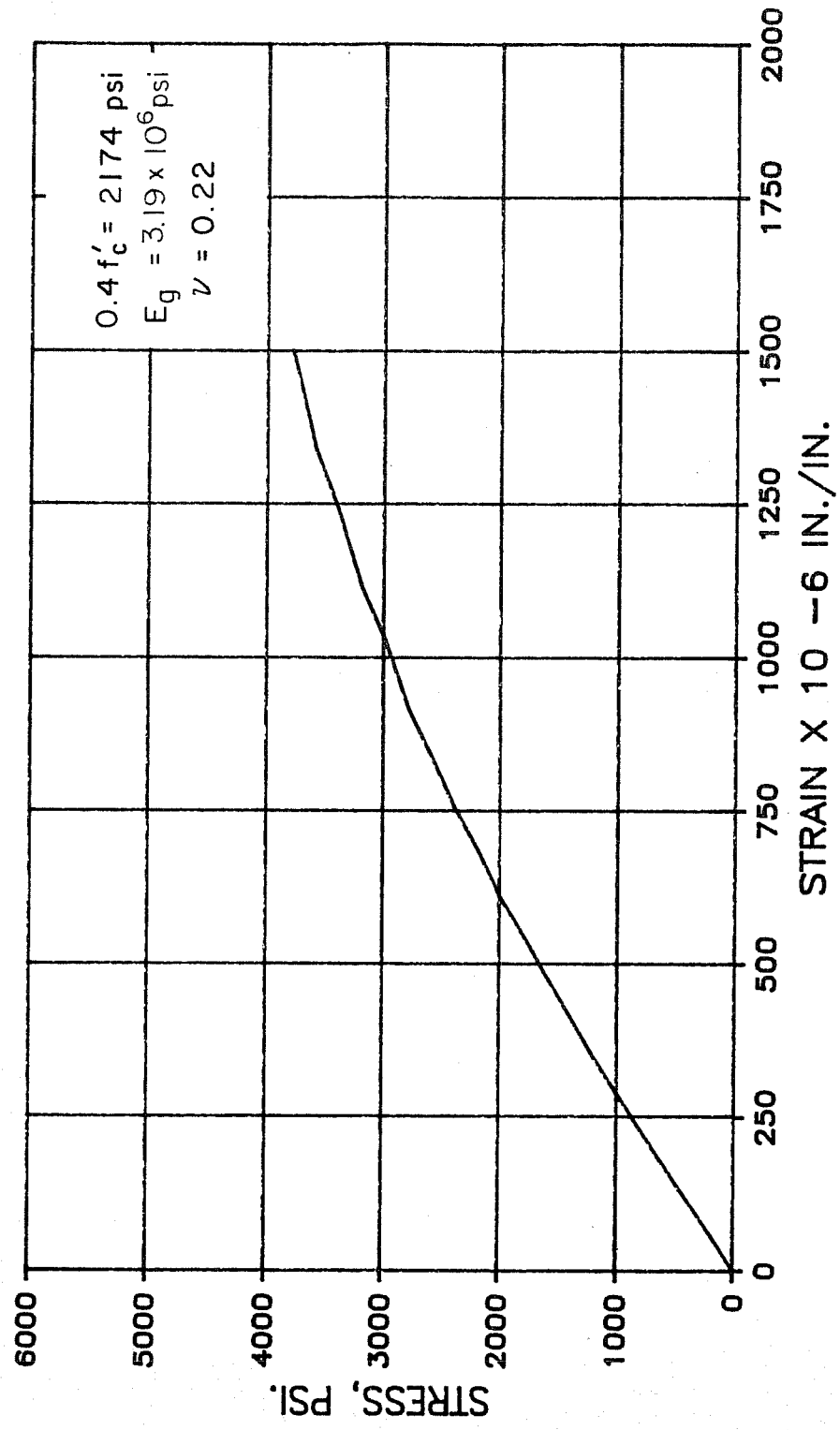


Fig. D.13

# STRESS VS STRAIN

GROUT MIX: J2 AGE= 2 DAYS

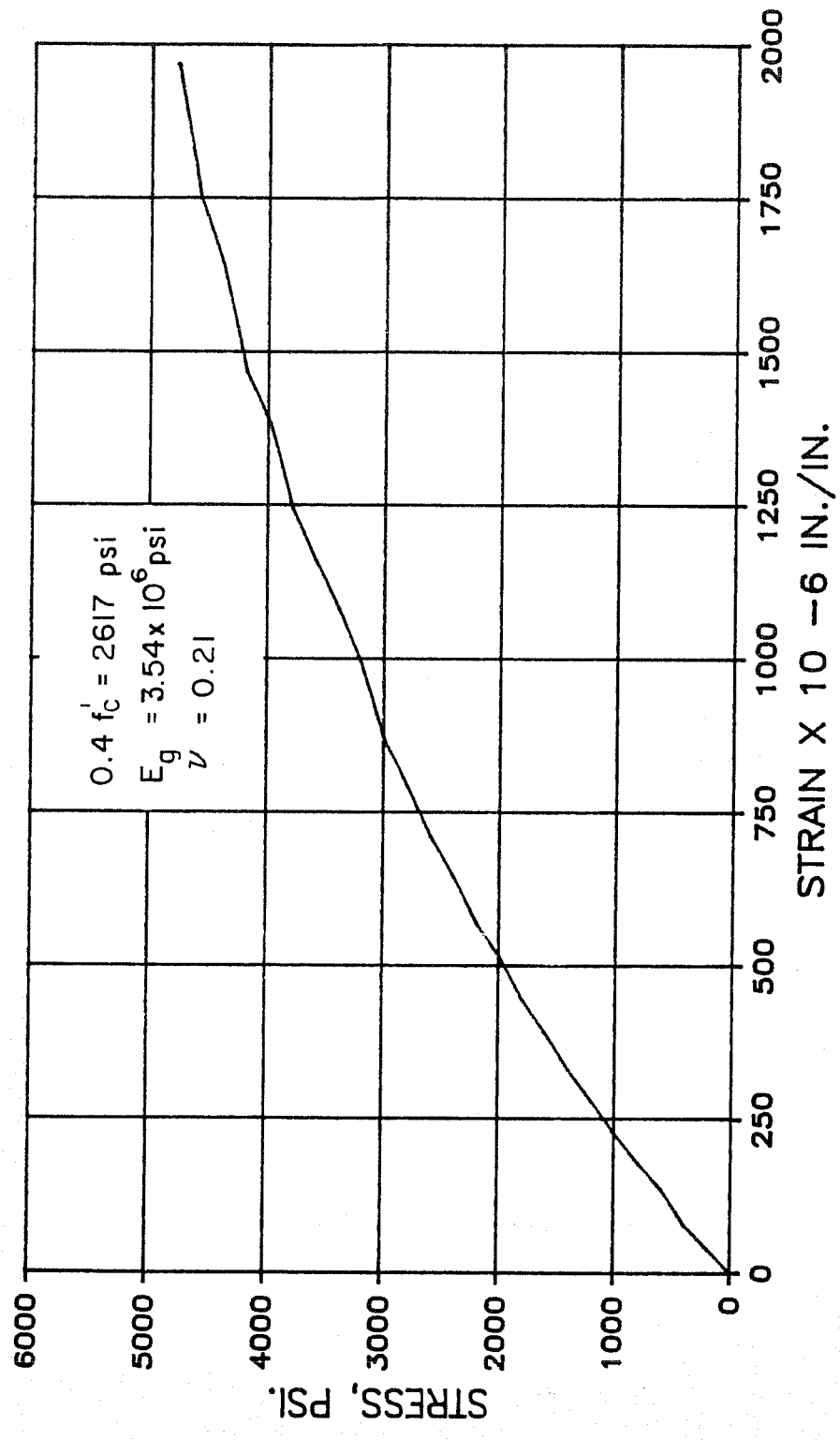


Fig. D.14

# STRESS VS STRAIN

GROUT MIX: J2 AGE= 25 DAYS

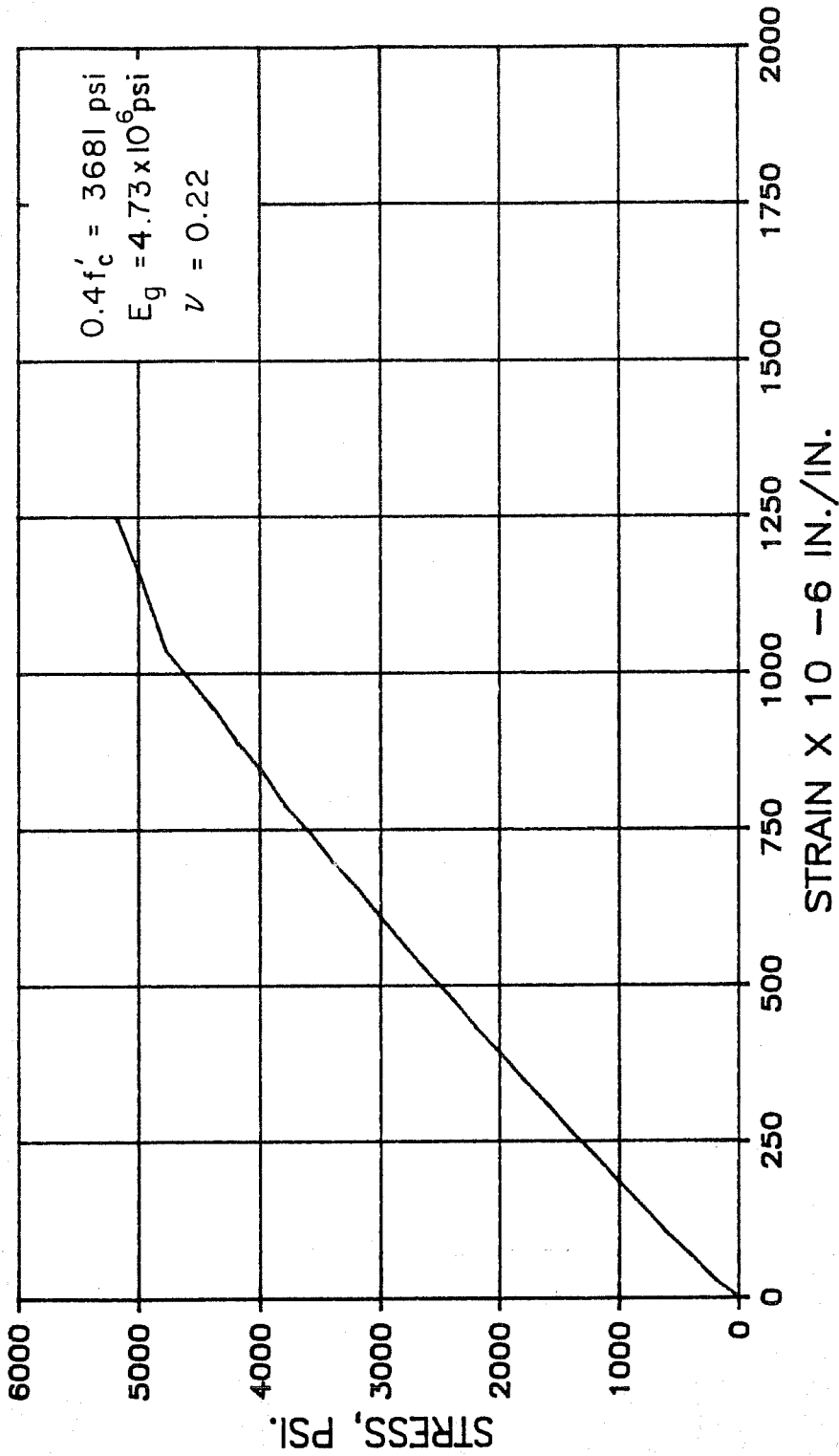


Fig. D.15

# GROUT SHRINKAGE/ SWELL VS TIME

GROUT MIX: 15

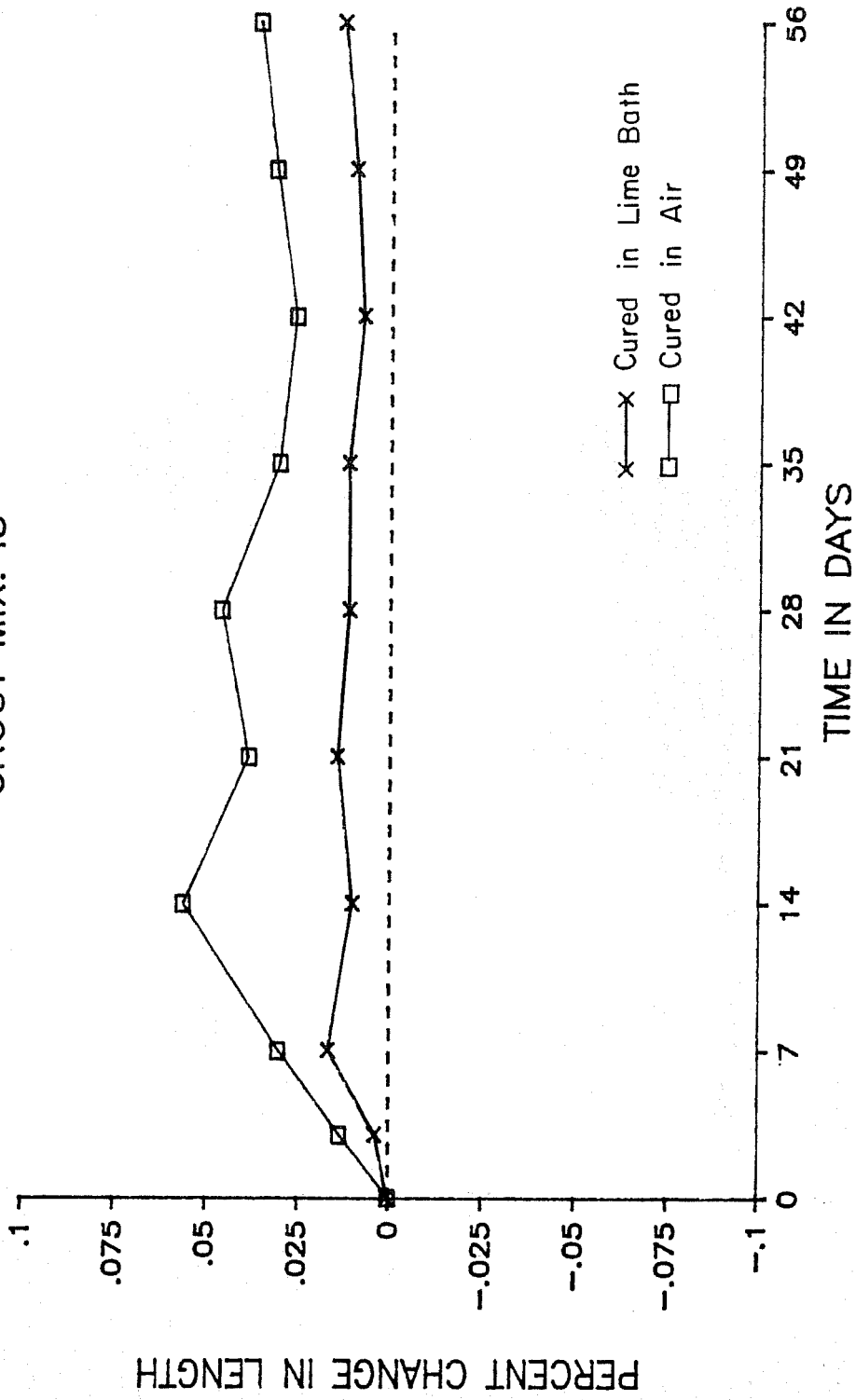


Fig. D.16

# GROUT SHRINKAGE / SWELL VS TIME

GROUT MIX: 16

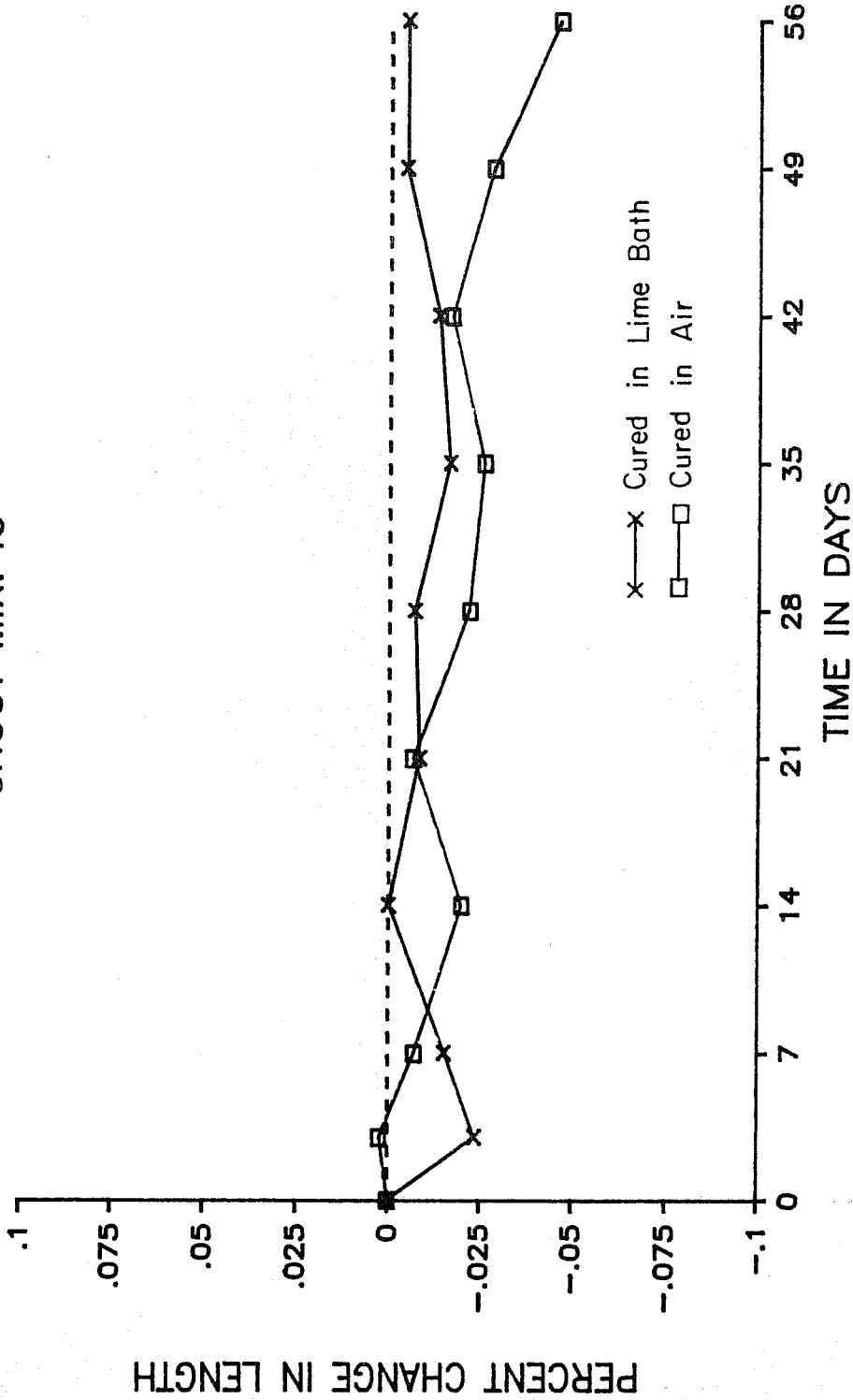


Fig. D.17

# GROUT SHRINKAGE / SWELL VS TIME

GROUT MIX: 17

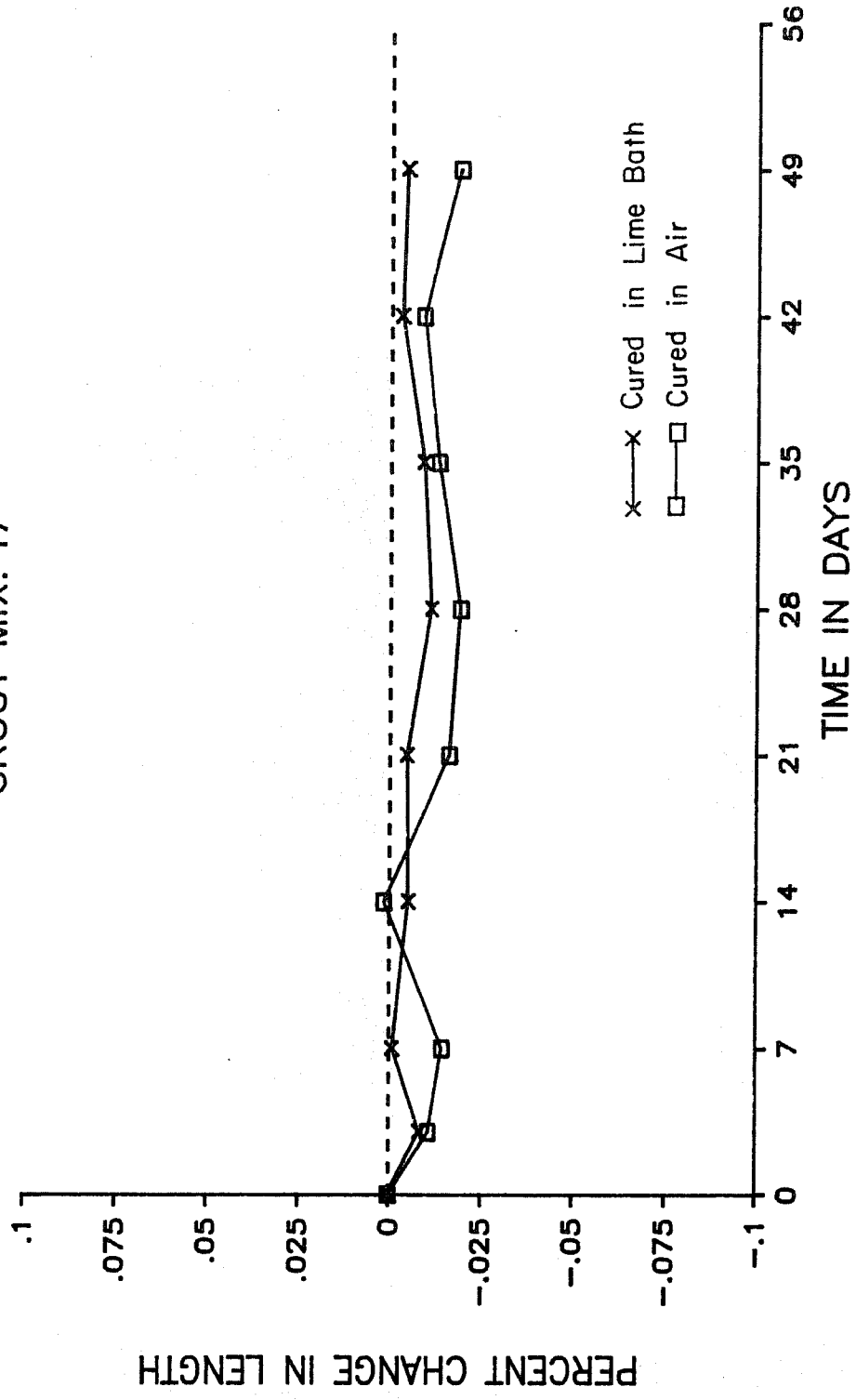


Fig. D.18

# GROUT SHRINKAGE / SWELL VS TIME

GROUT MIX: J2

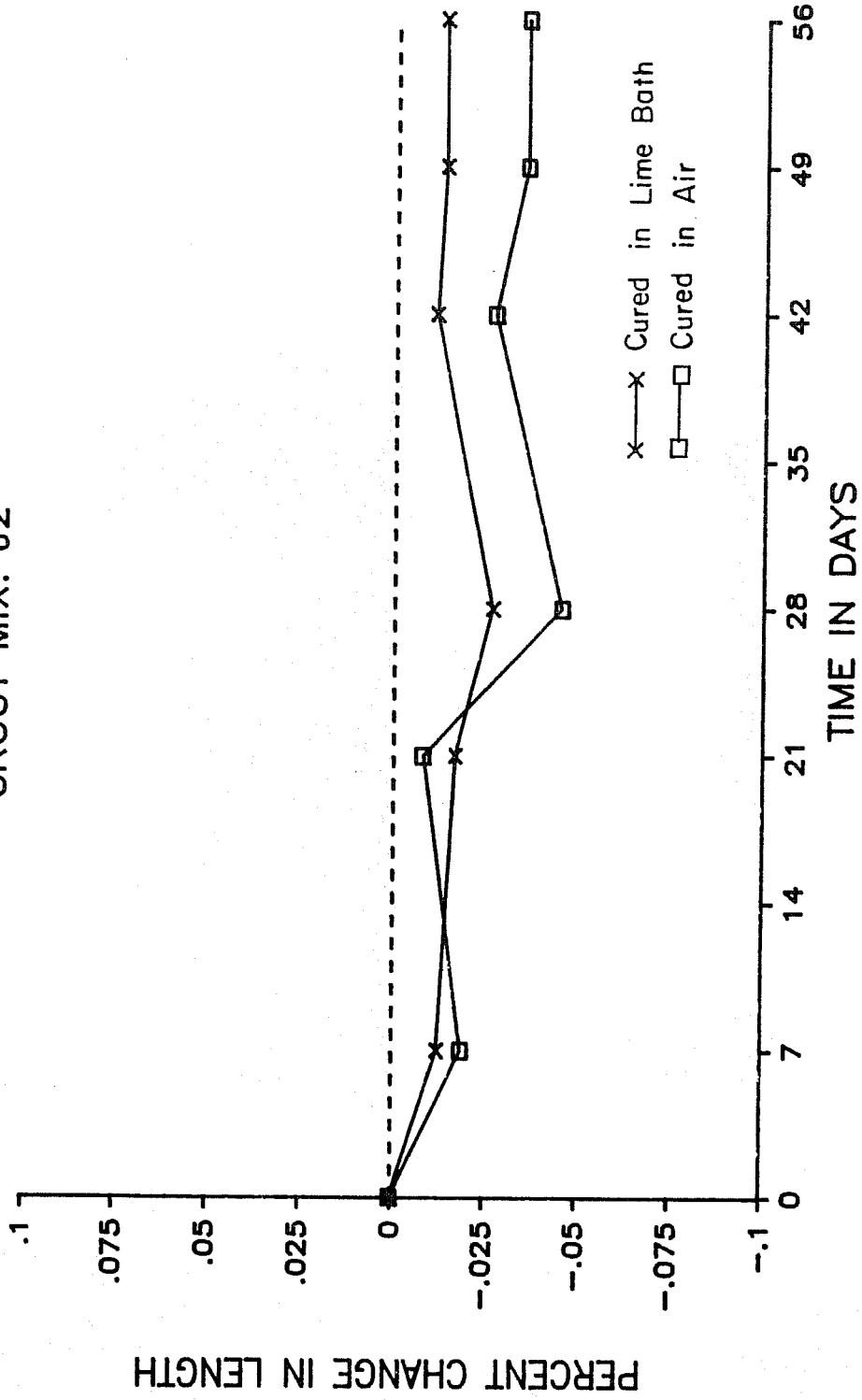


Fig. D.19

# FCU' COL. CUBES VS. FCU ASTM CUBES

GROUT MIX: I1

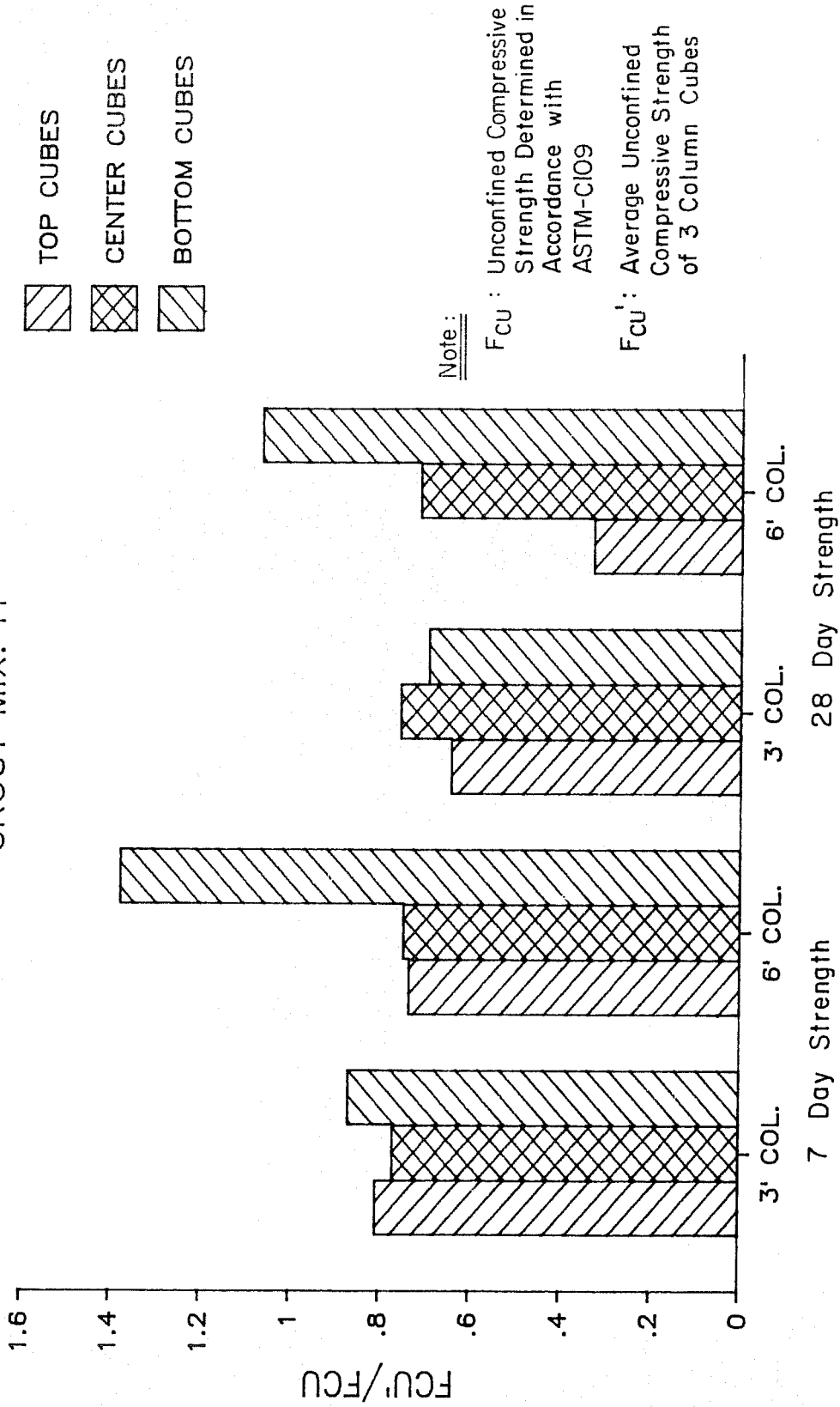


Fig. D.20



# FCU' COL. CUBES VS. FCU ASTM CUBES

GROUT MIX: 12

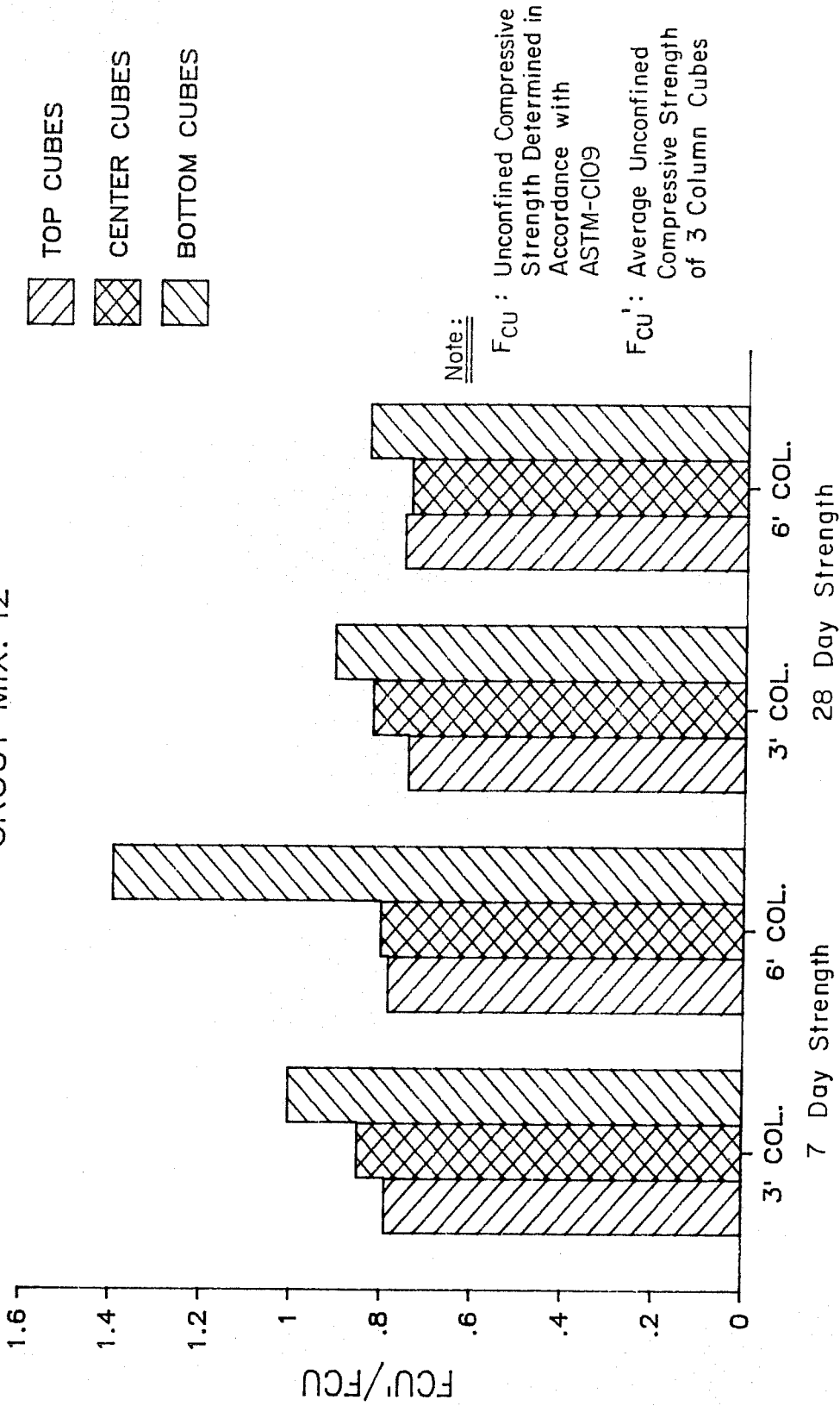


Fig. D.21

# FCU' COL. CUBES VS. FCU ASTM CUBES

GROUT MIX: 14

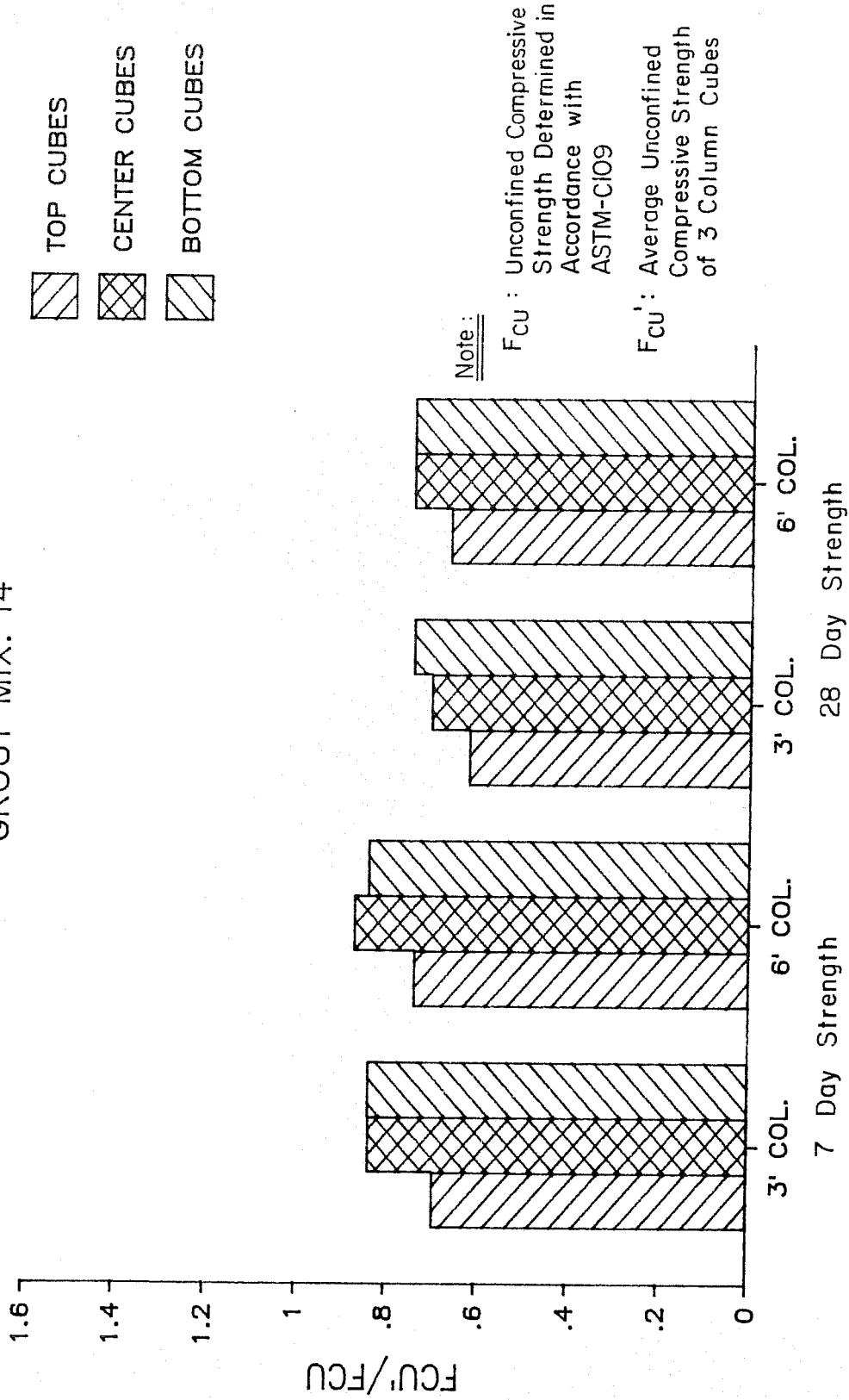


Fig. D.22

# FCU' COL. CUBES VS. FCU ASTM CUBES

GROUT MIX: 15

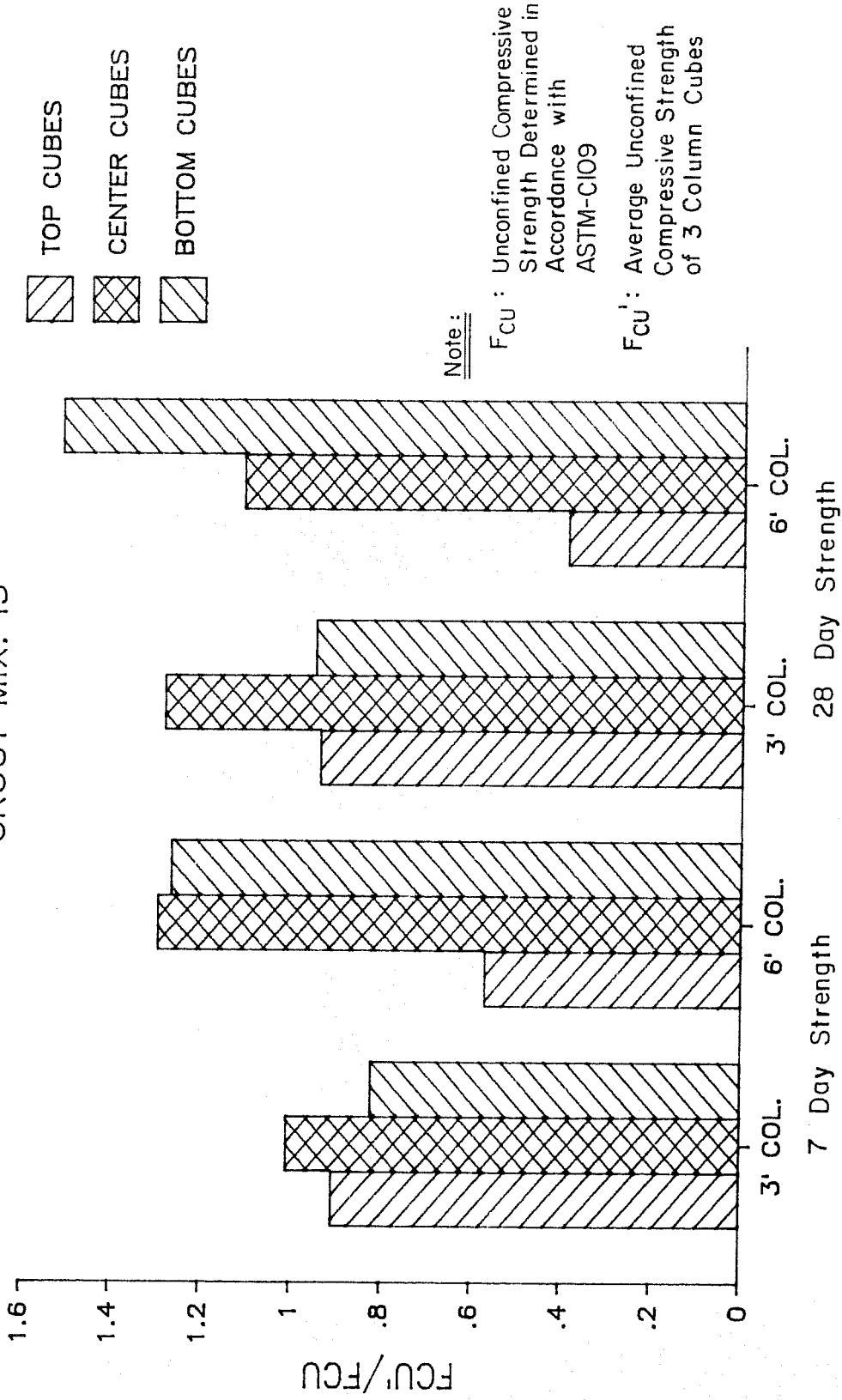


Fig. D.23

# FCU' COL. CUBES VS. FCU ASTM CUBES

GROUT MIX: 16

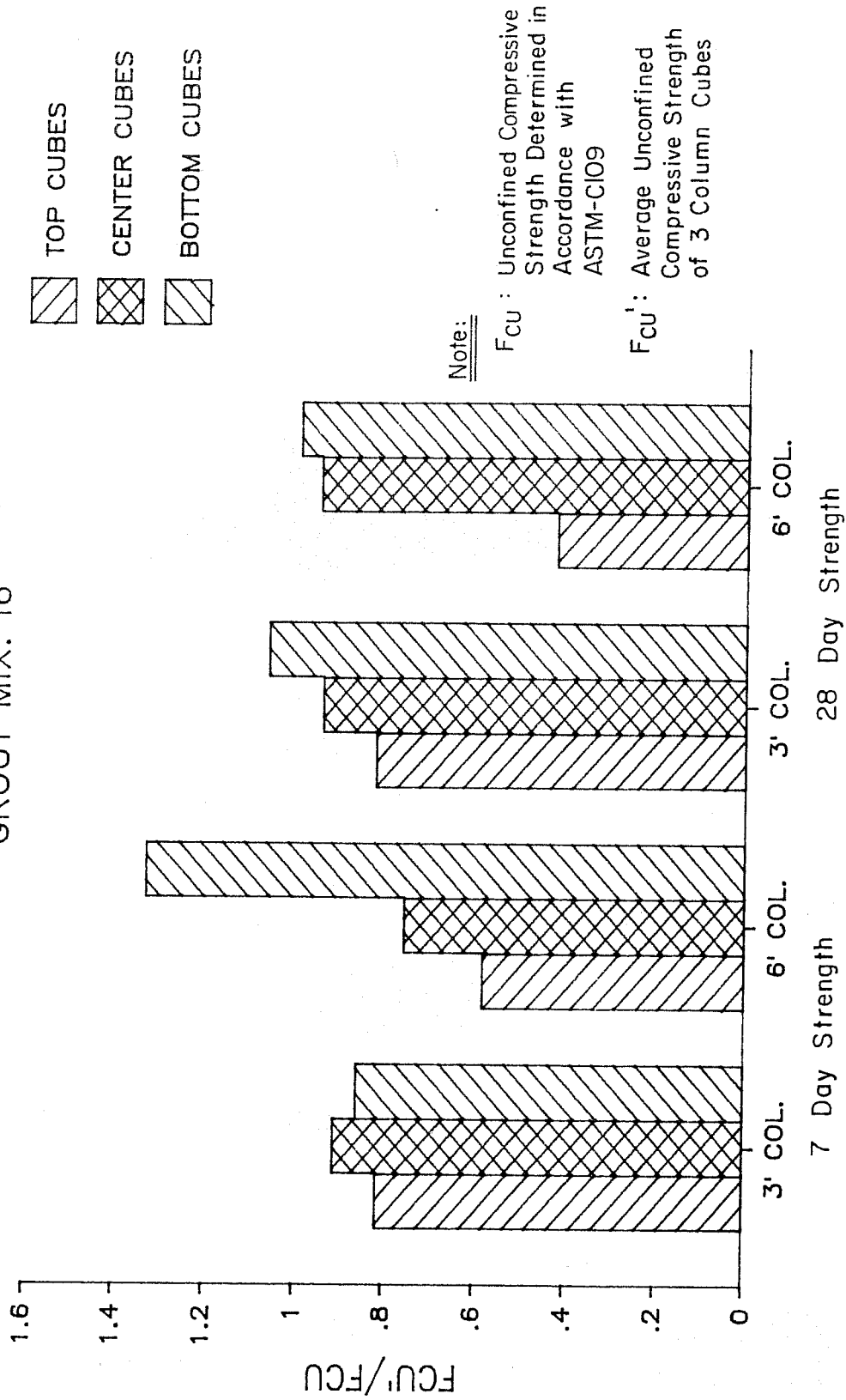


Fig. D.24

# FCU' COL. CUBES VS. FCU ASTM CUBES

GROUT MIX: 17

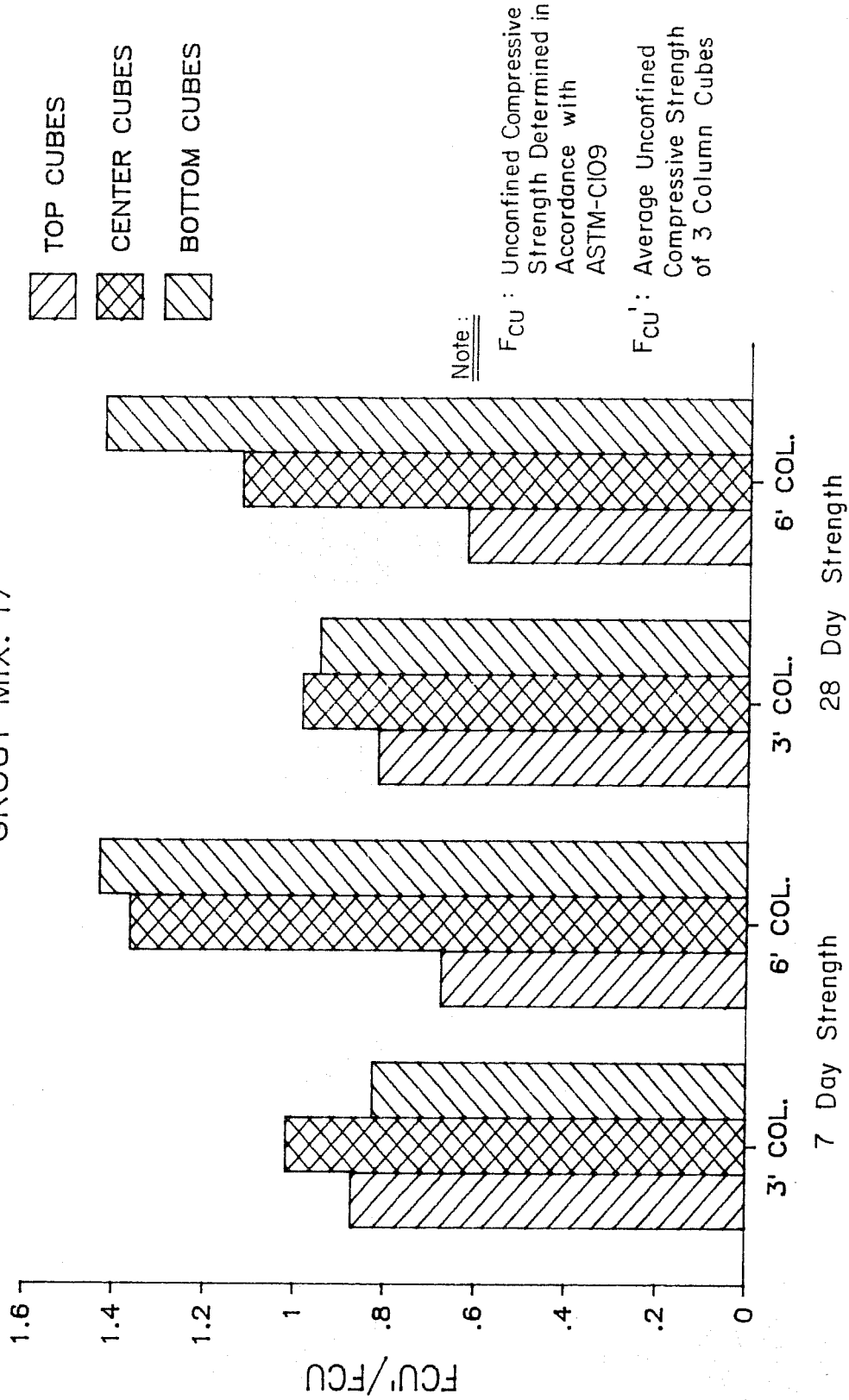


Fig. D.25

# FCU' COL. CUBES VS. FCU ASTM CUBES

## GROUT MIX: I

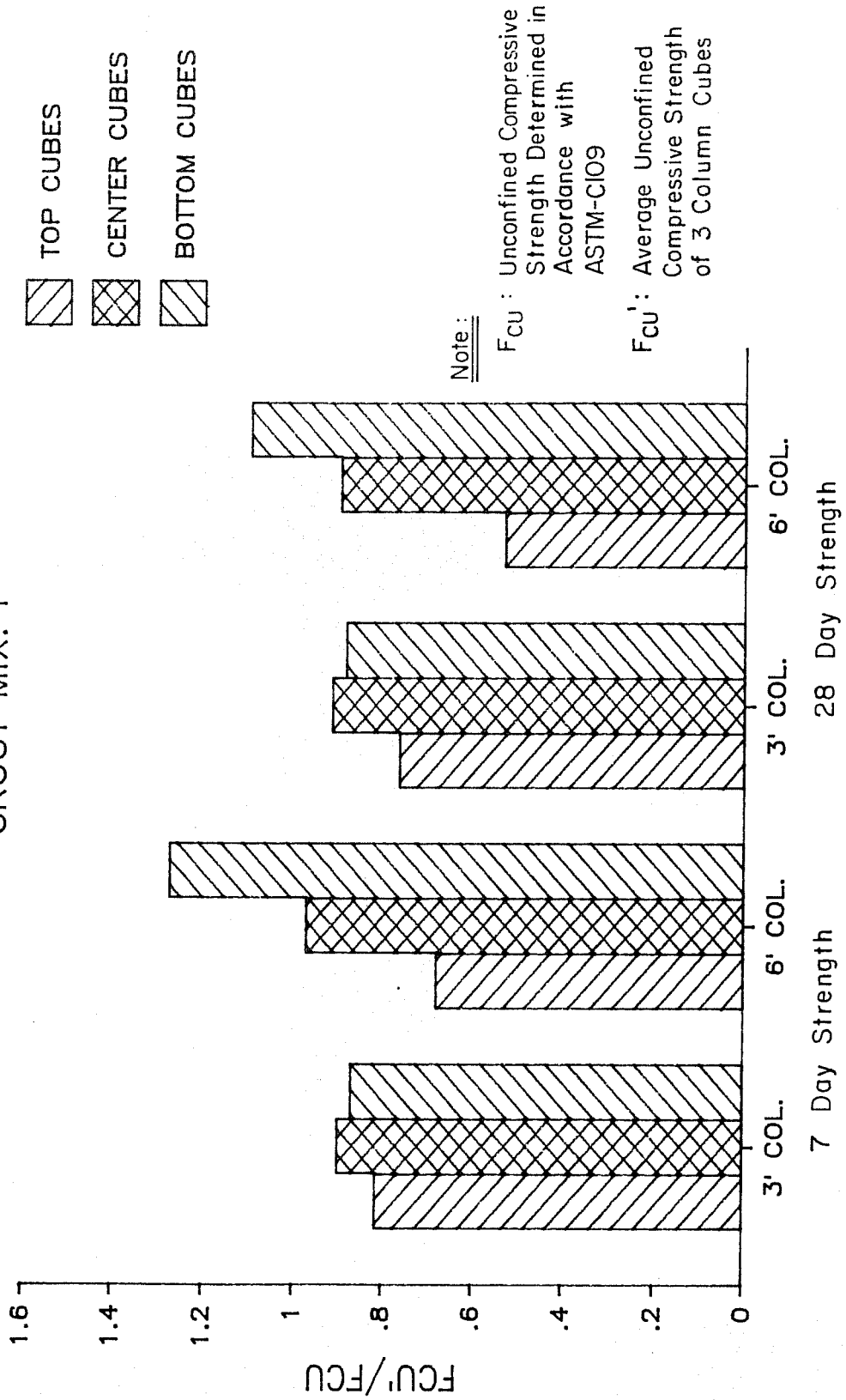


Fig. D.26

# FCU' COL. CUBES VS. FCU ASTM CUBES

GROUT MIX: J1

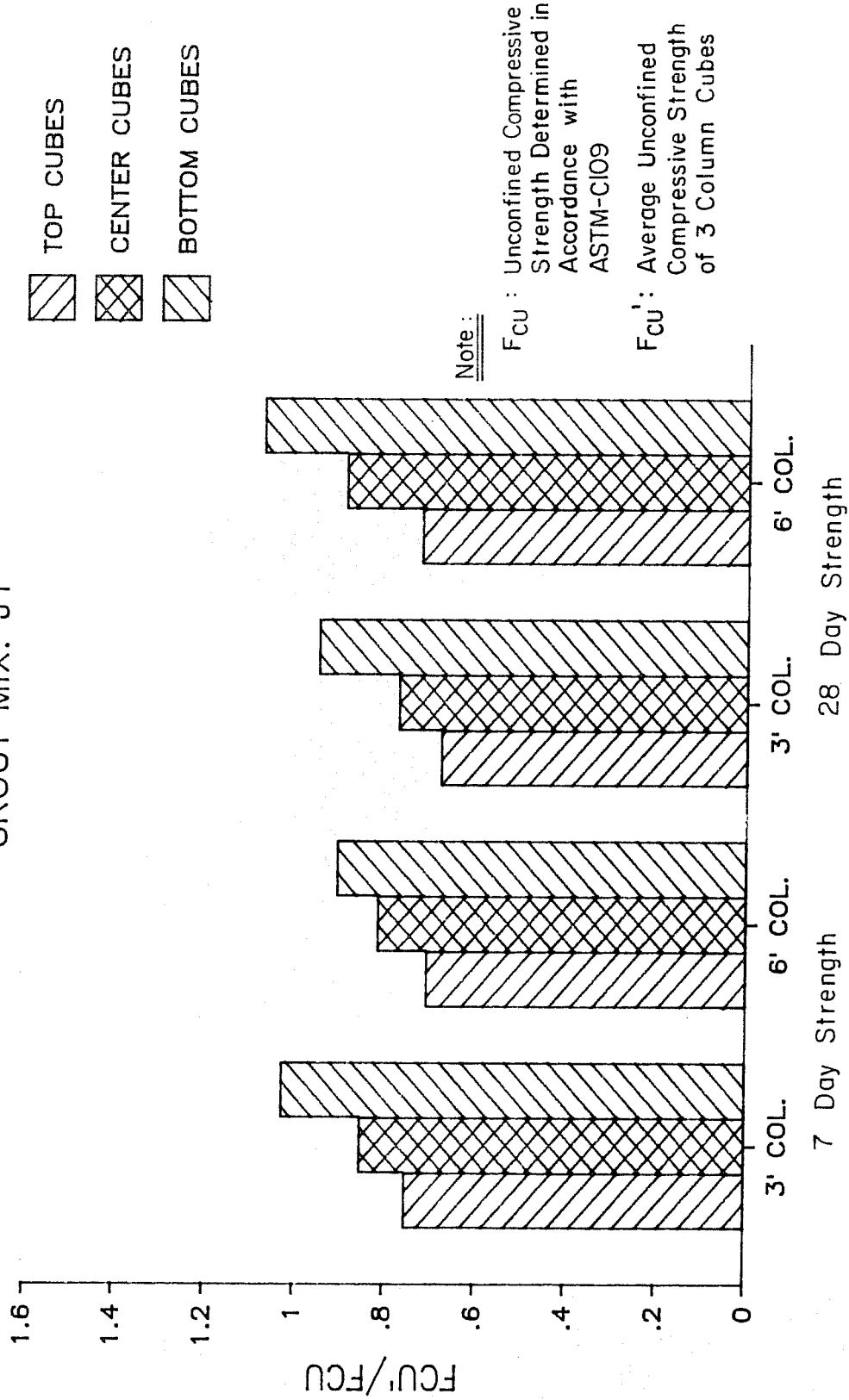


Fig. D.27

**APPENDIX E**



# SERIES 1: TEST UTA1

## AVE. BOND STRESS VS DISPLACEMENT

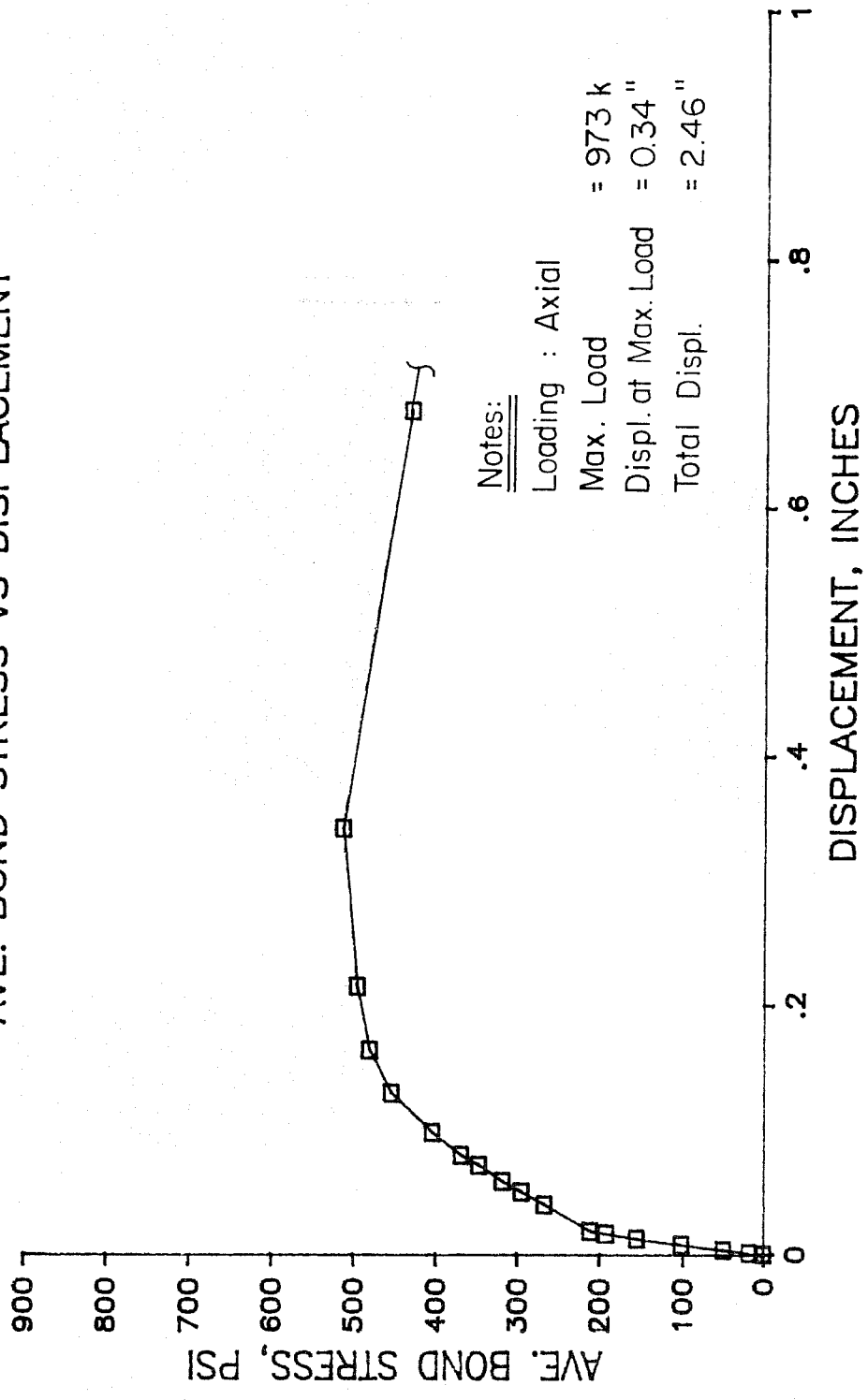


Fig. E.1

**SERIES 1: TEST UTA2**  
**AVE. BOND STRESS VS DISPLACEMENT**

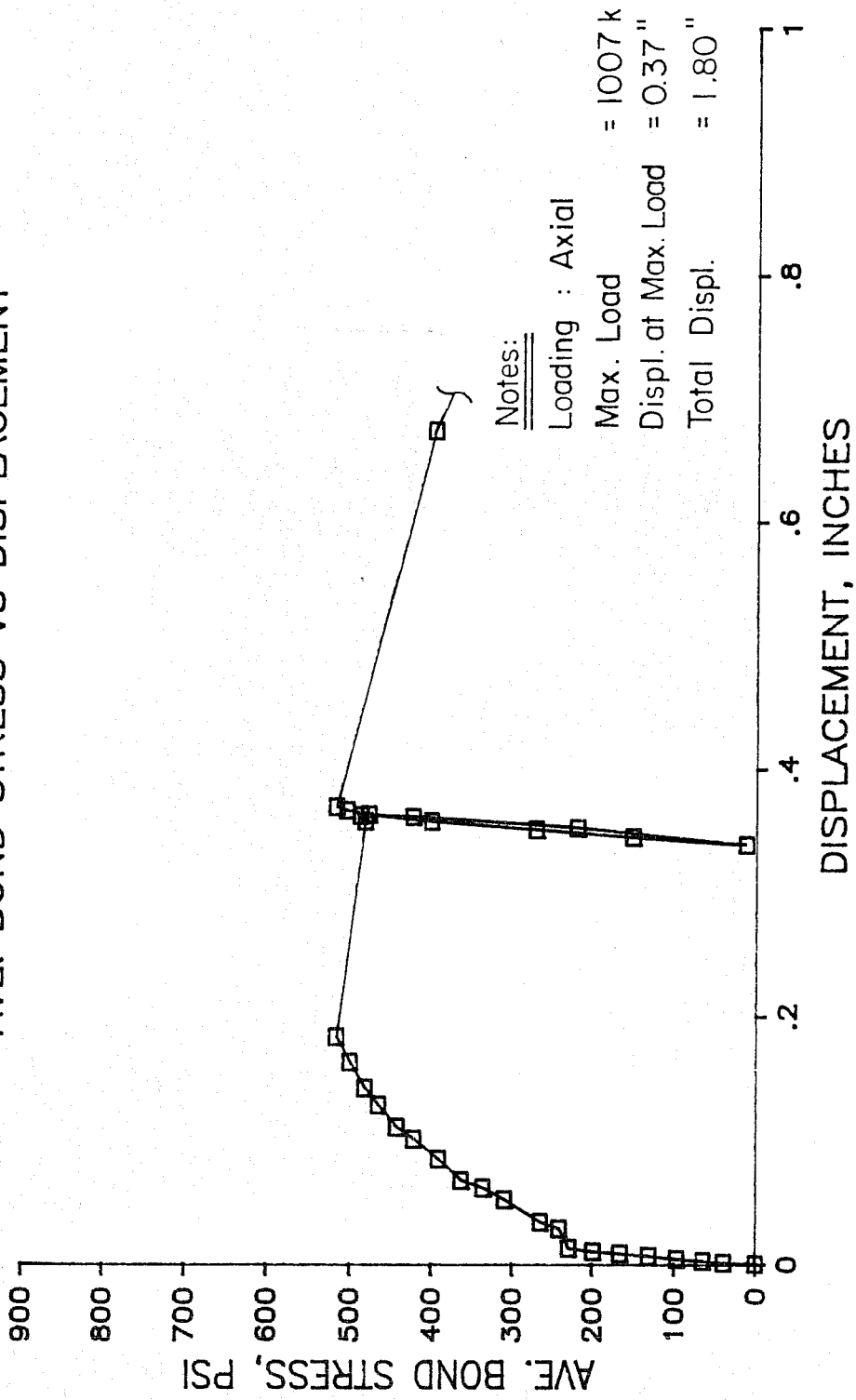


Fig. E.2

# SERIES 1: TEST UTA3

## AVE. BOND STRESS VS DISPLACEMENT

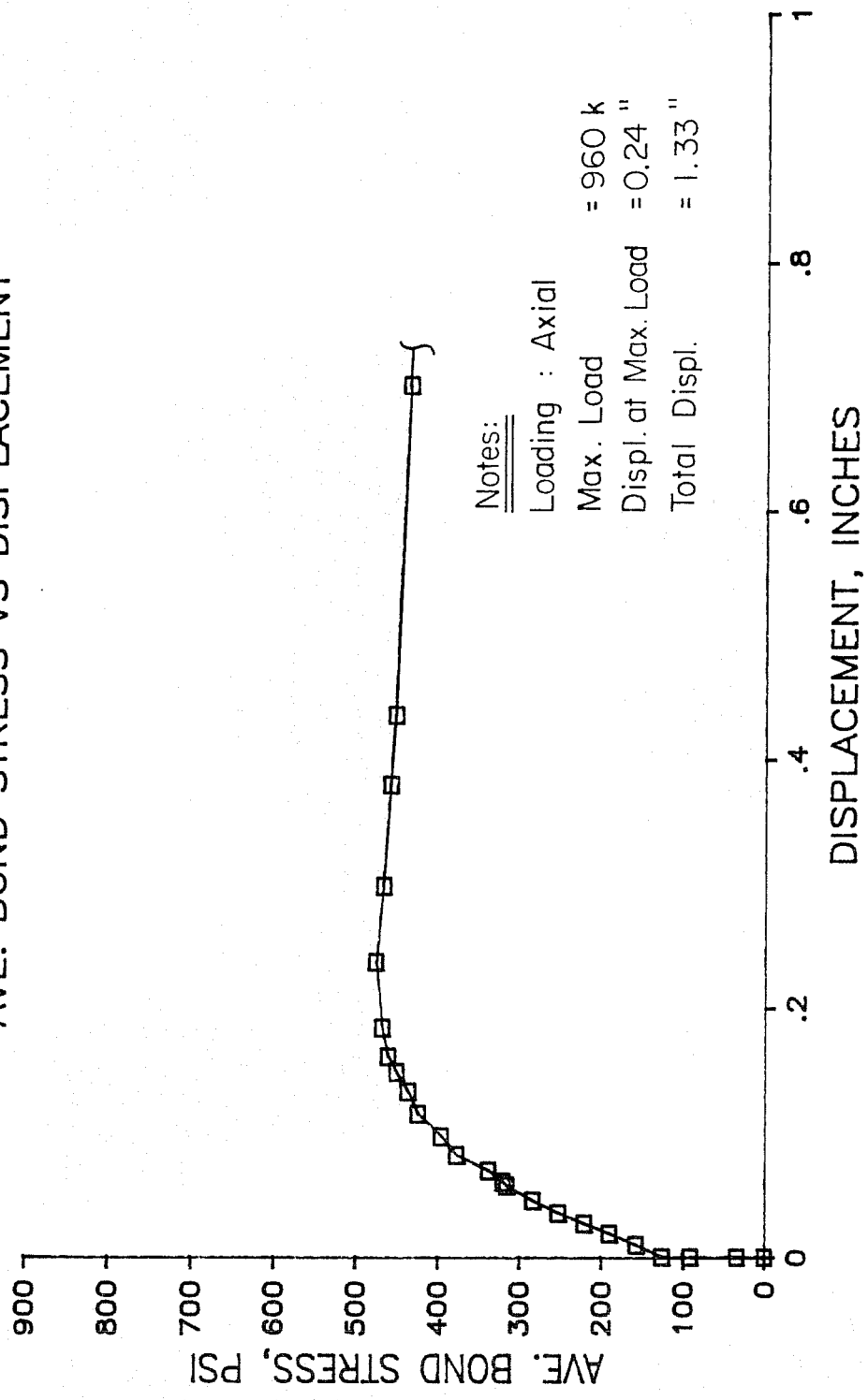


Fig. E.3

# SERIES 2: TEST UTM1

## AVE. BOND STRESS VS DISPLACEMENT

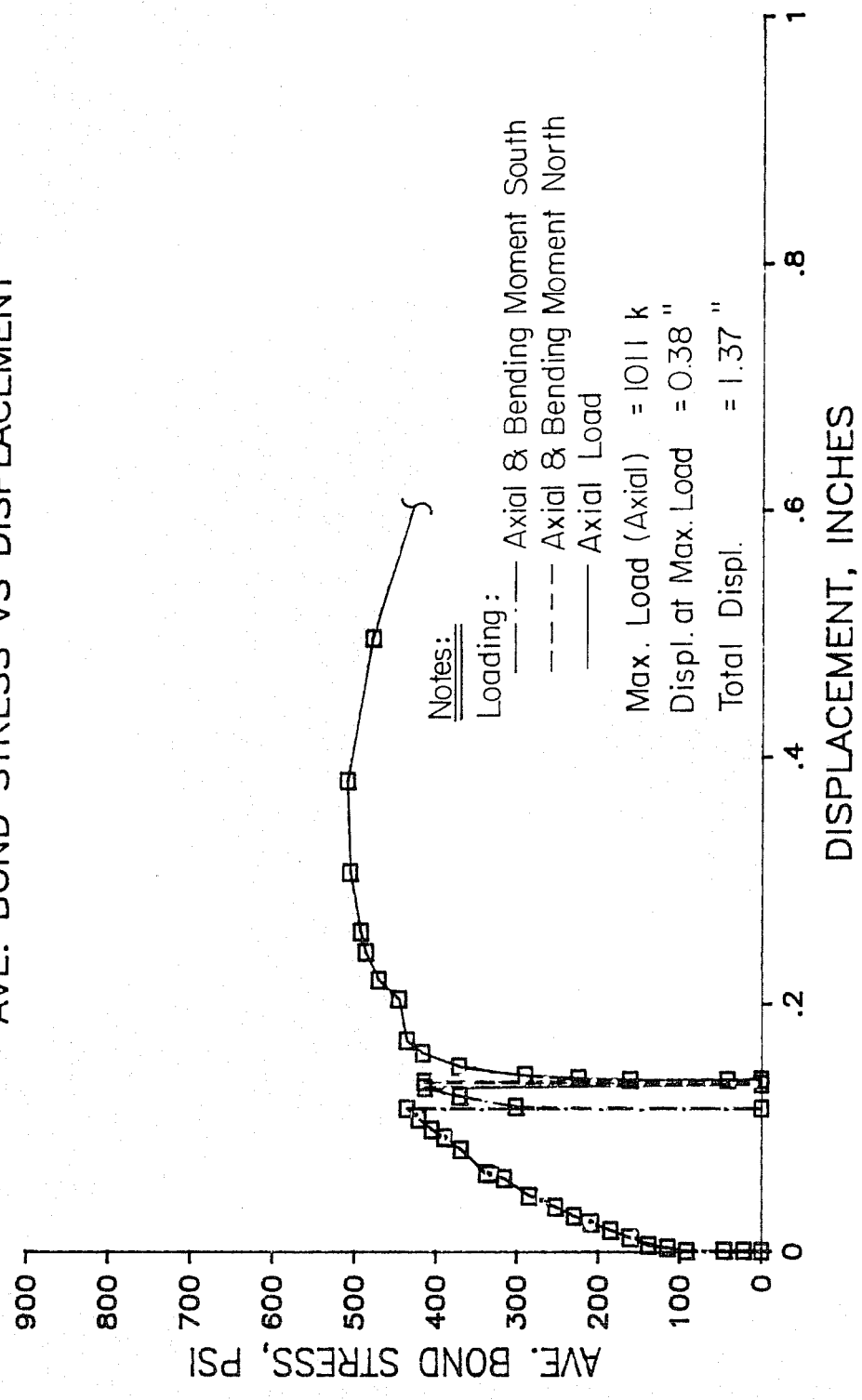


Fig. E.4

# SERIES 2: TEST UTM2

## AVE. BOND STRESS VS DISPLACEMENT

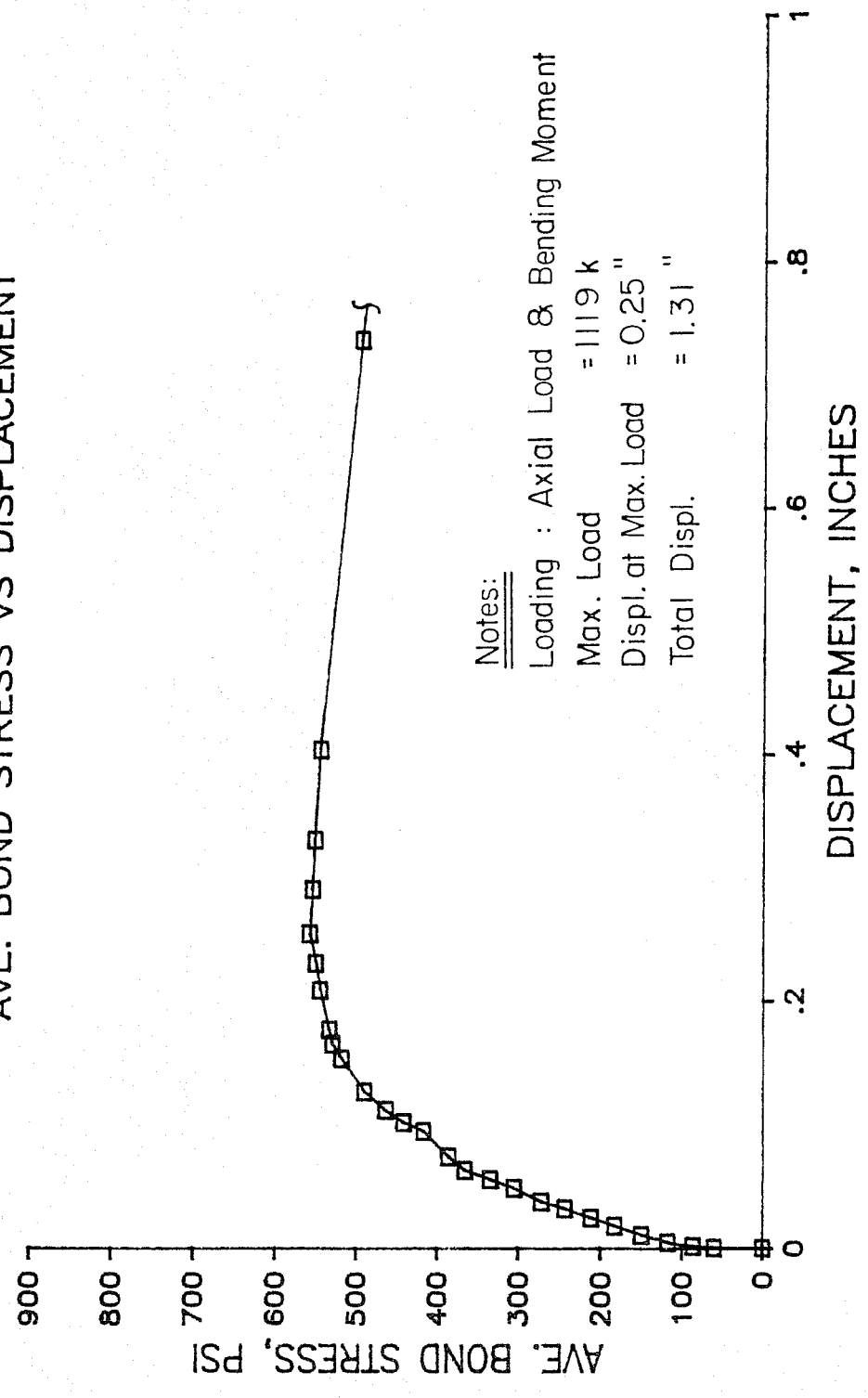


Fig. E.5

# SERIES 2: TEST UTM3

## AVE. BOND STRESS VS DISPLACEMENT

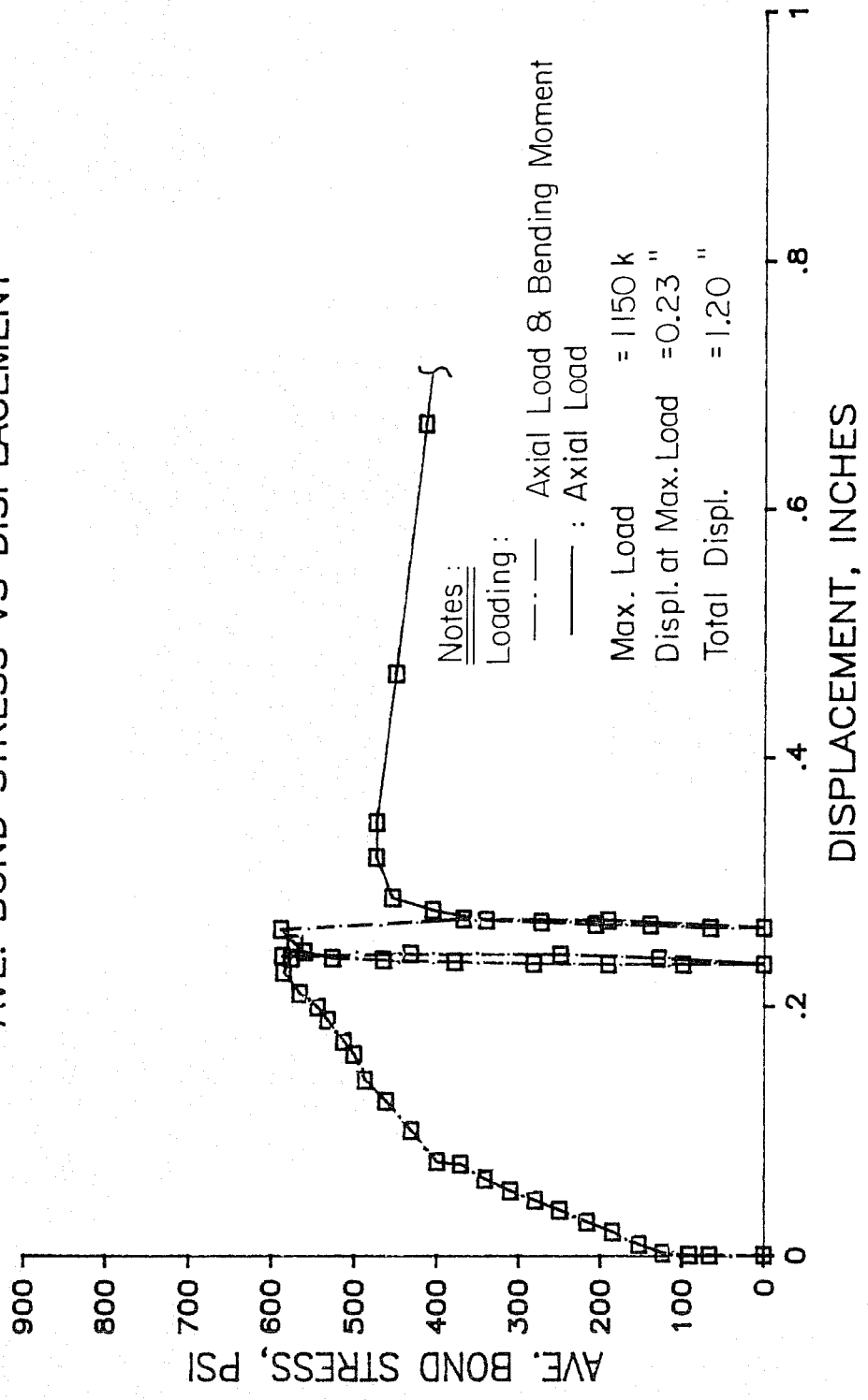


Fig. E.6

### SERIES 3: TEST UTA4

AVE. BOND STRESS VS DISPLACEMENT

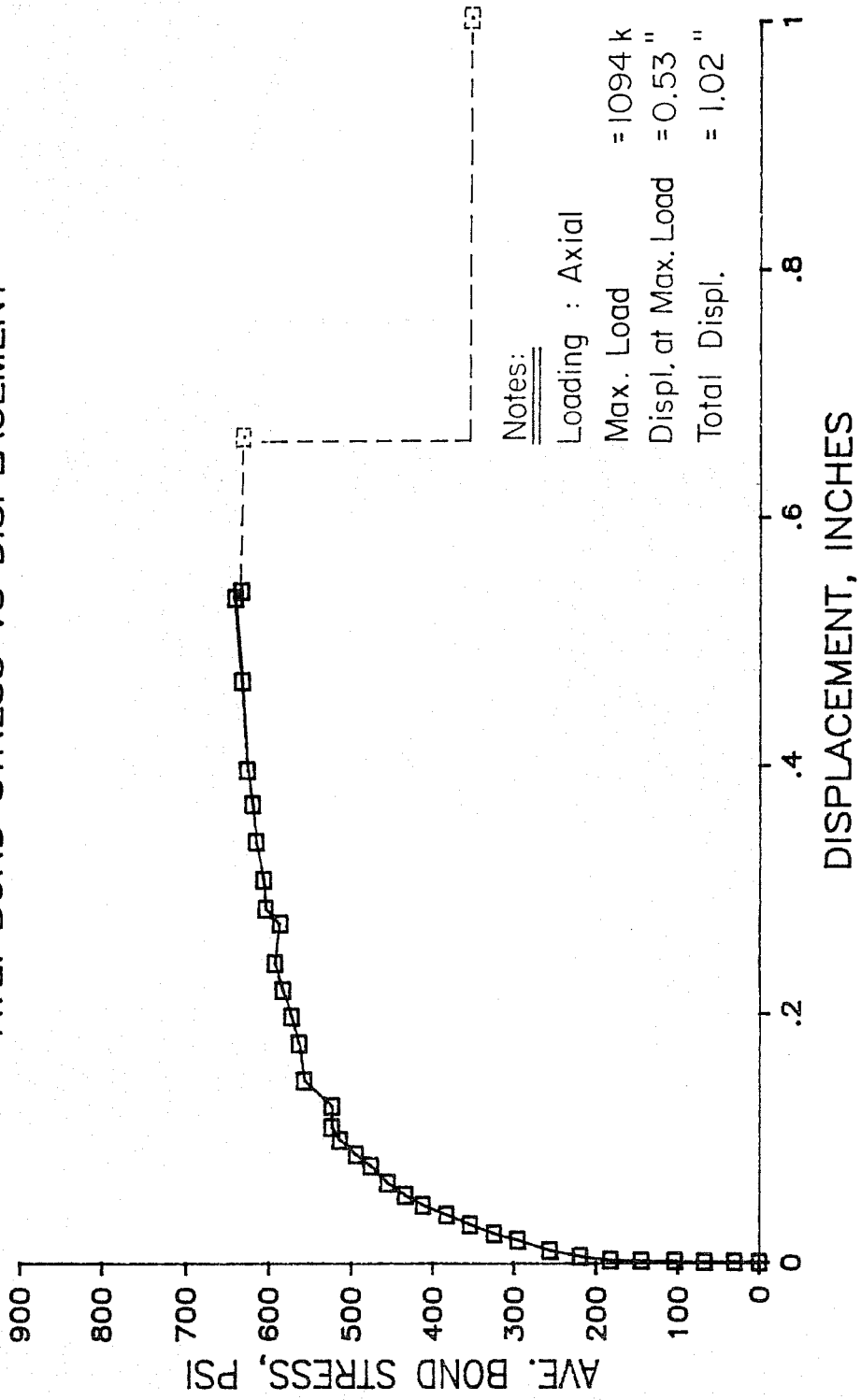
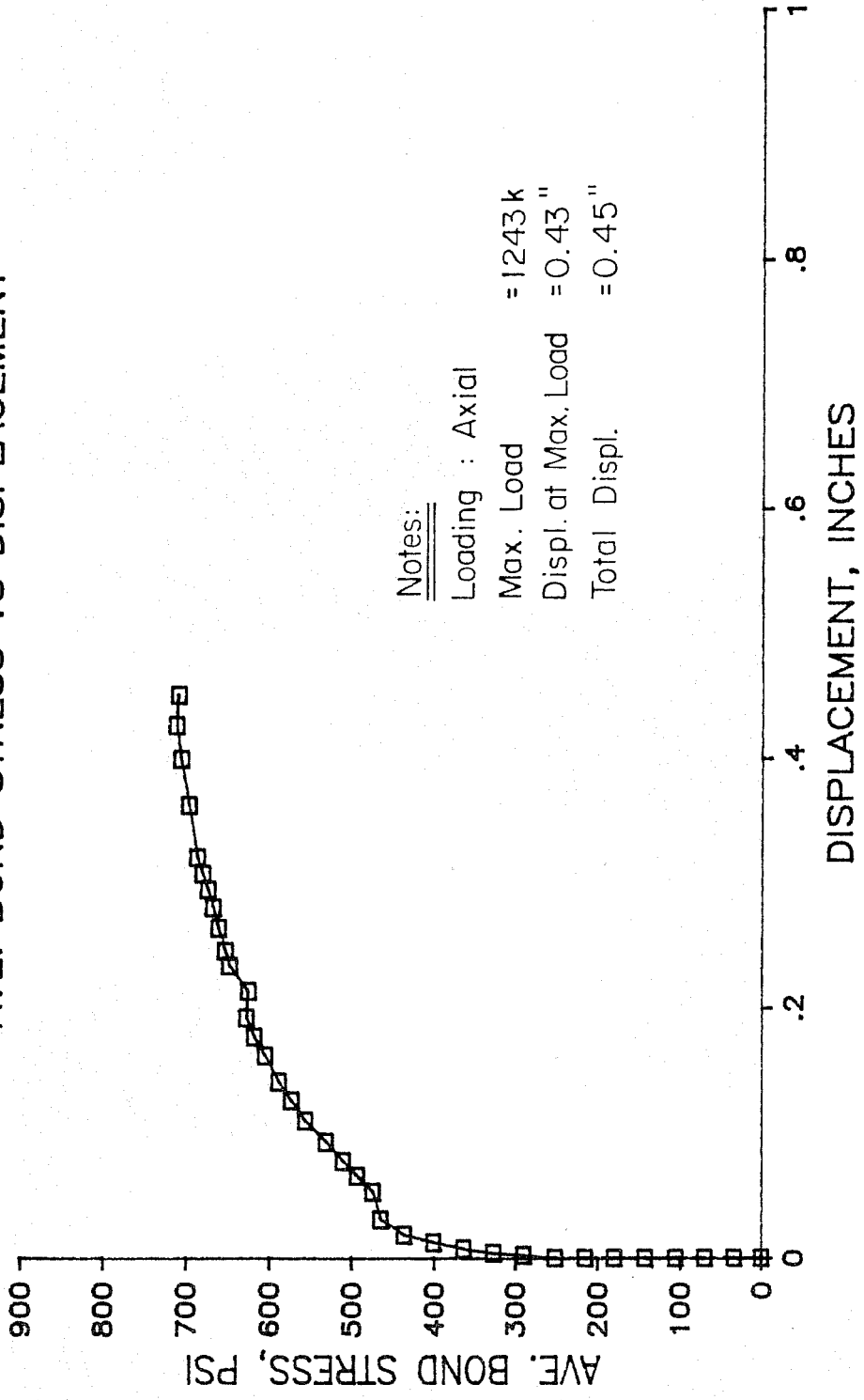


Fig. E.7

# SERIES 3: TEST UTA5

## AVE. BOND STRESS VS DISPLACEMENT



Notes:

Loading : Axial  
Max. Load = 1243 k  
Displ. at Max. Load = 0.43"  
Total Displ. = 0.45"

Fig. E.8



### SERIES 3: TEST UTA6

AVE. BOND STRESS VS DISPLACEMENT

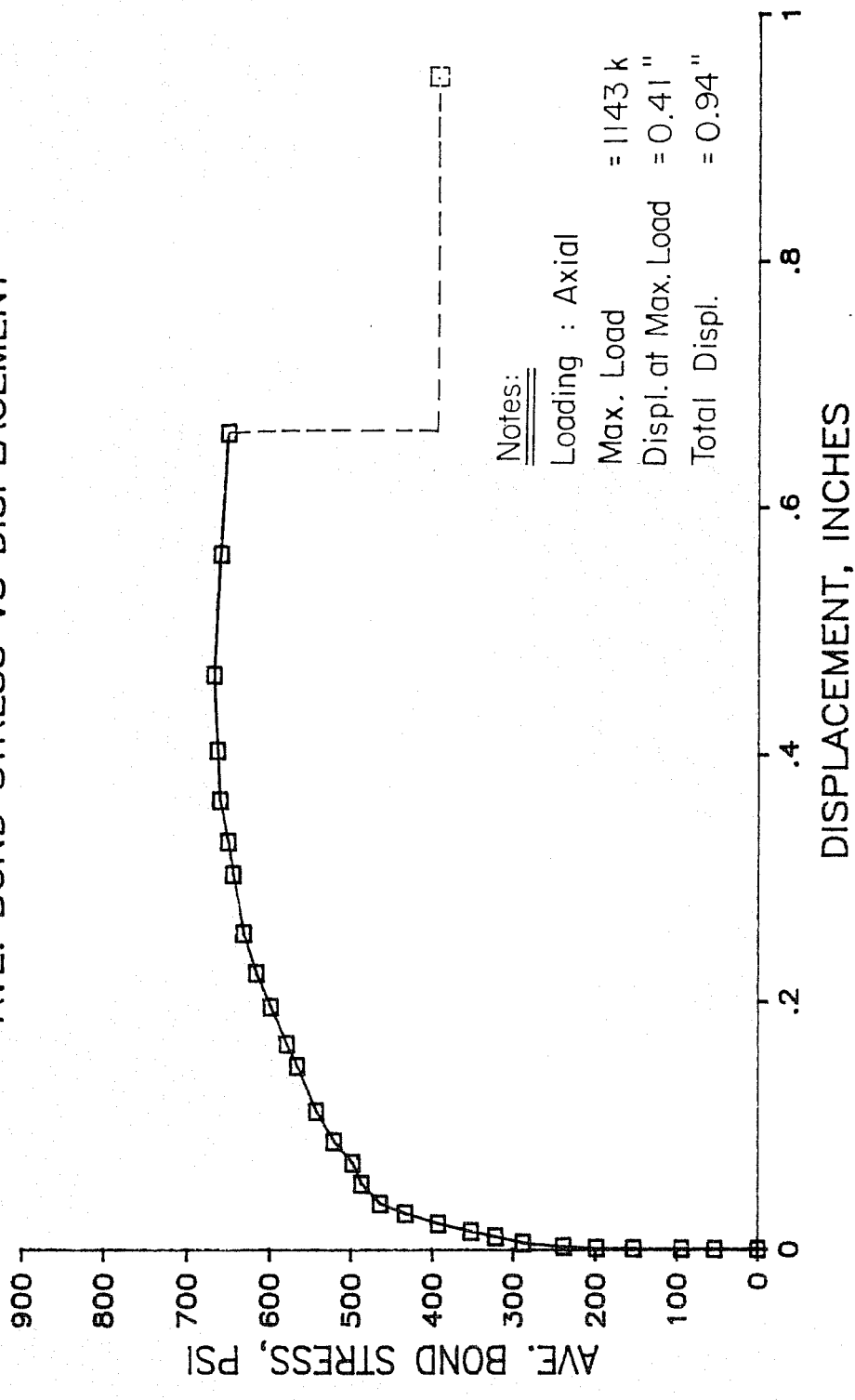


Fig. E.9

# SERIES 4: TEST UTA13

## AVE. BOND STRESS VS DISPLACEMENT

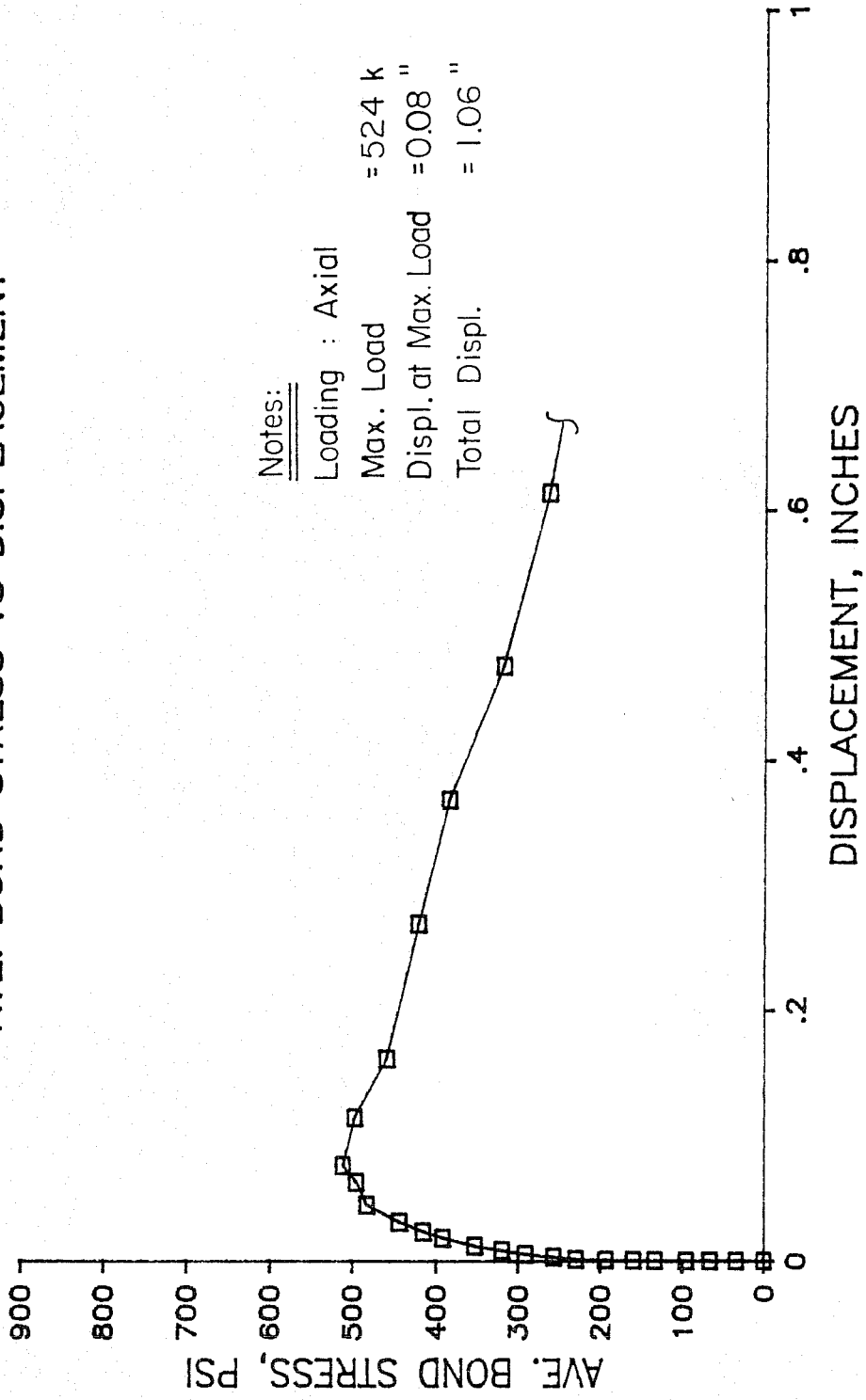
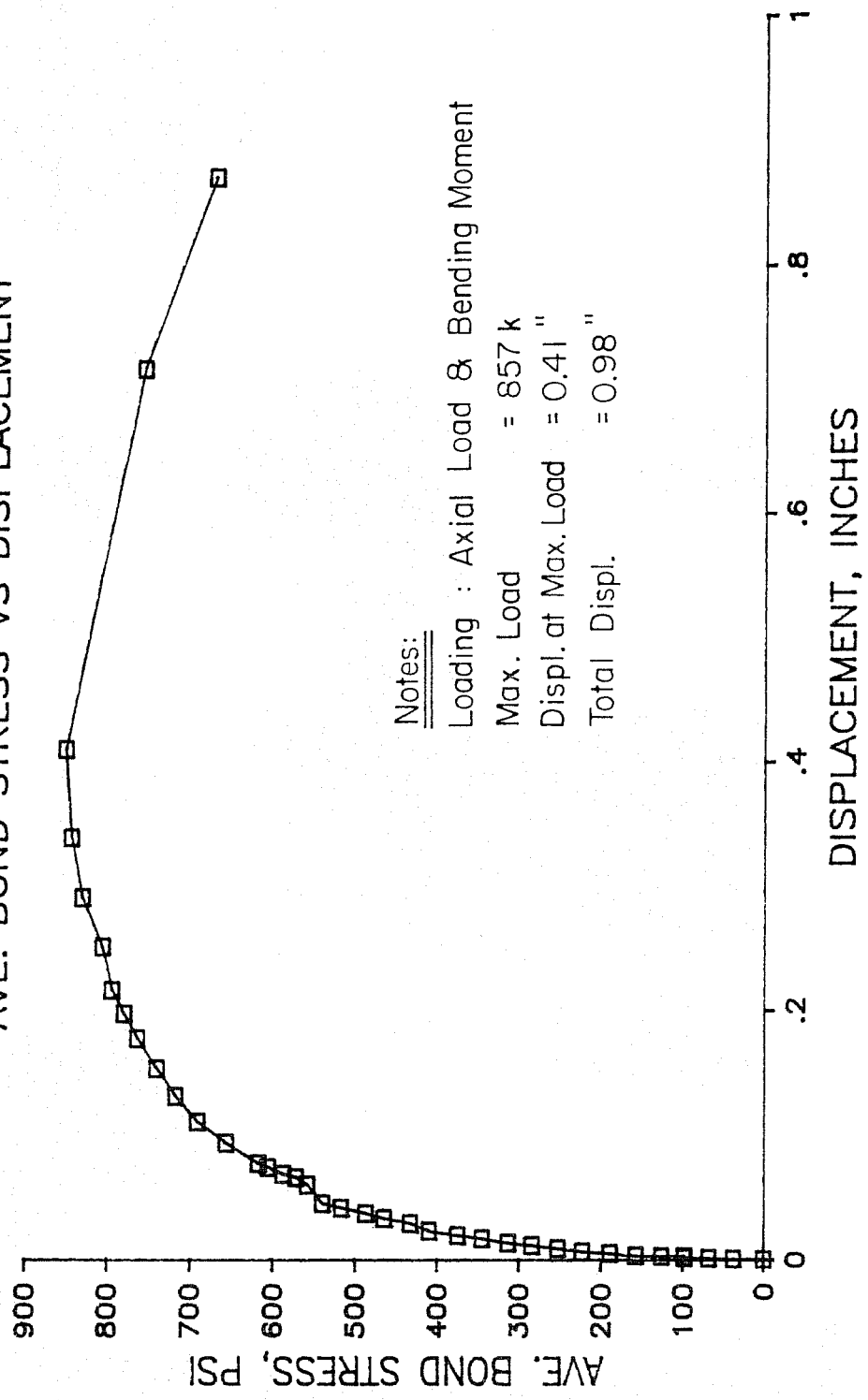


Fig. E.10

# SERIES 4: TEST UTM5

## AVE. BOND STRESS VS DISPLACEMENT



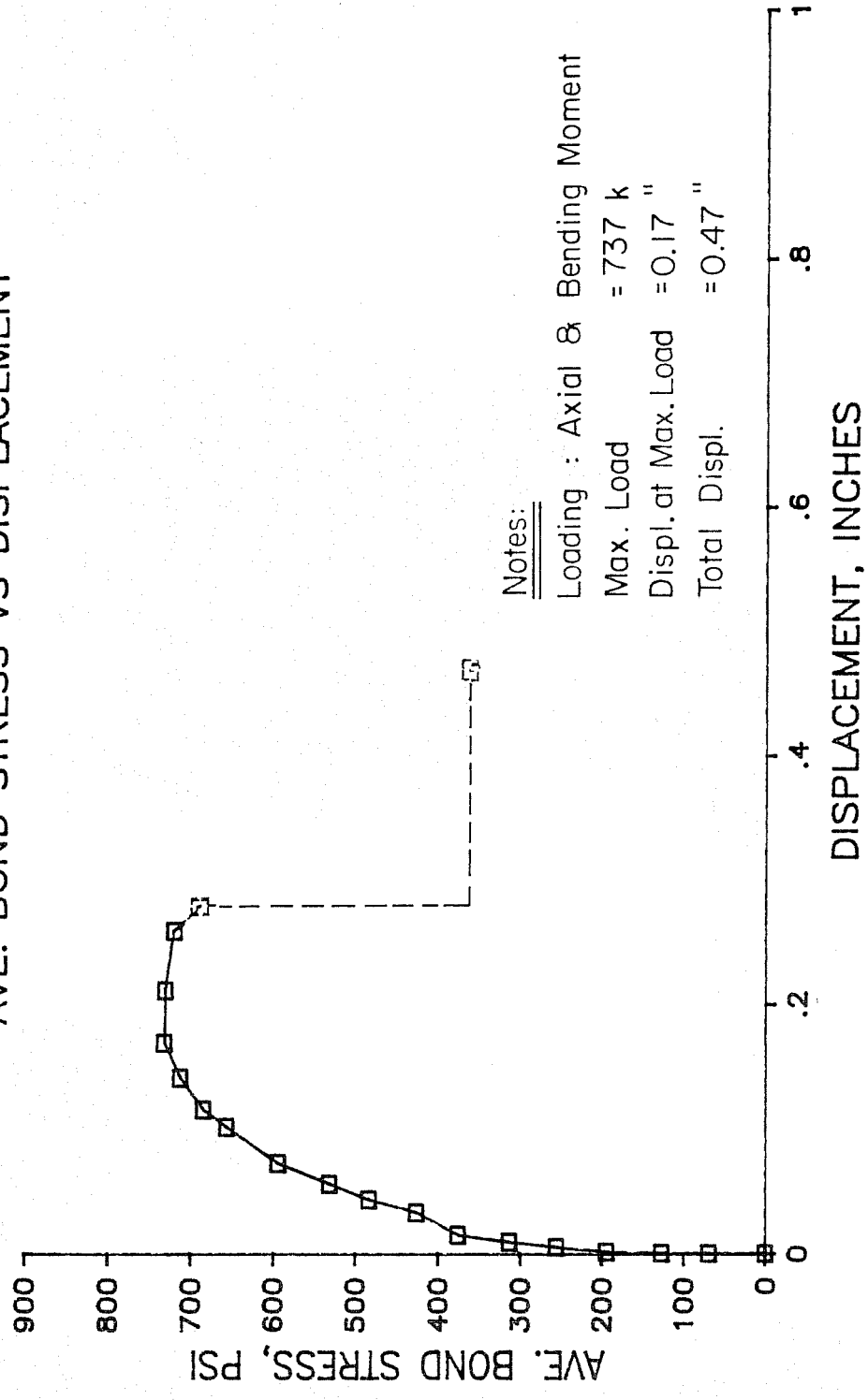
Notes:

Loading : Axial Load & Bending Moment  
Max. Load = 857 k  
Displ. at Max. Load = 0.41 "  
Total Displ. = 0.98 "

Fig. E.11

# SERIES 4: TEST UTM6

## AVE. BOND STRESS VS DISPLACEMENT



Notes:  
Loading : Axial & Bending Moment  
Max. Load = 737 k  
Displ. at Max. Load = 0.17 "  
Total Displ. = 0.47 "

Fig. E.12

SERIES 5: TEST UTA7  
AVE. BOND STRESS VS DISPLACEMENT

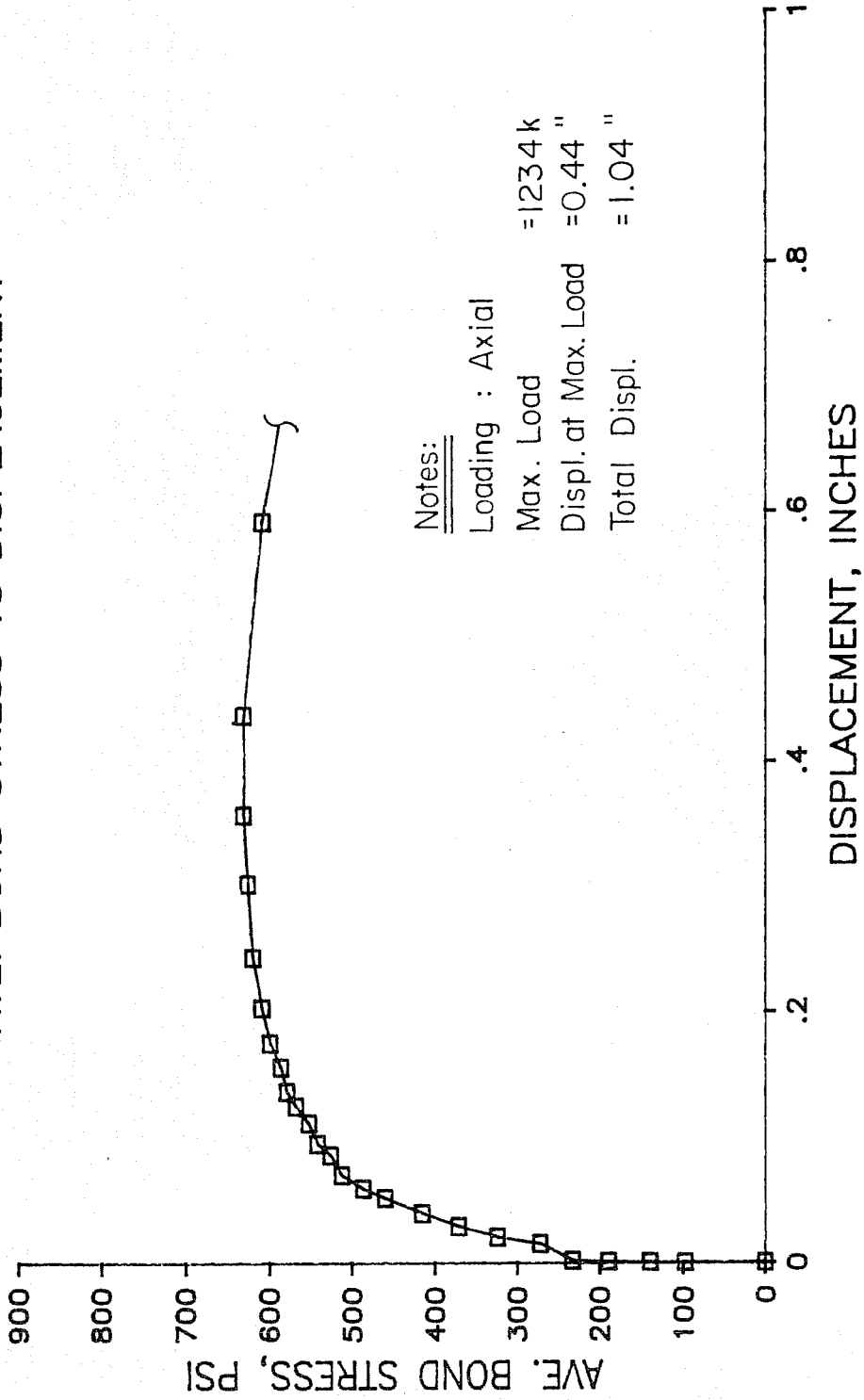
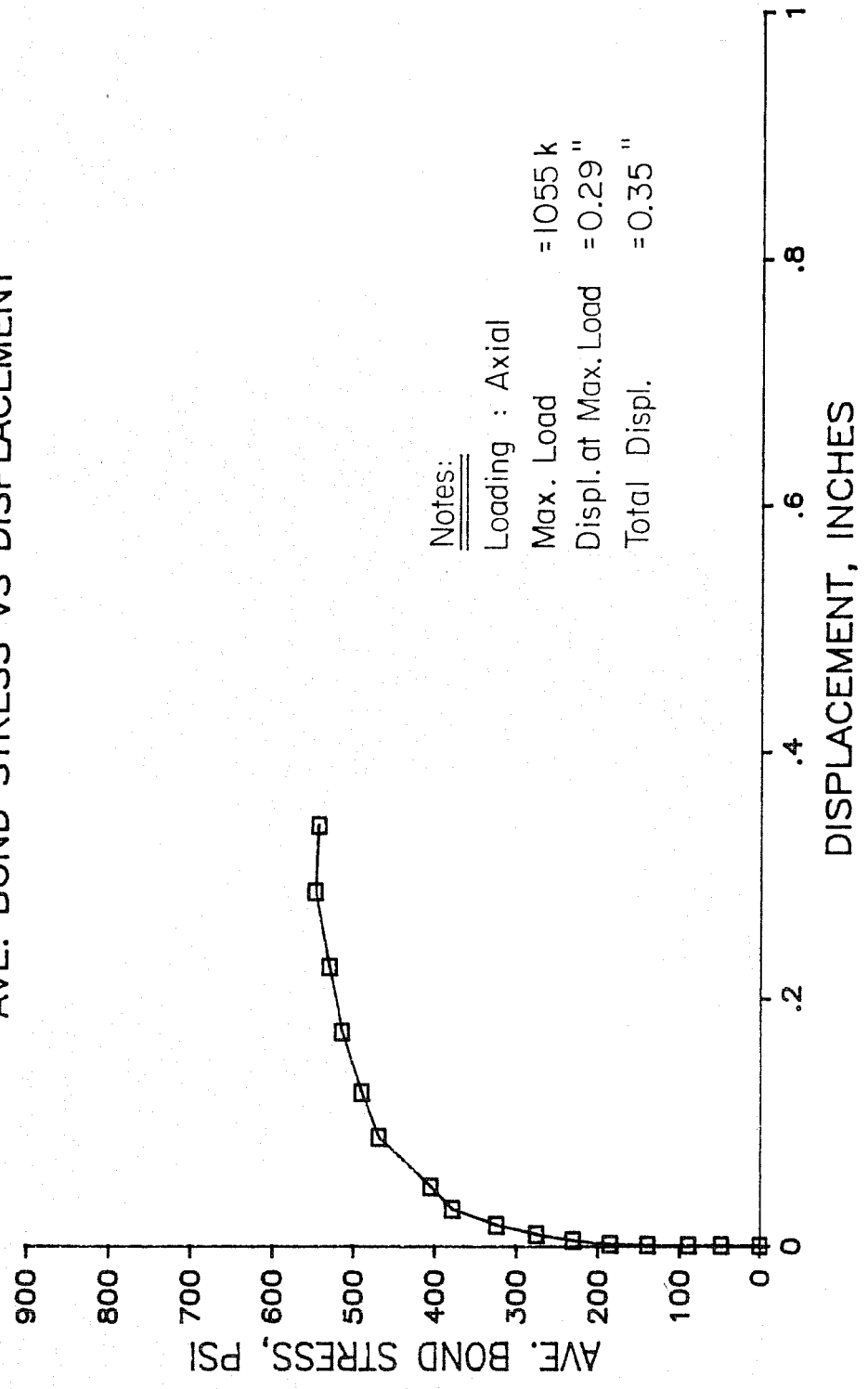


Fig. E.13

# SERIES 5: TEST UTA8

## AVE. BOND STRESS VS DISPLACEMENT



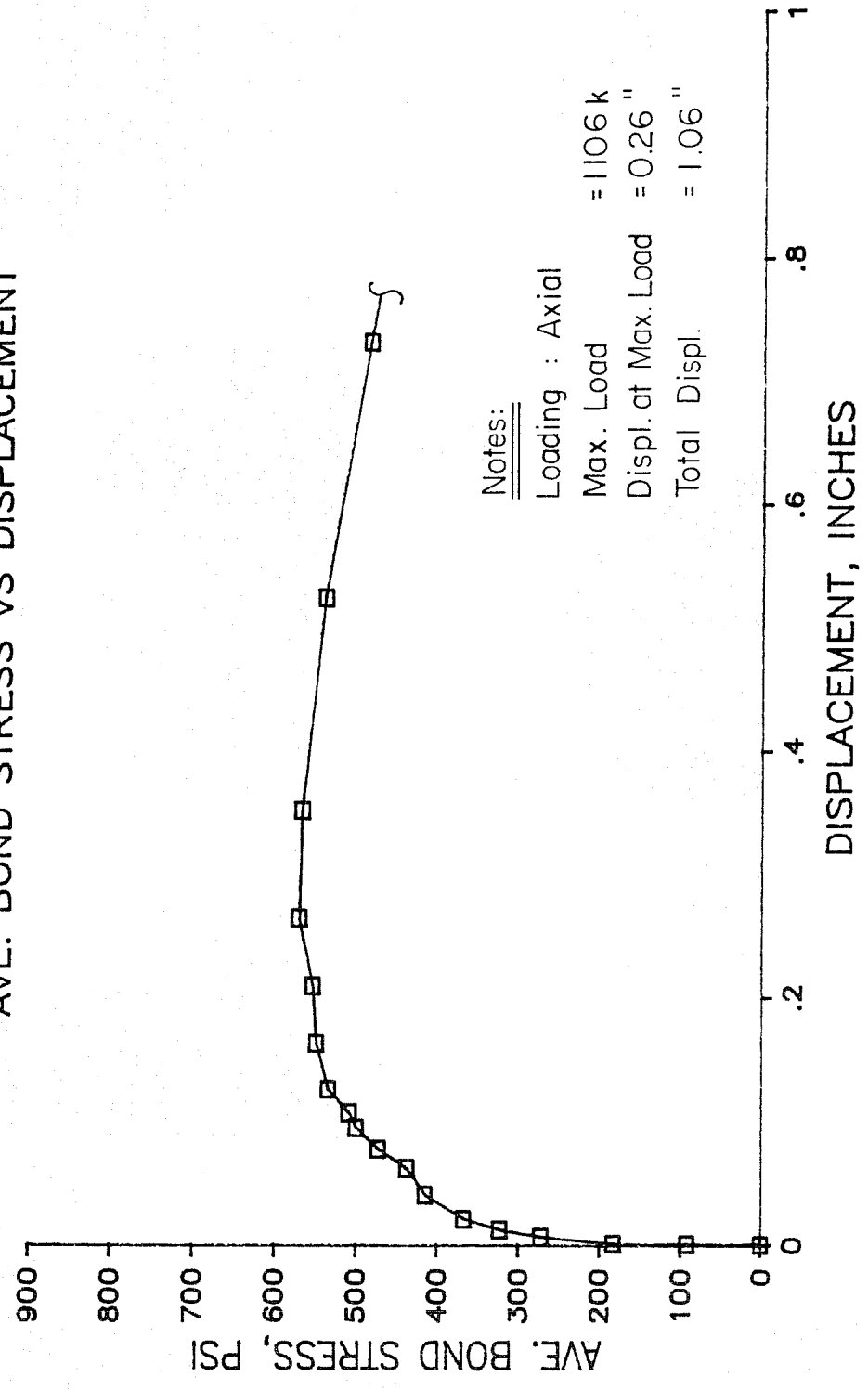
Notes:

- Loading : Axial
- Max. Load = 1055 k
- Displ. at Max. Load = 0.29 "
- Total Displ. = 0.35 "

Fig. E.14

# SERIES 5: TEST UTA9

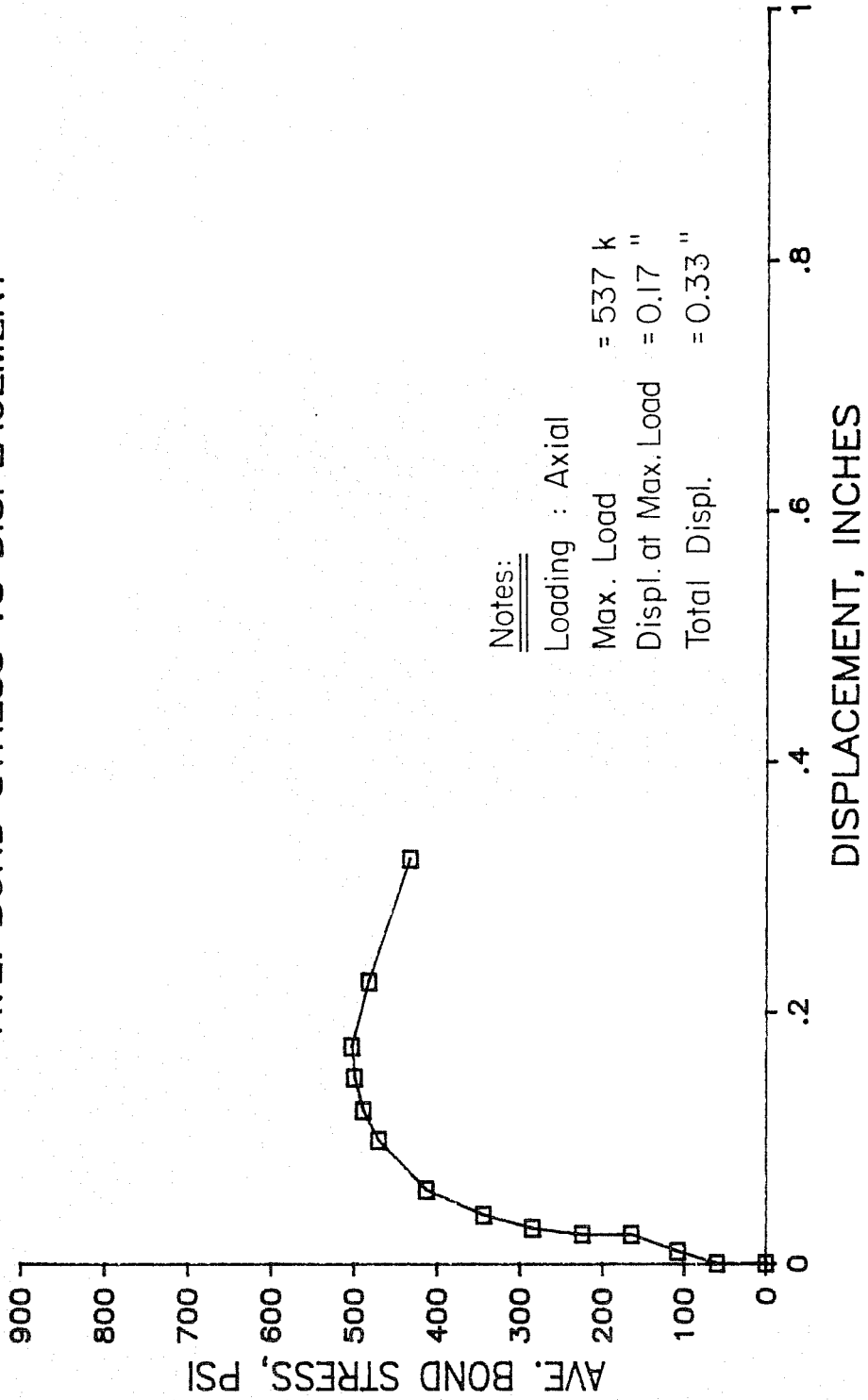
## AVE. BOND STRESS VS DISPLACEMENT



Notes:  
Loading : Axial  
Max. Load = 1106 k  
Displ. at Max. Load = 0.26 "  
Total Displ. = 1.06 "

Fig. E.15

**SERIES 6: TEST UTA10**  
**AVE. BOND STRESS VS DISPLACEMENT**



Notes:  
 Loading : Axial  
 Max. Load = 537 k  
 Displ. at Max. Load = 0.17 "  
 Total Displ. = 0.33 "

Fig. E.16



# SERIES 6: TEST UTA11

## AVE. BOND STRESS VS DISPLACEMENT

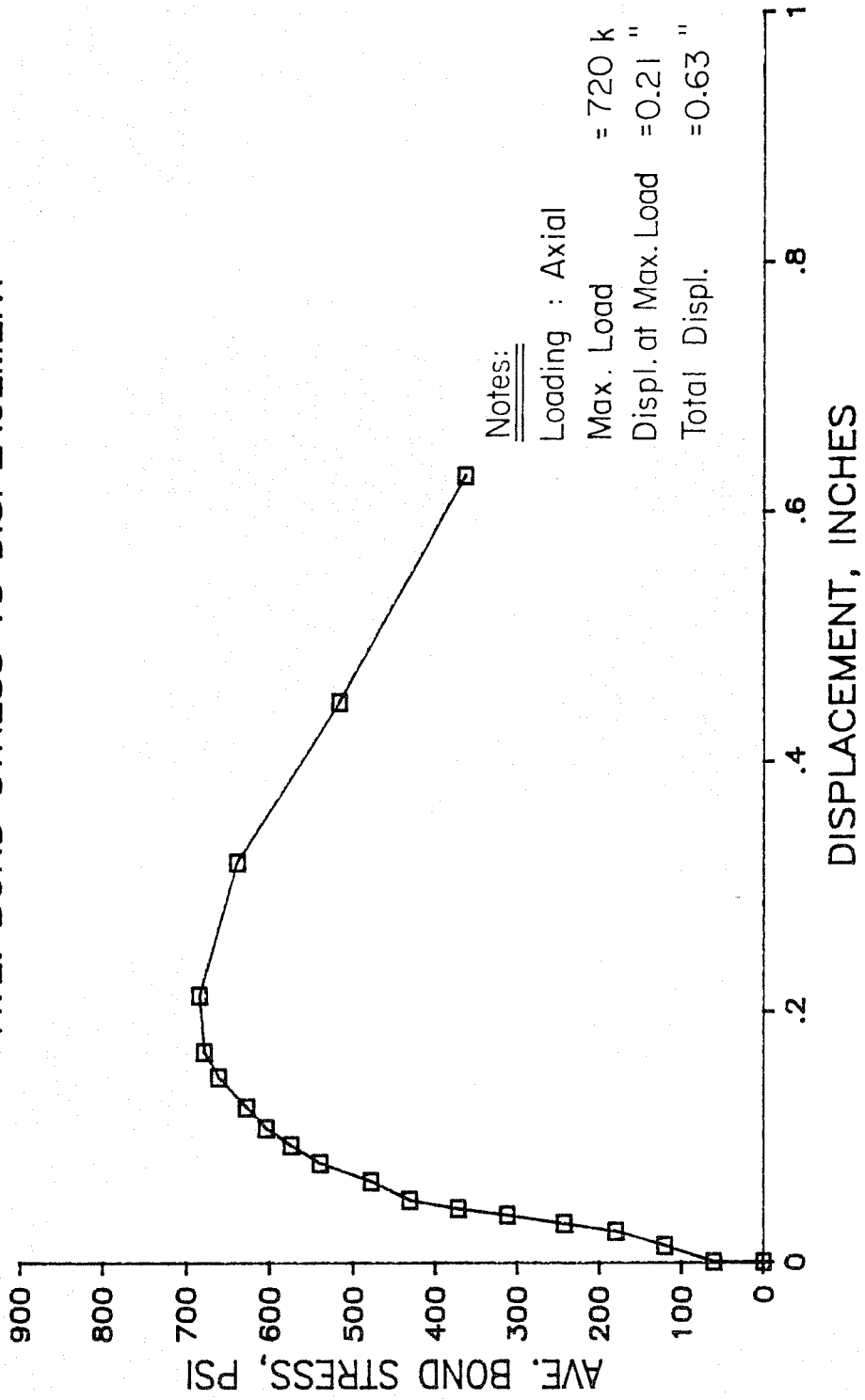


Fig. E.17

# SERIES 6: TEST UTA12

## AVE. BOND STRESS VS DISPLACEMENT

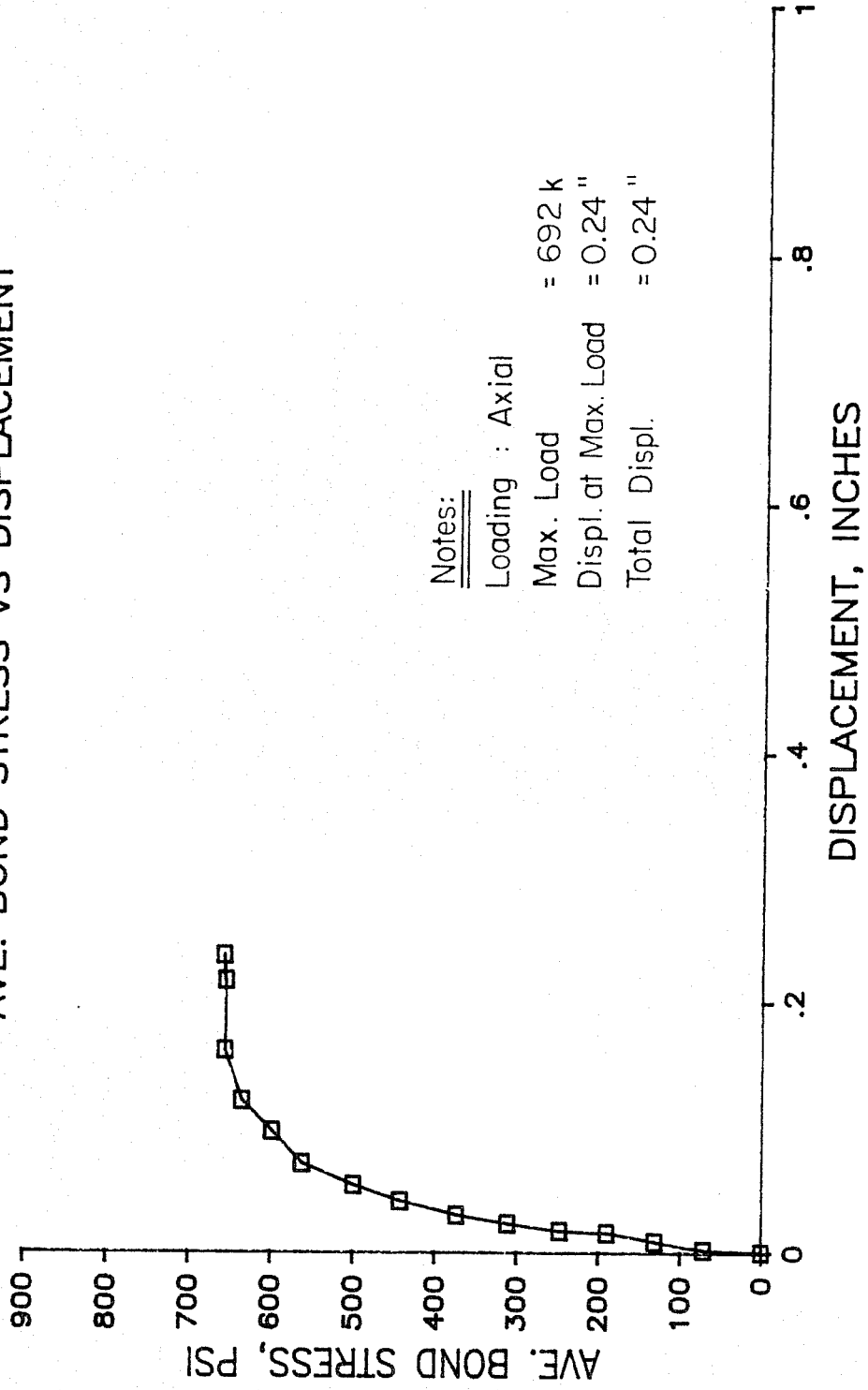


Fig. E.18

APPENDIX F

## Appendix F

Calculation of Ultimate Bond Stress  $f_{bu}^1$ :

Specimen UTAl

Ultimate load (Table 3.1) = 973 k

Average grouted length (Table 2.9) = 33.54 in.

Pile diameter = 18 in.

$$f_{bu}^1 = \frac{973 \times 1000}{\pi(33.54)(18)} = 513 \text{ psi}$$

Calculation of Ultimate Bond Stress  $f_{bu}^2$ :

Specimen UTAl

Ultimate load (Table 3.1) = 973 k

Grouted length Series 1 (Table 3.2) = 31.9 in.

Pile diameter = 18 in.

$$f_{bu}^2 = \frac{973 \times 1000}{\pi(31.9)(18)} = 540 \text{ psi}$$

Calculation of Stiffness Coefficient K: (Table 4.1)

Specimen UTAl

$$K = 1/m (D/t)_g^{-1} + \left[ (D/t)_s + (D/t)_p \right]^{-1} \quad (4)$$

m (Table 3.1) = 10.0

 $D_g = 20 \text{ in.}$                        $t_g$  (Table 2.9) = 0.99 $D_s = 21 \text{ in.}$                        $t_s = 0.50 \text{ in.}$  $D_p = 18 \text{ in.}$                        $t_p = 0.625 \text{ in.}$ 

$$K = 1/10.0(20/0.99)^{-1} + \left[ (21.0/0.50) + (18.0/0.625) \right]^{-1} = 0.0191$$

Calculation of Ultimate Bond Stress  $f_{bu}$  for 2-in. cubes using Eq. 5:  
(Table 4.1)

Specimen UTAl

$$f_{bu} = 16KC_L(9C_s + 1100h/s)f_{cu}^{0.5} \quad (5)$$

$$K \text{ (Table 4.1)} = 0.191$$

$$C_L \text{ (Section 4.3)} = 1.0$$

$$C_s \text{ (Section 4.3)} = 1.0$$

$$h/s \text{ (Table 2.5)} = 0.016$$

$$f_{cu} \text{ (Table 3.1)} = 3930 \text{ psi}$$

$$f_{bu} = 16(0.0191)(1.0)[9(1.0) + 1100(0.016)](3930)^{0.5} = 510 \text{ psi}$$

Calculation of Ultimate Bond Stress  $f_{bu}$  for 2-in. cubes using Eq. 9:  
(Table 4.1)

Specimen UTAl

$$f_{bu} = 167 + 172f_{cu} h/s \quad (9)$$

$$f_{cu} \text{ (Table 3.1)} = 3930 \text{ psi}$$

$$h/s \text{ (Table 2.5)} = 0.016$$

$$f_{bu} = 167 + 1.72(3930)(0.016) = 275 \text{ psi}$$

Calculation of Allowable Bond Stress  $f_{ba}$  for 2-in. cubes using Eq. 8:  
(Table 4.2)

Specimen UTAl

$$f_{ba} = 2KC_L[9C_s + 1100h/s]f_{cu}^{0.5} \quad (8)$$

$$K \text{ (Table 4.1)} = 0.0191$$

$$C_L \text{ (Section 4.3)} = 1.0$$

$$C_s \text{ (Section 4.3)} = 1.0$$

$$h/s \text{ (Table 2.5)} = 0.016$$

$$f_{cu} \text{ (Table 3.1)} = 3930 \text{ psi}$$

$$f_{ba} = 2(0.0191)(1.0)[9(1.0) + 1100(0.016)](3930)^{0.5} = 63.7 \text{ psi}$$

Calculation of Allowable Bond Stress  $f_{ba}$  for 2-in. cubes using Eq. 10:

(Table 4.2)

Specimen UTA1

$$f_{ba} = 20 + 0.5f_{cu}h/s \quad (10)$$

$$f_{cu} \text{ (Table 3.1)} = 3930 \text{ psi}$$

$$h/s \text{ (Table 2.5)} = 0.016$$

$$f_{ba} = 20 + 0.5 (3930)(0.016) = 51.4 \text{ psi}$$

APPENDIX G (PART A: CHEN)

## APPENDIX G

```

PROGRAM CHEN(INPUT,OUTPUT,TAPE5=INPUT,TAPE6=OUTPUT)
C *****
C THIS PROGRAM USES CHENS CONSTITUTIVE RELATIONS TO DETERMINE
C THE ULTIMATE STRENGTH OF A GROUTED PILE-TO-SLEEVE CONNECTION WITH
C INFINITELY STIFF TUBES. THE RELATIONSHIP BETWEEN THE AXIAL STRESS
C AND SHEARING STRESS ARE ASSUMED, BASED ON EXPERIMENTAL
C OBSERVATIONS. THE UNKNOWN STRESSES AND STRAINS ARE THEN DETERMINED
C USING THESE RELATIONS.
C *****
C DECLARATION OF VARIABLES
C A1-----AREA OF SHEAR KEY
C A2-----VERTICAL AREA OF GROUT COMPRESSION STRUT ALONG CRITICAL
C PLANE
C ALPHA--CONSTANT DEFINED IN TERMS OF MATERIAL CONSTANTS GIVEN
C ABOVE
C AO-----CONSTANT DEFINING LOCATION OF INITIAL YIELD SURFACE
C AU-----CONSTANT DEFINING LOCATION OF FAILURE SURFACE
C BETA---CONSTANT DEFINED IN TERMS OF THE MATERIAL CONSTANTS
C GIVEN ABOVE
C BFL----BOND FRICTION LOAD ST ANY LOAD LEVEL
C CF-----ASSUMED COEFFICIENT OF FRICTION FOR STEEL-GROUT INTERFACE
C DEP33--INCREMENTAL CHANGE IN AXIAL STRAIN
C DEP31--INCREMENTAL CHANGE IN SHEAR STRAIN
C DJ2----CURRENT VALUE OF THE SECOND DEVIATORIC STRESS INVARIANT
C DP-----INCREMENTAL CHANGE IN LOAD
C DSIG1--CALCULATED VALUE OF THE INCREMENTAL CHANGE IN RADIAL STRESS
C DSIG2--CALCULATED VALUE OF THE INCREMENTAL CHANGE IN HOOP STRESS
C DSIG11-INCREMENTAL CHANGE IN RADIAL STRESS
C DSIG22-INCREMENTAL CHANGE IN HOOP STRESS
C DSIG33-INCREMENTAL CHANGE IN AXIAL STRESS
C DSIG31-INCREMENTAL CHANGE IN AVE. SHEAR STRESS
C E-----ELASTIC MODULUS OF ELASTICITY
C E1,E2--VALUES FOR MODULUS OF ELASTICITY PAST THE ELASTIC RANGE
C EC1----COEFFICIENT OF USIG33 TERM IN SECOND DEGREE EQUATION
C REPRESENTING THE UNIAXIAL STRESS-STRAIN CURVE
C EC2----COEFFICIENT OF USIG33**2 TERM IN SECOND DEGREE EQUATION
C REPRESENTING THE UNIAXIAL STRESS-STRAIN CURVE
C EP33---AXIAL STRAIN AT ANY LOAD STEP
C EP31---AVE. SHEARING STRAIN AT ANY LOAD STEP
C FBCR---NONDIMENSIONAL BIAXIAL STRENGTH IN TERMS OF FC
C FC-----UNIAXIAL COMPRESSIVE STRENGTH OF GROUT IN PSI,>0
C FCI----INITIAL YIELD SURFACE AS FRACTION OF FC
C FCR---NONDIMENSIONAL UNIAXIAL ELASTIC STRENGTH IN TERMS OF FC
C GAMMA--ANGLE OF GROUT COMPRESSION STRUT FROM HORIZONTAL
C H-----HEIGHT OF SHEAR KEY
C HE-----WORK HARDENING MODULUS
C I-----COUNTER TO CHECK CONVERGENCE OF A LOAD STEP

```



```

C      J-----INPUT VARIABLE: IF J EQUAL 1 ALL INTERMEDIATE VALUES
C          OF STRESS, STRAIN, LOAD, AND TAU WILL BE PRINTED
C      K-----COUNTER USED TO COUNT THE TOTAL NUMBER OF LOAD STEPS
C          REQUIRED TO REACH THE FAILURE SURFACE
C      N-----TOTAL NUMBER OF STRUTS IN CONNECTION
C      OMEGA--CONSTANT AS DEFINE BY CHEN
C      P-----TOTAL VALUE OF LOAD IN LBS.
C      PHI##--TERMS IN THE PLASTIC STIFFNESS TENSOR
C      PR-----POISSON'S RATIO
C      R1-----RATIO OF SIGMA11 TO SIGMA33
C      RO-----CONSTANT AS DEFINE BY CHEN
C      RP-----OUTSIDE RADIUS OF FILE
C      S-----SPACING OF SHEAR KEY
C      SC-----PREDICTED STRENGTH OF SINGLE GROUT COMPRESSION STRUT
C      SIG11--RADIAL STRESS AT ANY LOAD STEP
C      SIG22--HOOP STRESS AT ANY LOAD STEP
C      SIG33--AXIAL STRESS AT ANY LOAD STEP
C      SIG31--AVE. SHEARING STRESS AT ANY LOAD STEP
C      SI1----FIRST STRESS INVARIANT
C      S33----DEVAITORIC PART OF THE SIG33 STRESS
C      S11----DEVAITORIC PART OF THE SIG22 STRESS
C      S22----DEVAITORIC PART OF THE SIG22 STRESS
C      TAUO---CONSTANT DEFINING LOCATION OF INITIAL YIELD SURFACE
C      TAUU---CONSTANT DEFINING LOCATION OF FAILURE SURFACE
C      TAU2---CURRENT LOCATION OF STRESS VECTOR RELATIVE TO FAILURE
C          SURFACE
C      TBFL---TOTAL LOAD DUE TO BOND FRICTION
C      TG-----THICKNESS OF GROUT
C      TOL----TOLERANCE VALUE FOR SOLUTION
C      TSL----TOTAL KEY STRENGTH OF ALL STRUTS IN CONNECTION
C      UEP33--AXIAL STRAIN FROM UNIAXIAL STRESS-STRAIN CURVE
C      US-----ULTIMATE STRENGTH OF CONNECTION
C      USIG33-AXIAL STRESS FROM UNIAXIAL STRESS-STRAIN CURVE
C      *****
C      READ SPECIMEN DESIGNATION FROM DATA FILE
C      READ(5,5) NAME
C      READ DP, FC, PR, RP, H, S, TG, FCI, N, J, CF, EC1, AND EC2
C      FROM DATA FILE
C      READ(5,*)DP,FC,PR,RP,H,S,TG,E,FCI,N,J,CF,EC1,EC2
C      *****
C      WRITE INPUT DATA TO OUTPUT FILE
C      WRITE(6,15)
C      WRITE(6,255) NAME
C      WRITE(6,25) DP
C      WRITE(6,35) FC
C      WRITE(6,45) FCI
C      WRITE(6,55) ER
C      WRITE(6,65) RP
C      WRITE(6,75) H
C      WRITE(6,85) S

```

```

WRITE(6,95) TG
WRITE(6,105) CF
WRITE(6,285) N
WRITE(6,115) E
WRITE(6,125)
C *****
C RATIOS FOR INTIAL YIELD SURFACE
FBCI = 1.16*FCI
FTI = 0.09*FCI
C *****
C RATIOS FOR THE FAILURE SURFACE
FBCF = 1.16
FTF = 0.09
C *****
C CALCUALTION OF STRUT ANGLE
GAMMA = 45.0
C CONVERT GAMMA TO RADIANS
PI = 3.14159
GAMMA = PI*GAMMA/180.0
C *****
C SET TOLERANCE ON FAILURE SURFACE
TOL = 1.0E-10
C *****
C CALCULATE AREAS USED TO DETERMINE STRESSES
A1 = PI*((RP+H)**2-RP**2)
A2 = PI*2.0*(RP+H)*(S/2.0-TG*TAN(GAMMA))
C *****
C DETERMINE VALUE OF P AT INITIAL YIELDING
C ASSUME COMPRESSION-COMPRESSION REGION
AO = ((FBCI**2-FCI**2)/(2.0*FBCI-FCI))*FC
AU = ((FBCF**2-1.0)/(2.0*FBCF-1.0))*FC
TAUO = ((FCI*FBCI*(2.0*FCI-FBCI))/(3.0*(2.0*FBCI-FCI))*FC**2
TAUU = ((FBCF*(2.0-FBCF))/(3.0*(2.0*FBCF-1.0))*FC**2
ALPHA = (AU-AO)/(TAUU-TAUO)
BETA = (AO*TAUU-AU*TAUO)/(TAUU-TAUO)
A = (1.0-(PR/(1.0-PR)))**2/(3.0*A1**2)+1.0/A2**2
B = (TAUO*ALPHA+BETA)*(1.0+(2.0*PR/(1.0-PR)))/(3.0*A1)
P = (-B-(B**2+4.0*A*TAUO)**0.5)/(2.0*A)
BFL = CF*P*(TG-H/2.0)/(TG*(TAN(GAMMA)-CF))
SIG33 = P/A1
SIG11 = PR*SIG33/(1.0-PR)
SIG22 = PR*SIG33/(1.0-PR)
SIG31 = P/A2
EP33 = ((1.0+PR)*(1.0-2.0*PR)*SIG33)/(E*(1.0-PR))
EP31 = (2.0*(1.0+PR)*SIG31)/E
R1 = SIG11/SIG33
C *****
C CHECK ASSUMPTION ON COMPRESSION-COMPRESSION REGION
DJ2 = ((SIG22-SIG33)**2+(SIG33-SIG11)**2)/6.0+SIG31**2
SI1 = SIG33+SIG22+SIG11

```

```

C = DJ2**0.5+SI1/3.0**0.5
IF (SI1.GT.0.0.OR.C.GT.0.0) THEN
C  TENSION-COMPRESSION REGION CONTROLS
AO = ((FCI-FTI)/2.0)*FC
AU = ((1.0-FTF)/2.0)*FC
TAUO = (FCI*FTI/6.0)*FC**2
TAUU = FTF*FC**2/6.0
ALPHA = (AU-AO)/(TAUU-TAUO)
BETA = (AO*TAUU-AU*TAUO)/(TAUU-TAUO)
A = (1.0-(PR/(1.0-PR)))**2/(3.0*A1**2)+1.0/A2**2-(1.0+2.0*
+PR/(1.0-PR))**2/(6.0*A1**2)
B = (TAUO*ALPHA+BETA)*(1.0+2.0*PR/(1.0-PR))/(3.0*A1)
P = (-B-(B**2+4.0*A*TAUO)**0.5)/(2.0*A)
BFL = CF*P*(TG-H/2.0)/(TG*(TAN(GAMMA)-CF))
SIG33 = P/A1
SIG11 = PR*SIG33/(1.0-PR)
SIG22 = PR*SIG33/(1.0-PR)
SIG31 = P/A2
EP33 = ((1.0+PR)*(1.0-2.0*PR)*SIG33)/(E*(1.0-PR))
EP31 = (2.0*(1.0+PR)*SIG31)/E
R1 = SIG11/SIG33
END IF
C  SET COUNTER TO KEEP TRACK OF NUMBER OF ITERATIONS REQUIRED TO
C  REACH FAILURE SURFACE
K = 1
I = 1
TAU2 = TAUO
IF(J.EQ.1) THEN
WRITE(6,135)
WRITE(6,145)K,I,P,SIG33,SIG11,SIG22,SIG31,R1,EP33,EP31,
+TAU2,TAU2,E
END IF
C  *****
FN = DP*(TG-H/2.0)/(TG*(TAN(GAMMA)-CF))
C  CALCULATE THE KNOWN STRESS INCREMENTS
DSIG33 = DP/A1
DSIG31 = (DP+CF*FN)/A2
C  *****
C  CALL SUBROUTINE ITER TO CALCULATE INCREMENTAL INCREASES IN STRESSES
10 CALL ITER(SIG33,SIG11,SIG22,SIG31,DSIG33,DSIG31,HE,FC,
+E,ALPHA,BETA,PR,DSIG11,DSIG22,DEP33,DEP31,TAU2,I,EC1,EC2)
C  CHECK CONVERGENCE OF LOAD STEP
C  IF (I.GT.100) THEN
C  WRITE(6,155)
C  GO TO 20
C  END IF
C
C  *****
C  UPDATE THE VALUE OF THE LOAD
P = P+DP

```

```

      BFL = BFL+CF*FN
C     UPDATE VALUES OF STRESSES
      SIG33 = SIG33+DSIG33
      SIG11 = SIG11+DSIG11
      SIG22 = SIG22+DSIG22
      SIG31 = SIG31+DSIG31
      R1 = SIG11/SIG33
C     UPDATE VALUES OF STRAINS
      EP33 = EP33+DEP33
      EP31 = EP31+DEP31
      K = K+1
      IF(J.EQ.1) THEN
      WRITE(6,145)K,I,P,SIG33,SIG11,SIG22,SIG31,R1,EP33,EP31,
+TAUU,TAU2,HE
      END IF
      IF (K.GT.10000) THEN
      GO TO 20
      END IF
C
C
C     *****
C     CHECK IF LOAD HAS REACHED FAILURE SURFACE
      C = (TAUU-TAU2)/TAUU
      IF (C.GT.TOL) THEN
      GO TO 10
      END IF
      TSL = N*P
      TBFL = BFL*N
      SC = P+BFL
      US = TSL + TBFL
C     CONVERT GAMMA BACK INTO DEGREES
      GAMMA = GAMMA*180.0/PI
      WRITE(6,165)
      WRITE(6,175) GAMMA
      WRITE(6,185) P
      WRITE(6,265) BFL
      WRITE(6,295) SC
      WRITE(6,195) SIG33
      WRITE(6,205) SIG31
      WRITE(6,215) SIG11
      WRITE(6,225) TSL
      WRITE(6,235) TBFL
      WRITE(6,245) US
      WRITE(6,125)
5     FORMAT(A6)
15    FORMAT('1',5X,'***** CHENS MODEL *****
+*****')
25    FORMAT(10X,'LOAD STEP SIZE =',34X,F6.1)
35    FORMAT(10X,'GROUT STRENGTH =',32X,F8.1)
45    FORMAT(10X,'INITIAL YIELD SURFACE AS FRACTION OF FC =',11X,F5.2)
55    FORMAT(10X,'POISSONS RATIO =',36X,F5.2)

```

```

65  FORMAT(10X,'OUTSIDE PILE RADIUS =',30X,F5.1)
75  FORMAT(10X,'SHEAR KEY HEIGHT =',34X,F6.3)
85  FORMAT(10X,'SHEAR KEY SPACING =',33X,F5.2)
95  FORMAT(10X,'THICKNESS OF GROUT ANNULUS =',24X,F5.2)
105 FORMAT(10X,'ASSUMED COEFFICIENT OF FRICTION =',19X,F5.2)
115 FORMAT(10X,'MODULUS OF ELASTICITY IN ELASTIC REGION =',5X,F10.1)
125 FORMAT(6X,'*****')
+*****')
135 FORMAT(////,4X,'K',4X,'I',7X,'P',7X,'SIG33',5X,'SIG11',5X
+, 'SIG22',6X,'SIG31',5X,'R1',6X,'EP33',7X,'EP31'
+,7X,'TAUU',10X,'TAU2',10X,'E')
145 FORMAT(1X,I4,2X,I3,2X,F9.1,4(2X,F8.2),2X,F6.3,2(3X,F8.6)
+,3(3X,F10.2))
155 FORMAT(10X,'CONVERGENCE NOT OBTAINED AFTER 100 ITERATIONS')
165 FORMAT(////,6X,'***** OUTPUT DATA *****')
+*****')
175 FORMAT(10X,'ANGLE OF COMPRESSION STRUT FROM HORIZTONTAL =',6X,
+F5.1)
185 FORMAT(10X,'LOAD PER STRUT DUE TO STRUT ACTION =',11X,F9.1)
195 FORMAT(10X,'ULTIMATE AXIAL STRESS =',25X,F8.1)
205 FORMAT(10X,'ULTIMATE AVE. SHEARING STRESS =',17X,F8.1)
215 FORMAT(10X,'CONFINING STRESS AT ULTIMATE LOAD =',13X,F8.1)
225 FORMAT(10X,'TOTAL LOAD DUE TO STRUT ACTION =',14X,F10.1)
235 FORMAT(10X,'TOTAL BOND FRICTION LOAD =',20X,F10.1)
245 FORMAT(10X,'PREDICTED ULTIMATE STRENGTH =',17X,F10.1)
255 FORMAT(10X,'SPECIMEN DESIGNATION: ',A6)
265 FORMAT(10X,'LOAD PER STRUT DUE TO BOND FRICTION =',10X,F9.1)
275 FORMAT(10X,'TOTAL LOAD PER STRUT =',24X,F9.1)
285 FORMAT(10X,'NUMBER OF STRUTS IN CONNECTION =',19X,I3)
295 FORMAT(10X,'TOTAL STRUT LOAD =',29X,F9.1)
20  STOP
    END

```



```

UEP33 = (EC1-(EC1**2-4.0*EC2*USIG33)**0.5)/(2.0*EC2)
HE = EC1-2.0*EC2*UEP33
ELSE
HE = 0.0
END IF

C
C   CALCULATE VALUE OF OMEGA
OMEGA = 1.0/(((1.0-2.0*PR)*(2.0*DJ2+3.0*RO**2)+9.0*PR*RO**2)+
+(2.0*TAU2**0.5*
+HE*(1.0+PR)*(1.0-2.0*PR)/E)*(2.0*DJ2+3.0*RO**2)**0.5*
+(1.0-ALPHA*SI1/3.0))

C
C   CALCULATE UPPER PORTION OF THE PHI MATRIX
S11 = (SIG11+DSIG11) - SI1/3.0
S22 = (SIG22+DSIG22) - SI1/3.0
S33 = (SIG33+DSIG33) - SI1/3.0
PHI33 = 1.0-PR-OMEGA*((1.0-2.0*PR)*(S33+RO)+3.0*PR*RO)**2
PHI36 = -OMEGA*((1.0-2.0*PR)*(S33+RO)+3.0*PR*RO)
+*((1.0-2.0*PR)*(SIG31+DSIG31))
PHI66 = ((1.0-2.0*PR)/2.0)-OMEGA*((1.0-2.0*PR)*(SIG31+DSIG31))**2

C
C   SOLVE FOR THE UNKNOWN STRAINS EP33 AND EP31
DET = ((1.0+PR)*(1.0-2.0*PR))/(E*(PHI33*PHI66-PHI36**2))
DEP33 = DSIG33*DET*PHI66-DSIG31*DET*PHI36
DEP31 = -DSIG33*DET*PHI36+DSIG31*DET*PHI33

C
C   CALCULATE THE LOWER PORTION OF THE PHI MATRIX
PHI13 = PR-OMEGA*((1.0-2.0*PR)*(S11+RO)+3.0*PR*RO)*((1.0-2.0*PR)
+*(S33+RO)+3.0*PR*RO)
PHI16 = -OMEGA*((1.0-2.0*PR)*(S11+RO)+3.0*PR*RO)*((1.0-2.0*PR)*
+(SIG31+DSIG31))
PHI23 = PR-OMEGA*((1.0-2.0*PR)*(S22+RO)+3.0*PR*RO)*((1.0-2.0*PR)*
+(S33+RO)+3.0*PR*RO)
PHI26 = -OMEGA*((1.0-2.0*PR)*(S22+RO)+3.0*PR*RO)*((1.0-2.0*PR)*
+(SIG31+DSIG31))

C
C   CALCULATE THE NEW VALUES OF THE INCREMENTAL STRESSES SIG11
C   AND SIG22
DSIG1= (E/((1.0+PR)*(1.0-2.0*PR)))*(PHI13*DEP33 + PHI16*DEP31)
DSIG2= (E/((1.0+PR)*(1.0-2.0*PR)))*(PHI23*DEP33 + PHI26*DEP31)

C
C   CHECK CURRENT STRESSES AND ASSUMED VALUES OF STRESSES AGAINST
C   TOLERANCE
X1 = ((DSIG11-DSIG1)**2+(DSIG22-DSIG2)**2)**0.5
X2 = (DSIG11**2+DSIG22**2)**0.5
IF (X2.EQ.0.0) GO TO 30
X3 = X1/X2
IF (X3.LT.TOL) THEN
DSIG11 = DSIG1
DSIG22 = DSIG2

```

```
ELSE
30  DSIG11 = DSIG1
    DSIG22 = DSIG2
    I = I+1
    IF (I.GT.100) THEN
        GO TO 20
    END IF
    GO TO 10
    END IF
20  RETURN
    END
```



APPENDIX G (PART B: FARDIS)

```

PROGRAM FARDIS(INPUT,OUTPUT,TAPE5=INPUT,TAPE6=OUTPUT)
C *****
C THIS PROGRAM USES FARDIS CONSTITUTIVE RELATIONS TO DETERMINE
C THE ULITMATE STRENGTH OF A GROUTED PILE-TO-SLEEVE CONNECTION
C WITH INFINITELY STIFF TUBES. THE RELATIONSHIP BETWEEN THE
C AXIAL STRESS AND SHEARING STRESS ARE ASSUMED BASED ON
C EXPERIMENTAL OBSERVATIONS. THE UNKNOWN STRESSES AND STRAINS
C ARE THEN OBTAINED USING THESE RELATIONS.
C *****
C DECLARATION OF VARIABLES
C A1-----AREA OF SHEAR KEY
C A2-----VERTICAL AREA OF GROUT COMPRESSION STRUT ALONG
C          CRITICAL PLANE
C BFL-----VALUE OF BOND FRICTION LOAD AT ANY LOAD STEP
C CF-----ASSUMED COEFFICIENT OF FRICTION FOR STEEL-GROUT INTERFACE
C D-----DISTANCE OF LAST STRESS POINT FROM BOUNDING SURFACE IN
C          DIRECTION OF DSIGMA IJ
C DEP33---INCREMENTAL CHANGE IN AXIAL STRAIN
C DEP31---INCREMENTAL CHANGE IN AVE. SHEARING STRAIN
C DMAX---MAXIMUM DISTANCE OF D CALCULATED UP TO THE CURRENT
C          STRESS POINT
C DP-----LOAD STEP SIZE
C DR-----RATIO OF D TO DMAX
C DSIG11--INCREMENTAL VALUE OF THE RADIAL STRESS
C DSIG22--INCREMENTAL VALUE OF THE HOOP STRESS
C DSIG33--INCREMENTAL VALUE OF THE AXIAL STRESS
C DSIG31--INCREMENTAL VALUE OF THE AVE. SHEAR STRESS
C E-----SECANT MODULUS OF ELASTICITY AT 0.4FC
C EP33----TOTAL AXIAL STRAIN AT ANY LOAD STEP
C EP31----TOTAL AVE. SHEAR STRAIN AT ANY LOAD STEP
C EMAX----MAXIMUM COMPRESSIVE STRAIN IN THE GROUT UP TO THE CURRENT
C          LOAD STEP
C F-----VALUE OF F AT THE CURRENT LOAD STEP AS DEFINED BY FARDIS
C FC-----UNIAXIAL COMPRESSIVE STRENGTH OF GROUT, > 0
C FN-----NORMAL FORCE CALCULATED FROM STRUT STATICS
C GAMMA---ANGLE OF GROUT STRUT FROM HORITZONTAL
C GMAX----MULTIPLE OF DSIG IJ REQUIRED TO REACH BOUNDING SURFACE
C          FROM THE ORIGIN IN DIRECTION OF DSIG IJ
C H-----HEIGHT OF SHEAR KEY
C HP-----VALUE OF GENERALIZED SHEAR MODULUS FOR CURRENT LOAD STEP
C HPMAX---MAXIMUM VALUE OF THE GENERALIZED SHEAR MODULUS
C I-----COUNTER USED TO COUNT TOTAL NUMBER OF LOAD STEPS REQUIRED
C          TO REACH BOUNDING SURFACE
C J-----INPUT VARIABLE: IF J EQUAL 1 THEN ALL INTERMEDIATE VALUES
C          OF STRESS,STRAIN,LOAD,D,DMAX AND DR WILL BE PRINTED
C K-----COUNTER TO CHECK CONVERGENCE OF A LOAD STEP

```

```

C   L-----COUNTER USED TO SWITCH CONVERGENCE SCHEME TO SECANT METHOD
C           AFTER 100 ITERATIONS
C   N-----NUMBER OF COMPRESSION STRUTS IN CONNECTION
C   P-----VALUE OF TOTAL LOAD AT ANY LOAD STEP
C   PR-----INITIAL POISSON'S RATIO
C   R1-----RATIO OF SIG11 TO SIG33
C   RP-----OUTSIDE RADIUS OF PILE
C   S-----SPACING OF SHEAR KEYS
C   SC-----PREDICTED STRENGTH OF SINGLE GROUT COMPRESSION STRUT
C   SIG11---TOTAL RADIAL STRESS AT ANY LOAD STEP
C   SIG22---TOTAL HOOP STRESS AT ANY LOAD STEP
C   SIG33---TOTAL AXIAL STRESS AT ANY LOAD STEP
C   SIG31---TOTAL AVE. SHEAR STRESS AT ANY LOAD STEP
C   S11&S33-DEVIATORIC STRESSES
C   S31-----DEVIATORIC STRESS
C   SI1-----FIRST STRESS INVARIANT
C   SJ2-----SECOND DEVIATORIC STRESS INVARIANT
C   SJ3-----THIRD DEVIATORIC STRESS INVARIANT
C   TBFL----TOTAL LOAD DUE TO BOND FRICTION
C   TG-----TICKNESS OF GROUT ANNULUS
C   TKO-----INITIAL VALUE OF TANGENT MODULUS
C   TKT-----VALUE OF TANGENT MODULUS AT ANY LOAD STEP
C   TOL-----PRESCRIBED TOLERANCE
C   TSL-----TOTAL KEY STRENGTH OF ALL STRUTS IN CONNECTION
C   US-----ULTIMATE STRENGTH OF CONNECTION
C   X(1-3)--VALUES USED TO DETERMINE EUCLIDEAN NORM
C   *****
C   DIMENSION ARRAYS FOR UP TO 15000 LOAD STEPS
C   DIMENSION SIG11(15000),SIG22(15000),SIG33(15000)
C   DIMENSION SIG31(15000),EP33(15000),EP31(15000)
C   *****
C   READ SPECIMEN DESIGNATION FROM INPUT DATA FILE
C   READ(5,5) NAME
C   READ DP, FC, E, PR, RP, H, S, TG, N, J AND CF FROM
C   DATA FILE
C   READ(5,*) DP,FC,E,PR,RP,H,S,TG,N,J,CF
C   *****
C   CALCULATE INITIAL VALUES OF GENERALIZED SHEAR MODULUS AND INITIAL
C   TANGENT MODULUS
C   HPMAX = E/(1.0+PR)
C   TKO = E/(3.0*(1.0-2.0*PR))
C   *****
C   WRITE INPUT DATA TO OUTPUT FILE
C   WRITE(6,15)
C   WRITE(6,255) NAME
C   WRITE(6,25) DP
C   WRITE(6,35) FC
C   WRITE(6,265) E
C   WRITE(6,275) PR
C   WRITE(6,45) RP

```

```

WRITE(6,55) H
WRITE(6,65) S
WRITE(6,75) TG
WRITE(6,85) HPMAX
WRITE(6,95) TKO
WRITE(6,105) CF
WRITE(6,305) N
WRITE(6,115)
C *****
C ASSUMED ANGLE OF STRUT
GAMMA = 45.0
C CONVERT GAMMA TO RADIANS
PI = 3.14159265
GAMMA = PI*GAMMA/180.0
C SET TOLERANCE ON STRESSES
TOL = 0.001
C SET COUNTERS
K = 1
L = 1
C *****
FN = DP*(TG-H/2.0)/(TG*(TAN(GAMMA))-CF)
C CALCULATE AREAS TO BE USED TO DETERMINE STRESSES
A1 = PI*((RP+H)**2-RP**2)
A2 = PI*2.0*(RP+H)*(S/2.0-TG*TAN(GAMMA))
C *****
C CALCULATE KNOWN INCREMENTAL STRESS CHANGES
DSIG33 = DP/A1
DSIG31 = (DP+CF*FN)/A2
C ASSUME VALUES OF UNKNOWN STRESSES TO START ITERATION
DSIG11 = 0.0
DSIG22 = DSIG11
IF(J.EQ.1) WRITE(6,125)
C *****
C INITIALIZE LOAD,STRESS AND STRAIN VECTORS TO ZERO
I = 1
P = 0.0
BFL = 0.0
SIG11(1) = 0.0
SIG22(1) = 0.0
SIG33(1) = 0.0
SIG31(1) = 0.0
R1 = 0.0
EP33(1) = 0.0
EP31(1) = 0.0
C *****
C CALL SUBROUTINE STRESS1 TO CALCULATE THE VALUES OF THE UNKNOWN
C STRESSES AT THE FIRST LOAD STEP
CALL STRESS1(DSIG11,DSIG22,DSIG33,DSIG31,HPMAX,TKO,
+DEP33,DEP31)
C CALL SUBROUTINE TO CALCULATE THE VALUE OF DMAX

```

```

CALL BDMAX(DSIG11,DSIG22,DSIG33,DSIG31,FC,GMAX,DMAX)
DSIG1 = DSIG11
DSIG2 = DSIG22
D = DMAX
DR = D/DMAX
C *****
C CALL SUBROUTINE TO CALCULATE THE CURRENT LENGTH OF D FOR ALL
C POINTS AFTER THE INITIAL POINT
10 IF(I.GT.1) THEN
C SET MAXIMUM NUMBER OF ITERATIONS ALLOWED TO REACH BOUNDING
C SURFACE
IF(I.GT.14999) GO TO 20
CALL DCUR(SIG11,SIG22,SIG33,SIG31,DSIG11,DSIG22,DSIG33,
+DSIG31,FC,I,GMAX,D)
C CHECK TO SEE IF D IS GREATER THAN DMAX
IF(D.GT.DMAX) THEN
DR = 1.0
ELSE
DR = D/DMAX
END IF
C CALL SUBROUTINE TO CALCULATE THE VALUES OF THE UNKNOWN
C INCREMENTAL STRESSES
CALL STRESS(I,HMAX,TKO,SIG11,SIG22,SIG33,SIG31,DSIG33,DSIG31,
+DR,FC,EMAX,DSIG1,DSIG2,DEP33,DEP31)
END IF
C *****
C DETERMINE IF STRESSES ARE WITHIN THE PRESCRIBED TOLERANCES
X1 = ((DSIG11-DSIG1)**2+(DSIG22-DSIG2)**2)**0.5
X2 = (DSIG11**2+DSIG22**2)**0.5
X3 = X1/X2
C IF WITHIN TOLERANCE INCREMENT THE STRESSES AND STRAINS
IF (X3.LT.TOL) THEN
DSIG11 = DSIG1
DSIG22 = DSIG2
EP33(I+1) = EP33(I)+DEP33
EP31(I+1) = EP31(I)+DEP31
ELSE
C CHECK FOR CONVERGANCE OF LOAD STEP WITHIN PRESCRIBED NUMBER
C OF ITERATIONS
K = K+1
IF(K.GT.100) THEN
IF(K.GT.500) THEN
WRITE(6,135)
GO TO 20
END IF
IF(L.EQ.1) THEN
DSIG11 = DSIG1 + (DSIG11-DSIG1)/2.0
DSIG22 = DSIG11
L = 0
GO TO 10

```

```

ELSE
DSIG11 = DSIG11 - (DSIG11-DSIG1)/2.0
DSIG22 = DSIG11
L = 1
GO TO 10
END IF
END IF
DSIG11 = DSIG1
DSIG22 = DSIG2
GO TO 10
END IF
C   UPDATE VALUES OF STRESSES
SIG11(I+1) = SIG11(I)+DSIG11
SIG22(I+1) = SIG22(I)+DSIG22
SIG33(I+1) = SIG33(I)+DSIG33
SIG31(I+1) = SIG31(I)+DSIG31
IF(I.EQ.1) THEN
EMAX = 0.0
IF(J.EQ.1) THEN
WRITE(6,145)I,K,P,SIG11(I),SIG22(I),SIG33(I),SIG31(I),R1,
+EP33(I),EP31(I),EMAX,D,DR
END IF
END IF
C   UPDATE VALUE OF LOAD
P = P+DP
BFL = BFL+CF*FN
R1 = SIG11(I+1)/SIG33(I+1)
IF(J.EQ.1) THEN
WRITE(6,145)I+1,K,P,SIG11(I+1),SIG22(I+1),SIG33(I+1),
+SIG31(I+1),R1,EP33(I+1),EP31(I+1),EMAX,D,DR
END IF
C   *****
C   CHECK TO SEE IF DMAX SHOULD BE RESET
IF(D.GT.DMAX) DMAX = D
C   CALL SUBROUTINE TO CALCULATE THE MAXIMUM STRAIN THE MATERIAL
C   HAS BEEN SUBJECTED TOO
I = I+1
CALL STRAIN(I,EP33,EP31,EMAX)
C   CHECK TO SEE IF INCREMENT IS WITHIN TOLERANCE OF
C   BOUNDING SURFACE
SI1 = SIG11(I)+SIG22(I)+SIG33(I)
SJ2 = ((SIG22(I)-SIG33(I))**2+(SIG33(I)-SIG11(I))**2)/6.0
++SIG31(I)**2
S11 = SIG11(I)-SI1/3.0
S33 = SIG33(I)-SI1/3.0
S31 = SIG31(I)
SJ3 = (2.0*S11**3+S33**3+3.0*S31**2*(S11+S33))/3.0
B = (12.0-28.57884*SJ3/SJ2**1.5)**0.16667
F = (SI1/FC+0.3)-B*(0.7*SJ2/FC**2+1.85*SJ2**0.5/FC)
IF(F.LT.0.0) THEN

```

```

TSL = P*N
TBFL = BFL*N
SC = P+BFL
US = TSL+TBFL
C  CHANGE GAMMA BACK TO DEGREES
   GAMMA = GAMMA*180.0/PI
   WRITE(6,155)
   WRITE(6,165) GAMMA
   WRITE(6,175) F
   WRITE(6,185) P
   WRITE(6,285) BFL
   WRITE(6,295) SC
   WRITE(6,195) SIG33(I)
   WRITE(6,205) SIG31(I)
   WRITE(6,215) SIG11(I)
   WRITE(6,225) TSL
   WRITE(6,235) TBFL
   WRITE(6,245) US
   WRITE(6,115)
   GO TO 20
   END IF
   K = 1
   L = 1
   GO TO 10
5  FORMAT(A6)
15  FORMAT('1',5X,'***** FARDIS MODEL *****
+*****')
25  FORMAT(10X,'LOAD STEP SIZE =',28X,F6.1)
35  FORMAT(10X,'GROUT STRENGTH =',26X,F8.1)
45  FORMAT(10X,'OUTSIDE PILE RADIUS =',24X,F5.1)
55  FORMAT(10X,'SHEAR KEY HEIGHT =',28X,F6.3)
65  FORMAT(10X,'SHEAR KEY SPACING =',27X,F5.2)
75  FORMAT(10X,'THICKNESS OF GROUT ANNULUS =',18X,F5.2)
85  FORMAT(10X,'MAXIMUM GENERALIZED SHEAR MODULUS =',4X,F10.1)
95  FORMAT(10X,'INITIAL TANGENT MODULUS =',15X,F10.1)
105  FORMAT(10X,'ASSUMED COEFFICIENT OF FRICTION =',13X,F5.2)
115  FORMAT(6X,'*****
+*****')
125  FORMAT(////,4X,'I',3X,'K',7X,'P',7X,'SIG11',5X,'SIG22',5X,
+'SIG33',5X,'SIG31',4X,'R1',6X,'EP33',6X,'EP31',6X,'EMAX',5X,
+'DMAX',8X,'D',7X,'DR')
135  FORMAT(10X,'STRESSES DO NOT CONVERGE AFTER 500 CYCLES')
145  FORMAT(1X,I4,1X,I3,2X,F9.1,4(2X,F8.2),1X,F6.3,3(2X,F8.6)
+2(2X,F8.1),1X,F6.3)
155  FORMAT(////,6X,'***** OUTPUT DATA *****
+*****')
165  FORMAT(10X,'ANGLE OF COMPRESSION STRUT FROM HORIZTONTAL =',
+1X,F5.1)
175  FORMAT(10X,'VALUE OF F AT THE FAILURE LOAD =',15X,F7.4)
185  FORMAT(10X,'LOAD PER STRUT DUE TO STRUT ACTION =',6X,F9.1)

```

```
195  FORMAT(10X,'ULTIMATE AXIAL STRESS =',20X,F8.1)
205  FORMAT(10X,'ULTIMATE AVE. SHEARING STRESS =',12X,F8.1)
215  FORMAT(10X,'CONFINING STRESS AT ULTIMATE LOAD =',8X,F8.1)
225  FORMAT(10X,'TOTAL LOAD DUE TO STRUT ACTION =',9X,F10.1)
235  FORMAT(10X,'TOTAL BOND FRICTION LOAD =',15X,F10.1)
245  FORMAT(10X,'PREDICTED ULTIMATE STRENGTH =',12X,F10.1)
255  FORMAT(10X,'SPECIMEN DESIGNINATION : ',A6)
265  FORMAT(10X,'SECANT MODULUS AT 0.4FC =',15X,F10.1)
275  FORMAT(10X,'INITIAL POISSONS RATIO =',22X,F5.2)
285  FORMAT(10X,'LOAD PER STRUT DUE TO BOND FRICTION =',4X,F10.1)
295  FORMAT(10X,'TOTAL LOAD PER STRUT =',19X,F10.1)
305  FORMAT(10X,'NUMBER OF STRUTS IN CONNECTION =',13X,I3)
20   STOP
     END
```



C  
C  
C  
C  
C  
C  
C  
C  
C  
CSUBROUTINE STRESS1(DSIG11,DSIG22,DSIG33,DSIG31,HPMAX,TKO,  
+DEP33,DEP31)C \*\*\*\*\*  
C THIS SUBROUTINE CALCULATES THE VALUES OF THE UNKNOWN  
C INCREMENTAL STRESSES SIGMA 11 AND SIGMA 22 USING THE STRESS-  
C STRAIN RELATIONSHIP GIVEN BY EQUATION 14 OF FARDIS PAPER  
C \*\*\*\*\*  
TOL = 1.0E-10  
10 SI1 = 2.0\*DSIG11+DSIG33  
C NEWTON-RAPHSON ITERATION TO DETERMINE THE INCREMENTAL STRESSES  
F1 = (DSIG11-DSIG33)/(3.0\*HPMAX)+SI1/(9.0\*TKO)  
DF1 = 1.0/(3.0\*HPMAX)+2.0/(9.0\*TKO)  
DSIG1 = DSIG11-F1/DF1  
IF(ABS(DSIG1-DSIG11).LT.TOL) THEN  
GO TO 20  
ELSE  
DSIG11 = DSIG1  
GO TO 10  
END IF  
20 DSIG11 = DSIG1  
DSIG22 = DSIG11  
C SOLVE FOR THE UNKNOWN STRAINS DEP33 AND DEP31  
DSI1 = DSIG11+DSIG22+DSIG33  
DS33 = DSIG33-DSI1/3.0  
DEP33 = DS33/HPMAX+(2.0\*DSIG11+DSIG33)/(9.0\*TKO)  
DEP31 = DSIG31/HPMAX  
RETURN  
END

C  
C  
C  
C  
C  
C  
C  
C  
C  
C  
C

```

SUBROUTINE BDMAX(DSIG11,DSIG22,DSIG33,DSIG31,FC,GMAX,DMAX)
*****
THIS SUBROUTINE CALCUALTES DMAX IN THE DIRECTION OF THE
INCREMENTAL STRESSES DETERMINED IN THE SUBROUTINE STRESS1, USING
EQUATION 5 OF FARDIS PAPER.
*****
A1 = (2.0*DSIG11+DSIG33)/FC
A2 = (12.0-9.52628*(2.0*(DSIG11/3.0-DSIG33/3.0)**3+
+(2.0*DSIG33/3.0-2.0*DSIG11/3.0)**3+DSIG31**2*(DSIG33-
+DSIG11))/((DSIG22-DSIG33)**2/3.0+DSIG31**2)**1.5)**0.16667
A3 = 0.7*((DSIG22-DSIG33)**2/3.0+DSIG31**2)/FC**2
A4 = 1.85*((DSIG22-DSIG33)**2/3.0+DSIG31**2)**0.5/FC
B = (A1-A2*A4)/(A2*A3)
C = -0.3/(A2*A3)
GMAX = (B+(B**2-4.0*C)**0.5)/2.0
DMAX = (GMAX**2*(DSIG11**2+DSIG22**2+DSIG33**2+2.0*DSIG31**2))
+**0.5
RETURN
END

```

C  
C  
C  
C  
C  
C  
C  
C  
C  
C  
C

SUBROUTINE DCUR(SIG11,SIG22,SIG33,SIG31,DSIG11,DSIG22,DSIG33,  
+DSIG31,FC,I,GMAX,D)

C \*\*\*\*\*  
C THIS SUBROUTINE DETERMINES THE DISTANCE OF CURRENT STRESS POINT  
C FROM THE BOUNDING SURFACE IN THE DIRECTION OF DSIGMA IJ.  
C FOR FIRST ITERATION WILL ASSUME D TO BE IN SAME DIRECTION AS  
C PREVIOUS INCREMENT.  
C \*\*\*\*\*  
C DIMENSION SIG11(15000),SIG22(15000),SIG33(15000),SIG31(15000)  
C TOL = 1.E-10  
C F0 = 0.3  
C G1 = 2.0\*GMAX  
C \*\*\*\*\*  
C NEWTON-RAPHSON ITERATION TO DETERMINE DISTANCE OF CURRENT POINT  
C FROM BOUNDING SURFACE  
C SI1 = SIG11(I)+SIG22(I)+SIG33(I)  
C SI1T = SI1  
C S11 = SIG11(I)-SI1/3.0  
C S33 = SIG33(I)-SI1/3.0  
C S31 = SIG31(I)  
C DSI1 = DSIG11+DSIG22+DSIG33  
C DS11 = DSIG11-DSI1/3.0  
C DS33 = DSIG33-DSI1/3.0  
C DS31 = DSIG31  
10 SI1 = SI1T+G1\*(DSIG11+DSIG22+DSIG33)  
C SJ2 = ((SIG22(I)+G1\*DSIG22-(SIG33(I)+G1\*  
+DSIG33))\*2+(SIG33(I)+G1\*DSIG33-(SIG11(I)+G1  
+\*DSIG11))\*2)/6.0+(SIG31(I)+G1\*DSIG31)\*\*2  
C SJ3 = (2.0\*(S11+G1\*DS11)\*\*3+(S33+G1\*DS33)\*\*3+3.0\*(  
+S31+G1\*DS31)\*\*2\*(S11+S33+G1\*(DS11+DS33)))/3.0  
C B1 = 12.0-28.57884\*SJ3/SJ2\*\*1.5  
C F1 = (SI1/FC+0.3)-B1\*\*0.16667\*(0.7\*SJ2/FC\*\*2+1.85\*SJ2\*\*0.5/FC)  
C EVALUATE THE DERIVATIVE AT G1  
C DSJ2 = (2.0\*(SIG11(I)+G1\*DSIG11)\*DSIG11-2.0\*(SIG11(I)\*DSIG33+  
+2.0\*G1\*DSIG11\*DSIG33+SIG33(I)\*DSIG11)+2.0\*(SIG33(I)+G1\*DSIG33  
+)\*DSIG33)/3.0+2.0\*(SIG31(I)+G1\*DSIG31)\*DSIG31  
C  
C DSJ3 = 2.0\*(S11+G1\*DS11)\*\*2\*DS11+(S33+G1\*DS33)\*\*2\*DS33+(S31+  
+G1\*DS31)\*\*2\*(DS11+DS33)+2.0\*(S31+G1\*DS31)\*(S11+S33+G1\*(DS11+  
+DS33))\*DS31

C

$$B2 = (SJ2^{**1.5} * DSJ3 - SJ3 * 1.5 * SJ2^{**0.5} * DSJ2) / SJ2^{**3}$$

C

$$DF1 = DSII / FC - 0.7 / FC^{**2} * (B1^{**0.16667} * DSJ2 - 4.7631397 * SJ2 / B1$$

$$+ **0.83333 * B2) - 1.85 / FC * (B1^{**0.16667} * 0.5 / SJ2^{**0.5} * DSJ2 - 4.7631397$$

$$+ * SJ2^{**0.5} / B1^{**0.83333} * B2)$$

$$G2 = G1 - F1 / DF1$$

$$SI1 = SI1T + G2 * (DSIG11 + DSIG22 + DSIG33)$$

$$SJ2 = ((SIG22(I) + G2 * DSIG22 - (SIG33(I) + G2 * DSIG33))^{**2} + (SIG33(I) + G2 * DSIG33 - (SIG11(I) + G2$$

$$+ * DSIG11))^{**2}) / 6.0 + (SIG31(I) + G2 * DSIG31)^{**2}$$

$$SJ3 = (2.0 * (S11 + G2 * DS11)^{**3} + (S33 + G2 * DS33)^{**3} + 3.0 * ($$

$$+ S31 + G2 * DS31)^{**2} * (S11 + S33 + G2 * (DS11 + DS33))) / 3.0$$

$$F2 = (SI1 / FC + 0.3) - (12.0 - 28.57884 * SJ3 / SJ2^{**$$

$$+ 1.5)^{**0.16667} * (0.7 * SJ2 / FC^{**2} + 1.85 * SJ2^{**0.5} / FC)$$

$$\text{IF}(\text{ABS}(F2) . \text{LT.} \text{TOL} * \text{ABS}(F0)) \text{ GO TO } 30$$

$$G1 = G2$$

$$\text{GO TO } 10$$

$$30 \text{ D} = (G2^{**2} * (DSIG11^{**2} + DSIG22^{**2} + DSIG33^{**2} + 2.0 * DSIG31^{**2}))$$

$$+ **0.5$$

$$GMAX = 2.0 * G2$$

$$\text{RETURN}$$

$$\text{END}$$

C  
C  
C  
C  
C  
C  
C  
C  
C  
C  
C

SUBROUTINE STRESS(I,HPMAX,TKO,SIG11,SIG22,SIG33,SIG31,DSIG33,  
+DSIG31,DR,FC,EMAX,DSIG1,DSIG2,DEP33,DEP31)

C \*\*\*\*\*  
C THIS SUBROUTINE CALCULATES THE UNKNOWN STRESSES SIGMA 11 AND  
C SIGMA 22 USING THE STRESS-STRAIN RELATIONSHIP GIVEN BY  
C EQUATION OF FARDIS PAPER.  
C \*\*\*\*\*  
C DIMENSION SIG11(15000),SIG22(15000),SIG33(15000),SIG31(15000)  
C FIND CURRENT VALUES OF SHEAR COMPACTION/DILATANCY FACTOR  
C GENERALIZED PLASTIC SHEAR MODULUS AND TANGENT BULK MODULUS  
C IF(FC.LT.10000.0) THEN  
C BETA = 9.0\*EMAX\*\*0.25\*(DR-0.1)  
C HP = 16.0\*FC\*(DR/EMAX)\*\*0.55  
C ELSE  
C BETA = 0.0  
C HP = 29.0\*FC\*(DR/EMAX)\*\*0.55  
C END IF  
C IF (HP.GT.HPMAX) HP = HPMAX  
C \*\*\*\*\*  
C CALCULATE THE DEVIATORIC STRESS COMPONENTS  
C SI1 = SIG11(I)+SIG22(I)+SIG33(I)  
C S11 = SIG11(I)-SI1/3.0  
C S22 = SIG22(I)-SI1/3.0  
C S33 = SIG33(I)-SI1/3.0  
C S31 = SIG31(I)  
C TAUO = ((S11\*\*2+S22\*\*2+S33\*\*2+2.0\*S31\*\*2)/3.0)\*\*0.5  
C TKT = TKO/(1.0+(SI1/(3.0\*FC)))  
C \*\*\*\*\*  
C CALCULATE THE COEFFICIENTS FOR THE COMPILANCE MATRIX  
C C7 = 1.0/(9.0\*TKT)  
C C2 = (S22/TAUO+BETA/3.0)/(3.0\*HP\*TAUO)  
C C3 = (S33/TAUO+BETA/3.0)/(3.0\*HP\*TAUO)  
C C6 = S31/(3.0\*HP\*TAUO\*\*2)  
C C21 = C2\*S11+C7  
C C22 = C2\*S22+C7  
C C23 = C2\*S33+C7  
C C26 = 2.0\*C2\*S31  
C C31 = C3\*S11+C7  
C C32 = C3\*S22+C7  
C C33 = C3\*S33+C7

```
C36 = 2.0*C3*S31
C61 = C6*S11
C62 = C6*S22
C63 = C6*S33
C66 = 2.0*C6*S31
C *****
C CALCULATE INCREMENTAL CHANGES IN STRESSES SIGMA11 AND SIGMA22
C *****
C CALCULATE STRESSES DSIG1 AND DSIG2 AND COMPARE WITH ASSUMED
C VALUES
DSIG2 = -(C23*DSIG33+C26*DSIG31)/(C21+C22)
DSIG1 = DSIG2
C SOLVE FOR THE UNKNOWN STRAINS DEP33 AND DEP31
DEP33 = C31*DSIG1+C32*DSIG2+C33*DSIG33+C36*DSIG31
DEP31 = C61*DSIG1+C62*DSIG2+C63*DSIG33+C66*DSIG31
RETURN
END
```

C  
C  
C  
C  
C  
C  
C  
C  
C  
C  
C

SUBROUTINE STRAIN(I,EP33,EP31,EMAX)

C \*\*\*\*\*  
C THIS SUBROUTINE CALCULATES THE MAXIMUM STRAIN EVER EXPERIENCED  
C BY THE MATERIAL  
C \*\*\*\*\*

DIMENSION EP33(15000),EP31(15000)

EMAX = EP33(I)/2.0+((EP33(I)/2.0)\*\*2+EP31(I)\*\*2)\*\*0.5

RETURN

END

## REFERENCES

1. Graff, W. J., Introduction to Offshore Structures, Gulf Publishing Company, Houston, 1981.
2. Lee, G. C., "Offshore Structures: Past, Present, Future, and Design Considerations," Proceeding of the Offshore Exploration Conference, (OECON), 1968, pp. 169-196.
3. McClelland, B., Focht, J. A., Jr., Emrich, W. J., "Designing and Constructing Heavily Loaded Piles," Ocean Industry, Jan. 1969, pp. 56 - 59.
4. Billington, C. J., and Tebbett, I. E., "The Basis of New Design Formulae for Grouted Jacket to Pile Connections," Offshore Technology Conference, Proceedings, Vol.1, No. 3788, Houston, TX., May 5- 8, 1980.
5. Krahl, N. W., and Karsan, D. I., "Axial Strength of Grouted Pile-to-Sleeve Connections," Journal of the Structural Division, ASCE, Vol. 111, No. 4, April, 1985, pp.889-905.
6. Loset, Oystien, "Grouted Connections in Steel Platforms - Testing and Design," Institute of Structural Engineers Informal Study Group-Model Analysis as a Design Tool, Joint I. Struct. E./B.R.E., Two Day Seminar on the Use of Physical Models in the Design of Offshore Structures, Paper No. 8, Building Research Station Garston, Watford, England, Nov. 15-16.,1979.
7. Lewis, G. H. G., Livetti I. G., McLaughlin, R. T. P., and Mead K. C., "A Cost Saving Design for Pile to Structure Connection Applied to Magnus Design," Offshore Technology Conference, Proceedings, Vol. 1, No. 3789, Houston, TX., May, 1980.
8. American Petroleum Institute, Recommended Practice for Planning, Designing and Constructing Fixed Offshore Platforms, API RP 2A, 7th Edition, Dallas, TX.,1977.
9. Wimpey Laboratories Ltd., "Joint Industry Project Grouted Pile/Sleeve Connections Length, Longitudal Stiffening and Size Effects; Study Final Issue," Report No. WOL 55/84B, December, 1984.
10. Wimpey Laboratories Ltd., "United Kingdom Department of Energy - Report of the Working Party on the Strength of Grouted Pile Sleeve Connections for Offshore Structures," Report No. ST41/80C, October, 1980.



11. United Kingdom Department of Energy, "Report of the Working Party on the Strength of Grouted Pile/Sleeve Connections for Offshore Structures," Offshore Technology Paper 11, UDC 624.155, OT-R- 8258, Ciria Publication, September, 1982.
12. Wimpey Laboratories Ltd., Brown and Root (UK) Ltd. - BP Forties Field Phase I, Report on Grout Bond Tests for Large Diameter Piles, Report BM/112, September, 1973.
13. Wimpey Laboratories Ltd., "CJB Offshore Limited - BP Magnus Field Grout Bond Tests," Report ST 58/79, September, 1979.
14. Wimpey Laboratories Ltd., "Burmah Oil Development Limited - Thistle Field Grout Bond Testing, Report on Test Series 1 to 18," Report ST 13/76, July, 1976.
15. Wimpey Laboratories Ltd., "Chevron Petroleum (UK) Limited - Ninian Field - Report on Grout Bond Tests," Report ST 11/77, March, 1977.
16. Wimpey Laboratories Ltd., "Union Oil of Great Britian - Heather Field - Grout Bond Tests Results," Report ST7/77, March 1977.
17. Wimpey Laboratories Ltd., "United Kingdom Department of Energy - The Strength of Grouted Pile/Sleeve Connections - Phase I - Final Report - Static Tests," Report No. ST22/80, April, 1980.
18. Wimpey Laboratories Ltd., "Department of Energy - Grouted Pile/Sleeve Connections, Progress Report No. 3, A Further Review of Static Test Results," Report No. ST 31/79, 1979.
19. Wimpey Laboratories Ltd., "Department of Energy - Grouted Repairs to Steel Offshore Structures, Final Report on Phase 1 - Pipe to Pipe Tests and Preliminary Node Tests," Report ST 28/80, March, 1980.
20. Wimpey Laboratories Ltd., "United Kingdom Department of Energy - Report of the Working Party on the Strength of Grouted Pile Sleeve Connections for Offshore Structures," Report No. ST41/80B, August, 1980.
21. Tebbett, I. E., and Billington C. J., "Recent Developments in the Design of Grouted Connections," Offshore Technology Conference Proceedings, Vol. 1, No. 4890, Houston, TX., May 6-9, 1985.

22. Billington, Collin J., Lewis, Gael H. G., "The Strength of Large Diameter Grouted Connections," Offshore Technology Conference Proceedings, Vol. 1, No. 3083, Houston, TX., May 8-11, 1978.
23. United Kingdom Department of Energy, "Offshore Installations, Guidance on Design and Construction, Amendment No. 4," April, 1984.
24. Karsan, D. I., and Krahl, N. W., " New API Equation for Grouted Pile-to-Structure Connections," Offshore Technology Conference Proceedings, Vol. 1, No. 4715, Houston, TX., May 7-9, 1984.
25. American Petroleum Institute, Recommended Practice for Planning, Designing, and Constructing Fixed Offshore Platforms, RP 2A, 14th Edition, Dallas, TX., July 10, 1984.
26. Paslay Incorporated, "Development of an Analytical Model for the Ultimate Capacity of Axial Loaded Grouted Pile to Jacket Connections," Final Report to API, May, 1980.
27. Chilvers, G. A., "Analysis of the Structural Behavior of Grouted Pile/Sleeve Connections for Offshore Structures," Dissertation Presented to The City University, London, England, February, 1984.
28. Van Lee, R., "Behavior of Grouted Pile Connections," unpublished Master's thesis, Massachusetts Institute of Technology, Cambridge, Massachusetts, June, 1980.
29. Krahl, N. W., and Karsan D. I., " The Strength of Grouted Tubular Connections," Brown and Root International, Inc., Marine Research and Development Department.
30. American Petroleum Institution, API Specification for Fabricated Structural Steel Pipe, API Specification 2B, 3rd Edition, November, 1977.
31. American Society for Testing Materials, Standard Methods and Definitions for Mechanical Testing of Steel Products, ASTM P370-71.
32. Boone, T. J., Yura, J. A., and Hoadley, P. W., "Chord Stress Effects on the Ultimate Strength of Tubular Connections," Phil M. Ferguson Structural Engineering Laboratory, The University of Texas at Austin, Report No. 83-3, December, 1983.

33. Wimpey Laboratories Ltd., "Department of Energy - Review of Offshore Grout Strengths," Report ST 55/79, October, 1979.
34. United Kingdom Department of Energy, "The Strength of Grouted Pile/Sleeve Connections," A Composite Report on a Programme of Tests for the Department of Energy, Offshore Technology Report OTH 86 210, Her Majesty's Stationary Office, London, England.
35. Rabbat, B. G., and Russell, H. G., "Friction Coefficient of Steel on Concrete or Grout," Journal of the Structural Division, ASCE, Vol. 111, No.3, March, 1985, pp. 505-515.
36. Chen, A. C. T., and Chen, W. F., "Constitutive Relations for Concrete," Journal of the Structural Division, ASCE, Vol. 101, No. EM4, August, 1975, pp. 465-481.
37. Fardis, M. N., Alibe, B., and Tassoulas J. L., "Monotonic and Cyclic Constitutive Law for Concrete," Journal of the Engineering Mechanics Division, ASCE, Vol. 109, April, 1983, pp. 516- 536.
38. Ottosen, N. S., "A Failure Criterion of Concrete," Journal of the Engineering Mechanics Division, ASCE, Vol. 109, April, 1983, pp. 527-535.
39. William, K. J. and Warnke, E. P., "Constitutive Model for the Triaxial Behavior of Concrete," International Association of Bridge and Structural Engineers, Seminar on Concrete Structures Subjected to Triaxial Stresses, Paper III-1, Bergamo, Italy, May 17-19, 1974.
40. Kupfer, H., Hilsdorf, H. K., and Rusch, H., "Behavior of Concrete Under Biaxial Stresses," ACI Journal, Vol. 66, No. 8, August, 1969, pp. 656- 666.
41. Martin, J. B., Plasticity: Fundamentals and General Results, The MIT Press, Massachusetts, 1975.
42. Chen, W. F., Plasticity in Reinforced Concrete, McGraw-Hill, New York, 1982.
43. Prager, W., An Introduction to Plasticity, Addison-Wesley, Massachusetts, 1959.
44. Malvern, L. E., Introduction to the Mechanics of a Continuous Medium, Prentice-Hall, New Jersey, 1969.
45. Wimpey Laboratories Ltd., "Department of Energy - Review of Offshore Grout Strengths," Report ST 55/79, October, 1979.

46. Carrasquillo, R. L., Nilson, A. H., and Slate, F. O., "Properties of High Strength Concrete Subjected to Short-term Loads," ACI Journal, Vol. 78, No. 3, May-June, 1981, pp. 171-178.
47. Carrasquillo, R. L., "Microcracking and Engineering Properties of High Strength Concrete," Department of Structural Engineering, School of Civil and Environmental Engineering, Cornell University, Ithaca, New York, Feb., 1980, Report No. 80-1.
48. Perenchio, W. F., and Klieger, P., "Some Physical Properties of High-Strength Concrete," Research and Development Bulletin No. Rd056.01T, Portland Cement Association, Skokie, 1978.
49. Knox, C. L., and Sutton D. L., "An Assessment of Grouting Materials, Placement Methods, Monitoring Equipment, and Floation Equipment for Offshore Structures," Presented at Offshore South East Asia Conference, Febuary, 1980.
50. Wilson, J., "The Modernization of Grouting Methods," Offshore, November, 1978, pp. 67-71.
51. Tragesser, A. F., Dalton, C., and Kay, F. J., "Pressure Grouting: An Improved Method for Offshore Structure Grouting," Offshore Technology Conference, Proceedings, Vol. 1, No. 2082, Houston, TX., May, 1974.
52. Krahl, N. W., Communication to James Jirsa, The University of Texas at Austin, Austin, TX., April 15, 1985.
53. Kennedy, J. G., Sverdvik, T., Domone, P. L., and Adams, M. A. J., "Foundation Grouting of Concrete Gravity Structures," Presented at the European Offshore Petroleum Conference and Exhibition, London, October, 1978.
54. Meith, R. M., Communication to James Jirsa, The University of Texas at Austin, Austin, TX., May 7, 1985.
55. Mott, G. E., Communication to James Jirsa, The University of Texas at Austin, Austin, TX., April 30, 1985.
56. Lloyd, J. P., Maxson, O. G., and House, H. F., "Investigation of Cement Grouts for Offshore Skirt-Pile Connections," Offshore Technology Conference, Proceedings, Vol.1, No. 4891, Houston, TX., May, 1985.

57. Woodward, J. C., "Cement Grouts in Offshore Steel Structures," Proceedings of the Conference on Grouting in Geotechnical Engineering, New Orleans, February, 1982, pp. 836-848.
58. Littlejohn, G. S., "Design of Cement Based Grouts," Proceedings of the Conference on Grouting in Geotechnical Engineering, New Orleans, February, 1982, pp. 35-48.
59. American Petroleum Institute, Specification 10-84, Dallas, TX., 1984.

## VITA

William Bruce Lamport was born in Sioux City, Iowa on January 17, 1956. He entered Iowa Lakes Community College in Esterville, Iowa in September 1975, then transferred to Buena Vista College in September of 1977 and graduated summa cum laude with a degree of Bachelor of Science in Mathematics and Personnel Systems and Management in May 1979. He entered Graduate school at Iowa State University in Ames in September 1979 where he served as a Graduate Research Assistant and Instructor until receiving the degree of Master of Science in Civil Engineering in December 1984. He entered Graduate school at The University of Texas, at Austin in September of 1984. While working towards a degree of Doctor of Philosophy in Civil Engineering he served as a Research Assistant at the Phil M. Ferguson Structural Engineering Laboratory. He married Rochelle Kay Clark in August 1976. His son was born February 1980 and daughter March 1984.

Permanent Address: 818 4th Street S.W.  
Spencer, Iowa 51301

This dissertation was typed by Sharon Cunningham.